The University of Nottingham

School of Physics & Astronomy

Optical properties of nanostructured semiconductors grown by MBE on non-conventional GaAs substrates

by

ALMONTASER BELLAH FATHY KHATAB

Thesis submitted to the University of Nottingham
for the degree of Doctor of Philosophy

February 2014

ABSTRACT

This thesis reports the optical properties of InAlAs QDs and InGaAsN QWs grown by Molecular Beam Epitaxy (MBE) on both the conventional (100) and high Miller index surfaces.

InAlAs QDs on AlGaAs matrix are grown by MBE on the conventional (100) and non-(100) GaAs substrates using different growth conditions, namely, growth temperature, different confinement barriers, and amount of deposited material. PL measurements revealed differences in the optical properties that are caused by substrate orientation effects. The PL emission energies of QDs grown on high Miller index surfaces such as (311)A and (311)B are found to be strongly dependent on the atomic terminated surface [A (Ga face) or B (As face)] of the substrate. The QDs grown on (311)B plane show superior optical properties over QDs grown on (311)A and (100) planes. The optimum structure to achieve the highest optical efficiency of QDs emitting in the visible red part of electromagnetic spectrum (~ 666 nm) consisted of 4.4MLs $Al_{0.35}In_{0.65}As/Al_{0.45}Ga_{0.55}As$ QDs grown on (311)B plane at a growth temperature of 550 ^{0}C.

In addition, a further investigation was carried out to study the effect of post-growth thermal annealing on the optical properties of InAlAs QDs grown on (100), (311)A, and (311)B planes. A noticeable enhancement of the PL intensity at 10 K for all planes was observed by increasing the annealing temperature up to 700 ^{0}C. Thermal annealing of (311)A InAlAs/GaAlAs QDs resulted in a negligible blue shift, while a large blue shift was observed from (311)B and (100) QDs. This is explained by the smaller size of QDs, smaller strain, and lower In segregation from (311)A GaAs orientation.

PL and Transmission Electron Microscopy (TEM) have been used to investigate the optical and structural properties, respectively, of $In_{0.36}Ga_{0.64}As_{1-y}N_y/GaAs$ double quantum wells (QWs) grown both on the conventional (100) and non-(100) GaAs substrates. These include $In_{0.36}Ga_{0.64}As_{1-y}N_y/GaAs$ QWs with three different compositions of nitrogen, namely, 0%, 1%, and 2%.

QWs grown on (311)A GaAs plane show higher nitrogen incorporation over all the other planes. TEM measurements show that (311)B QWs have inferior structural

properties than QWs grown on (311)A and (100). TEM images demonstrated that the (311)B QWs interfaces are undulated and not uniform. In contrast QWs grown on (311)A and (100) display very uniform and very flat interfaces.

The effect of thermal annealing on the optical properties of $In_{0.36}Ga_{0.64}As_{1-y}N_y/GaAs$ double QWs grown on different planes was investigated for two sets of samples having 0% and 1% nitrogen. It was found that annealing at 700 ^{0}C for 30 seconds is the optimum annealing temperature which improves the PL efficiency for all QWs. The PL enhancement is larger in samples with 1% nitrogen than 0%.

PUBLICATIONS AND CONFERENCE PRESENTATIONS

1) A. Khatab, M. Shafi, R. H. Mari, M. Aziz, M. Henini, G. Patriarche, D. Troadec, M. Sadeghi, and S. Wang, Comparative Optical Studies of InGaAs/GaAs Quantum Wells Grown by MBE on (100) and (311)A GaAs planes, Physica Status Solidi (c), 9(7), 1621 (2012).

2) Poster presentation at Semiconducting and Insulating Materials Conference (SIMC- XVI), held at the KTH, Kista-Stokholm, Sweden, June 20-23, (2011), Comparative optical studies of InGaAs/GaAs quantum wells grown by MBE on (100) and (311)A GaAs plane

Work not included in the thesis:

3) A. J. Ramsay, S. J. Boyle, T. M. Godden, R. S. Kolodka, A. F. A. Khatab, J. B. Oliveira, J. Skiba-Szymanska, H. Y. Liu, M. Hopkinson, A. M. Fox, and M. S. Skolnick, Towards Coherent Optical Control of a Single Hole Spin: Rabi Rotation of a Trion Conditional on the Spin State of the Hole, Solid State Communications, 149, 1458 (2009).

4) A. F. A. Khatab, A. J. Ramsay, S. J. Boyle, A. M. Fox, and M. S. Skolnick, Inversion Recovery Measurements of Exciton Fine-Structure Beats in a Single Quantum Dot, Journal of Physics: Conference Series 245**,** 012010 (2010).

5) M. Shafi, R. H. Mari, A. Khatab, D. Taylor, and M. Henini, Deep-level Transient Spectroscopy of GaAs/AlGaAs Multi-Quantum Wells Grown on (100) and (311)B GaAs Substrates, Nanoscale Research Letters, 5, 1948 (2010).

6) R. H. Mari, Muhammad Shafi, Mohsin Aziz, Almontaser Khatab, David Taylor, and Mohamed Henini, Electrical Characterisation of Deep Level Defects in Be-

doped AlGaAs grown on (100) and (311)A GaAs substrates by MBE, Nanoscale Research Letters 6,180 (2011).

7) D. L. Sales, E. Guerrero, J. F. Rodrigo, P. L. Galindo, A. Yáñez, M. Shafi, A. Khatab, R. H. Mari, M. Henini, S. Novikov, M. F. Chisholmand, and S. I. Molina, Distribution of Bismuth Atoms in Epitaxial GaAsBi, Applied Physics Letters, 98, 101902 (2011).

8) M. Shafi, R. H. Mari, A. Khatab, M. Henini, A. Polimeni, M. Capizzi, and M. Hopkinson, Deep levels in H-irradiated $GaAs_{1-x}N_x$ ($x < 0.01$) grown by Molecular Beam Epitaxy, Journal of Applied Physics, 110, 124508 (2011).

9) O. M. Lemine, M. Bououdina, M. Sajieddine, A. M. Al-Saie, M. Shafi, A. Khatab, M. Al-hilali, and M. Henini, Synthesis, Structural, Magnetic and Optical Properties of Nanocrystalline $ZnFe_2O_4$, Physica B, 406, 1989 (2011).

10) M. Ayvacikli, A. Khatab, A. Ege, I. Sabikoglu, M. Henini, and N. Can, Absorption and Photoluminescence Spectroscopy of Er^{3+} -Doped $SrAl_2O_4$ Ceramic Phosphors, Philosophical Magazine Letters, 92(4), 194 (2012).

11) S. U. Satilmis, A. Ege, M. Ayvacikli, A. Khatab, E. Ekdal, E. J. Popovici, M. Henini, and N. Can, Luminescence Characterization of Cerium Doped Yttrium Gadolinium Aluminate Phosphors, Optical Materials, 34, 1921 (2012).

12) R. H. Mari, M. Aziz, M. Shafi, A. Khatab, D. Taylor, and M. Henini, Effect of Epitaxial Layer Thickness on the Deep level Defects in MBE Grown n-Type $Al_{0.33}Ga_{0.67}As$, Physica Status Solidi (C), 9 (7), 1643 (2012).

13) M. Ayvacikli, Z. Kotan, E. Ekdal, Y. Karabulut, A. Canimoglu, J. GarciaGuinea, A. Khatab, M. Henini, and N. Can, Solid State Synthesis of $SrAl_2O_4$: Mn^{2+} Co-doped with Nd^{3+} Phosphor and its Optical Properties, Journal of Luminescence 144, 128 (2013).

14) A. Khatab, O. M. Lemine, A. Alkaoud, A. Falamas, M. Aziz, Y. Galvão Gobatod, M. Henini, Photoluminescence Intensity Enhancement in Self-Assembled InAs Quantum Dots Grown on (311)B, and (100) GaAs Substrates and Coated with Gold Nanoparticles, physica E, 54, 233 (2013).

15) M. Aziz, P. Ferrandis, A. Mesli, R. H. Mari, J. F. Felix, A. Sellai, D. Jameel, N. Al Saqri, A. khatab, D. Taylor, M. Henini, Deep-level Transient Spectroscopy of Interfacial States in “Buffer-Free” p-i-n GaSb/GaAs Devices, Journal Of Applied Physics 114, 134507 (2013).

ACKNOWLEDGEMENTS

"**All praise is due to Allah**, **the Lord of the Worlds"**.

First and foremost, I would like to acknowledge and express my deepest gratitude to my supervisor Prof. **M. Henini** for numerous opportunities he made possible to me during my PhD; from conferences to collaborations. Many thanks for always having faith in my work. I have been a very privileged student.

I would like to thank **Dr. David Scurr** from School of Pharmacy, Nottingham University for helping with SIMS measurements and analysis. Specials thanks to Mr **David Taylor** for his assistance in processing, **Robert Chettle** for electronic support.

I am also grateful to Prof **Yara Gobato,** Universidade Federal de São Carlos, Brazil, for the useful discussions on the PL data.

I would like to thank all my collaborators; Dr **M. Sadeghi**, and Prof **S. Wang** in Photonics Laboratory, Department of Microtechnology and Nanoscience, Chalmers University of Technology, Sweden, for providing me with nitrogen quantum well samples; Drs **G. Patriarche** and **D. Troadec** from CNRS ((France) for TEM characterization.

I would like to thank **Dr M. Shafi, Dr. Riaz Mari** and **Mr Mohsin Aziz** for their support and friendship.

The financial support of University of Cairo, and higher ministry of Education, Egypt is very much appreciated.

Most importantly, thanks to **my mother**, **my beloved wife**, my uncle (**Ibrhaim**) and my whole family for their love and support. Finally, I would like to dedicate this work to the late father.

TABLE OF CONTENTS

LIST OF FIGURES

LIST OF TABLES

CHAPTER 1: INTRODUCTION

1.1 INTRODUCTION

Modern electronic devices (e.g., integrated circuits) are dominated by silicon material. However, there are some basic limitations of Si. These include lower carrier mobility and the indirect nature of its energy-gap as compared for example to GaAs. These properties limit its applications in the field of high speed/frequency electronics and optoelectronics.

The III–V compounds particularly GaAs are alternative and important semiconductors for various device applications. In general, these materials crystallize with a relatively high degree of stoichiometry and can easily be doped as n or p-type. Many of these III– V semiconductors materials (e.g., GaAs, InAs, InP, and InSb) have direct energy gaps in addition to high carrier mobilities (a direct indication of the speed electrons attain and the distance they travel before a scattering event occurs). Therefore, this family of semiconductors offers a wide range of applications in the field of optoelectronic devices for both the detection and generation of electromagnetic radiation, and also in high-speed electronic devices.

Along with the binary III– V compounds, ternary III-V semiconductor materials (e.g. $Al_xGa_{1-x}As$ and $GaAs_{1-x}In_x$) and quaternary (e.g. $Ga_xIn_{1-x}As_{1-y}N_y$) alloys with "tunable" properties have great importance in many versatile applications.

By choosing carefully the composition (i.e., x and y), it is possible to select a particular semiconductor property (e.g., the energy gap) to fit specific device requirements.

In such cases, these compounds are typically grown as epitaxial layers in heterojunction systems on substrates such as GaAs or InP, e.g., $Al_xGa_{1-x}As$ on GaAs, or $Ga_xIn_{1-x}As_yN_{1-y}$ on InP. One of the important parameters that should be taken into account in the epitaxial growth of heterostructures is the lattice constant mismatch between the epitaxial layer and the substrate. A larger lattice mismatch results in the generation of dislocations in the epitaxial layer.

GaAs is often used as substrate material for the epitaxial growth of many III-V semiconductors including InAlAs and GaInNAs. The properties of such substrates have a major effect on the subsequent growth and properties of the epitaxial layers.

The conventional plane direction of GaAs substrate is (100) but other non-conventional plane directions have been used previously. For example, the structural,

optical and electrical properties of III-V based structures are found to change and/or improve by growing on non-conventional (n11) planes. In addition, the study of molecular beam epitaxy (MBE) growth on substrates with different orientations has provided useful information on the epitaxial growth mechanism.

Semiconductors structures grown on high index substrates have fascinating properties which are not found in similar structures grown on (100) oriented substrates such as optical anisotropy[1,2], high hole mobility[3,4] and better optical efficiency[5-11].

In this thesis two emerging and technologically important III-V semiconductors, namely InAlAs Quantum dots and dilute nitrides InGaAsN Quantum wells grown on conventional and non-conventional GaAs substrates, have been studied using structural and optical techniques. A brief summary of the importance of these two materials systems is given in the following sections.

1.2 InAlAs QUANTUM DOTS

Nanotechnology is considered to be one of the corner stone of the next technological revolution after the industrial revolution of the middle of the eighteenth century.

Quantum Dots (QDs) and Quantum Wells (QWs) are nanoscale structures created by confining free electrons (or holes) in a three-dimensional (3D) and two-dimensional (2D) semiconducting matrix, respectively. These nanostructures of confined electrons present many interesting electronic and optoelectronic properties. They are of potential importance for applications in quantum computing, biological labeling, and lasers, to name only a few.

During the last years, considerable interest has been devoted to the fabrication of self-assembled quantum dots (QDs). Stranski-Krastanow (SK) MBE technique has been used to grow these QD nanostructures where 3D confinement regions were obtained. This process leads to a strained epitaxial layer. The deposited material often grows in a layer-by-layer mode until a certain critical thickness, beyond which 3D islands form through what is known as the SK transition.

Compared to the $In_xGa_{(1-x)}As/GaAs$ QDs that emit in the infrared region, relatively few investigations on InAlAs/AlGaAs QDs emitting in the visible region have been

reported in the literature. InAlAs QDs have the advantage of having a luminescence in the red part of the electromagnetic spectrum. This visible wavelength in particular is advantageous for ophthalmology treatment[12]. In addition, it is important for many other different applications ranging from high-density optical storage to photodynamic therapy[13,14]. However, there are some difficulties in fabricating high optical quality InAlAs/AlGaAs QDs. These are due to the incorporation of impurities such as oxygen and formation of group-III vacancies during the growth process[15,16]. The use of high index planes could improve the optical and structural properties of InAlAs/AlGaAs QDs as demonstrated in many other QDs systems.

1.3 DILUTE NITRIDE III-V ALLOYS (InGaAsN)

Lasers emitting in the wavelengths 1.3 μm and 1.55 μm have generated great interest for applications in optical fiber communications. The 1.3 μm wavelength is attractive due to zero dispersion in the silica based optical fiber, and 1.55 μm, has the lowest optical loss. For these reasons, it is important to have a light emitter which works at wavelengths of 1.3 and 1.55 μm.

Currently, telecommunication edge-emitting lasers operating in 1.3 μm and 1.55μm range are based on the conventional GaInAsP alloys grown on InP substrates. However, InP substrates are very expensive compared to GaAs substrates. Therefore, an attractive approach to reduce cost is to fabricate telecommunication lasers on GaAs substrates.

The introduction of N into GaAs leads to giant bowing of bandgap energy, unlike the conventional III-V alloys (shown in Figure 1.1). Incorporation of 1% nitrogen leads to a band gap reduction of GaAs by 125 meV[17]. The lowering of the bandgap energy of GaAs extends the emission wavelength of GaAs-based devices to 1.3 μm (and beyond) and makes it suitable for fabricating infrared lasers which would be alternative to GaInAsP/InP lasers.

Nitrogen incorporation in GaAs lattice introduces a tensile strain. While incorporation of In leads to a compressive strain. Therefore, a lattice matching with GaAs can be achieved by strain compensation between nitrogen and indium.

GaInNAs alloy will be lattice matched to GaAs provided that the In:N ratio is ~ 3:1[18].

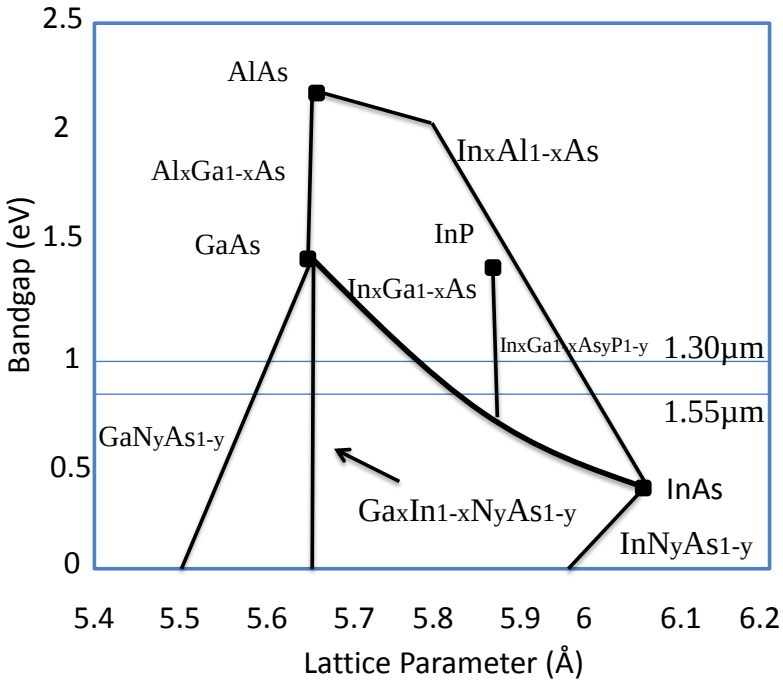

Figure 1.1: Band gap versus lattice constant for various III-V alloys[19].

GaInAsN alloys grown on GaAs have several additional advantages vis-a-vis InGaAsP/InP. GaAs based material systems (InGaAsN/GaAs) offer high conduction band (CB) offset, which provides stronger carrier confinement over GaInAsP /InP leading to devices which have properties that are temperature-insensitive and operate at higher maximum temperatures[20,21]. For example, Tansu et al[22] demonstrated an InGaAsN/GaAs laser with a room-temperature emission wavelength and threshold current density of 1.3 µm and 210-270 A/cm^2, respectively.

Another advantage of GaInNAs is that it can easily be integrated with highly reflective GaAs/AlAs Brag mirrors which are used for the fabrication of vertical cavity surface emitting lasers (VCSELs). Integration techniques of GaAs/AlAs Brag mirrors are already mature.

The first GaAsN alloy was grown by metalorganic chemical vapor deposition[23], and a strong bandgap reduction of the alloys was observed. Shortly after GaAsN was successfully grown using gas source MBE with a N composition of 4%[24].

In order to achieve such longer emission wavelengths, nitrogen incorporation is a major issue that has to be further addressed. Growth mechanisms depend strongly on the surface atomic arrangement and the substrate orientation. Taking into account these two parameters in the growth of dilute III-V nitrides could yield an enhancement of nitrogen incorporation and optical efficiency. However, it was observed that both the optical and crystal quality of N-diluted alloys are partially degraded when the N concentration is increased[25]. In addition, the use of high index GaAs planes could also improve the optical quality of III- V dilute nitrides alloys.

In this thesis, the results of a comprehensive study of the optical properties of InAlAs QDs and InGaAsN QWs grown by MBE on both the conventional (100) and high Miller index surfaces are presented.

1.4 ORGANIZATION OF THE THESIS

This thesis is organized as follows:

Chapter 1 contains the research motivations and outlay of the thesis.

Chapter 2 is devoted to the description of the fundamental concepts of semiconductors, including their crystal structure and optical processes. The principles of III-V compound heterostructures and dilute III-V nitride alloys are presented. The importance and growth of III-V compound materials on high index planes will be also covered

Chapter 3 provides information on fundamental concepts and molecular beam epitaxial growth of low dimensional semiconductor structures.

Chapter 4 explains the experimental techniques used in this thesis including Photoluminescence (PL), Transmission electron microscopy (TEM), and Secondary

ion mass spectroscopy (SIMS). The description of their hardware and soft software implementation will be presented.

Chapter 5 is based on the PL experimental results for a set of InAlAs QDs grown at different growth conditions (growth temperature, amount of material, different capping composition) on (100), (311)A and (311)B GaAs substrates.

Chapter 6 reports the effect of annealing on the as-grown InAlAs QDs grown on (100), (311)A and (311)B GaAs substrates

Chapter 7 presents the effect of nitrogen incorporation on the optical and structural properties of GaInNAs/GaAs double quantum well (DQWs) grown on different GaAs substrate orientations, namely (100), (311)A, and (311)B.

Chapter 8 describes the effect of annealing on the as-grown $GaInAs_{1-x}N_x$ (x=0, and 1%) double QWs grown on (100), (311)A and (311)B GaAs substrates.

Chapter 9 is based on the overall conclusion of the research work carried out in this thesis and suggestions for future work.

REFERENCES

[1] E. C. Valadares, Physical Review B, 46 (1992) 3935.

[2] R. Notzel, N. N. Ledentsov, L. Daweritz, K. Ploog, M. Hohenstein, Physical Review B, 45 (1992) 3507.

[3] W. I. Wang, E. E. Mendez, Y. Iye, B. Lee, M. H. Kim, and G. E. Stillman, Journal of Applied physics, 60, 1834, (1986).

[4] A. Davies, J. Frost, D. Ritchie, D. Peacock, R. Newbury, E. Linfield, M. Pepper, and G. Jones, Journal of Crystal Growth, 111, 318 (1991).

[5] D. I. Lubyshev, P. P. Gonzalez-Borrero, E. Marega, E. Petitprez, and P. Basmaji, The Journal of Vacuum Science and Technology B, 14 (3), 2212 (1996).

[6] P. O. Vaccaro, M. Hirai, K. Fujita, and T. Watanabe, Journal of Physics D: Applied Physics, 29 (9), 2221(1996).

[7] R. Notzel, Semiconductor Science and Technology, 11 (10), 1365 (1996).

[8] K. Nishi, T. Anan, A. Gomyo, S. Kohmoto, and S. Sugou, Applied Physics Letters, 70 (26) 3579, (1997).

[9] M. Kawabe, Y. J. Chen, S. Nakajima, and K. Akahare, Japanese Journal of Applied Physics, 36 (6B) 4078 (1997).

[10] K. Nishi, R. Mirin, D. Leonard, G. Medeiros-Ribeiro, P. M. Petroff, and A. Gossard, Journal of Applied Physics, 80 (6), 3466 (1996).

[11] M. Henini, A. Polimeni, A. Patane, L. Eavesa, P.C. Maina, and G. Hill, Microelectronics Journal, 30, 319 (1999).

[12] D. J. Browning, and C. M. Fraser. Ophthalmology , 112, 1054 (2005).

[13] R. Singh, D. Bull, F. P. Dabkowski, E. Clausen, and A. K. Chin, Applied Physics Letters, 75, 2002 (1999).

[14] K. Hinzer, J. Lapointe, Y. Feng, A. Delage, S. Fafard, A. J. SpringThorpe, and E. M. Griswold, Journal of Applied Physics, 87, 1496 (2000).

[15] W. I. Wang, S. Judaprawira, C. E. C. Wood, and L. F. Eastman, Applied Physics Letters, 38, 708 (1981).

[16] Y. Horikoshi, M. Kawashima, and H. Yamaguchi, Applied Physics Letters, 50, 1686 (1987).

[17] S. Tixier, M. Adamcyk, T. Tiedje, S. Francoeur, A. Mascarenhas, P. Wei, and F. Schiettekatte, Applied Physics Letters, 82, 2245, (2003).

[18] L. Bellaiche, Applied Physics Letters, 75, 2578, (1999).

[19] Dilute Nitride Semiconductors, Edited by M. Henini, Elsevier Science (2005).

[20] M. Kondow, S. Nakatsuka, T. Kikatani, Y. Yazawa, and M. Okai, Japanese Journal of Applied Physics, 35(11), 5711 (1996).

[21] M. Kondow, K. Uomi, A. Niwa, T. Kitatani, S. Watahiki, and Y. Yazawa, Japanese Journal of Applied Physics, 33, 1273 (1996).

[22] N. Tansu, JY. Yeh, and L. Mawst, Applied Physics letter, 83, 2512, (2003).

[23] M. Weyers, and M. Sato. Japanese Journal of Applied Physics, 853, 31, (1992).

[24] M. Kondow, K. Uomi, K. Hosomi, and T. Mozume, Japanese Journal of Applied Physics, L1056, 33, (1994).

[25] H. P. Xin, K. L. Kavanagh, and C. W. Tu, Journal of Crystal Growth, 208, 145 (2000).

CHAPTER 2: FUNDAMENTAL CONCEPTS OF SEMICONDUCTORS

In this chapter the fundamental concepts of semiconductors will be presented including their crystal structure and optical processes. The emphasis will be on heterostructures and meaning of high index plane since these form a key aspect to understanding the optical properties of quantum dots and quantum wells investigated in this work.

2.1 INTRODUCTION

In the last thirty years substantial advances have been realised in the research and applications of semiconductors. It is well known that semiconductor technology has a great impact on our society. For example it is well-known that personal computers, which are in almost everyone's house and office, have changed the way we communicate. Semiconductor applications are present everywhere around us: on roads, in houses, in schools, and even in our pockets. Semiconductor research is still attracting increased interest at all scientific levels because of their multitude of applications.

Solid materials are generally classified according to the value of the energy gap between their conduction and valence bands. Most of the common materials have energy gaps in the range from zero to few electron volts (eV). According to this classification materials having an energy gap of ~ 0 eV are referred to as metals or semi-metals. On the other hand, materials with energy gaps larger than 3 eV are frequently known as insulators, whereas semiconductor materials have energy gaps bridging from ~0.1 eV to ~ 3 eV.

Semiconductors behave as insulators at absolute zero temperature (T = 0K) but their electrical conductivity increases rapidly with increasing temperature. Furthermore, the electrical conductivity can be controlled by adding small amounts of certain impurities, so-called dopants, or by illumination with particular wavelengths of light. These properties contrast strongly with those of good conductors such as metals, which contain large densities of free electrons that originate from the valence electrons of the metal atoms. The electrical conductivity of metals, which is many orders of magnitude larger than that of semiconductors, decreases relatively weakly

with increasing temperature and, to a good approximation, is not affected by small levels of impurities or illumination.

Semiconductor materials are classified according to their chemical composition. There are elementary semiconductors such as Si and Ge which are elements of group IV of the periodic table of elements. Some of the elemental semiconductors and their properties are listed in Table 2.1.

Table 2.1: lattice constant (a), energy gap (E_g) at 300K, type of energy gap, and lattice structure of group IV elements.

Material	a (nm)	E_g (eV)	Type	Structure
Diamond (C)	0.357	5.48	Indirect	Cubic
Silicon (Si)	0.543	1.12	Indirect	Cubic
Germanium (Ge)	0.566	0.664	Indirect	Cubic

Compound semiconductor materials are formed from two or more elements from the different groups of the periodic table. For example GaAs is the best known III-V compound material, which is formed by combining Gallium (Ga), group III element, with Arsenic (As), group V element. Other III-V compound semiconductors include InP and GaP. One can combine GaAs and AlAs to obtain ternary III-V compound $Al_xGa_{1-x}As$, where x and (1-x) represent the content of Al and Ga in the alloy, respectively. Another important class of semiconductors is known as II-VI compound materials such as Zinc Sulphide (ZnS) and Mercury Cadmium Telluride (HgCdTe). Most important III-V compounds are presented in Table 2.2 together with their respective properties.

Table 2.2: lattice constant, energy gap, type and crystal structure of most important III-V compound semiconductors[1].

Material	a (nm)	E_g (eV)	Type	Structure
GaAs	0.565	1.424	Direct	Cubic
InAs	0.606	0.354	Direct	Cubic
AlAs	0.566	2.15	Indirect	Cubic

GaN	a=0.318, c=0.517	3.44	Direct	Hexagonal
InN	a=0.354, c=0.870	1.89	Direct	Hexagonal

The electrical conductivity of semiconductors can be controlled widely both in terms of polarity and magnitude by means of (i) intentional incorporation of impurities (e.g. doping), (ii) temperature (i.e. thermal excitation), and (iii) optical excitation (i.e excitation with photons having energies greater than the energy gap (Eg). The following section discusses another type of semiconductor classification based on their type of doping.

2.2 INTRINSIC AND EXTRINSIC SEMICONDUCTORS

Intrinsic semiconductors are known as undoped semiconductors or pure semiconductors. Intrinsic semiconductors possess equal number of electrons (n) and holes (h) in the conduction and valence bands, respectively, at 0K and behave as insulators at this absolute temperature.

$$n = p = n_i \qquad 2.1$$

Where n_i is the intrinsic carrier concentration.

There is, therefore, no flow of charge carrier to contribute to its conductivity unless a thermal excitation or photo-excitation is applied. However, the current can flow through these types of materials at a certain temperature which is sufficient to provide the thermal energy to excite the electrons from the valence band (VB) to the conduction band (CB). At room temperature, relatively few electrons have enough thermal energy to make the jump from VB to CB. For example at room temperature intrinsic Silicon (Si) has n_i value equal to 1.45×10^{10} cm^{-3}.

Extrinsic semiconductors are obtained by introducing different atoms, called dopant atoms, into the host crystal. Two types of extrinsic materials can be fabricated as shown in Figure 2.1 for the case of silicon semiconductor:

(1) n-type material: the dopant atoms added to the semiconductor crystal are called donor atoms.

For silicon, phosphorus (P), arsenic (As) or antimony (Sb) can be used as donors. These donors that belong to column V in the periodic table have five electrons in their outermost shell. When these atoms are incorporated in the silicon crystal, one of the electrons in this shell can easily jump to the conduction band, leaving a positively charged atom behind. This process is sometimes called "activation" or "ionization" of the donor atoms. This energy is very small compared to the silicon band gap so it can easily be ionized at room temperature. The positively charged donor atoms that are left behind after ionization is immobile and does not contribute to electrical conduction. The electron leaving the atom is free and contribute to the electron concentration (n). Because the activation energy is low, almost all of the donor atoms intentionally incorporated in the crystal will give an electron to the conduction band at room temperature. So if N_D is the donor concentration with one additional valence electron, for an n-type material at $T \neq 0K$, excess electrons from dopant atoms may be excited thermally from their states within the forbidden band gap which is located slightly below the bottom of the conduction band, increasing the free electron density (n_0).

$$n_0 \approx N_D \ (cm^{-3}) \qquad 2.2$$

(2) p-type material: the dopant atoms in this case are named acceptor atoms. In silicon, Boron (B), Aluminium (Al) and Gallium (Ga) are employed as acceptors. These atoms which belong to column III have three electrons in their outermost shell. When these atoms are added in the silicon crystal, one of the electrons in the silicon valence band can easily jump to the valence shell of one of the acceptor atoms, leaving a hole behind and making the acceptor atom negatively charged. The negatively charged acceptor atom is immobile and does not contribute to the electrical conduction. The hole left behind contributes to the hole concentration (p). Because the activation energy at room temperature is low almost all of the

incorporated acceptor atoms will accept an electron from the valence band. So if N_A is the acceptor concentration, for a p-type material at room temperature excess free hole density (p_0) in valence band is:

$$p_0 \approx N_A \ (cm^{-3}) \qquad 2.3$$

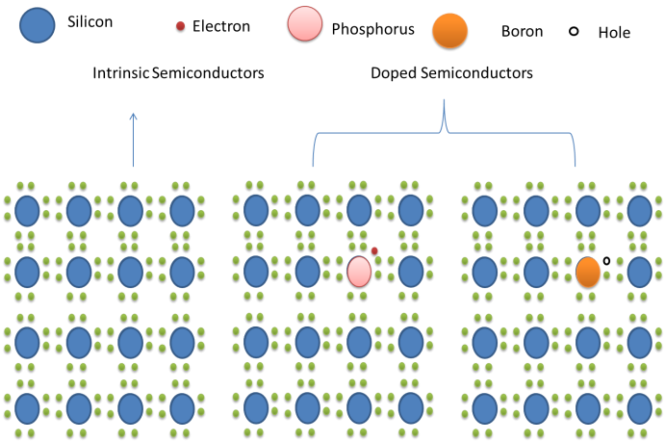

Figure 2.1: intrinsic and extrinsic silicon.

2.3 CRYSTAL STRUCTURE OF SEMICONDUCTORS

High performance semiconductor devices are based on crystalline materials. Crystals are periodic structures made up of identical building blocks. To define the crystal structure, two important concepts are introduced.

1- The lattice represents a set of points in space forming a periodic structure.
2- A building block of atoms called the basis is then attached to each lattice point yielding the physical crystal structure. This block may be a single atom or group of atoms as shown in Figure 2.2.

The crystalline structure is now produced by attaching the basis to each of these lattice points.

Lattice + basis = crystal structure

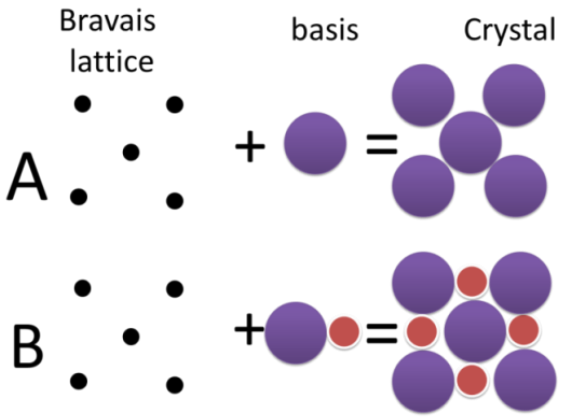

Figure 2.2: The formation of the crystal structure from the combination of lattice and basis is shown. The basis may consist of one atom (A) or group of atoms (B).

To define a lattice one need to define three primitive translation vectors a_1, a_2, and a3, such that any lattice point C can be obtained from any other lattice point R by a translation

$$\mathbf{C} = \mathbf{R} + c_1\mathbf{a}_1 + c_2\mathbf{a}_2 + c_3\mathbf{a}_3 \qquad 2.4$$

Where c_1, c_2, c_3 are integers.

The translation vectors $\mathbf{a}_1$, $\mathbf{a}_2$, and $\mathbf{a}_3$ are called primitive if the volume of the cell formed by them is the smallest possible. The volume cell enclosed by the primitive vectors is called the primitive unit cell. There is no unique way to choose the primitive vectors. It is possible to define more than one set of primitive vectors for a given lattice, and often the choice depends upon convenience.

2.3.1 Basic Lattice Types

There are 14 types of lattices. These lattice classes are defined by the relationships between the primitive vectors $\mathbf{a}_1$, $\mathbf{a}_2$, and $\mathbf{a}_3$, and the angles α, β, and γ between them. The most important types of primitive cells, known as cubic and hexagonal lattices, underlay the structure taken by all semiconductors.

There are 3 kinds of cubic lattices: simple cubic, body centred cubic (bbc), and face centred cubic (fcc).

The simple cubic lattice shown in Figure 2.3 is generated by the primitive vectors a**x**, a**y**, a**z** where **x, y, z** are unit vectors.

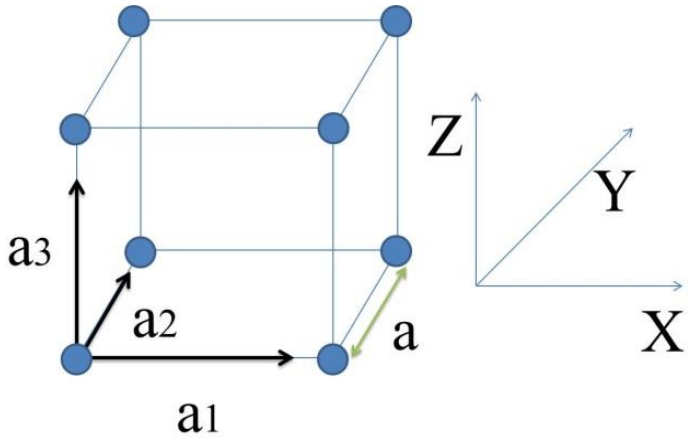

Figure 2.3: A simple cubic lattice showing the primitive vectors. The crystal is produced by repeating the cubic cell through space.

The bcc lattice, shown in Figure 2.4 can be generated from the simple cubic structure by placing a lattice point at the centre of the cube. If $\hat{x}$, $\hat{y}$, and $\hat{z}$ are three orthogonal unit vectors, then a set of primitive vectors for the bbc lattice is given by

$$a_1 = a\,\hat{x}\,,\ a_2 = a\,\hat{y}\,,\ a_3 = \frac{a}{2}(\hat{x}+\hat{y}+\hat{z}) \qquad 2.5$$

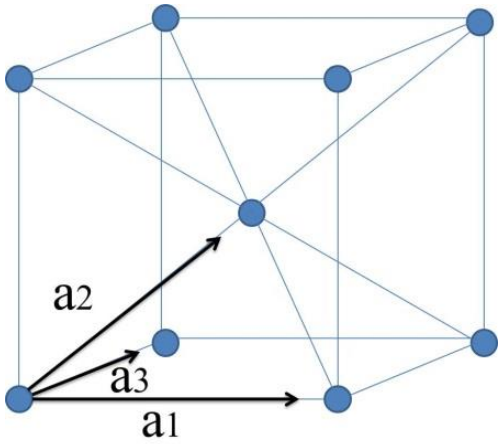

Figure 2.4: The body centred cubic lattice along with a choice of primitive vectors.

The fcc lattice, shown in Figure 2.5, can be obtained by extending the cubic lattice by adding an atom to the center of each face of the cube (leading to a lattice with 14 atoms). The lattice constant a is the side dimension of this cube.

A symmetric set of primitive vectors for the fcc lattice are given by:

$$a_1 = \frac{a}{2}(\hat{y} + \hat{z}), a_2 = \frac{a}{2}(\hat{z} + \hat{x}), a_3 = \frac{a}{2}(\hat{x} + \hat{y}) \qquad 2.6$$

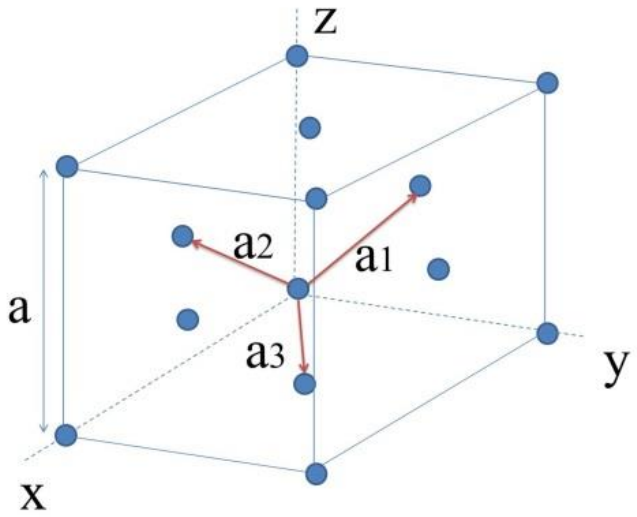

Figure 2.5: Primitive basis vectors for the face centered cubic lattice**.**

The semiconductors studied in this work have an underlying fcc lattice. The full lattice structure as illustrated in Figure 2.6 combines two of these fcc lattices, one lattice interpenetrating the other (i.e., the corner of one cube is positioned within the interior of the other cube, with the faces remaining parallel). The coordinates of the two basis atoms are (000) and $\left(\frac{a}{4},\frac{a}{4},\frac{a}{4}\right)$. For the III-V and II-VI semiconductors with this fcc lattice foundation, one fcc lattice is constructed from one type of element (e.g., atom from group III) and the second fcc lattice is constructed from the other type of element (e.g., atom from group V). In the case of ternary and quaternary semiconductors, elements from the same atomic group are placed on the same fcc lattice. All bonds between atoms occur between atoms in different fcc

lattices. For example, all Ga atoms in the GaAs crystal are located on one of the fcc lattices and are bonded to As atoms, all of which appear on the second fcc lattice. The interatomic distances between neighbouring atoms are therefore less than the lattice constant. If the two fcc lattices contain elements from different groups of the periodic chart, the overall crystal structure is called the zinc blende lattice. Most popular elemental semiconductor materials such as silicon, germanium, and carbon have the diamond like structure, which is formed between the same types of atoms. In diamond structure each atom makes bonds with four adjacent atoms of the same group. The bonds between silicon atoms in the silicon crystal extend between fcc sublattices.

Although the common semiconductor materials share this basic diamond/zinc blende lattice structure, some semiconductor crystals are based on a hexagonal close-packed (hcp) lattice. Typical examples are CdS and CdSe from the II-VI semiconductor family. In this example, all the Cd atoms are located on one hcp lattice while the other atom (S or Se) is located on a second hcp lattice. Similarly to the diamond and zinc blende lattices described above, the complete lattice is constructed by interpenetrating these two hcp lattices. The overall crystal structure is called a wurtzite lattice.

IV-VI semiconductors (PbS, PbSe, PbTe, and SnTe) exhibit a narrow band gap and have been used for infrared detectors. Their lattice structure is the simple cubic lattice, also the so-called NaCl lattice.

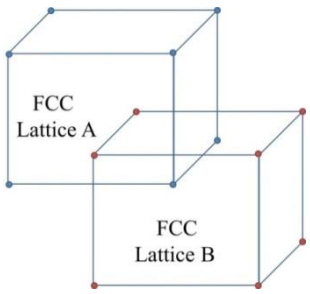

Figure 2.6: The zinc blende crystal structure consists of the interpenetrating fcc lattices, one displaced from the other by a distance $\left(\frac{a}{4},\frac{a}{4},\frac{a}{4}\right)$ along the body diagonal. The underlying Bravais lattice is fcc with a two atoms basis. The positions of the two atoms is (000) and $\left(\frac{a}{4},\frac{a}{4},\frac{a}{4}\right)$.

2.3.2 The Reciprocal Lattice and Miller Indices

Miller indices are used to label crystal planes with the familiar (hkl) notation based on their intercepts with the crystallographic reference axes. As for directions, negative indices are often indicated by a bar or minus sign written above the corresponding index, e.g. $(00\bar{1})$. Every crystal has two lattices associated with it, a crystal lattice and a reciprocal lattice. A diffraction pattern of a crystal is a map of the reciprocal lattice of the crystal.
The reciprocal basis vectors can be derived as follow:

The crystalline solid can be described by a, b, and c, which are the primitive basis vectors in such a way that the crystal structure remains the same under translation through a vector. The translation vector is an integral multiple of the basis vectors (a, b, and c) and is defined as

$$R = ma + nb + rc \qquad 2.7$$

here m, n, and r are integers and a, b ,and c are the primitive vectors

This definition then leads to expressions for the reciprocal basis vectors:

$$\mathbf{a^*} = (\mathbf{b} \times \mathbf{c}) / \mathbf{a} \cdot (\mathbf{b} \times \mathbf{c}) \qquad 2.8$$

$$\mathbf{b^*} = (\mathbf{c} \times \mathbf{a}) / \mathbf{a} \cdot (\mathbf{b} \times \mathbf{c}) \qquad 2.9$$

$$\mathbf{c^*} = (\mathbf{a} \times \mathbf{b}) / \mathbf{a} \cdot (\mathbf{b} \times \mathbf{c}) \qquad 2.10$$

The reciprocal lattice vector **g**, with components (h,k,l) is perpendicular to the plane with Miller indices (hkl), so often denoted as $\mathbf{g}_{hkl}$:

$$\mathbf{g}_{hkl} = ha^* + kb^* + lc^* \qquad 2.11$$

And

$$|\mathbf{g}_{hkl}| = 1/d_{hkl} \qquad 2.12$$

Where d_{hkl} is the spacing between lattice planes

Figure 2.7 shows some planes of a cubic lattice with their Miller indices. Similarly to directions, some of the planes are also equivalent for symmetry reasons, e.g. planes (110), $(\bar{1}10)$, $(0\bar{1}1)$ etc. in a cubic crystal. Such equivalent planes are collectively denoted as {110}. The method of finding the Miller indices is discussed below.
Consider a three dimensional crystal plane whose three basis vectors are **x**, **y**, and **z**. The Miller indices of this plane can be obtained in the following way:

(i) Find the intercepts of the planes along three basis vectors (these intercepts can be in terms of lattice constant or primitive cells).

(ii) Take the reciprocals of intercepts along each axis.

(iii) Reduce the reciprocals of these intercepts into smallest values in such a way that the smallest three integers have the same ratio.

The result obtained from above three steps is enclosed in a parenthesis (hkl) called the Miller indices of a single plane with intercepts at 1/h, 1/k, and 1/l on the **x**, **y**, and **z**-axis, respectively. However, {hkl} represents the Miller indices of a full set of planes of equivalent symmetry.

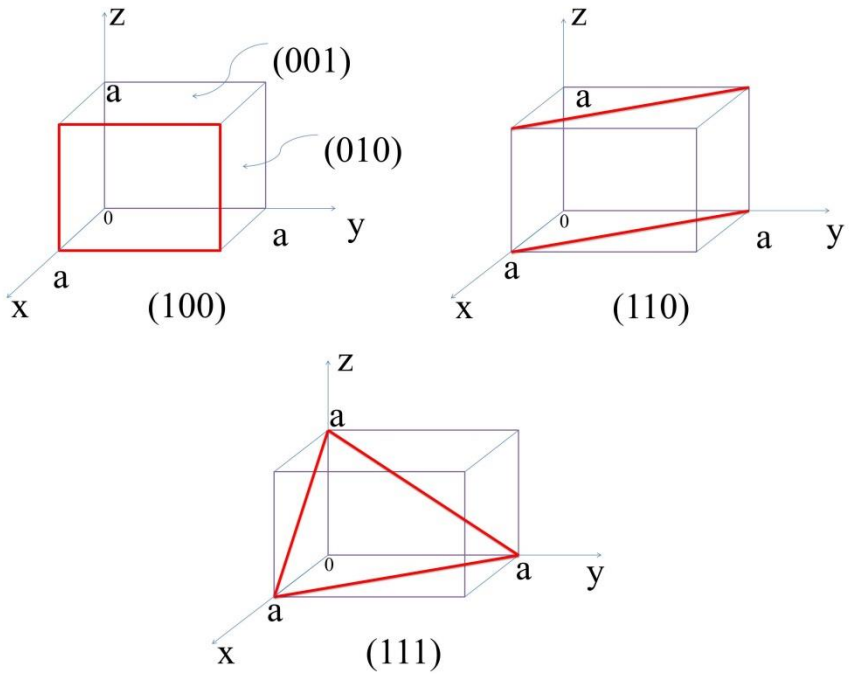

Figure 2.7: Miller indices of some important planes in a cubic crystal.

Table 2.3: Miller indices and their represented plane or direction of a crystal surface[2].

Miller Indices	Description of plane or direction
(h k l)	For a plane that intercepts l/h, l/k, 1/l on the x-, *y*-, and z-axis, respectively.
($\bar{h}$ k l)	For a plane that intercepts the negative x-axis.
{ h k l }	For a full set of planes of equivalent symmetry, such as {100} for (100), (0l0), (00 l) , ($\bar{1}$ 00) , (0 $\bar{1}$ 0) , and(00 $\bar{1}$) in cubic symmetry.
[h k l]	For a direction of a crystal such as [100] for the x-axis.
$\langle hkl \rangle$	For a full set of equivalent directions.

The (100), (110) and (111) planes are the so-called low index planes of a cubic crystal system (the "low" refers to the Miller indices being small numbers; 0 or 1 in this case). Whereas, values greater than these are called high index planes such as (210).

2.3.3 Conventional and Non-Conventional Plane

The interest in the growth of III-V compound semiconductors such as GaAs and AlGaAs on high index planes has increased tremendously over the last decade. The structural, optical and electrical properties of III-V based structures are found to improve by growing on (n11) planes. The study of the molecular beam epitaxy (MBE) growth on substrates with different orientations could provide useful information on the epitaxial growth mechanism as well and on the physics of dopant incorporation. The use of high Miller index substrate orientations permits the engineering of quantum dots properties such as shape, size distribution, and transition energy and emission polarisation, thus opening a wide range of device design opportunities. The growth of epitaxial layers on high-index planes represents a step forward in semiconductor material engineering, as it offers an additional degree of freedom to develop applications with improved properties with respect to the conventional (100) grown devices. The interest in non-(100) semiconductor structures is manifold and concerns growth, impurity incorporation, electronic properties, lasing performance, and piezoelectric effects. To mention a few examples, the use of non (001) substrates has allowed the fabrication of ultrahigh mobility two-dimensional hole gases in GaAs/AlGaAs heterostructures, high-performance InAs/GaAs quantum dot (QD) lasers, InGaAs/GaAs QDs with enhanced piezoelectric effects, and GaMnAs epilayers with modified Mn incorporation and magnetic anisotropies[3-6].

The possibility of changing and improving the fundamental material properties, growth mechanisms, surface kinetics and impurity incorporation by growing on crystal orientations other than (100) has motivated a strong effort to study these aspects. Some very interesting features have emerged concerning the piezoelectric

effect, the dopant incorporation, the self-organization of microstructures, the ordering of ternary alloys and the over layer strain[7].

Many high index polarized surfaces, such as GaAs (311)A[8] and (311)B[9-13], GaAs (411)A[14] and (411) B[15], have drawn greater attention because QDs grown on theses surfaces have some unique properties, such as the narrow size distribution and high QDs density. These structure properties can further improve the performance of devices. It is worth mentioning here that for the GaAs high index planes, A and B refer to Ga and As surface, respectively.

Tilted substrates, in which the surface is other than (100), allow device researchers to make use of extra parameters in the search for better technological structures due to the fact that the natural roughness on high index substrates influences the dot formation and the electronic properties of the dots, such that the photoluminescence (PL) energy, the PL intensity, or the PL line width can change according to the substrate orientation. Figure 2.8 illustrates such (100) plane and non-(100) planes, also called tilted or high index planes.

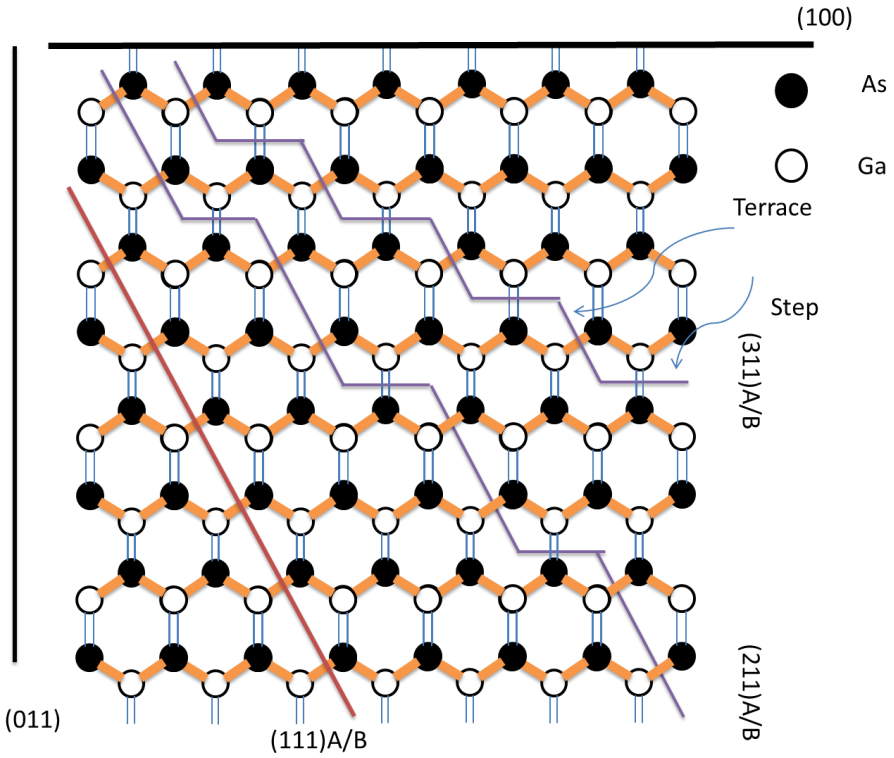

Figure 2.8: illustration of (100) plane and non-100 planes (tilted or high index planes). The black and white circles represent group V and group III atoms, respectively.

The surface structure of the (211) and (311) planes are very similar, with components of both (100) and (111) bonding geometries. The microscopic surface structure of (211)A can be considered to be composed of periodic steps with one (100) step edge atom and two (111) terrace atoms, while the (311) surface is composed of equal numbers of (100) step edge and (111) terrace atoms. The (311)B surface has a sequence of pairs consisting of an As surface atom with two dangling bonds, as for the (100) configuration, and a Ga surface atom with one dangling bond, as for the (111)A configuration that is identical to that of the (311)A surface with the Ga and As atoms interchanged.

Depending on the polarity of the (111) component, the three-bond site can be group III atom (Ga) site for (311)A orientation or group V atom (As) site for (311)B orientation.

Each (111)B surface atom has one single-dangling bond and each (100) surface atom has one double-dangling bond. In contrast to this, the (211)B, (311)B, and (511)B surfaces are composed of both single-dangling bond sites and double-dangling bond sites, making the surfaces partially (111)-like and partially (100)-like. In the case of the (211)B surface (Figure 2.9), there are twice as many single-dangling bond sites as there are double-dangling bond sites. Thus, the (111)-like character outweighs the (100)-like character.

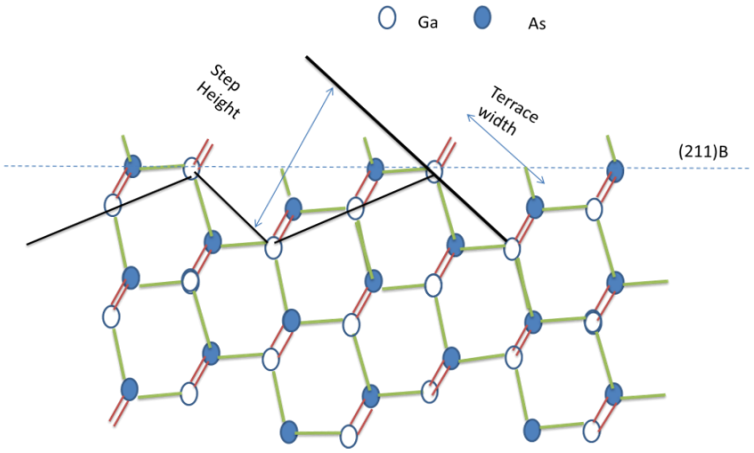

Figure 2.9: (211)B GaAs viewed along the (011) direction. The heavy line highlights the (100) terrace structure[16].

The (311)B surface (Figure 2.10) consists of equal densities of single- and double-dangling bond sites resulting in equal weighting of the (111)-like and (l00)-like

components. For the (51l)B (Figure 2.11) orientation and higher index planes, the (l00)-like double dangling bonds outnumber the (111)-like single-dangling bonds and thus the (l00)-like character will dominate.

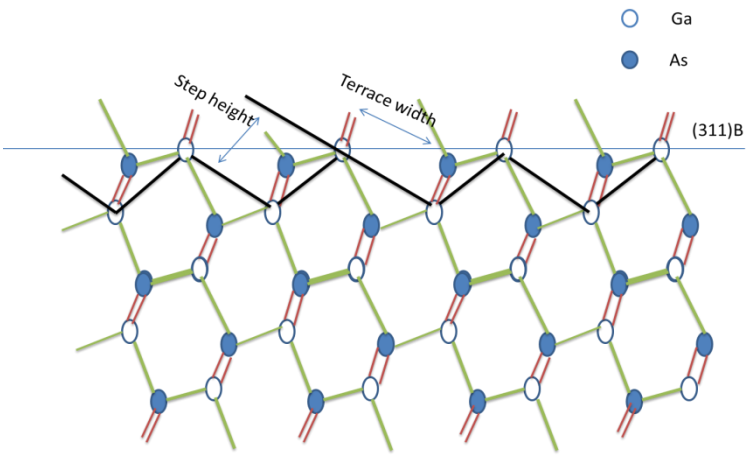

Figure 2.10: (311)B GaAs viewed along the (011) direction. The heavy line highlights the (100) terrace structure[16].

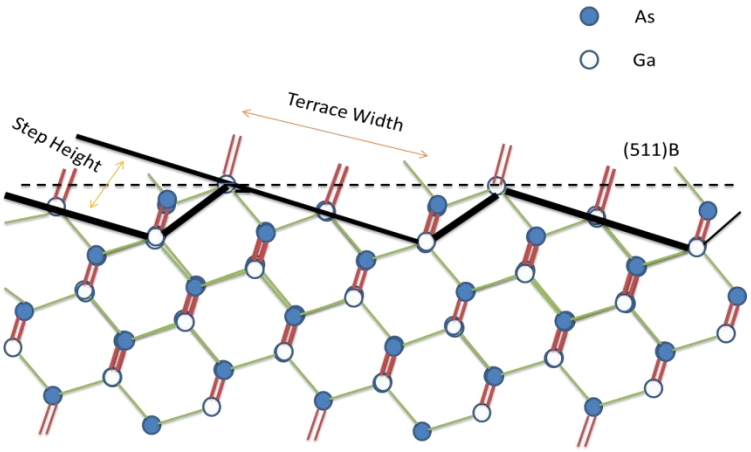

Figure 2.11: (511)B GaAs viewed along the (011) direction. The heavy line highlights the (100) terrace structure[16]

Compared with an atomically flat (100) surface, a (311) plane has corrugations due to the presence of edge steps[17,18]. This could give rise to the formation of dots having microscopic and electronic properties quite different from the ones formed on (100). The differences between (311)B and (311)A substrates can be explained by taking into account the surface polarity.

The major difference between differently misoriented substrates is in the surface step density. The surface corresponding to the maximum step density is the (311) orientation.

2.4 ENERGY BAND GAP

The band structure of crystalline solids, that is Energy –Momentum (E- *k*) relation, is obtained by solving the Schrodinger equation of one-electron problem. For any semiconductor there is a forbidden energy region in which allowed energy states cannot exist. Energy regions or energy bands are permitted above and below this energy gap. The upper bands and lower bands are called the conduction bands and valence bands, respectively. The separation between the energy of the lowest conduction band (E_c) and that of the highest valence band (E_v) is called the band gap Eg which is the most important parameter of semiconductors

The shape of the conduction band and valence band near $k = 0$ is approximately parabolic and their energy is given by:-

$$E_C = E_g + \frac{h^2 k^2}{8\pi^2 m_e^*} \qquad 2.13$$

$$E_V = E_g - \frac{h^2 k^2}{8\pi^2 m_h^*} \qquad 2.14$$

Where h is the Plank's constant, m_e^* and m_h^* are the effective mass of electron and hole, respectively.

The energy-momentum relationship is described by:-

$$E = \frac{p^2}{2m^*} \qquad 2.15$$

The effective mass can be obtained from the second derivative of E with respect to *p*

$$m_e^* = \left(\frac{d^2 E}{dp^2} \right)^{-1} \qquad 2.16$$

Similar expression can be obtained for holes (with subscript *h* instead of e). The electrons and holes are treated as free particles by assigning them a modified mass, the effective mass, which combines their potential and kinetic energies into a single kinetic-like energy. As an example, the semiconductor GaAs has an electron effective mass $m_e^* = 0.067 m_0$ and a hole effective mass $m_h^* = 0.35 m_0$ where m_0 is the free electron mass.

At zero Kelvin, all the electrons are confined to the valence band and the material behaves as an insulator. Above zero Kelvin, some electrons can have sufficient energy to make a transition to the conduction band and contribute to the electrical conduction process

Figure 2.12 shows a simplified energy–band structure of semiconductors. The electron energy is conventionally defined to be positive when measured upward and the hole energy is positive when measured downwards.

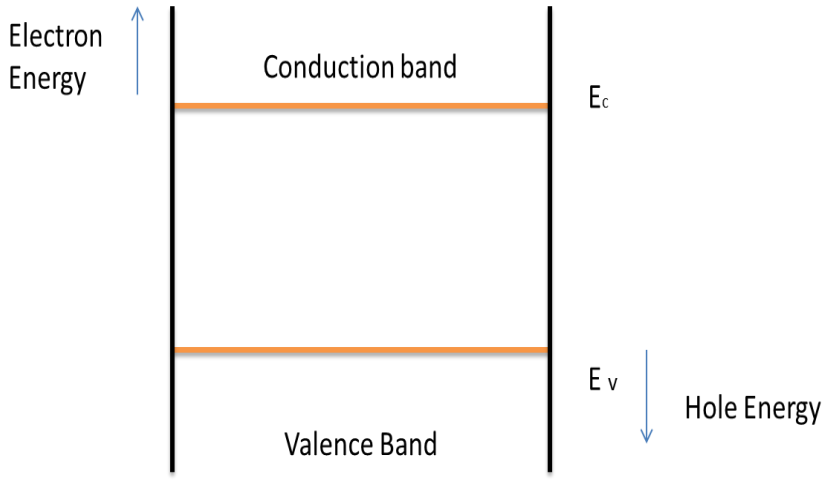

Figure 2.12: simplified energy–band structures of semiconductors.

2.5 DIRECT AND INDIRECT BAND GAP SEMICONDUCTOR

Bulk semiconductors are characterized by the structure of their conduction and valence bands as being direct or indirect. The optical properties of direct gap semiconductors differ considerably from those of indirect gap semiconductors. Direct semiconductor (e.g. GaAs, CdS) are characterized by having the minimum transition energy to promote an electron from the valence band to the conduction band without a change in the electron momentum (the energy is known as the band-gap). For indirect semiconductors, however, excitation at the band gap energy must be accompanied by a change in the electron's momentum (supplied by a phonon).

In indirect semiconductors, the only possible scenario for interband optical transitions is that a phonon causes a vertical virtual transition at $k = 0$ with subsequent electron-phonon scattering processes, i.e., optical transitions are allowed only if phonons are absorbed or emitted to conserve the crystal momentum[19], as shown schematically in Figure 2.13. In the optical absorption process a phonon is emitted or absorbed to conserve the crystal momentum.

$$E_{electron} = E_{photon} \pm E_{phonon} \qquad 2.17$$

and

$$\boldsymbol{k}_{\mathbf{electron}} = \pm \boldsymbol{k}_{phonon} \qquad 2.18$$

In optical emission, a similar process takes place.

$$E_{photon} = E_{electron} \pm E_{phonon} \qquad 2.19$$

In optical transition processes in bulk silicon for example, phonons play an important role, including transverse optical (TO) phonons (~56 meV) and transverse acoustic (TA) phonons (~18.7 meV)[19].

However, it has been shown that, accompanying the reduction in size of silicon nanostructures, such as in silicon nanocrystals and porous silicon, zero-phonon optical transitions are partially allowed and the oscillator strength of zero-phonon transitions is significantly enhanced. This increases the radiative recombination rate via a direct band-to-band recombination process[20-22].

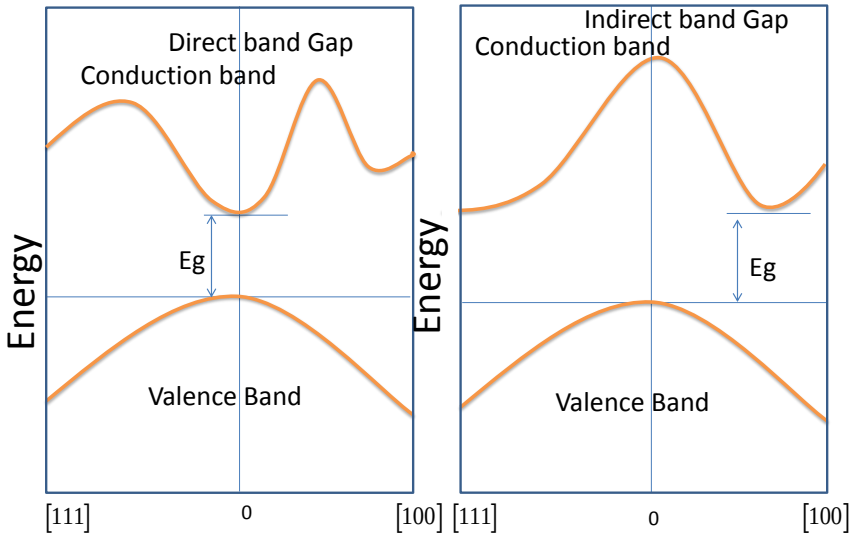

Figure 2.13: energy band structures of direct semiconductor (left) and indirect semiconductor (right).

2.6 TEMPERATURE DEPENDENCE OF THE ENERGY BAND GAP

The energy band gap of semiconductors tends to decrease as the temperature is increased (see Figure 2.14 for Si, Ge and GaAs). This behaviour can be better understood if one considers that the interatomic spacing increases when the amplitude of the atomic vibrations increases due to the increased thermal energy. This effect is quantified by the linear expansion coefficient of a material. An increase

of the interatomic spacing decreases the potential seen by the electrons in the material, which in turn reduces the size of the energy band gap. A direct modulation of the interatomic distance, by applying for example high compressive (tensile) stress, also causes an increase (decrease) of the band gap.

For many semiconductors the temperature dependence can be described with the empirical Varshni formula[23].

$$E_g(T) = Eg(0) - \frac{\alpha T^2}{\beta + T} \qquad 2.20$$

Where $E_g(0)$ is the band gap energy at zero Kelvin, α and β are empirical parameters related to the material.

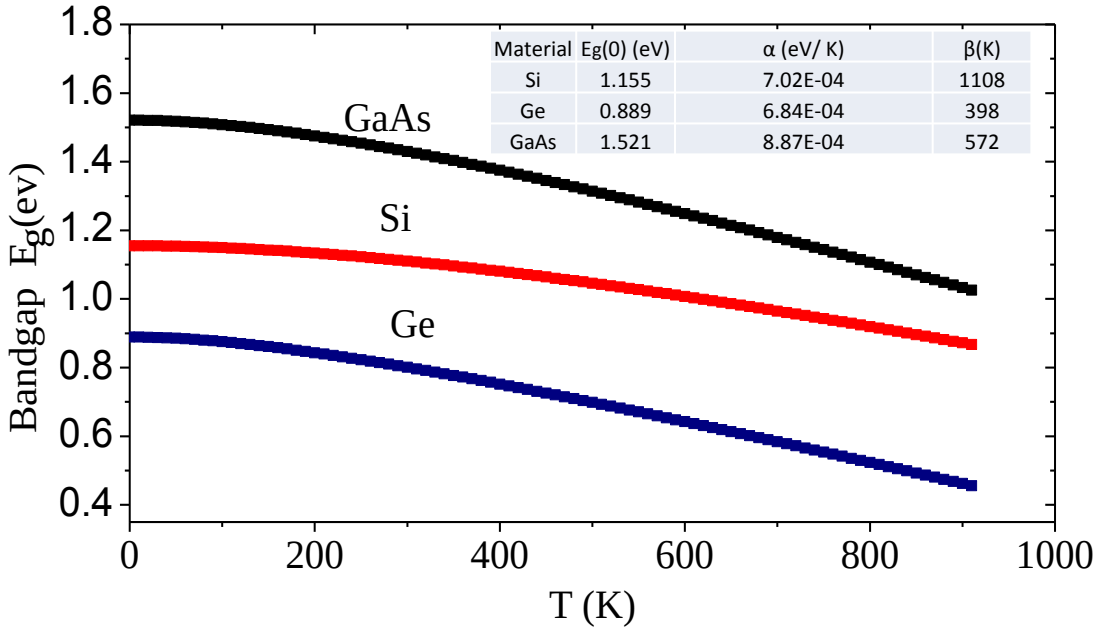

Figure 2.14: energy band gap as a function of temperature of GaAs, Si, and Ge[23] .

The inset table shows Varshni's parameters for GaAs, Si and GaAs semiconductors.

2.7 BAND STRUCTURE MODIFICATION

Tailoring of semiconductor band gap energy is important for the design of novel electronic devices with superior properties. There are two widely used approaches for band gap tailoring, also called band gap engineering. These will be discussed briefly in the following.

2.7.1 Alloys

Semiconductor alloys provide a means of modification of the magnitude of the energy band gap and other material parameters so as to optimise and widen the application of semiconductor devices. For example, the band gap of GaAs is too small for light emission in the visible range. GaP, on the other hand, has a band gap in the green portion of the spectrum but the gap is indirect and therefore GaP is an inefficient emitter without the help of suitable dopants (e.g. nitrogen)[24]. A well-chosen alloy of GaAs and GaP can ensure that most of the characteristics of GaAs are retained (e.g. direct gap) while the magnitude of the forbidden gap is altered sufficiently[25]. On the other hand using alloys help create a material with a proper lattice constant to match that of a substrate. For example, $In_{0.53}Ga_{0.47}As$ alloy is used to lattice-match with InP substrates[26], which are employed as substrates for a number of devices.

Figure 2.15 illustrates the relationship between the band gap and the lattice constant for several families of III-V semiconductors. The band gaps of some III-V semiconductor alloys span the range 0.18 - 2.4 eV. Most of these materials have a direct gap in E-k space, which means that the minimum and maximum of the conduction and valence bands, respectively, fall at the same k-value. The solid lines represent direct band gap regions and the dotted lines the indirect gap regions. The lines on this diagram represent ternary compounds which are alloys of the binaries named at their end-points. The triangular areas enclosed by lines between three binaries represent quaternaries. GaAs/AlGaAs is one of the most important

heterostructure for device applications. The substitution of Al for Ga in GaAs does not change the lattice constant appreciably (see Figure 2.15). This means that any alloy of $Al_xGa_{1x}As$ grown on GaAs substrate, will be lattice matched, and therefore no misfit dislocations or other structural defects should form. This fact made GaAlAs/GaAs heterojunction lasers emerge as the first notable example of a new generation of optoelectronic devices based on semiconductor alloys.

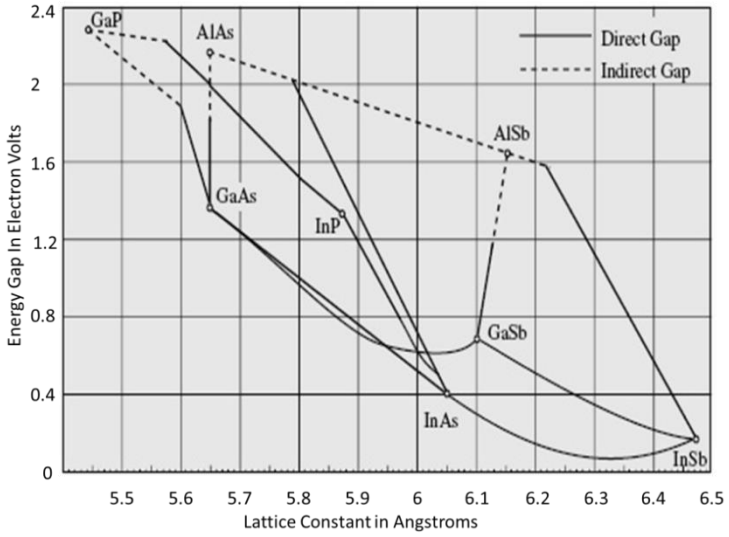

Figure 2.15: Band gap energy versus lattice constant of various III-V semiconductors at room temperature[27].

Vegard's law is an approximate empirical rule that describes a linear relation between the crystal lattice constant of an alloy and the concentrations of the constituent elements at constant temperature[28,29]. When an alloy A_xB_{1-x} is produced by a random mixing of two elements (the concepts can be applied to ternary and quaternary alloys as well) the lattice constant of the alloy is given by Vegard's law:

$$a_{alloy} = xa_A + (1-x)a_B \qquad 2.21$$

The change in the energy gap of the resulting alloy can be given by:

$$E_g^{alloy} = (1-x)E_g^B + xE_g^A \qquad 2.22$$

However, in some alloys, there is a bowing influence arising from the increasing disorder due to the alloying. So equation (2.22) is slightly changed by including the bowing parameter (b).

$$E_g^{alloy} = (1-x)E_g^B + xE_g^A + bx(1-x) \qquad 2.23$$

Alloys are usually divided into three categories depending on the arrangement of their constituent atoms A and B.

1) Phase separated or clustered: if atom B is localized in a region different from the region which atom A is localized (Figure 2.16-a)

2) Superlattice or ordered: if A and B atom form well defined periodic structures (Figure 2.16-b)

3) Random alloy: no specific order (Figure 2.16-c)

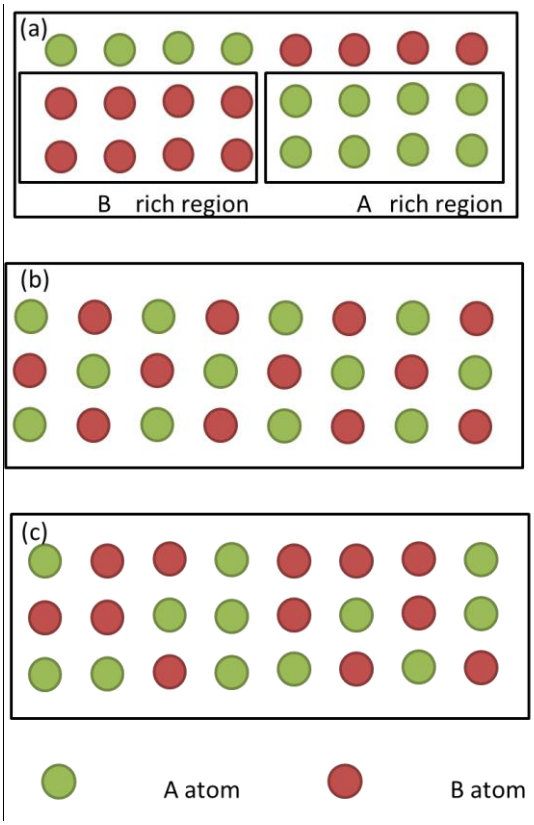

Figure 2.16: A schematic example of (a) a clustered, (b) an ordered, and (c) a random alloy.

Figure 2.17 shows the lattice constants versus mole fraction (x) for some important alloys[27].

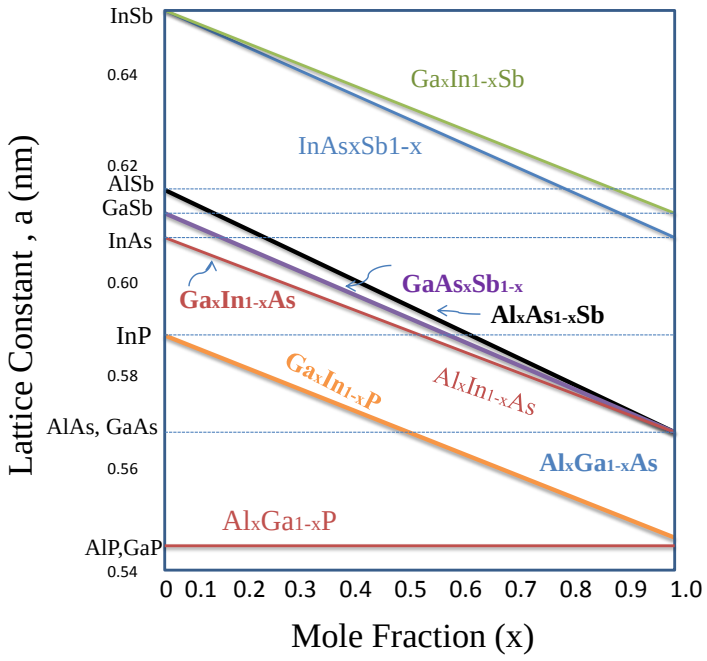

Figure 2.17: Lattice constant as a function of composition for ternary III-V semiconductors. All cases obey Vegard's law. The dashed lines show regions where miscibility gaps are expected[27].

2.7.2 Heterostructures

A heterostructure is obtained by the junction of two different crystalline semiconductors. The constituent materials of the heterojunction have different energy band gaps, atomic size or lattice parameters. Heterostructures offer the opportunity to manipulate the behaviour of the electrons and holes through band engineering. The use of heterojunctions, based on III-V semiconductor alloys, in the design and fabrication of semiconductor devices has led to the development of new structures with improved performance. One important parameter for the formation of heterojunctions is the band alignment between two semiconductor materials. Heterojunctions can be classified based on how the energy bands align with respect

to each other. There are three different types of band alignments as shown in Figure 2.18.

2.7.2.1 Type I Band Alignment

The band gap of material B lies completely inside the band gap of the material A, i.e. the minimum energy for both electrons and holes occurs in semiconductor B (Figure 2.18.a). This most commonly encountered alignment is called straddled alignment. GaAs/AlGaAs and InAs/GaAs are examples of this type of alignment.

2.7.2.2 Type II Band Alignment

Type II alignment arises when the minimum energy for electrons occurs in semiconductor B but the minimum energy for holes occurs in semiconductor A. This configuration, which results in spatially separated electrons and holes, is known as staggered alignment (Figure 2.18.b).

2.7.2.3 Type III Band Alignment

Figure 2.18.c shows another possibility of alignment known as type III hetrostructure where both group III and group V elements differ (e.g GaSb/InAs). In this case, the conduction band of one semiconductor lies below the valence band of the other semiconductor. It is worth pointing out that this alignment is also referred to as type II misaligned hetrojunction.

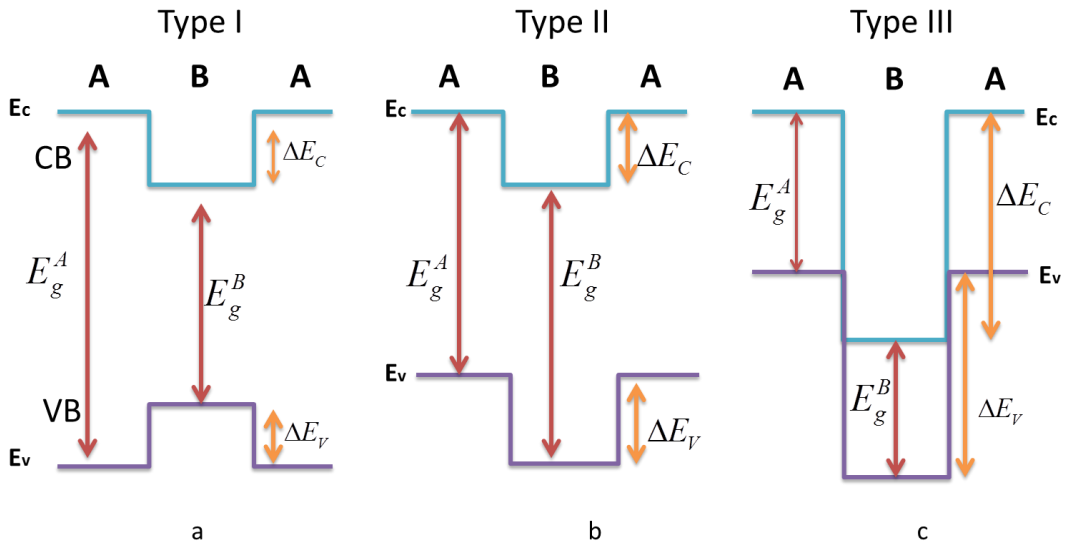

Figure 2.18: Classification of heterojunctions according to their band alignment, where E_C, E_V, Eg, ΔE_C, and ΔE_V are the conduction band, valence band, energy gap, conduction band offset, and valence band of the materials, respectively.

2.7.2.4 Anderson's rule

In 1962 Anderson[30] proposed the electron affinity model to calculate the band offset of an ideal heterostructure. Electron affinity is defined as the energy difference between the vacuum level and the bottom of the conduction band.

Consider two semiconductors which are brought into physical contact. The two semiconductors are assumed to have an electron affinity of χ_A and χ_B, and band gap energy of E_g^A and E_g^B, respectively, as illustrated in Figure 2.19. The electron affinity model is based on the fact that the energy balance of electron, moved from the vacuum level to semiconductor A, then to semiconductor B, and finally to the vacuum level, must be zero. This is given by:

$$\chi_A - \Delta E_C - \chi_B = 0 \qquad 2.24$$

or

$$\Delta E_C = \chi_A - \chi_B \qquad 2.25$$

The valence band discontinuity follows automatically as

$$\Delta E_V = E_g^A - E_g^B - \Delta E_C \qquad 2.26$$

The electron affinity rule is reasonably valid for some semiconductor pairs but it fails for many other materials. One of the basic reasons for its failure is the chemical character of the bonds in the adjacent material. For example by using this rule, the theoretical value of the band offset of the AlAs/GaAs heterostructure is 230 meV while the experimental value for this is near 530 meV. Kroemer[31] explained the failure of Andreson model by the formation of the semiconductor surface dipoles. These dipoles, which are formed due to the readjustments of the atoms at the semiconductor surface, affect the values of the electron affinity, and consequently the band offset of the heterostructures.

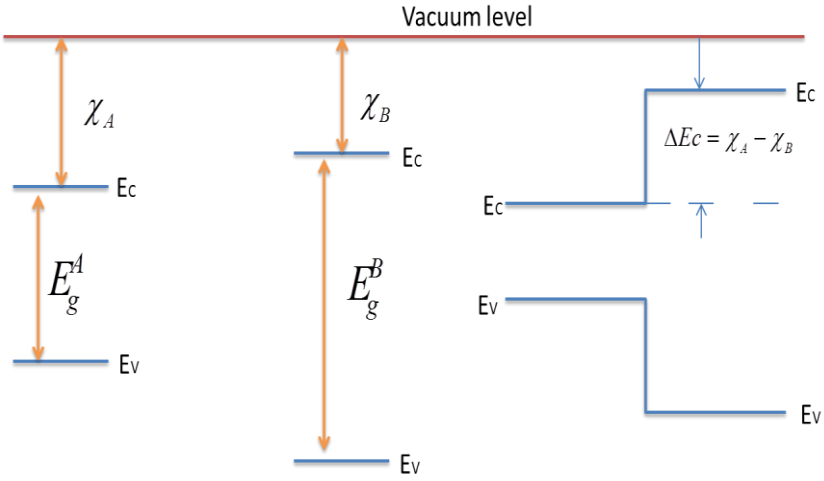

Figure 2.19: Band diagram of (a) two separated semiconductors and (b) two semiconductors in contact. The semiconductors have a band gap energy E_g^A and E_g^B and an electron affinity of χ_A and χ_B.

2.8 PROPERTIES OF SELECTED SEMICONDUCTOR MATERIALS

In this section some of the important properties of the semiconductors studied in this thesis will be reviewed.

2.8.1 Gallium Arsenide (GaAs)

GaAs is one of the most technologically important and most investigated III-V compound semiconductor material, and is formed by combining As (group-V) and Ga (group-III) elements from the periodic table. It was first produced by Goldschmidt in 1920's[32]. However, its properties remained unknown up to 1952. The crystal structure of GaAs is zincblende type, in which a face-centred cubic lattice (fcc) of As with Ga atoms positioned on the body diagonals as shown in Figure 2.20. Ga (As) atoms is displaced from the As (Ga) atom by a distance $\left(\frac{a}{4},\frac{a}{4},\frac{a}{4}\right)$ along the body diagonal, where a is the lattice constant of GaAs given by[33]:

$$a = 0.565325 + 3.88 \times 10^{-6} (T - 300\ K)\ nm \qquad 2.27$$

Where T is the temperature in Kelvin.

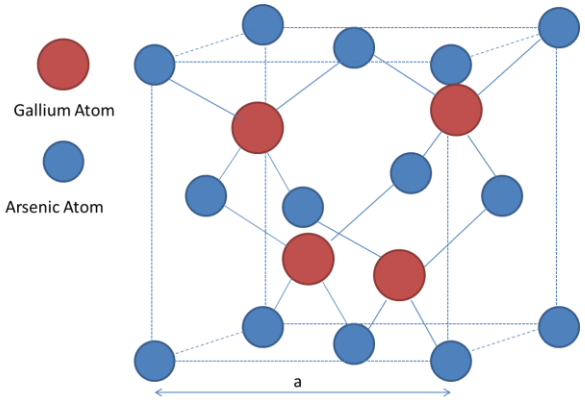

Figure 2.20: Conventional unit cube for GaAs.

Both the conduction band minima and the valence band maxima of GaAs lie at the same value of wave vector at k = 0. Therefore, the transition of an electron from the valence band to the conduction band doesn't need phonon assistance. According to the energy band diagram definition the nature of the GaAs band gap is direct. The direct band gap ensures excellent optical properties of GaAs as well as superior electron transport in the conduction band. This property makes GaAs superior over Si, which has an indirect band gap, for devices used in optoelectronics applications. Moreover, GaAs possesses higher carrier mobility than Si, and is preferably used in high frequency devices. Electrical properties of GaAs material makes it suitable to be used as a semi-insulating substrate for integrated circuits due to its high resistivity compared to Si material. In addition, due to the fact that the energy gap of GaAs is higher than that of Si, ($E_g^{GaAs} = 1.424eV > E_g^{Si} = 1.1eV$ at 300K), the GaAs devices are more reliable to operate at higher temperatures than Si devices.

Figure 2.21 shows the band dispersion for increasing k along two different directions of the Brillouin zone. The right hand side of the figure corresponds to moving from the zone centre where k = (0,0,0) along the (001) direction to the zone edge at k = $\frac{2\pi}{a}$ (1,0,0). The left hand side corresponds to moving from k = 0 along the body diagonal direction until reaching the zone edge at k = $\frac{\pi}{a}$ (1,1,1). The single conduction band corresponds to the (S) antibonding state. The three bands in the valence band correspond to the three bonding orbitals, namely heavy hole (HH), light hole (LH), and split off (SO) bands. Due to the large spin–orbit splitting, for most purposes, the SO band does not play any role in electronic or optoelectronic properties. Hole masses are $m*_{HH} = 0.45m_0$; $m*_{LH} = 0.08m_0$.

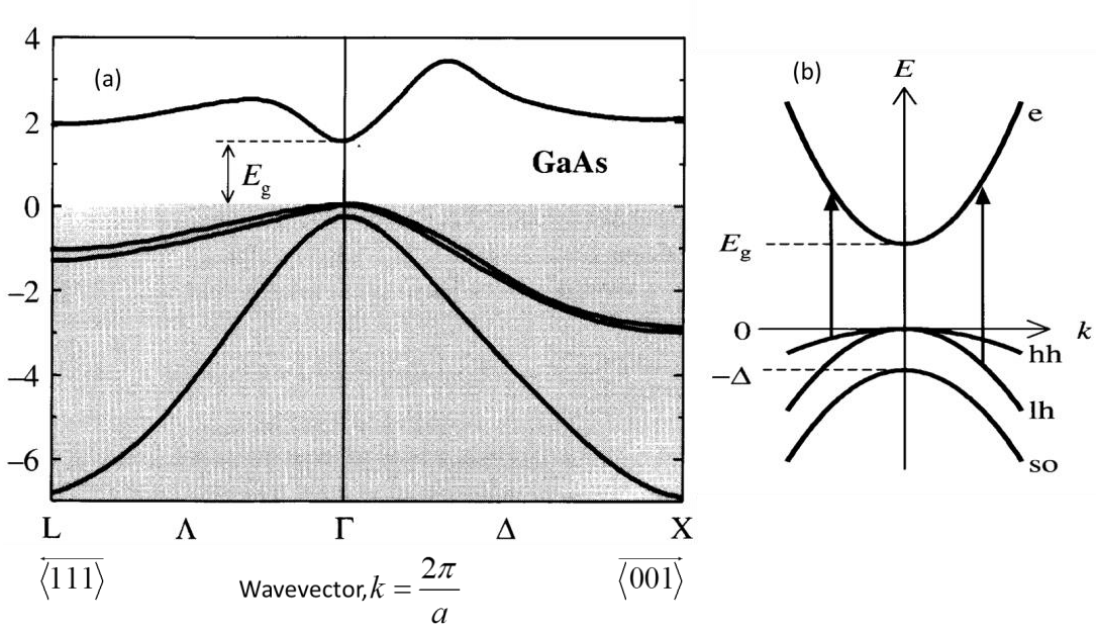

Figure 2.21: Diagram of the band structure in the vicinity of the energy gap of GaAs: (a) throughout the first Brillouin zone, (b) a magnified view near the zone center[34].

2.8.2 Aluminium Gallium Arsenide (AlGaAs)

The alloy $Al_xGa_{1-x}As$ has the same crystal structure as that of GaAs, except that a fraction x of Ga atoms have been replaced by Al atoms. The incorporation of Al into GaAs, which has the effect of increasing the band gap energy at 300 K from 1.42 eV (GaAs) for x = 0 to 2.168 eV (AlAs) for x = 1, extend the range of applications from near infrared to visible region. The energy change of the different conduction valleys (X, Γ, and L) at 300K as a function of Al content (x) is shown in Figure 2.22.

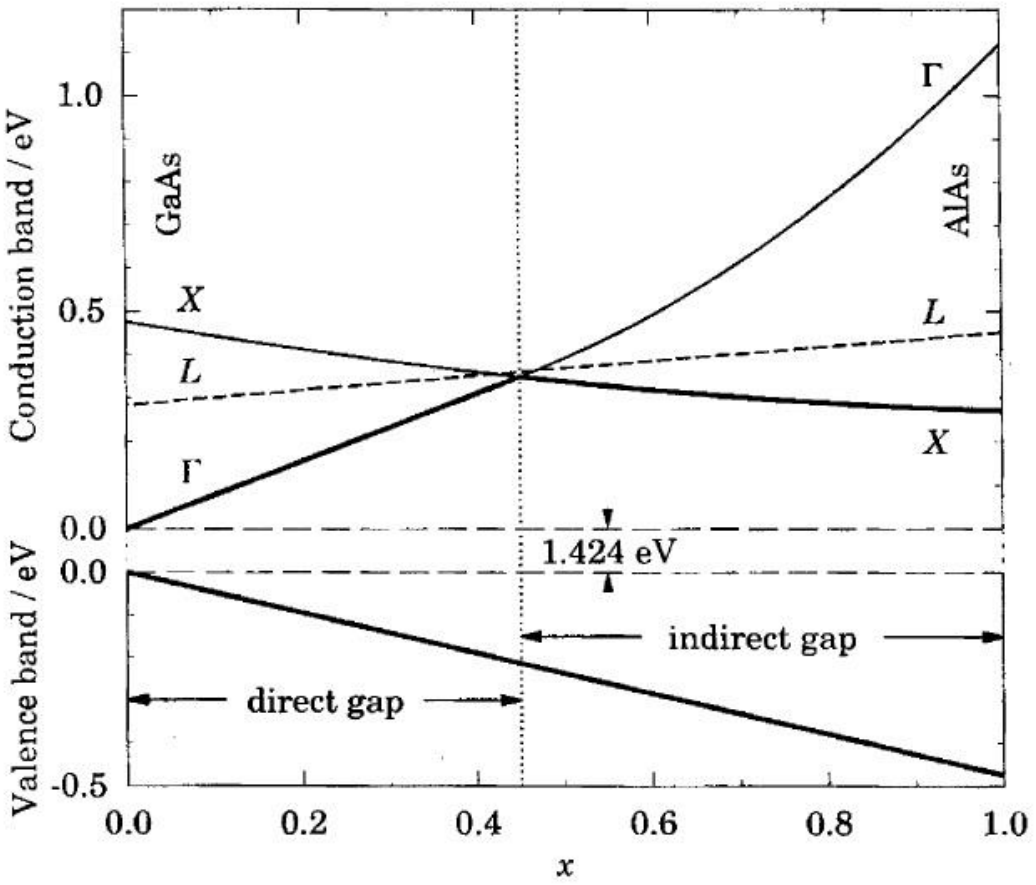

Figure 2.22: Variation of the conduction band valleys in $Al_xGa_{1-x}As$ as a function of Al composition (x) at 300 K[35].

In addition, it is worth pointing out that for Al content ≥ 0.44 the transition from direct to indirect band gap takes place for AlGaAs material. The properties of $Al_xGa_{1-x}As$ crystal are somewhat between those of GaAs and AlAs. The lattice constant, a, of $Al_xGa_{1-x}As$ is given, to a first approximation, by linearly interpolating the lattice constants of AlAs and GaAs. For example, the room temperature lattice constant of $Al_xGa_{1-x}As$ as a function of the aluminium fraction x is given by:

$$a(x) = (0.56533 + 0.00078x)\ \text{nm} \qquad 2.28$$

The difference in the lattice constant, a, between x = 0 and x = 1 (i.e. between the GaAs and AlAs crystals) is not more than 0.01a. Hence the interfaces between GaAs and (AlGa)As can be made extremely smooth. This lattice match condition gives

significant reduction in defects, which is very important for good device performance.

Besides the above mentioned selected properties, some other important properties of intrinsic GaAs, and AlGaAs at room temperature are given in Table 2.4.

Table 2.4: Some important properties of intrinsic GaAs, AlAs and AlGaAs at 300K; HH and LH stand for heavy hole and light hole, respectively[36,37].

Parameter	**GaAs**	**AlAs**	**$Al_xGa_{1-x}As$**
Crystal Structure	Zincblende	Zincblende	Zincblende
Lattice constant (Å)	5.6533	5.6611	5.6533 + 0.0078x
Crystal density (g/cm^3)	5.360	3.760	5.360 - 1.6x
Energy band gap (eV) at 300K	1.42	2.168	For x<0.45 (1.424+1.247x) For x>0.45 (1.9+0.125x+ $0.143x^2$)
Band type	Direct	Direct	Changes from direct to indirect for Al >0.45 content
Electron effective mass	0.063 m_0	0.150 m_0	0.063+0.083x m_o (x<0.45)
Hole effective mass	0.62m_0 (HH) 0.087m_0(LH)	0.76m_0 (HH) 0.15 m_0 (LH)	0.62 + 0.14x (HH) 0.087 + 0.063x (LH)
Dielectric constant (static)	12.85	10.06	12.85-2.84x

Specific heat (cal/g.K)	0.08	0.11	0.08+0.03x
Electron affinity (eV)	4.07	3.4	4.07-1.1x (0<x<0.45) 3.46-0.14x (0.45<x<1)

2.8.3 Dilute Nitride Alloys

In 1992 Weyers et al[38] made an interesting finding of a substantial reduction in the band gap energy of GaAs semiconductor when the group V anions are partially substituted by low concentration of highly electronegative N atoms. This reduction in the band gap energy behaviour was further explored by Kondow et al[39].

Nitrogen causes a giant band gap bowing and tends to stretch and compress the neighbouring bonds. Moreover a small amount of N in III-V material systems produces an increase in the effective mass (m_{eff}). This behavior is in contrast to the conventional semiconductors, where m_{eff} normally exhibits a decrease with reduction in the band gap energy.

The general reason for the reduction in the GaAs band gap and other associated effects is the presence of N-related localized states near the conduction band edge the incorporation of N produce a significant local potential due to large differences in atom size and electronegativity of N atoms and host anions[40].

Many of these effects can be explained by the simple two-level band anticrossing (BAC) model[41]. The (BAC) model in which the extended conduction band (CB) states of GaAs admix and hybridize with the localized N-level above the CB edge, is described briefly below.

The BAC model has predicted many interesting effects, such as an enhancement of donor-binding[42] energy and an electron effective mass[43] due to N incorporation in GaAs lattice, which have been experimentally proved. The BAC model describes the electronic structure of N-alloys in terms of an interaction between the localized state of nitrogen and the extended conduction band states of the host semiconductor matrix[44,45], which results in splitting of the conduction band into the E- and E+

bands, and a reduction of the fundamental band gap. The E_+ transition is shifted to higher energy and the E_- transition is shifted to lower energy from the N resonant level with increasing N concentration. The energy difference between them increases with increasing N concentration. Figure 2.23 shows the anticrossing behavior between the N-related state (E_N) and conduction band edge (E_{CB}) of GaAs. The N-related states are spread over the reciprocal space with constant energy because of its localised nature. These two energy states are represented in Figure 2.23 by dotted lines. According to the BAC model:

$$E_{\pm} = \frac{1}{2}\left[\left(E_N + E_{CB}(k)\right) \pm \sqrt{\left(\left(E_N - E_{CB}\right)^2 + 4V_{CB,N}^2\right)} \right] \qquad 2.29$$

Where E_{CB} (k) and E_N are the energies of the GaAs conduction band host matrix and nitrogen state, respectively, and $V_{CB,N}$ is the matrix element describing the interaction between the localized N states and extended CB states,

If one assumes that $V_{CB,N}$ is independent of k near the CB edge, then $V_{CB,N}$ can be written as:

$$V_{CB,N} = C_N \cdot x^{½} \qquad 2.30$$

Where C_N is a constant which depends on the host matrix and x is the mole fraction of substitutional N. Therefore equation 2.29 can be written as:

$$E_{\pm} = \frac{1}{2}\left[\left(E_N + E_{CB}(k)\right) \pm \sqrt{\left(\left(E_N - E_{CB}\right)^2 + 4C_N^2 x\right)} \right] \qquad 2.31$$

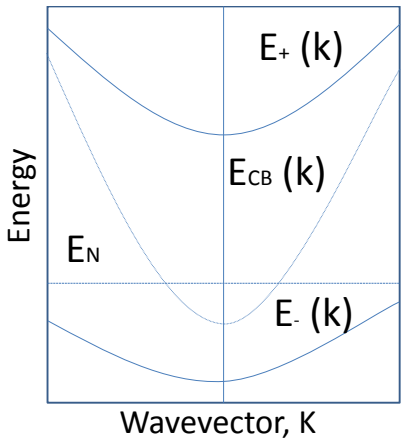

Figure 2.23: Schematic diagram of band anticrossing model of GaAsN. Solid lines: calculated dispersion relation for $E_{\pm}$ subbands of $GaAs_{1-x}N_x$ using BAC model. Dotted lines: unperturbed energies of the N level (E_N) and the GaAs conduction band.

The deficiency of the BAC model is that it is considered to work for single isovalent impurity level and conduction band edge interaction and, it does not consider the broadening of the energy levels or splitting of L-conduction band extreme. In spite of all its shortcomings, it has been a popular and most cited model in dilute nitride literature due to its simplicity and satisfactory fit to many characteristics of the alloy.

2.8.3.1 GaAsN Alloy

GaAsN was the first material system where reduction in the band gap as well as lattice parameter was reported with the introduction of a small concentration of N. The reduction of the band gap energy can be approximated by the empirical relationship[49] is given by:

$$E_{GaAs_{1-x}N_x}(x) = E_{GaAs} - (12x)\ eV \qquad 2.32$$

For $x < 0.015$

In addition, as demonstrated by absorption measurement[46-48] the nature of the band gap of GaN_xAs_{1-x} alloy is direct. Moreover, according to numerous spectroscopic

studies PL polarization[49], time resolved PL spectroscopy[50] and optically detected cyclotron resonance (ODCR)[51] the band alignment of GaAsN/GaAs hetrostructure system is of type I.

A different set of values of the electron effective mass of the fluctuating from $m_e^* \sim 0.8m_0$ to $0.1m_0$ has been reported in dilute nitrides materials[52-57]. For example m_e^* has been found to increase from the GaAs host mass of $0.065\ m_0$[58] up to $0.19\ m_0$ with N~ 2%. The trend of the increase of the effective mass value with N% is consistent with the BAC model. An electron effective mass of $0.11m_0$ for x~1.6% has been the most acceptable value to date[59].

2.8.3.2 GaInAsN Alloy

The large difference in electronegativity and lattice constant between GaAs and GaN results in large optical bowing coefficient[60] and significant band gap reduction following incorporation of small N concentration in the material. Moreover, in the GaInNAs/GaAs system, reduction in the GaInNAs band gap contributes to a large conduction band offset. Furthermore, incorporating N in GaInAs can compensate for the compressive strain due to In, and result in GaInNAs lattice-matched to GaAs substrate. For these reasons, the GaInNAs/GaAs system has been shown[61-63] to be the new key material system for long wavelength applications. The alloy $Ga_{(1-x)}In_xN_yAs_{(1-y)}$ is exactly lattice matched to GaAs when $y = 0.35x$.

2.9 OPTICAL PROPERTIES OF SEMICONDUCTORS

The wide-ranging optical properties observed in semiconductor materials can be classified into a number of general phenomena, namely scattering, reflection, transmission through the material or absorption in the material. If the incident photons on a semiconductor have sufficient energy, they can excite an electron from valence band to conduction band. The Created electron and hole pair may interact with the lattice vibrations and the electrons of localized defects. As a result, the

optical spectra of the semiconductor provide a rich source of information about the properties of the material.

2.9.1 Absorption Processes

The illumination of a semiconductor with photons of energy greater than the band gap energy generates an electron-hole pair by the optical process. In this case, a photon excites an electron from the filled valence band to the empty conduction band as shown in Figure 2.24 By applying the law of conservation of energy to the interband transition the following relationship holds:

$$E_f = E_i + \hbar\omega \qquad 2.33$$

Where E_i is the energy of the initial state in the lower band, E_f is the energy of the final state in the upper band, and $\hbar\omega$ is the photon energy. In bulk semiconductors there is a continuous range of energy states within the upper and lower bands, and therefore the interband transitions will be possible over a continuous range of frequencies. The range of frequencies is determined by the upper and lower energy limits of the bands. Interband transitions therefore give rise to a continuous absorption spectrum from the low energy threshold at Eg to an upper value set.

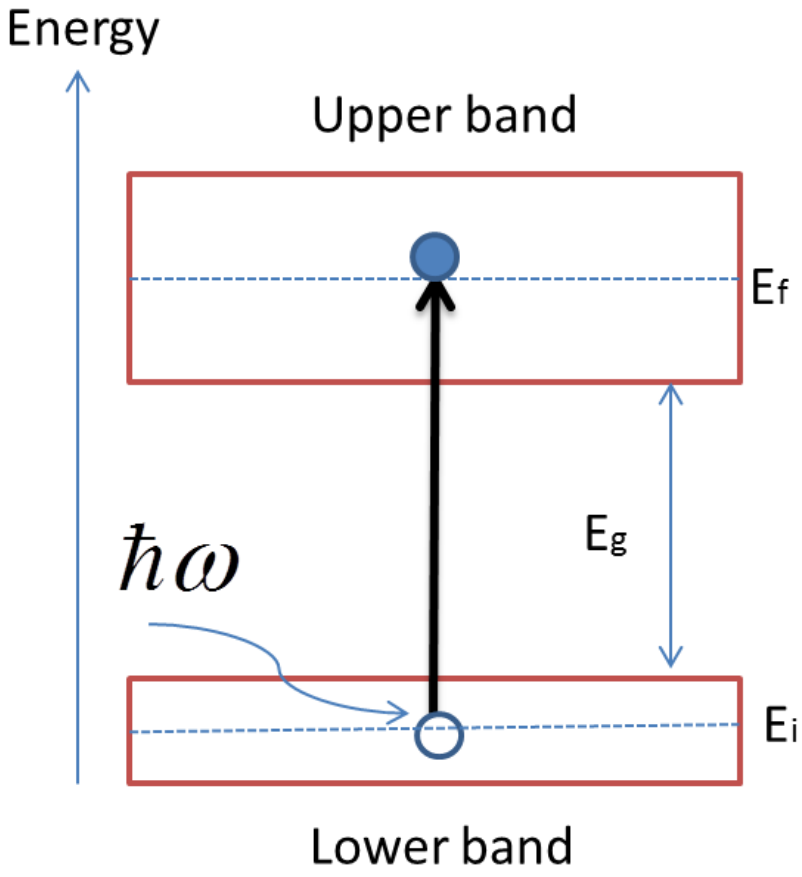

Figure 2.24: Interband optical absorption between an initial state of energy E_i in an occupied lower band and a final state at energy E_f in an upper band. The energy difference between the two bands is Eg.

The absorption spectrum of a given material is related to its band structure and in particular to the density of states for the transition. From the classical point of view, for the direct band gap semiconductors such as GaAs, the absorption coefficient (α) as a function of wavelength (λ) can be expressed as:

$$\alpha(\lambda) = A\left(\hbar\omega - E_g\right)^{\frac{1}{2}} \qquad 2.34$$

Where constant A depends upon the material properties, E_g is the energy gap and ħω is the incident photon energy. Figure 2.25 illustrates the absorption coefficient of Si and GaAs as a function of the energy of the incident light.

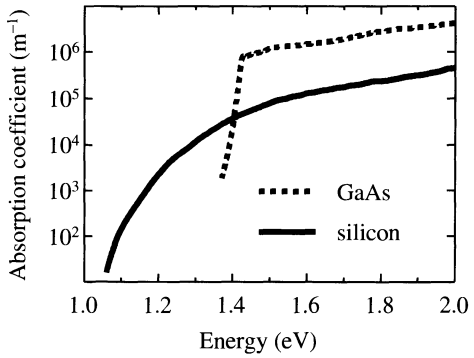

Figure 2.25: absorption coefficient as a function of energy of incident light of GaAs and silicon near their band edges[64]. Note that the vertical axis is logarithmic.

Semi classically, absorption is determined by the quantum mechanically transition rate $W_{i\to f}$ for exciting an electron in an initial quantum state ψ_i to a final state ψ_f by absorption of a photon of angular frequency ω. The transition rate is given by the Fermi's golden rule:

$$W_{i\to F} = \frac{2\pi}{\hbar}|M|^2 g(\hbar\omega) \qquad 2.35$$

The transition rate thus depends on two factors:

1- The matrix element M

2- The density of state g(ħω)

The matrix element M, which describes the interaction between photons and electrons, is given by:

$$M = \langle f|H'|i\rangle = \int \psi_f^{*}{}_{(r)} H'_{(r)} \psi_{i(r)} d^3{}_{(r)} \qquad 2.36$$

Where the limits of the integration are over the whole crystal.

H' is the perturbation associated with the light wave, and r is the position vector of the electron.

The electron states in a crystalline solid are described by Bloch functions. The wave functions can be expressed as a product of a plane wave and an envelope function that has the periodicity of the crystal lattice these are given by:

$$\psi_i(r) = \frac{1}{\sqrt{V}} U_i(r) e^{iK_i.r} \qquad 2.37$$

$$\psi_f(r) = \frac{1}{\sqrt{V}} U_f(r) e^{iK_f.r} \qquad 2.38$$

Where U_f and U_i are the appropriate envelope functions for the initial and final bands, respectively, and V is the normalization volume, k_i and k_f are the wave vectors of the initial and final electron states.

When photons are treated classically, the perturbation H' could be expressed as:

$$H' = -P_e.\varepsilon_{photon} \qquad 2.39$$

Where P_e is the electron dipole moment caused by electric field Ɛ.

2.9.2 Photoluminescence

In this section the re-emission of photons by interband luminescence after the semiconductor has been excited by a photon with energy greater than band gap (E_g) will be considered. The physical processes involved in photoluminescence are more complicated than those in absorption. This is because the generation of light by luminescence is intimately tied up with the energy relaxation mechanisms in the solid. The shape of the emission spectrum is affected by the thermal distributions of the electrons and holes within their bands.

In a photoluminescence experiment, a quantum of light (photon) from a laser is absorbed by an electron, thus making a transition from the valence band to the

conduction band. This produces a hole in the valence band. Following this optical excitation, electrons and holes undergo spatial and temporal evolution with characteristic times which depend on the various relaxation processes (see Table 2.5 and Figure 2.26) [65].

Table 2.5: Fundamental processes in semiconductors.

Microscopic process	**Characteristic time** (sec)
Carrier-carrier scattering	10^{-15}-10^{-12}
Intervalley scattering	10^{-14}
Intravalley scattering	10^{-13}
Carrier-optical phonon thermalization	10^{-12}
Optical phonon-acoustic phonon interaction	10^{-11}
Carrier diffusion	10^{-11}
Auger recombination (when carrier density > 10^{20} cm^{-3})	10^{-10}
Radiative recombination	10^{-9}
Lattice heat diffusion	10^{-8}

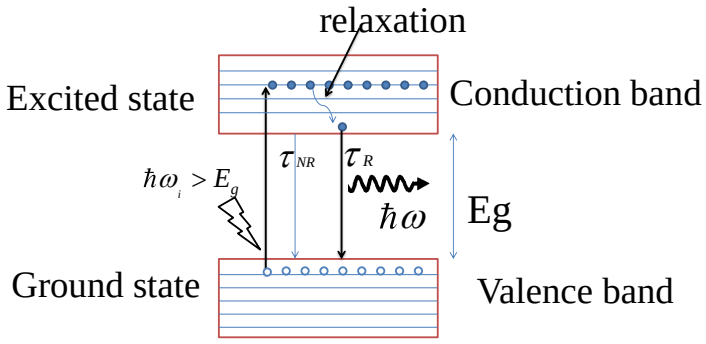

Figure 2.26: Photoluminescence in a solid. Incoming photons with energy higher than the band gap energy excite an electron from ground state to excited state. Electron relaxes to the lowest available level before dropping down to empty levels in the ground state band by emitting a photon.

The spontaneous emission rate for radiative transitions between two levels (see Figure 2. 27) is determined by the Einstein coefficient A as given below.

$$A = \frac{1}{\tau_R} \qquad 2.40$$

τ_R is the natural radiative lifetime of the excited sate

If the upper level has a population N at time t, the radiative emission rate is given by:

$$\left(\frac{dN}{dt}\right)_{radiative} = -AN \qquad 2.41$$

This rate equation can be solved to give:

$$N(t) = N(0)\exp(-At) = N(0)\exp(-\frac{t}{\tau_R}) \qquad 2.42$$

The Einstein A coefficient is directly proportional to the B coefficient[66], which determines the absorption probability.

$$A = \frac{8\pi h\nu^3}{c^3} B \qquad 2.43$$

This relationship tells us that transitions that have a high absorption probability will also have a high emission probability.

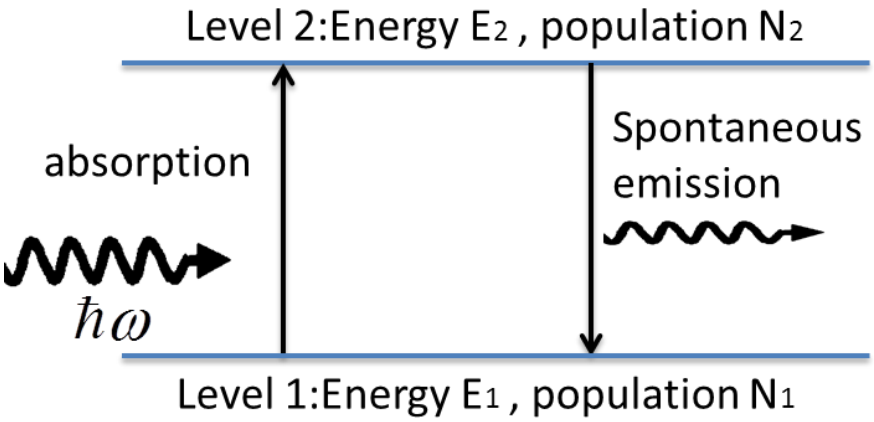

Figure 2. 27: Absorption,and spontaneous emission transitions between two levels of an atom in the presence of electromagnetic radiation.

The relationships between the A and B Einstein coefficients given in equation 2.41 have been derived for the case of an atom in equilibrium with black body radiation.

The luminescence intensity (*I*) at frequency (ν) can be written as:

$$I(h\nu) \propto |M|^2 \, g(h\nu) \text{ x Level occupancy factor} \qquad 2.44$$

Where the occupancy factor gives the probabilities that the relevant upper level is occupied and the lower level is empty.

The occupancy conditions for photon emission between the discrete energy levels E_2 and E_1 are stated as follows: a conduction-band state of energy E_2 is filled (with an electron) and a valence-band state of energy E_1 is emptied (i.e., filled with a hole).

The probabilities that these occupancy conditions are satisfied for various values of E_2 and E_1 are determined from the appropriate Fermi functions f_c and f_v associated with the conduction and valence bands. The probability $f_e(\nu)$ that the emission condition is satisfied for a photon of energy hν is the product of the probabilities that the upper state is filled and that the lower state is empty (these are independent events), i.e.,

$$f_e(\upsilon) = f_c(E_2)\left[1 - f_v(E_1)\right] \qquad 2.45$$

The other two terms are the matrix element (M) and the density of states (g) for the transition, which determine the quantum mechanical transition probability by Fermi's golden rule (equation 2.35).

The light is emitted between the electron and hole states that are thermally occupied (electrons and holes are thermally distributed within kT after their relaxation to their respective bands), and will therefore only be emitted within a narrow energy range from the lowest levels in the excited state band. This contrasts with the absorption spectrum, where photons can be absorbed to any state within the excited state band, no matter how far it is above the bottom of the band.

Radiative emission is not the only mechanism by which the electrons in an excited state can drop down to the ground state. The electron might, for example, lose its energy as heat by emitting phonons, or it may transfer the energy to impurities or defects called 'traps'. If these non-radiative relaxation processes occur on a faster time scale than the radiative transitions, then a very small number of photons will be emitted.

The luminescence efficiency η_R in this case is given by:

$$\eta_R = \frac{1}{1 + \tau_R / \tau_{NR}} \qquad 2.46$$

Where τ_R, and τ_{NR} are the radiative and non-radiative lifetimes, respectively.

If $\tau_R >> \tau_{NR}$ then η_R is very small and the light emission is very inefficient. Thus efficient luminescence requires that the radiative lifetime should be much shorter than the non-radiative lifetime.

REFERENCES

[1] L. Coldren, S. Corzine, M. Mashanovitch, Diode Lasers and Photonic Integrated Circuits, (Wiley Series in Microwave and Optical Engineering (1995).

[2] S. M. Sze, and K. K. Ng, "Physics of Semiconductor Devices". 3rd ed.: Wiley-Interscience, A John Wiley & Sons, Inc, Publication (2007).

[3] M. Henini, P. J. Rodgers, P. A. Crump, B. L. Gallagher, and G. Hill, Applied Physics Letters, 65, 2054, (1994).

[4] A. Polimeni, M. Henini, A. Patanè, L. Eaves, P. C. Main, and G. Hill, Applied Physics Letters, 73, 1415 (1998).

[5] A. Patanè, A. Levin, A. Polimeni, F. Schindler, P. C. Main, L. Eaves, and M. Henini, Applied Physics Letters, 77, 2979, (2000).

[6] K. Wang, K. Edmonds, L. Zhao, M. Sawicki, R. Campion, B. Gallagher, and C. Foxon, Physical Review B, 72, 115207 (2005).

[7] M.Henini, Ill-Vs Review, 11 (3), 48 (1998).

[8] H. Xu, Q. Gong, B. Xu, W. Jiang, J. Wang,W. Zhou, Z. Wang, Journal of Crystal Growth, 200, 70 (1999).

[9] M. Henini, Nanoscale Research Letters, 1, 32 (2006).

[10] Y. Temko, T. Suzuki, P. Kratzer, and K. Jacobi, Physical Review B, 68, 165310 (2003).

[11] T. Suzuki, Y. Temko, and K. Jacobi, Applied Physics Letters, 80, 4744 (2002).

[12] K. Jacobi, Progress in Surface Science, 71, 185 (2003).

[13] D. Lubyshev, P. Gonzalez-Borrero, E. Marega, E. Petitprez, and P. Basmaji, Journal of Vacuum Science & Technology B, 14, 2212 (1996).

[14] M. Xu, Y. Temko, T. Suzuki, and K. Jacobi, Physical Review B, 71, 075314 (2005).

[15] M. Xu, Y. Temko, T. Suzuki, and K. Jacobi, Surface Science, 576, 89 (2005).

[16] K. Longenbach , and W. Wang, Applied Physics Letters, 59, 2427 (1991).

[17] P. Vaccaro, M. Hirai, K. Fujita, T. Watanabe, Journal of Physics D: Applied Physics, 29, 2221 (1996).

[18] R. Notzel, Semiconductor Science and Technology, 11, 1365 (1996).

[19] D. Kovalev, H. Heckler, G.Polisski, and F. Koch, Physica Status Solidi B, 215, 871, (1999).

[20] P. Zhao, D. Hu, and X. Wu, Chinese Physics Letters, 22, 1492 (2005).

[21] M. Tabe, M. Kumezawa,Y. Ishikawa, and T. Mizuno, Applied Surface Science, 175, 613 (2001).

[22] S. Ding, M. Ikeda, M. Fukuda, S. Miyazaki, and M. Hirose, Applied Physics Letters, 73, 3881 (1998).

[23] Y. Varshni, Physica , 34, 149 (1967).

[24] M. Jaros, Reports on Progress in Physics, 48, 1091 (1985).

[25] A. Bergh, and P. Dean, Light Emitting Diodes (Oxford: Clarendon) (1976).

[26] J. Bahk, Z. Bian, M. Zebarjadi, J. Zide, H. Lu, D. Xu, J. Feser, G. Zeng, A. Majumdar, Arthur C. Gossard, A. Shakouri, and J. Bowers, Physical Review B, 81, 235209 (2010).

[27] Jasprit Singh "Electronic and Optoelectronic Properties of Semiconductor Structures", Cambridge University Press (2003).

[28] L. Vegard, Die Konstitution Der Mischkristalle Und Die Raumfüllung Der Atome, Zeitschrift Für Physik, 5, 17 (1921).

[29] A. Denton, and N. Ashcroft, Physical Review A, 43, 3161 (1991).

[30] R. Anderson, "Germanium-Gallium Arsenide Heterojunction" IBM Journal of Research and Development, 4(3), 283(1960).

[31] H. Kroemer, Reviews of Modern Physics, 73, 783 (2001).

[32] J. D. Bernal, M. A., F. "The Goldschmidt Memorial Lecture". Journal of the Chemical Society (Resumed), 1929 Republished 1949: p. 2108. V. M. B. Goldschmidt, J. D, The Goldschmidt Memorial Lecture. Journal of the Chemical Society (Resumed), 1929 Republished 1949: p. 7.

[33] Richard John Allan Hill, Tunnelling into InAs Quantum Dots (Nottingham university, PhD Thesis)

[34] M. Fox, optical properties of solids, Oxford University Press Inc., New York (2001).

[35] John. Davies, The physics of low-dimensional semiconductors an introduction, Cambridge University Press (1998).

[36] J. Blakemore, Journal of Applied Physics, 53, R123 (1982).

[37] S. Adachi, Journal of Applied Physics, 58, R1 (1985).

[38] M. Weyers, M. Sato, H. Ando, Japanese Journal of Applied Physics, 31, L853 (1992).

[39] M. Kondow, K. Uomi, K. Hosomi, T. Mozume, Japanese Journal of Applied Physics, 33, L1056 (1994).

[40] H. P. Hjalmarson, P. Vogl, D. J. Wolford, and J. D. Dow, Physical Review Letters, 44, 810 (1980).

[41] W. Shan, W. Walukiewicz, J. W. Ager III, E. E. Haller, J. F. Geisz, D. J. Friedman, and J. M. Olson and S. R. Kurtz, Physical Review Letters, 82, 1221(1999).

[42] K. M. Yu, W. Walukiewicz, W. Shan, J. W. Ager, III, J. Wu, E. E. Haller, J. F. Geisz, D. J. Friedman, and J. M. Olson, Physical Review B, 61, R13337 (2000).

[43] J. Geisz, D. Friedman, J. Olson, S. Kurtz, B. Keyes, Journal of Crystal Growth, 195, 401 (1998).

[44] A. Lindsay, and E. P. O'Reilly, Solid State Communications, 112, 443(1999).

[45] W. Shan, W. Walukiewicz, J. W. Ager, E. E. Haller, J.F. Geisz, D. J. Friedman, J. M. Olsonand, and S. R. Kurtz, Physical Review Letters, 82, 1221(1999).

[46] M. Weyers, M. Sato, H. Ando, Japanese Journal of Applied Physics, 31, L853 (1992).

[47] W. G. Bi, C. W Tu, Applied Physics Letters, 70, 1608, (1997).

[48] M. Kondow, K. Uomi, K. Hosomi, T. Mozume, Japanese Journal of Applied Physics, 33, L1056 (1994).

[49] Y. Zhang, A. Mascarenhas, H. P. Xin, C. W. Tu, Physical Review B, 61, 4433 (2000).

[50] A. Buyanova, G. Pozina, P. N. Hai, W. M. Chen, H. P. Xin, C. W. Tu, Physical Review B, 63, 033303 (2001).

[51] P. N. Hai, W. M. Chen, I. A. Buyanova, H. P. Xin, C. W. Tu, Applied Physics Letters, 77, 1843 (2000).

[52] M. Hetterich, M. D. Dawson, A. Yu. Egorov, D. Berklau and H. Riechert, Applied Physics Letters, 76, 1030 (2000).

[53] Z. Pan, L. H. Li, Y. W. Lin, B. Q. Sun, D. S. Jiang and W. K. Ge, Applied Physics Letters, 78, 2217 (2001).

[54] R. Mouillet, L. A. de Vaulchier, E. Deleporte, Y. Guldner, L. Travers and J. C. Harmand, Solid State Communications, 126, 333 (2003).

[55] M. Kondow, S. Fujisaki, S. Shirakata, T. Ikari and T. Kitatani, International Symposium on Compound Semiconductors", San Diego, CA76 (2003).

[56] C. Skierbiszewski, Semiconductor Science and Technology, 17, 803 (2002).

[57] J. B. Heroux, X. Yang, and W. I. Wang, Journal of Applied Physics, 92, 4361 (2002).

[58] P. N. Hai, W. M. Chen, I. A. Buyanova, H. P. Xin, C. W. Tu, Applied Physics Letters, 77, 1843 (2000).

[59] J. Wu, W. Shan,W. Walukiewicz, K. M. Yu, J. W. Ager III, E. E. Haller, H. P. Xin, C.W. Tu, Physical Review B, 64, 085320, (2001).

[60] S. Wei, and A. Zunger, Physical Review Letters, 76, 664 (1996).

[61] M. Kondow, K. Uomi, A. Niwa, T. Kitatani, S. Watahiki, Y. Yazawa, Japanese Journal of Applied Physics, 35, 1273 (1996).

[62] T. Miyamoto, K. Takeuchi, F. Koyama, K. Iga, IEEE Photonics Technology Letters, 9, 1448 (1997).

[63] M. Fischer, M. Reinhardt, A. Forchel, Electronics Letters, 36, 1208 (2000).

[64] E. D Palik, Handbook of the optical constants of solids. Academic Press, San Diego (1985).

[65] J.Shah, Solid state Electron, 21, 43,(1978).

[66] M. Fox, Appendix B, optical properties of solids, Oxford University Press Inc., New York (2001).

CHAPTER 3: THE GROWTH AND OPTICAL PROPERTIES OF LOW DIMENSIONAL SEMICONDUCTOR STRUCTURES

In this chapter the fundamental concepts of low dimensional semiconductor structures will be presented including their fabrication and properties which form a key aspect to understanding the optical studies of quantum dots and quantum wells investigated in this work

3.1 INTRODUCTION

Low dimensional semiconductor structures (LDSS) form a major new field of physics research. They are semiconductor structures which have a small scale in one, two or three spatial dimensions. Their electronic and optical properties, as compared to the same material in bulk form, are significantly changed by quantum confinement effects. A typical example of such a structure, in which charge carries are confined to move freely in only two dimensions, is a so-called quantum well. The interest in the preparation, study and applications of LDSS has revitalised condensed matter science and has increased worldwide. These advanced LDSS offer device engineers new design opportunities to tailor novel electronic devices. Thin epitaxial layers with nanometer size were first produced in the late 1970's and this allowed a surge in the study of LDSS. The main requirements, which in practice will be dependent upon the precise application being considered, for ideal LDSS are:

(1) Optical and structural quality: semiconductors produce light when an electron in the conduction band recombines with a hole in the valence band – a radiative process. However, the presence of defects which form energy states within the band gap may weaken the light emission process since recombination of electron – hole occur through this defect. If non-radiative processes become major then the optical efficiency, i.e the number of photons produced for each injected electron and hole, decreases. For semiconductor laser applications, nanostructures with small defect numbers are therefore required. Poor structural quality may also degrade the carrier mobility.
(2) Size: for many applications the majority of electrons and holes should lie in their lowest energy state, implying negligible thermal excitation to higher

states. The degree of thermal excitation is determined by the ratio of the energy separation of the confined states and the thermal energy k_BT, where K_B is the Boltzman constant and T is the temperature. At room temperature k_BT ~ 25 meV and as a rule of thumb the level separation should be at least three times this value (i.e. ~75 meV). As the energy spacing between the states is determined by the size of the structure, increasing the size of the structure results in a decrease of the energy spacing between the confined states. The above requirement sets an upper limit on the size of a nanostructure.

(3) Uniformity: devices will typically contain a large number of nanostructures. Ideally each nanostructure should have the same shape, size and composition.

(4) Growth compatibility: the epitaxial techniques of Molecular Beam Epitaxy (MBE) and Metal-Organic Vapour Phase Epitaxy (MOVPE) are used for the mass production of electronic and electro-optical devices. The commercial exploitation of nanostructures will be more likely if they can be fabricated using these techniques.

(5) Confinement potential: the potential wells confining electrons and holes in a LDSS must be relatively deep. If this is not the case then at high temperatures significant thermal excitation of carriers out of the nanostructure will occur. For electrical applications it is generally sufficient for either electrons or holes to be trapped or confined within the nanostructure. For electro-optical applications it is necessary for both types of carrier to be confined.

(6) p-i-n structures: the ability to place a nanostructure within the intrinsic region of a p-i-n structure allows the efficient injection or extraction of carriers.

3.2 QUANTUM CONFINEMENT

The nanostructured materials have unique optical and electronic properties that are completely different from those of the bulk. The tunability of their optical properties due to size variation allows many optoelectronic applications such as LED, lasers, and photovoltaic devices. These unusual properties of semiconductor nanomaterials are due to the so-called quantum confinement or quantum size effect.

The optical properties dependence on the size of the nanostructures is a consequence of the quantum confinement effect. The Heisenberg uncertainty principle states that if a particle is confined to a region of length Δx in the x axis, then an uncertainty is introduced in its momentum, and is given by:

$$\Delta P_x \sim \frac{\hbar}{\Delta x} \qquad 3.1$$

If the particle is otherwise free, and has a mass m, the confinement in the x direction gives it an additional kinetic energy of magnitude

$$E_{confinement} = \frac{(\Delta P_x)^2}{2m} \sim \frac{\hbar^2}{2m(\Delta x)^2} \qquad 3.2$$

This confinement energy will be important if it is equal to or greater than the kinetic energy of the particle due to its thermal motion in the confinement direction.

This condition may be written as:

$$E_{confinement} \sim \frac{\hbar^2}{2m(\Delta x)^2} > \frac{1}{2}k_B T \qquad 3.3$$

The quantum size effects will become important if

$$\Delta x \leq \sqrt{\frac{\hbar^2}{mk_B T}} \qquad 3.4$$

The criterion given in equation (3.4) provides an idea of how small the structure must be if the quantum confinement effects are to be observed.

3.3 DENSITY OF STATES

The electronic and optical performance of a device is controlled by the density of states (DOS), which is defined as the number of available electronic states per unit volume per unit energy at an energy E. The DOS depends on the dimensionality of the system and the energy versus the corresponding wave vector dispersion relation for the particle. The dispersion relation for an electron in bulk material is given by:

$$E = \frac{\hbar^2 k^2}{2m_e} \qquad 3.5$$

Where m_e , k and ħ are the effective mass of electron, wavevector number, and Plank's constant, respectively

For a three-dimensional (3D) bulk material, the DOS is defined as the number of available electronic states per unit volume per unit energy at energy E and is given by:

$$D(E) = \frac{\sqrt{2} m_e^{3/2}}{\pi^2 \hbar^3} E^{1/2} \qquad 3.6$$

Passing from three-dimensional bulk to two-dimensional (2D) structures, so called 'quantum well', the carrier movement is restricted to a plane. Such two-dimensional systems include thin films, quantum wells and super lattices. In 2D systems the DOS is modified with regards to the number of available electronic states per unit area per unit energy and is given by:

$$D(E) = \frac{m_e}{\pi \hbar^2} \qquad 3.7$$

Further reduction in the dimensionality of the system leads to a 'quantum wire' or one dimensional (1D) system. Examples of such 1D structure include nano tubes, semiconductor nanowires, and nanorods. For a quantum wire the DOS is given by:

$$D(E) = \frac{\sqrt{2} m_e^{1/2}}{n \hbar} E^{-1/2} \qquad 3.8$$

For a zero dimensional (0D) system, such as a quantum dot (QD), the confinement is along all three dimensions and the DOS becomes a delta function. The electron can only have certain discrete energies in the quantum dot. The energy of the states and the number of states available depends on the shape and size of the dot potential. For a quantum dot the DOS is given by:

$$D(E) = \delta(E - Ec) \qquad 3.9$$

Figure 3.1 demonstrate how the density of states in the conduction band changes with the degree of confinement.

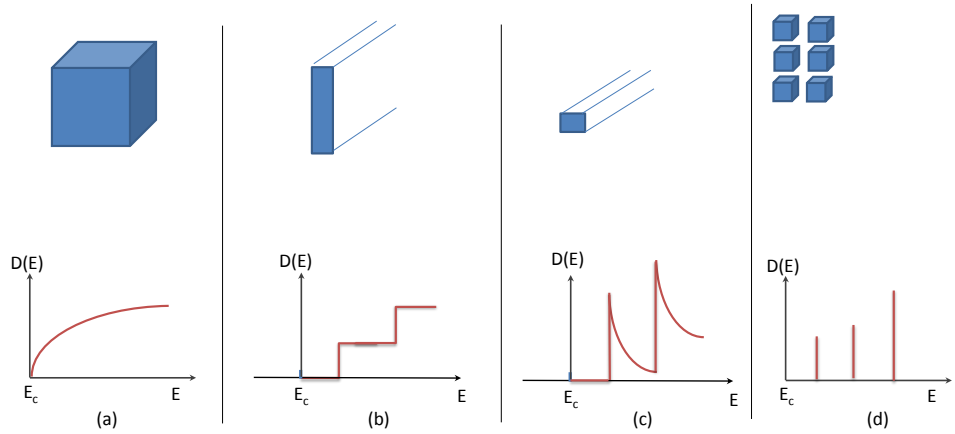

Figure 3.1: Density of states N(E) in the conduction band for (a) bulk semiconductor (3D), (b) quantum well (2D), (c) quantum wire (1D), and quantum dot (0D).

3.4 OPTICAL PROCESSES IN LOW DIMENSIONAL SEMICONDUCTOR STRUCTURES

In the following sections optical processes and carrier dynamics will be considered only for the case of quantum wells and quantum dots.

3.4.1 ABSORPTION IN SEMICONDUCTOR NANOSTRUCTURES

Semiconductor can absorb a photon in a process where an electron is promoted between the valence and conduction bands. The strength of this absorption is proportional to the density of states in both bands – the joint density of states. The joint density of states has a form similar to the density of states in both the conduction and valence bands, and is therefore a strong function of the dimensionality of the system. The absorption will be modified by the quantised energy levels of a nanostructure, resulting in a number of different energy transitions occurring between the confined hole and electron states. A further modification

arises from the influence of excitonic effects. Excitons are bound electron-hole pairs held together by their mutual Coulomb attraction. Since the optical transition can be considered as the creation of an electron-hole pair, the Coulomb attraction increases the absorption rate because it enhances the probability of forming the electron-hole pair. For an ideal two-dimensional system, the exciton binding energy is increased by a factor of four compared to the bulk value. In a real quantum well the electron and hole wave functions penetrate into the barriers, and the ideal two dimensional case is never achieved. However, an approximately twofold enhancement can be achieved. A larger binding energy decreases the probability of exciton ionisation at high temperatures and, as a consequence, stronger excitonic effects are observed in a nanostructure at room temperature than in a comparable bulk semiconductor. Figure 3.2 shows the absorption coefficient of a 40 period GaAs/AlAs multi-quantum wells (MQWs) structure with 7.6 nm wide QWs at 6 K. The spectrum consists of a series of steps, representing the density of states of a two dimensional system with an excitonic enhancement at the onset of each step. A number of transitions are observed between the confined hole state and confined electron state. These transitions are subject to the selection rules. The enhancement of the excitonic binding energy in the quantum well is a consequence of the quantum confinement of the electrons and holes. This forces the electrons and holes to be closer together than they would be in a bulk semiconductor, and hence increases the attractive potential.

One of the most useful consequences of the enhancement of the exciton binding energy in quantum wells is that the excitons are still stable at room temperature. This contrasts with bulk GaAs, which only shows strong excitonic effects at low temperatures. This can be clearly seen in the data presented in Figure 3.3. The enhancement of the excitonic strength in the QW, due to the increased exciton binding energy, is clearly visible.

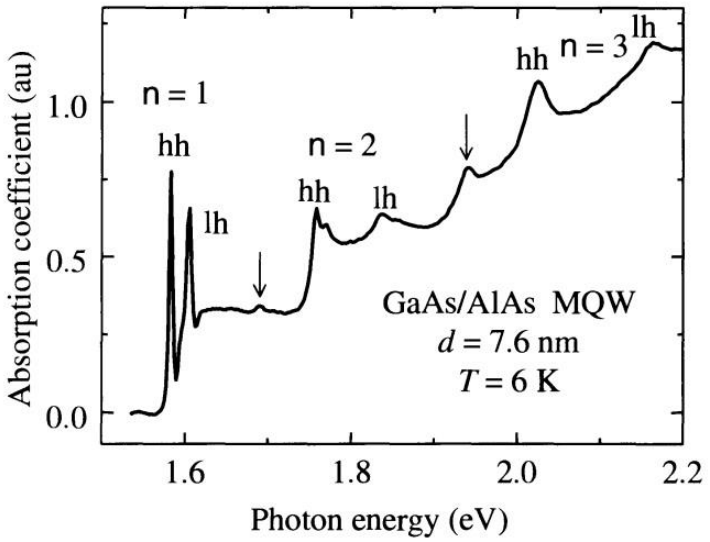

Figure 3.2: Low-temperature absorption spectrum of a 40-period GaAs/AlAs multiple quantum well structure with 7.6 nm wide wells. The most intense features result from transitions between the n^{th} (n = 1, 2, 3) confined light hole (lh) and heavy (hh) hole states and identical index electron states. In addition, two weaker transitions are observed between electron states (e1 and e3) and the first (hh1) and third heavy hole (hh3) states, namely hh3 - e1 and hh1 - e3[1].

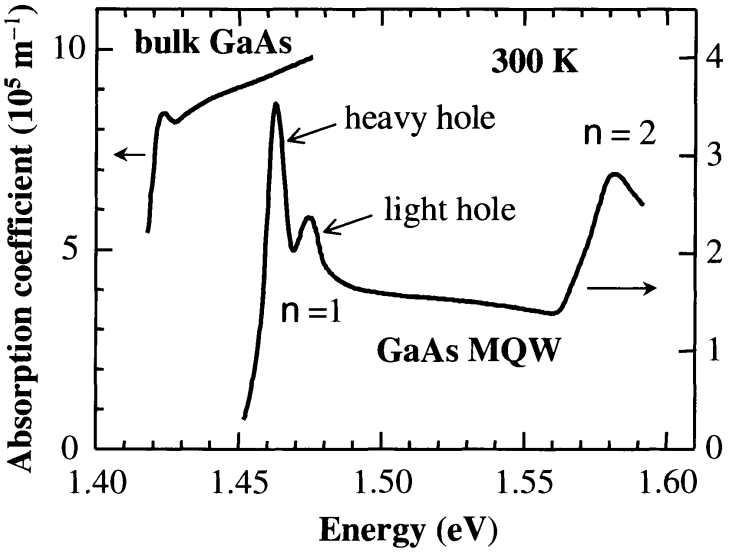

Figure 3.3: Room temperature absorption spectrum of a GaAs/$Al_{0.28}Ga_{0.72}As$ MQW structure containing 77 GaAs quantum wells of width 10 nm. The absorption spectrum of bulk GaAs at the same temperature is shown for comparison[2].

3.4.2 PHOTOLUMINESCENCE PROCESS IN NANOSTRUCTURES

Electrons and holes can be created in a semiconductor either optically with incident photons of energy greater than the band gap, or by electrical injection in a p-n junction. The electrons and holes are typically created with excess energies above their respective band edges. However, the time required to lose this excess energy is generally much shorter than the electron–hole recombination time. Consequently the electron and holes relax to their respective band edges before recombining to emit a photon. Emission therefore occurs at an energy corresponding to the band gap of the structure, with a small distribution due to the thermal energies of the electrons and holes. The influence of rapid carrier relaxation is demonstrated in the emission spectrum of a structure containing quantum wells of five different widths (see Figure 3.4). Only emission corresponding to the lowest-energy transition of each well is observed, even though the wider wells contain a number of confined states.

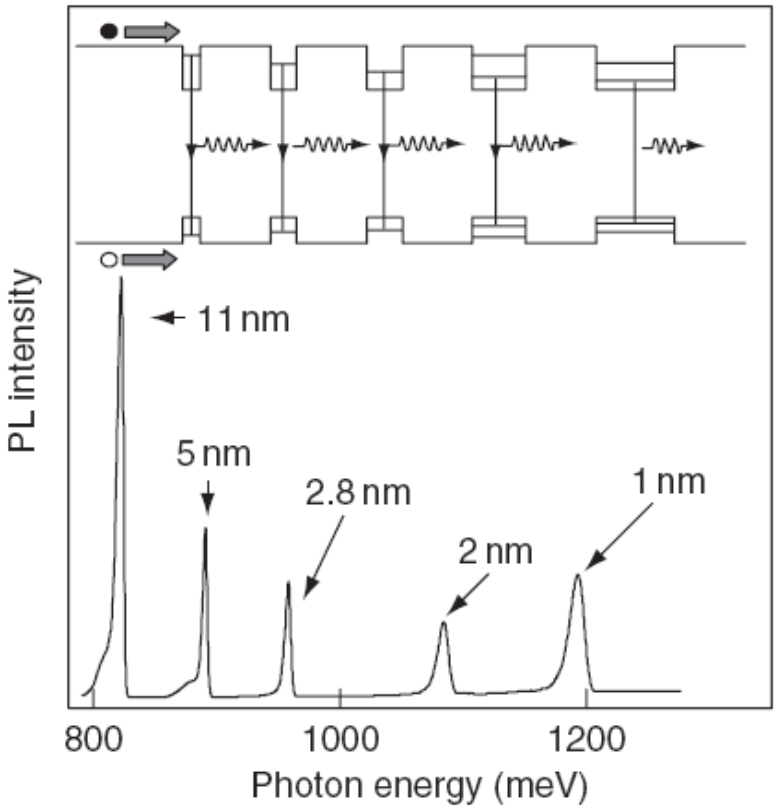

Figure 3.4: Emission spectrum of a quantum well structure containing five wells of different thicknesses. The wells are $Ga_{0.47}In_{0.53}As$ and the barriers are InP. The inset shows the electronic structure and the nature of the optical transitions[3].

Higher-energy transitions in a nanostructure can be observed in emission if the density of electrons and holes is sufficiently large that the underlying electron and hole states are populated. This can occur under high-excitation conditions where the lower energy states become fully occupied and carriers are prevented from relaxing into these states due to the Pauli Exclusion Principle. Figure 3.5 shows the emission spectra of an ensemble of self-assembled quantum dots for different optical excitation powers. At low powers the average number of electrons and holes in each dot is very small, and consequently only the lowest-energy (ground state) transition is observed. However, with increasing power the ground state, which has a degeneracy of two, is fully occupied and emission from higher-energy (excited) states are observed. Fluctuations in the size, shape and composition within an ensemble of quantum dots result in a significant inhomogeneous broadening of the optical spectra due to size non-uniformity of the quantum dots. However, by probing a very small number of dots, the predicted very sharp emission from these 0D nanostructures can be observed.

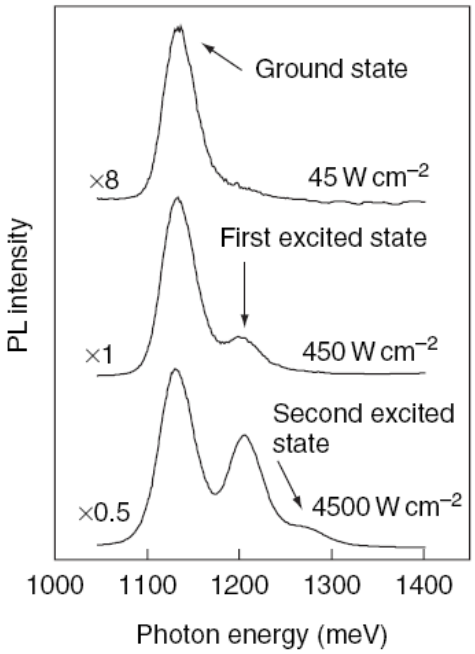

Figure 3.5: Emission spectra of an ensemble of InAs self-assembled quantum dots for three different laser power densities. At the highest power, emission from three different transitions is observed. The numbers by each spectrum indicate the relative intensity scale factors[4]

3.5 EPITAXIAL GROWTH OF LOW DIMENSIONAL SEMICONDUCTOR STRUCTURES

Epitaxy is a controlled way of growing a solid film on a crystalline substrate, in which the atoms of the growing film adjust to the atomic arrangement of the substrate atoms. The two main epitaxial methods used for growing low dimensional semiconductor structures are molecular beam epitaxy (MBE) and metal-organic vapour phase epitaxy (MOVPE). In MBE, the material to be deposited is evaporated in ultra-high vacuum (UHV), where epilayers crystallise when the atoms hit the hot substrate. Since MBE is operated under UHV condition, simultaneous characterisation of the growing film is possible. This fact makes this method very popular in research environments. However, the growth rate is very slow, which limits the thickness of the film to be grown. MOVPE is a chemical method used to grow semiconducting materials, which does not require as high vacuum as MBE and the growth rate is in general much higher than in MBE. MOVPE is therefore a preferred method to grow devices that require large thicknesses. To illustrate the importance of low dimensional semiconductor structures in optoelectronic devices, an example will be given to show the influence of confinement on the electronic transitions and optical properties of a QW.

3.5.1 MOLECULAR BEAM EPITAXY

MBE[5] is an epitaxial process involving the reaction of one or more thermal beams of atoms or molecules with a crystalline surface under UHV conditions, typically of the order of 5×10^{-11} mbar or better (atmospheric pressure is about 1000 mbar). MBE can achieve precise control in both chemical compositions and doping profiles. Single-crystal multilayer structures with dimensions on the order of atomic layers can be made using MBE. Thus, the MBE method enables the precise fabrication of semiconductor heterostructures having thin layers from a fraction of a micron down to a monolayer. The disadvantage of MBE is that the growth process is slow. Generally, the growth rate is about 1 μm per hour which translates to a rate of 1 monolayer per second. Advantages of MBE include highly abrupt junctions between

different materials, good control over the thickness of layers, good reproducibility, and the ability to scale the process for mass production.

The elements that constitute a heterostructure (e.g. Ga, As, and Al, etc) are vaporized in furnaces with orifices directed towards the substrate, but shielded from it by shutters. This is the Knudsen or molecular-flow regime of a gas, and the furnaces are called Knudsen or K-cells. Molecules that emerge from the K-cells do not diffuse as in a gas but form a molecular beam; travelling in straight lines without collisions until they impinge on the substrate (the mean free path of molecules between collisions is much larger than the width of the chamber at UHV condition). The substrate holder rotates continuously to achieve uniform epitaxial layers (e.g., ±1% in doping variations and ±0.5% in thickness variations).The flux of each element can be controlled through the temperature of each furnace. Growth starts when the shutters are opened. Dopants are added by using additional cells. The usual donor is Si, which belongs to group IV of the periodic table. However, it is not obvious whether it should act as a donor or acceptor in a group III-V compound. This depends on which host atom the Si will replace. Usually Si acts as a donor in conventional (100) GaAs substrate, but it can also act as an acceptor by growing on a different surface from the usual (100) orientation. It also tends to become amphoteric, acting both as a donor and acceptor, at very high concentrations (around 10^{-25} m^{-3}). Beryllium element is commonly used as an acceptor in III-V semiconductors.

3.5.2 GROWTH OF QUANTUM WELL STRUCTURES

A quantum well is a potential well within a semiconductor structure which is adequately thin to confine the carrier's movement on a length-scale similar to their de Broglie wavelength which, for an electron in GaAs at room temperature, is about 30 nm. When carriers are localized in this way their electronic and optical properties are determined by quantum mechanical aspects of their behaviour which are not apparent in bulk structures. Figure 3.6 (a) shows a schematic diagram of the simplest type of quantum well that can be grown. In this particular case, a GaAs/AlGaAs structure is grown on a GaAs substrate. The structure consists of a GaAs layer of

thickness (d) sandwiched between much thicker layers of the alloy semiconductor AlGaAs; d is chosen so that it is comparable to de Broglie wavelength.

$GaAs/Al_xGa_{1-x}As$ materials are unique among III-V semiconductors because the dimensions of the crystalline lattice of GaAs and $Al_xGa_{1-x}As$ match within 0.1% for all values of x. This property makes growth of $GaAs/Al_xGa_{1-x}As$ heterostructures straightforward without any possible defect. The difference in bandgaps of the two materials can vary at room temperature from 0 eV to as much as 1.6 eV (as x increases from 0 to 1).

As Ga is substituted by Al in the $Al_xGa_{1-x}As$ alloy system the direct band gap increases from 1.424 eV in GaAs (x = 0) to 3.018 eV in AlAs (x = 1). A quantum well is formed using a narrow GaAs layer sandwiched between barrier layers of $Al_xGa_{1-x}As$ having a composition chosen to give the desired well depth. The whole structure is grown on a GaAs substrate. The band discontinuity ratio between GaAs and $Al_xGa_{1-x}As$ is independent of alloy composition (ΔEc and ΔEv are constant fractions whereas ΔEg changes as x is varied). For a typical barrier composition of x = 0.3, ΔEg = 0.374 eV and ΔEc and ΔEv are 0.247 eV and 0.127 eV, respectively[6].

It is possible to fabricate a structure consisting of many quantum wells, with each well separated from neighbouring wells by a barrier. If the barriers are relatively thick, carriers located in different wells are essentially isolated. Therefore, the interaction between adjacent wells will be insignificant and the structure behaves identically to a single quantum well, although some properties (e.g., the photoluminescence) will increase linearly with the total number of wells. In this case the structure is known as a multiple quantum well. On the other hand, if the barrier thickness is reduced to 50 Å or less then there is a strong interaction between adjacent wells (i.e carriers in neighbouring quantum wells may interact via the part of their wave functions which penetrates into the barriers). This creates a continuous band of states through which conduction is much more readily allowed. The structures are then known as super lattices.

MQW structures with their distinctive tunability represent a vital class of semiconductors, which will have a great impact on future electronic technology. The most important application of some of these structures has been in optoelectronic devices, especially laser diodes. The optical properties of semiconductors are usually

reflected in terms of transitions of electrons between quantum mechanical energy levels, as in the Bohr atom. In the following, the optical emission from quantum wells as a result of external excitation will be discussed.

An external light source with photon energy greater than the effective band gap produces excess electron–hole pairs by excitation of electrons from the valence band to conduction band. Excited electrons rapidly lose their excess energy and thermalize to the sub-band edges to take up Fermi energy distributions. In few picoseconds after excitation, the electrons recombine to vacant valence band states by spontaneous emission. The shape of the spectrum corresponds to the thermal distribution of carriers in the bands.

Figure 3.6 (b) illustrates a transition of an electron between an occupied state at E_1 in the $n_z = 1$ sub-band in the conduction band and an empty state (i.e., a hole) at E_2 in the $n_z = 1$ sub-band in the valence band, resulting in emission of a photon of energy $h\nu = E_1 - E_2$ as required by energy conservation. This photoluminescence process (or spontaneous emission), which requires external excitation such as illumination (photoluminescence) or biasing a p-n junction (electroluminescence, as in a light-emitting diode).

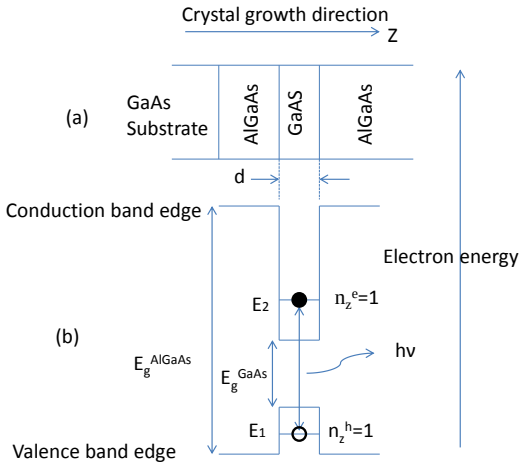

Figure 3.6: (a) Schematic diagram of a single GaAs/A1GaAs quantum well. The quantum well is formed in the thin GaAs layer sandwiched between AlGaAs layers which have a larger band gap. (b) Spatial variation of the conduction band, the valence band, and optical transition of an electron from a state in the $n_z = 1$ conduction sub-band to an empty state (hole) in the $n_z = 1$ valence sub-band resulting in emission of a photon of energy $h\nu = E_1 - E_2$.

At typical temperatures the electrons and holes are at energies near to their respective band edges, and therefore the photon energy hν is close to the separation of the n_z = 1 sub-bands. Since these energies are determined by the quantum well width, it is possible to change the photon energy for emission or absorption by changing the well width. As the well width is reduced the energy separation increases and the wavelength of light emitted by the structure is reduced. This ability to control the emission wavelength by simply adjusting the well width, without changing the chemical composition of the constituent materials, is one of the major attractions of quantum-confined structures6. The shortest wavelength possible for a given material combination is determined by the band gap of the wide gap barrier material alongside the well. The strength of the luminescence signal or the absorption is determined by the rates at which the electronic transitions occur.

There are many practical applications of quantum well structures (including quantum well heterostructure lasers). It has been shown that for a semiconductor laser the reduction in dimensionality should lead to an increase in efficiency, a decrease in the lasing threshold, less temperature dependence and narrower spectral lines. In a quantum well only the electrons near the edge of the energy band will contribute directly to the gain at the lasing process. All the other electrons in the energy band are effectively wasted. In QWs at T=0 all the electrons are near the edge of the bands because the bands are extremely narrow and therefore all the electrons can participate in the lasing process.

3.5.3 GROWTH OF QUANTUM WIRES

An obvious fabrication technique for quantum dots or wires is to start with a quantum well, which provides confinement along one direction, and selectively remove material to leave ridges or mesas, forming wires or dots, respectively. Material removal is achieved by the use of electron beam lithography followed by etching. The advantage of this technique is that any desired shape can be produced, although because the electron beam has to be scanned sequentially over the surface, writing large-area patterns is a very slow process

Figure 3.7 outlines of how quantum wires might be fabricated. A standard quantum well layer can be patterned with photo- or electron beam lithography and etched to leave a free standing strip of quantum well. The latter may or may not be filled with an overgrowth of the barrier material (in this case $Ga_{1-x}Al_xAs$). Any charge carriers are still confined along the heterostructure growth axis (z- axis) as they were in quantum well, but in addition (provided the strip is narrow enough) they are now confined along an additional direction, either the x- or the y- axis, depending on the lithography process. Figure 3.8 shows an expanded view of a single quantum wire, where clearly electron (or hole) is free to move only in one direction, in this case along the y-axis. Within the effective mass approximation along the confinement axis the wire can still be described by a parabolic dispersion (equation 3.5) similar to bulk and in-plane motion within a quantum well.

V-grooved quantum wires is another class of quantum wire that can be formed by patterning the substrate before growth[7,8].

The optical properties of a quantum wire should be similar to that of a quantum well, but with a further enhancement of the exciton binding energy provided by the additional quantum confinement. However, to date the quality of available quantum wires is not sufficient to observe these effects clearly. This is mainly due to spatial fluctuations of the wire cross-section leading to significant inhomogeneous broadening of the optical spectrum.

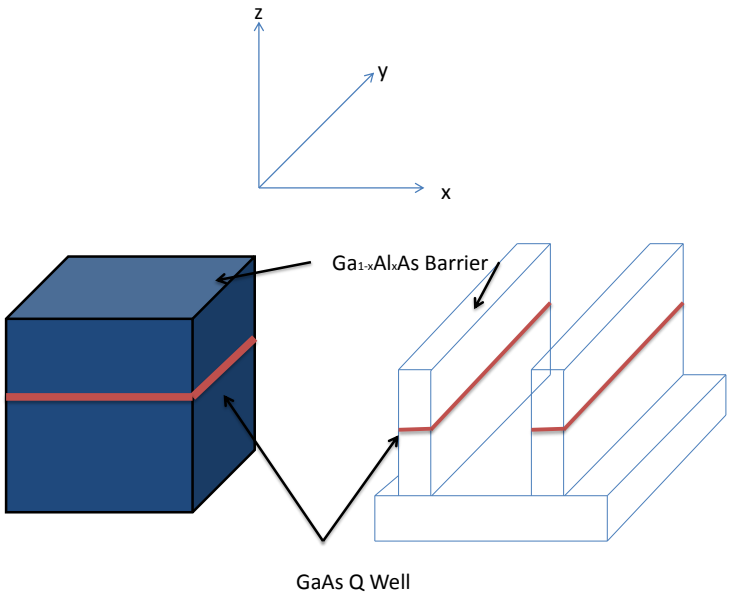

Figure 3.7: Fabrication of a quantum wire

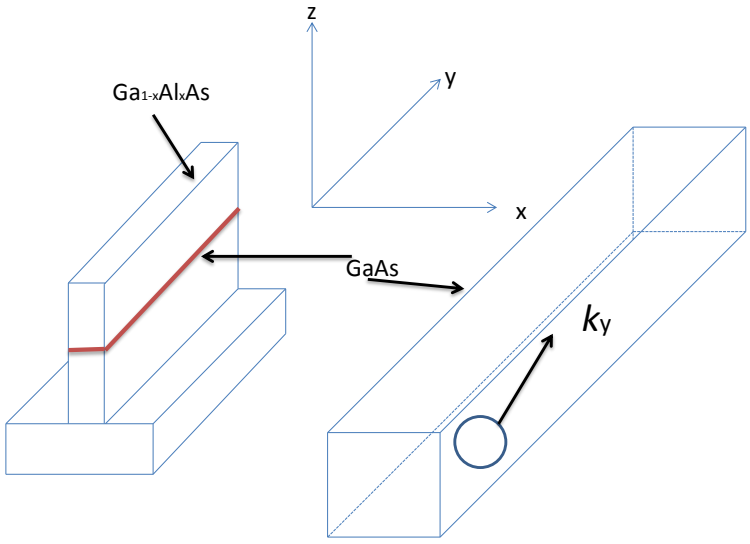

Figure 3.8: A single wire and an expanded view showing schematically the single degree of freedom in the electron momentum (k_y).

3.5.3 GROWTH OF QUANTUM DOTS

Semiconductor quantum dots (QDs) have been the subject of intensive research in recent years due to their great potential both in applications and in fundamental studies[9-11]. Especially, with the progress of epitaxial growth technology it is now

possible to precisely control the quantum dots in term of size, composition and density in order to achieve desired electrical and optical properties. On the applications side, quantum dots could be the best candidate for the next generation of photonics devices, such as high performance lasers and photo-detectors. Semiconductor quantum dots have unique discrete states due to the three dimensional confinement. In principle, quantum dot lasers can achieve high efficiency because nearly all of the energy is concentrated in the ground state and they can have excellent temperature stability due to the discrete energy levels. Quantum dot detectors can cover a very broad range of wavelengths because of the various discrete energy states in the QDs based on their inter-band and inter-subband transitions. In fundamental studies, quantum dots can be regarded as artificial atoms because they have discrete energy states like atoms or molecules; so it is possible to make quantum dots with various structures to study various quantum effects or discover new phenomena.

Quite a few methods for the fabrication of QDs have been used over the last twenty years including lithography-based technologies. This technique, which is widely used to fabricate QDs, predominantly by the combination of high-resolution electron beam lithography and etching lithographic methods and subsequent processing, has some drawbacks as highlighted below:

1. Size limitation prevents the observation of strong quantization effects
2. Formation of defects due etching
3. Size non-uniformity
4. Poor interface quality
5. Damage to the bulk crystal

A new attractive method of defect free 10 nm scale QD fabrication is the Stranski-Krastanov (SK) growth in lattice-mismatched systems. This can occur when a thin layer of a semiconductor is grown on a substrate whose lattice constant differs from that of the epilayer. In the SK growth mode the mismatched epitaxy is initially accommodated by biaxial compression in a layer-by-layer (2D) growth region, traditionally called the wetting layer. After deposition of a few monolayers the strain energy increases and the development of islands (0D) becomes more favourable than planar growth.

For a system in which this occurs the transition between coherently strained 2D growth and the onset of 0D island growth is reached after a 'critical thickness' (d_c) of epitaxial material has been deposited. The critical thickness is defined as:

$$d_c \cong \frac{a_s}{2|\varepsilon|} \qquad 3.10$$

Where a_s is the lattice constant of the substrate material and ε is the strain between the two materials. ε is defined as:

$$\varepsilon = \frac{a_s - a_l}{a_l} \qquad 3.11$$

Where a_l is the lattice constant of the epilayer

This critical thickness decreases by increasing the lattice mismatch (a_s - a_l) between the epitaxial material and the substrate. The transition from a purely 2D to 3D growth during the deposition of a strained epitaxial layer is referred to as the Stranski - Krastanow growth mode. Figure 3.9 shows SK growth mode of self-assembled quantum dots. In the first two stages (Figure 3.9. a,b), a strained but uniform layer of InAs grows with the same lattice parameter as that of GaAs substrate. This forms what is called wetting layer which is a narrow quantum well. Beyond a certain layer thickness called critical thickness, strain makes it energetically favourable for the InAs to form small three-dimensional islands (Figure 3.9.c), which constitute the self-assembled quantum dots. Growing more materials after that may lead to dislocations (Figure 3.9.d). To obtain a good optical efficiency from grown quantum dots, a capping layer (usually the same material as the substrate) is deposited over the dots. This protects the dots and avoids problems with surface recombination effects.

For InAs/GaAs QDs, SK growth occurs after as little as 1.7 monolayers (MLs) of InAs has been deposited. The critical thickness (d_c) increases with decreasing Indium (In) fraction, reaching ~4 MLs for $In_{0.5}Ga_{0.5}As$/GaAs QDs. The lowest In composition that can support islanding of the $In_xGa_{1-x}As$ layer appears to be ~25%.

One of the advantages of SK growth of QDs, an in-situ technique, is that no processing is required. Since the dots are grown in-situ, a homogeneous surface morphology is maintained and defect creation is avoided. However, the inherent problem associated with this method is the size non-uniformity (~10%) and the position uncontrollability of the QDs. Controlling the dimension and arrangement of the self-organized 0D structures is thought to be very important for obtaining good properties of the structures.

By adjusting the growth parameters such as deposition rates and temperature, the composition, size, shape and surface density of the dots can be controlled. Post-growth annealing provides an additional control parameter. The fabrication of self-assembled quantum dots (SAQDs) by the SK method has been applied to numerous combinations of semiconductor materials, including III-V semiconductor compounds ($In_xGa_{1-x}As/GaAs$, $In_xGa_{1-x}As/AlGaAs$, and InP/GaInP), II-VI materials (CdSe/ZnSe), and wide band gap nitrides (GaN/AlGaN).

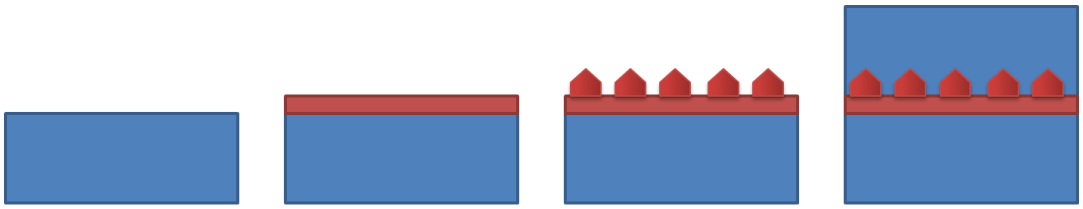

Figure 3.9: Stranski-Krastanow growth mode of self-assembled quantum dots. (a)-(d) show sequential stages in the growth of InAs quantum dots on a GaAs substrate. (a) shows the substrate only; (b) InAs is deposited on the substrate: a thin, uniform layer grows, forming a narrow quantum well called the wetting layer; (c) beyond a certain layer thickness, the strain due to the lattice constant mismatch between the materials causes small islands of InAs to form; (d) a GaAs capping layer is grown over the dots for optical characterisation.

3.6 CARRIER DYNAMICS IN LOW DIMENSIONAL SEMICONDUCTOR STRUCTURES

Due to the hetero-interface of two materials and the discrete nature of the quantum dot levels, carrier dynamics in QD structures are considerably more complex than in bulk materials. Figure 3.10 depicts a simplified band diagram of a semiconductor QD structure under excitation with light, as found for instance in photoluminescence experiments. Here, the excitation is assumed to occur in the barrier, i.e. the material surrounding the QDs, for example GaAs in the InAs/GaAs system. The wetting layer (WL), on which the QDs form in self-assembled growth, acts as an additional QW in the structure. The dynamic carrier processes thus include:

1. Excitation of electrons from the barrier valence band into the conduction band, thereby creating free electrons in the conduction band and free holes in the valence band.
2. Relaxation from the barrier to the wetting layer.
3. Capture of the carriers into the quantum dots. The capture can occur either to the ground state or to higher energy states with subsequent relaxation. Capture directly from barrier states is also possible.
4. Carrier relaxation via carrier-carrier interaction (Auger effect) or carrier phonon interaction.
5. Carrier transfer from the QD to nearby deep level traps leading to carrier trapping and/or nonradiative recombination.
6. Radiative recombination where an electron and hole annihilate each other. The energy released in the process is emitted via creation of a photon. Other possible processes are radiative and nonradiative recombination of carriers in WL and barrier conduction/valence band and thermal escape of the electrons and holes from the quantum dots.

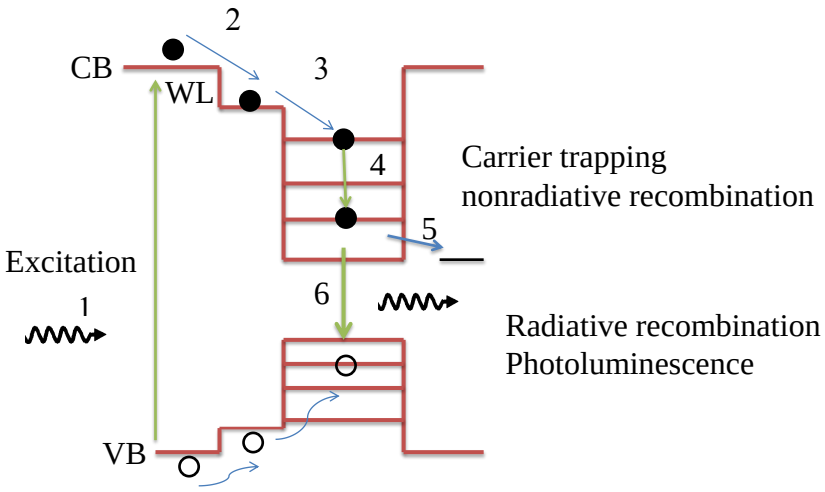

Figure 3.10: simplified band diagram of a semiconductor QD structure under excitation with light showing the different processes as explained above.

Higher-energy transitions in a nanostructure can be observed in emission if a powerful excitation source is used. The density of electrons and holes is sufficiently large that the underlying electron and hole states are populated. The lower energy states become fully occupied and carriers are prohibited from relaxing into these states by the Pauli Exclusion Principle.

REFERENCES

[1] A. Fox, Contemporary Physics, 37, 111 (1996).

[2] D. Miller, D. Chemla, D. Eilenberger, P. Smith, A. Gossard, and W. Tsang, Applied Physics Letters, 41, 679 (1982).

[3] D. Mowbray, chapter 3, Nanoscale Science and Technology, book, Edited by R. W. Kelsall, The University of Leeds, UK John Wiley & Sons Ltd (2005).

[4] M. J. Steer, D. J. Mowbray, W. R. Tribe, M. S. Skolnick, M. D. Sturge, M. Hopkinson, A. G. Cullis, C. R. Whitehouse, and R. Murray, Physical Review B, 54, 17738 (1996).

[5] M. A. Herman, and H. Sitter, Molecular Beam Epitaxy, Springer-Verlag, Berlin, (1996).

[6] P. Blood, Semiconductor physics / quantum wells and GaAs-based structures, Encyclopedia of Modern Optics, 9 (2005).

[7]J. Wang, D. A. Thompson, B. J. Robinson, and J. G. Simmons, Journal of Crystal Growth, Volumes, 175–Part 2, 793 (1997).

[8] S. Kim, J. Ro, K. Park, and E. Lee, Journal of Crystal Growth, 201 , 828 (1999).

[9] L. Jacak, P. Hawrylak, and A. Wojs, Quantum dots. Berlin: Springer Verlag, (1998).

[10] D. Bimberg, M. Grundmann, and N. N. Ledentsov, Quantum Dot Heterostructures. New York, John Wiley & Son Ltd, (1999).

[11] D. G. Deppe, H. Huang, and O. B. Shchekin, IEEE Journal of Quantum Electronics, 38, 1587, (2002).

CHAPTER 4: EXPERIMENTAL TECHNIQUES

This chapter describes the optical Photoluminescence (PL) spectroscopy, transmission electron microscopy (TEM) and secondary ion mass spectroscopy (SIMS) characterization techniques used to investigate the semiconductor samples presented in this thesis. The hardware and software required to implement these methods are also presented. The sample growth and annealing conditions are described in the relevant chapters

4.1 PHOTOLUMINESCENCE

Photoluminescence (PL) is the spontaneous emission of light from a material under optical excitation. The term "luminescence" (the literal translation from Latin is "weak glow") was introduced into the literature by Wiedemann in1888. Prefix photo refer to this luminescence initiated by photoexcitation. There are several types of luminescence depending on the cause or duration. Excitation by absorbance of a photon leads to a major class of technically important luminescent species which fluoresce or phosphoresce. In general, fluorescence is "fast" (ns time scale) while phosphorescence is "slow" (longer time scale, up to hours or even days).

Photoluminescence (PL) provides information about the size and quality of semiconductor structures containing quantum wells, wires or dots. In a PL experiment light of sufficient energy greater than the bandgap of investigated sample is incident on a material; photons are absorbed followed by electron hole pair creation. Once the electrons and holes have relaxed to their band edges excitons may form. Recombination of the carriers now occurs via either radiative or non-radiative processes. If radiative relaxation occurs, the emitted light is called PL.

Fig. 4.1 (a) shows the photo-excitation of an electron from the valence into the conduction band and intra band relaxation to band edge Fig. 4.1 (b) and finally the electron–hole recombination and photon production are illustrated in Fig. 4.1 (c).

The emitted light can be collected and analyzed to yield a wealth of information about the photoexcited material. PL investigations can be used to characterize a variety of material parameters. The PL spectrum provides the transition energies, which can be used to determine electronic energy levels. The PL intensity gives a measure of the relative rates of radiative and nonradiative recombination. The

intensity and full width at half maxmuim (FWHM) of the PL signal as well provides information on the quality of sample.

PL is simple, versatile, and nondestructive. Indeed, the technique requires very little sample preparation or environmental control. Because the sample is excited optically, there is no need for electrical contacts or junctions and high-resistivity materials cause no practical difficulty. This feature makes PL mostly attractive for samples having higher resistivity or undeveloped contact/junction technology. Another advantage of the PL is that the luminescence can be investigated at different regions on the sample surface.

The main disadvantage of PL analysis originates from its reliance on optical techniques: the sample under investigation must emit photons. Indirect-bandgap semiconductors, where the conduction band minimum and the valence band maximum don't have the same value in momentum space, have inherently low PL efficiency. Nonradiative recombination tends to dominate the relaxation of excited populations in these materials. Another shortcoming of PL is the difficulty in estimating the density of traps and impurity states. When these states have radiative levels, they are readily identified in the PL spectrum, and the intensity of the associated PL peaks provides a relative measure of their presence in the sample. However, measuring the absolute density of these state is different[1].

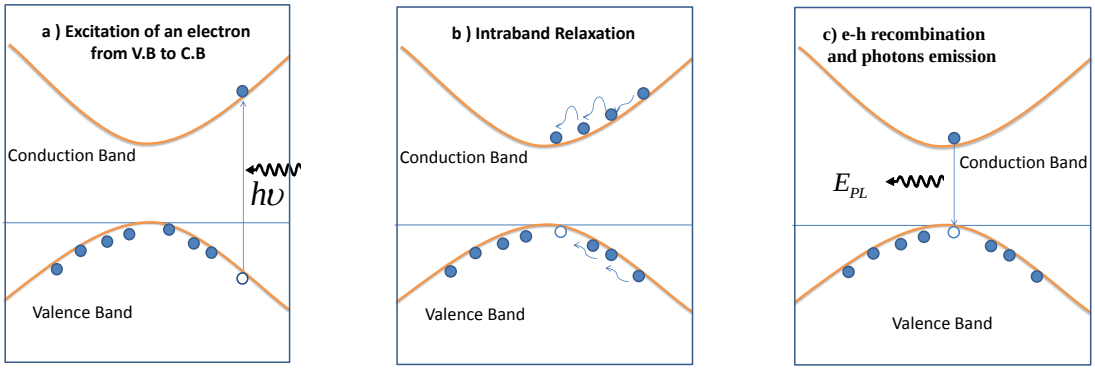

Figure 4.1: Schematic illustration of the basic processes involved in luminescence emission from optically excited semiconductors.

4.1.1 SYSTEM HARDWARE IMPLEMENTATION

This section describes the hardware required to implement a PL system which is interfaced with a computer. The PL system is capable to operate over the temperature range 10K-350K.

The block diagram and photograph of the PL system used in this work is shown in Figures 4.2 and 4.3, respectively. Some of the important elements of the PL system are described below.

4.1.1.1 SPECTROMETER

To allow spectral analysis, the emitted photoluminescence was dispersed using a grating spectrometer. The iHR 550 spectrometer used in this study was purchased from Horiba Jobin Yvon. It has a focal length of 0.55 m and aperture of f/6.4. It offers a motorized grating turret which has the capacity to hold three different gratings. Gratings with the following specifications are used: 1200 grooves/mm blazed at 500 nm, 600 grooves/mm blazed at 2000 nm and 300 grooves/mm blazed at 3000 nm. The entry and exit slits are adjustable from 0.1mm to 2mm. The spectrometer is capable of scanning with a speed of 160 nm/sec. The iHR 550 allows minimum step size of 0.025nm. It also offers a motorized internal filter wheel with capacity to accommodate six different filters which are placed just after the entry slit inside the spectrometer. The iHR550 has two entrance and two exit ports available. One exit port is configured for use with a photomultiplier tube detector (PMT), and the other one configured with a Si/InGaAs dual detector.

4.1.1.2 LASERS, LIGHT CHOPPER AND OPTICS

The PL setup is equipped with excitation sources consisting of blue, green and red lasers. The power of the laser incident on the sample can be tuned manually by using a natural density filter. A mechanical light chopper is utilised to chop the laser light. A band-pass filter is implemented in the path of the laser light to stop the unwanted higher order lines of the laser light. Optics including lenses and reflectors are

employed to focus the light onto the sample and to focus the PL signal on the entry slit of the spectrometer are shown in Figure 4.2

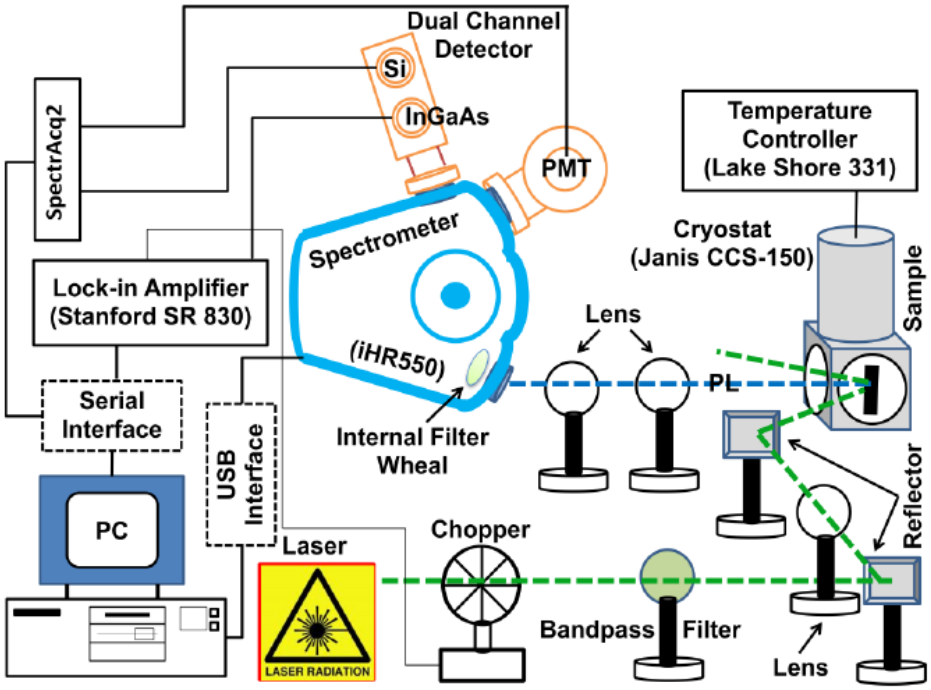

Figure 4.2: A systematic diagram of photoluminescence (PL) apparatus[2].

Figure 4.3: Photograph of photoluminescence (PL) ppparatus[2].

4.1.1.3 DETECTORS

Optical detectors are opto-electronic devices used to convert incident photons to electronic signals; the spectrometer is equipped with two detectors. One dual channel solid state detector Si/InGaAs from Horiba Jobin Yvon is attached at the side exit of the spectrometer. It can cover the optical range from 300 nm to 1700 nm. The silicon operates up to 1.1 µm above which it becomes transparent and the InGaAs detector operates from ~1.1 µm up to 1.7 µm . A single channel photomultiplier tube (PMT) is placed at the front exit of the spectrometer. PMT detectors typically offer much higher sensitivity than solid state detectors and operate effectively in the UV/VIS and NIR. However, typically their spectral coverage is limited to about 950 nm. PMT detectors also require high voltage power supplies. It can detect the light in the spectral range from 180nm to 900nm.

4.1.1.4 SPECTRACQ2

To process and amplify the collected signals from the detectors, data acquisition units are commonly used. SpectrAcq2 is a data acquisition module from Horiba Jobin Yvon. It is a high speed unit that has the capability to capture and process 1000 data points per second collected from PMT or from Si/InGaAs detectors, and store data of up to 5000 data points. SpectrAcq2 is Configurable for current or voltage signal inputs. This module provides an analog high voltage output for controlling PMT (~ 950 Volts). Communication between the computer and SpectrAcq2 is via a serial port RS-232.

4.1.1.5 LOCK-IN AMPLIFIER

Lock-in amplifiers (LIA) are usually employed when very small AC signals need to be detected and any other unwanted signals have to be rectified. The LIA measurement is based on the phase sensitive detection, which basically refers to the demodulation or rectification of the noisy signal from the detector by mixing with a

reference signal coming from the mechanical chopper that is used to chop the light with fixed frequency.

The lock-in amplifier is fed by two signals; one is a control signal from a detector connected to the chopper, and the other is a response signal from the monitoring device. The purpose of the lock-in amplifier is then to selectively amplify only components of the response signal which oscillate at the same frequency as the control signal. The result is a very effective discrimination of noise, and hence a large increase in the signal to noise ratio is obtained

A digital lock-in amplifier, model Stanford SR830 DSP has been implemented in the PL setup. SR830 has the capability to measure and amplify very small signals down to few nano-volts (nV) with sensitivity of 2 nV.

4.1.1.6 CRYOSTAT AND TEMPERATURE CONTROLLER

For the temperature dependent PL measurements a state-of-the-art cryostat, model Janis CCS-150 has been used. To control the temperature of the sample, a temperature controller, model Lake Shore 331, along with cryostat have been implemented for our low temperature PL setup. It also consists of a cold finger, radiation shield, homemade sample holder, aluminium vacuum shroud and thermal sensors. The principle of refrigeration is based on close-cycle flow of helium gas (He) through a compressor. It allows scanning the temperature from 10K to 350K.

4.1.1.7 COMPUTER INTERFACE

A computer with 120MB RAM, 200MB hard disk, windows XP as an operating system, a high speed USB port, a serial port RS-232 is the minimum requirement for the PL apparatus interface. The spectrometer is interfaced with computer via USB port. Data acquisition box spectrAcq2 and lock-in amplifier are connected to the computer by means of serial port RS-232 and can be initialized and controlled from computer. A filter wheel fitted inside the spectrometer can also be controlled through high speed USB port[2].

4.1.1.8 SYSTEM CONTROLLING SOFTWARE

Software, named SynerJY, which has been supplied by Horiba Jobin Yvon is used to control each equipment of the PL system remotely. The software facilitates the selection of suitable grating, detector and entry/exit slit widths etc. Different parameters which are required to perform the PL measurement can be entered through software. The software is flexible in terms of recording and processing data simultaneously. The software can drive the turret containing three gratings, slits, and shutters. It also has control over the entrance and exit mirrors to select detector at axial and side positions. A filter wheel having different colour filters situated inside the spectrometer can also be controlled using the software.

4.2 STRUCTURAL CHARACTERIZATION

Structural characterization of the samples was made using a transmission electron microscopy (TEM) technique to build up a full picture of the epitaxial layers. A visual image of the quantum wells was achieved with TEM. Elemental analysis was carried out using energy dispersive X-ray (EDX) technique.

4.2.1 ELECTRON MICROSCOPY

Transmission electron microscopy (TEM) is perhaps the most powerful analytical tool available to material analysis. TEM can yield information about the topography (surface features of an object), morphology (shape and size of the particles making up the object), composition (the elements and compounds that the object is composed of and the relative composition) and crystallographic information (how the atoms are arranged in the material).TEM operates by exciting highly energetic electrons from a source, where the electrons are focused and collimated along the optic axis of the microscope and passed through a thin specimen (normally less than 1 μm). The transmitted electrons are then used to form an image, diffraction pattern, or chemical spectrum of the specimen.

The basic components in all electron microscopes (EMs) are the following:

1- Electron gun producing a stream of electrons in high vacuum. This stream is accelerated towards the specimen (with a positive electrical potential).
2- Metal apertures and magnetic lenses to confine and focus electron beam into a thin, focused, monochromatic beam.
3- the imaging system

When an accelerated beam of electrons impinges upon a sample a rich variety of interactions takes place (see Figure 4.4). The versatility of electron microscopy and X-ray micro analysis is derived in large measure from this variety of interactions that the electrons undergo in the specimen. The interactions that occur during the collision of the electron beam and the sample include directly transmitted electrons, backscattered electrons, secondary electrons, coherent elastic scattered electrons, incoherent inelastic electrons, incoherent elastic forward scattered electrons, characteristic x-rays, and Auger electrons. In principle all these products of primary beam interaction can be used to derive information on the nature of the specimen.

TEM produces images by detecting electrons that are transmitted through the sample, while the Scanning Electron Microscope (SEM) produces images by detecting secondary electrons which are emitted from the surface due to excitation by the primary electron beam. Generally, TEM resolution is about an order of magnitude better than SEM resolution.

Energy Dispersive X-ray (EDX) spectrometry makes use of the X-ray spectrum emitted by a solid sample bombarded with electrons to obtain a chemical analysis.

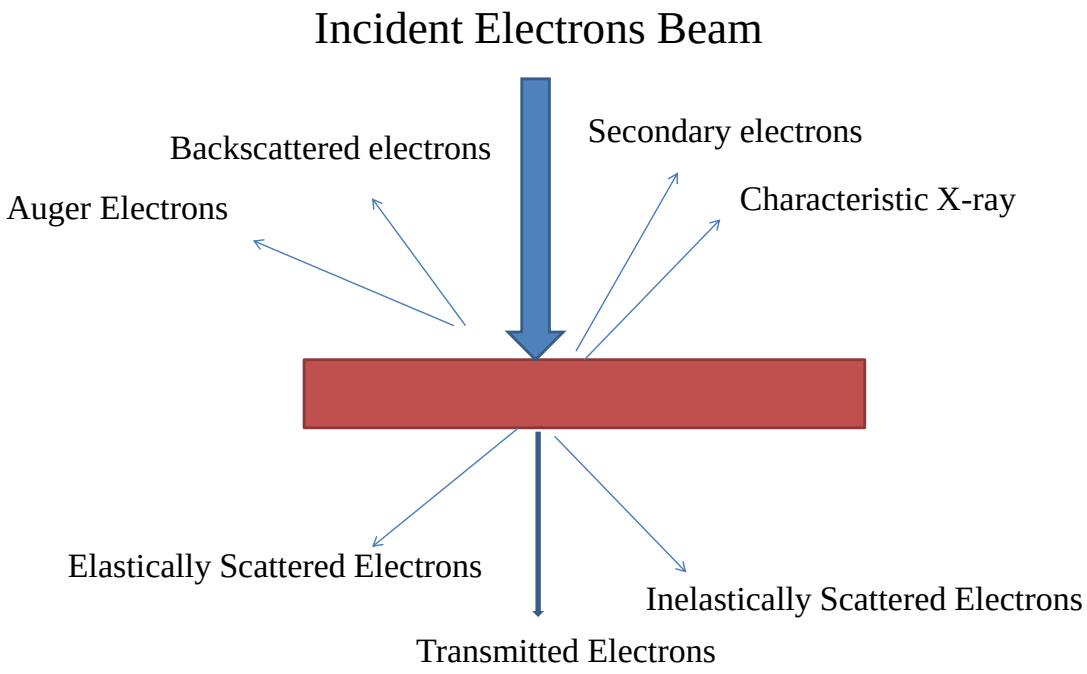

Figure 4.4: Effects produced by electron bombardment of a material

4.2.2 TEM INSTRUMENTATION

TEM and EDX measurements were carried out at LPN, CNRS, France by Dr G. Patriarche, and Dr D. Troadec.

TEM was performed on a 200 kV Jeol2200FS microscope with a spherical aberration corrector on the scanning transmission electron microscope (STEM) probe. The STEM-HAADF (high-angle annular dark- field) images are detected with a half angle of 100 mrad (inner detector angle) and170 mrad (outer angle). The corrected convergence half angle of the STEM probe is 30 mrad and the probe intensity is 55 pA. The acquisition time is 38.7 s per image (1024×1024 pixels).

4.3 TIME OF FLIGHT SECONDARY ION MASS SPECTROMETRY

4.3.1 INTRODUCTION TO SECONDARY ION MASS SPECTROMETRY (SIMS)

Secondary ion mass spectrometry (SIMS) is an ultra-high vacuum (UHV) technique that measures the ionized particles that are released when a surface is bombarded with an energetic primary particle. Primary ion sources commonly used in SIMS include cesium, gallium and bismuth[3].

The secondary particles are emitted from the surface after bombardment from the primary ions as the ion beam is pulsed for short periods. The energy is transferred from primary ions to the surface which allows surface atoms and molecules of approximately the top 2-3 molecular layers to overcome their surface binding energy[4,5] (i. e. the top 2 nm of sample). Emitted particles can take the form of electrons, neutral atoms or molecular species, cluster and atomic ions. The production of secondary ions from a surface is represented schematically in Figure 4.5.

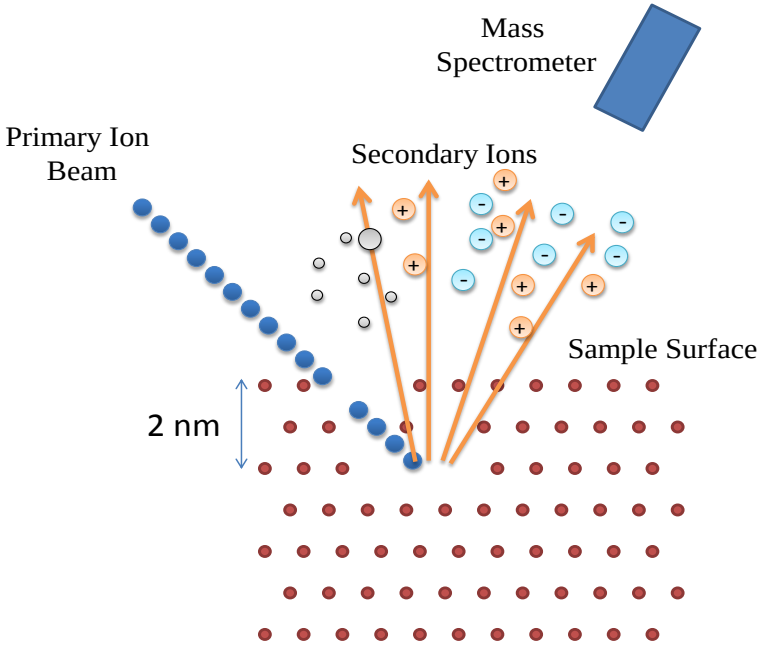

Figure 4.5: Diagram illustrating the production of secondary ions from a surface.

Secondary ion emission by a solid surface under ion bombardment supplies information about the elemental, isotopic and molecular composition of its uppermost atomic layers. The secondary ion yields will vary greatly according to the chemical environment and the sputtering conditions (ion, energy, and angle). These results in a mass spectrum that characterizes the chemical composition of the sample under investigation, The spectra produced can be used to provide detailed information on the spatial distribution of components, structure[6] and orientation[7] of chemistries at the surface[8].

4.3.2 THEORY OF TOF-SIMS OPERATION

A time-of-flight instrument allows much greater mass resolution to be obtained than older systems which employ quadrupole detectors. Secondary emitted ions are accelerated over a very short distance resulting in all the ions having almost the same kinetic energies, which is vital to the working of the time-of-flight spectrometer. The energy and angular dispersion of the secondary ions can be compensated using focusing elements such as a reflectron resulting in improved mass spectrum[9]. Secondary emitted ions can have a spread of energies, and this will lead to low mass resolution analysis. Ions with diverse energies will penetrate the reflectron to different depths, i.e. the higher the energy of the ion, the deeper the penetration before it travels further towards the detector. This additional step before detection lead to compensation of the difference in energy spread[10].

The ionised species then travel through a flight tube on their way to the mass analyzer. A fixed voltage accelerates the secondary ions into the ToF analyzer, with its polarity determining whether positive or negative secondary ions are analyzed. The ions are separated by mass, and as the lower mass ions have a higher velocity they will reach the detector faster than heavier ions. The flight tube has a known path length (L). The time (*t*) taken for each ion to arrive at the detector at the end of tube can be measured[11]. A simple equation can be used to produce a ToF-SIMS spectrum and thus derive the mass of the ions.

The ion velocity, *v*, is the length of the flight path, *L*, divided by the flight time, *t*

$$v = \frac{L}{t} \qquad 4.1$$

Substituting this expression for *v* into the kinetic energy relation, one can derive the working equation for the time-of-flight mass spectrometer:

$$t = L\sqrt{(\frac{m}{2zv})} \qquad 4.2$$

Technological advances in computing have allowed the whole mass spectrum to be collected in parallel. The mass spectra consist of the ion mass charge ratio versus the number of ions detected. ToF mass analysers are currently the most widely used type of analyser for SIMS and have been employed in all work shown in this thesis.

4.3.3 MODES OF ANALYSIS USING TOF-SIMS

There are three basic modes of SIMS operation:

- Point Analysis: a focused stationary beam is used to determine the composition at a certain point. The target size is usually between 1 and 25 µm but is dependent on the application.
- Imaging: rastering the primary ion beam to obtain compositional images of the surface. SIMS images with a spatial resolution of better than 50 nm are obtainable.
- Depth profiling: scanning a sputter ion source over the surface of the sample causes the surface layers to be slowly eroded, revealing the compositional change with depth.

The aim of depth profiling is to obtain information on the variation of composition with depth below the initial surface. This is useful for the analysis of layered structures and has been employed to investigate samples discussed in this thesis.

The depth profile is obtained using two separate beams mounted at 180^0 to one another where one beam is used to progressively etch a crater in the surface of the sample under study, whilst short-pulses of a second beam are used to analyze the centre of the crater. This has the advantage that one can be confident that the analysis is exclusively from the base of the etch crater and not affected by sputtering from the crater-walls. Depth profiling is undertaken in dynamic SIMS (DSIMS) mode (dose of primary ion larger than static limit ($> 1\times10^{13}$ ions/cm^2).

4.3.4 TOF-SIMS INSTRUMENTATION[12]

SIMS measurements have been performed at the School of Pharmacy, Nottingham University by Dr David Scurr.

A ToF-SIMS IV (ION-TOF, Münster, Germany) fitted with Cs^+ column was used for all SIMS data shown in this thesis. An automated electronic stage control module was used to move the stage within the main chamber. The pressure was maintained below 6×10^{-8} Torr for analysis but within the initial load lock a pressure of 1×10^{-6} was sufficient to move the sample stage from the load lock to the main chamber (see Figure 4.6). When loading the sample stage into the ToF-SIMS, anti-static gloves were used in order to reduce the opportunity for any static charge to influence electronics within the main chamber.

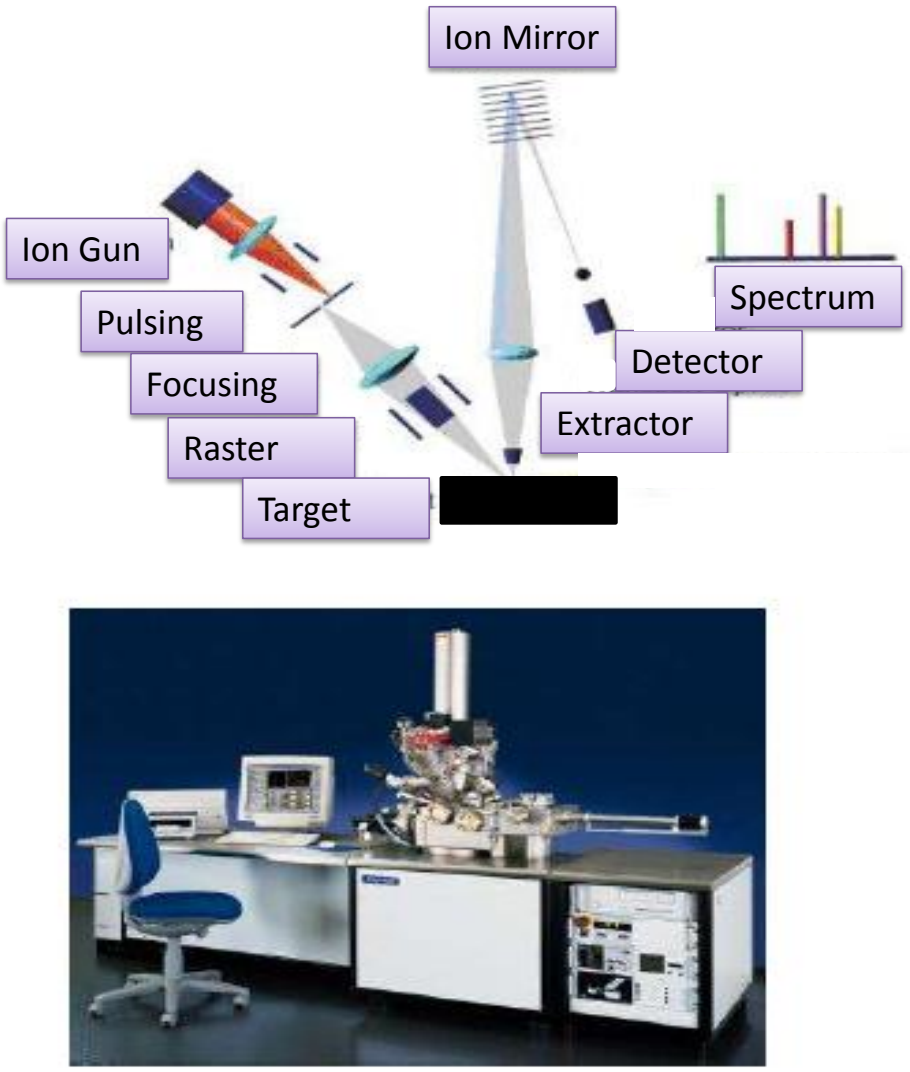

Figure 4.6: Schematic of the ToF-SIMS machine and typical set up of IonTOF ToF-SIMS IV instrument.

REFERENCES

[1] T. H. Gfroerer, Encyclopedia of Analytical Chemistry R.A. Meyers (Ed.), John Wiley & Sons Ltd, Chichester, 9209 (2000).

[2] M. Shafi, Electrical And Optical Studies Of Dilute Nitride And Bismide Compound Semiconductors, PhD Thesis, Nottingham University (2011).

[3] J. Vickerman, and D. Briggs, ToF-SIMS: Surface Analysis by Mass Spectroscopy, Manchester: IM Publications and Surface Spectra Limited (2001).

[4] R. La, and S. A. John, American Journal of Physiology, 266, 1(1994).

[5] J. C. Vickerman, and D. Briggs. TOF-SIMS: Surface analysis by mass spectrometry, Chichester: IM Publications (2001).

[6] M. S. Wagner, and D.G. Castner, Langmuir, 17(15), 4649 (2001).

[7] P. Bertrand, Applied Surface Science, 252(19), 6986 (2006).

[8]A. M. Belu, D. J. Graham, and D. G. Castner, Biomaterials, 24(21), 3635 (2003).

[9]A. M. Belu, D. J. Graham, and D.G. Castner, Biomaterials, 24(21), 3635 (2003).

[10] D. Briggs, Surface Analysis of Polymers by XPS and Static SIMS. Cambridge: Cambridge University Press, (1998).

[11]J. C. Vickerman, and I.S. Gilmore, Surface Analysis: The Principal Techniques, Vol 2, John Wiley & Sons Ltd. (2009).

[12] A. rafati, PhD Thesis, The Analysis of Polymers For Biomedical Applications, Nottingham University (2011).

CHAPTER 5: OPTICAL PROPERTIES OF SELF-ASSEMBLED InAlAs/AlGaAs QDs GROWN BY MBE ON DIFFERENT GaAs SUBSTRATE ORIENTATIONS

In this Chapter, optical characterization technique, namely photoluminescence (PL) has been employed to study the effect of GaAs substrate orientation [i.e, (100), (311)A, (311)B)] on the optical properties of InAlAs/GaAlAs/GaAs Quantum Dots (QDs). Optical properties of InAlAs/GaAlAs QDs formed under different growth conditions (growth temperature, different confinement barriers, and amount of deposited material) have been studied.

5.1 INTRODUCTION

During the last years, the fabrication of self-assembled quantum dots (SAQDs) by Stranski Krastanow (SK) growth mode[1] has attracted much attention both for basic physics and optoelectronic device applications. SAQDs that emit in the infrared region, have been successfully fabricated with many different material combinations including In(Ga)As/GaAs[2,3], GaSb/GaAs[4], InP/InGaP[5] and In(Ga,Al)As/InP[6-8]. However, there are only few reports on the use of SAQDs that emit in the red part of the visible spectrum. These are based on AlInAs/AIGaAs material system that has a larger band gap[9] than for example InAs/GaAs system.

InAlAs/AlGaAs QDs exhibit a shorter photoluminescence (PL) peak wavelength, typically, around 700 nm (1.77 eV) at 10 K, whereas the typical peak is around 1070 nm (1.158 eV) for InAs/GaAs QDs[10]. In addition, the PL spectra have a relatively narrow line width, typically, 50–60 meV. Visible emissions with narrow line width are important in many applications, including high density optical storage.

W. Zhou et al[11] investigated 10 MLs self-organized $In_{0.55}Al_{0.45}As$ QDs on $Al_{0.5}Ga_{0.5}As$ matrix deposited on (100) GaAs substrates by MBE. The AlGaAs matrix and the InAlAs QDs were grown at a temperature of 700 ^{0}C and 600 ^{0}C, respectively. A bimodal distribution of quantum dot sizes has been demonstrated by atomic force microscopy (AFM). There are two predominant families of the lateral dot sizes. Their average sizes were about 26±5nm and 53±7nm, and their densities were about 5.9 x10^{10} cm^{-2} and 1.5x10^{10} cm^{-2}, respectively. The optical properties of lateral size bimodal distribution of these QDs were studied, and by taking into account quantum-size effect on the peak energy, they proposed that the high (low) energy peak results from a smaller (larger) dot family. The PL emission energies

from the small and large QDs were found to be ~ 1.941 eV (~640 nm) and, ~1.85 eV (~670nm) respectively.

X. Lu et al[12] studied the effects of growth conditions on the size and density of self-assembled InAlAs/AlGaAs QDs grown on GaAs by MBE. Their aim was to achieve low density QDs, which is relevant for investigations of single QD spectroscopy. It has been observed that the diameter increases and the density decreases with increasing substrate temperature or with decreasing growth rate. They obtained a dot density as low as $1x10^{10}$ cm^{-2} for optimized growth conditions.

S. Fafard et al[13] carried out a systematic study on the optical and structural properties of MBE grown $In_xAl_{(1-x)}As/Al_yGa_{(1-y)}As$ QDs with various In and Al compositions by using low-temperature PL and transmission electron microscopy (TEM). All these QDs emitted in the visible range. The major aims of their study was to determine (i) the dependence of the 2D to 3D transition on the interfacial energy by varying the amount of Al in the $Al_yGa_{1-y}As$ cladding layers surrounding InAlAs QDs, and (ii) the critical thickness for the formation of $In_xAl_{1-x}As$ surrounded by $Al_yGa_{(1-y)}As$ cladding layers. It was found that (i) the number of monolayers deposited until the 2D/3D transition occurs does not depend on the Al content of the cladding layers; (ii) the critical thickness increases as the Al content in the QD increases.

A. Tsatsulnikov et al[14] studied structural and optical properties of $In_xAl_{1-x}As$ QDs embedded in an $A1_{0.3}Ga_{0.7}As$ matrix as a function of InAs mole fraction (x). A decrease in indium composition to values less than ~ 0.43 resulted in a gradual disappearance of bound electron states in QDs. In this case, the PL emission is governed by a type-II optical transition between electrons localized in the $A1_{0.3}Ga_{0.7}As$ layer and holes localized in the QDs. Reflection high-energy electron diffraction (RHEED) showed that QD formation started after depositing ~ 9 Å and ~ 14 Å InA1As for In =54% and 43%, respectively. By decreasing the In material content to a value ~34%, no dots are formed even with increasing the deposition material to 22 Å. $In_{0.54}Al_{0.46}As$ QDs have a peak PL emission at 1.6 eV with Full Width at Half Maximum (FWHM) of ~100 meV. By decreasing the In content by ~10 percentage, a shift in PL maximum towards higher photon energies (~100 meV) occurred. The QDs have a lateral size of about ~ 180Å and height of ~ 30 Å.

H. Liu et al[15] have employed AFM, PL, and EL (electroluminescence) to study the effect of the growth temperature on the optical and structural properties of 5MLs $In_{0.65}Al_{0.35}As/Al_{0.35}Ga_{0.65}As$ QDs. The best optical and structural quality of the $In_{0.65}Al_{0.35}As/Al_{0.35}Ga_{0.65}As$ QDs has been demonstrated at the growth temperature of 560 °C. Furthermore, under continuous wave conditions the QD laser diodes with the $In_{0.65}Al_{0.35}As/Al_{0.35}Ga_{0.65}As$ QD active layer grown at 560 °C emit at an energy of 1.651 eV with a threshold current density of 410 A/cm^2 at 220 K. This threshold current is much lower than that of the InAlAs/AlGaAs QD laser with the active region grown at 530 °C. The QD lateral size distribution obtained from AFM images reveal an average island size of 27 nm in base width and an areal density of ~7.0x10^{10}/cm^2 for the QDs grown at 530 °C. With increasing the growth temperature to 560 °C, the density of the islands decreases to 5.3x10^{10}/cm^2. Furthermore, the QD size distribution becomes slightly narrower. The typical QD separation is estimated by AFM to be 6.5 nm.

Theoretically, it is well established fact that the radiative lifetime in QDs is independent of temperature due to the delta function of the density of states, which leads to the limited thermal distribution as long as the energy separation is larger than the thermal energy. However, B.L. Liu et al[16] show the divergent results for InAlAs/AlGaAs QD sample grown on (100)-oriented GaAs substrate. Using Time-Resolved PL (TRPL), the constant decay time has not been observed even at low temperature. Instead, the observed decay time increases quickly with increasing temperature, showing 2D properties in the transient dynamic process. The measured decay time increased from 1.47 ns at 12K to 3.6 ns at 30 K. They explain this longer decay time at low temperature and this quickly increasing with temperature to the lateral coupling in InAlAs/AlGaAs QDs due to their high density, which results in the formation of the local minibands or extended states from the discrete energy levels.

The surface morphology of self-assembled QDs is a key factor in determining their optical properties, and it is very sensitive to the sample structure, such as the composition of the buffer layer[17], surface reconstruction[18], and substrate orientation.

Up to date, most of the reported studies focused on the QDs grown on the conventional (100) GaAs substrates. Recently, many high index polarized GaAs

surfaces, such as (311)A[19], (311)B[20-24], (411)A[25], and (411)B[26], have drawn greater attention because these surfaces provide a natural structural corrugation[27]. QDs grown on theses surfaces have some unique properties, such as narrow size distribution and high density. These enhanced properties can be used to further improve the performance of devices.

QD formation on many high-index surfaces have been studied, and QDs formed on some surfaces exhibit good structural and/or optical properties that are comparable or superior to QDs on (100) surface.

S.Zhong-zhe et al[28] studied ~13 MLs $In_{0.9}Al_{0.1}As$ SAQDs formed by MBE on (100) and (N11)B (N = 2, 3, 4, 5) InP substrates. QDs formation for all samples was confirmed by TEM and PL. The PL spectra revealed striking differences in peak position, line width, intensity and peak shape between different oriented surfaces. QDs formed on (411)B surface gave the highest PL intensity, while QDs on (211)B and (311)B orientations showed weaker PL emissions. These results show that QDs emission can be improved by using non-conventional InP substrates. It is worth pointing out that the trend of peak shift reported by S.Zhong-zhe is not similar to the published results from InAs QD on high-index[29] where blue shift is observed for (N11)B surfaces, whereas red shift is observed for (N11)A orientations. This could probably be attributed to the different material system or respective growth conditions.

5.2 EXPERIMENTAL RESULTS AND ANALYSIS

The investigation of the optical properties of InAlAs QDs was carried in the following sequence in order to determine the best GaAs substrate orientation and the optimised growth conditions for the growth of these QDs:

1- Comparative study of the optical properties of $Al_{0.35}In_{0.65}As$ QDs formed on $Al_{0.45}Ga_{0.55}As$ matrix and grown on different GaAs substrate orientations [(100), (311)A and (311)B] at a growth temperature of 450 ^{0}C.

   Two different $Al_{0.35}In_{0.65}As$ coverage were investigated, namely 11 Å (3.7 MLs), and 13 Å (4.4 MLs).

2- Study of the effect of the $Al_yGa_{1-y}As$ matrix confining barrier (y= 0.25, 0.35, 0.45, and 0.55) on the optical properties of $Al_{0.35}In_{0.65}As$ QDs grown on (311)B plane at a temperature of 450 ^{0}C.
3- Study the effect of growth temperature (500 ^{0}C and 550 ^{0}C)on the optical properties of (311)B $Al_{0.35}In_{0.65}As$ QDs grown on $Al_{0.45}Ga_{0.55}As$ matrix.

5.2.1 STUDY OF THE INFLUENCE OF THE SUBSTRATE ORIENTATION ON THE OPTICAL PROPERTIES OF $Al_{0.35}In_{0.65}As/Al_{0.45}Ga_{0.55}As$ QUANTUM DOTS

This section will report on the optical properties of InAlAs QDs grown on the conventional (100) and high index planes, namely (311)A and (311)B, GaAs substrates. The aim is to determine the optimal substrate orientation for the growth of these QDs on AlGaAs matrix.

All QD samples studied in this work have been grown by MBE on semi-insulating GaAs substrates with orientations (100), (311)A and (311)B. All the growths were carried out simultaneously and under the same conditions for comparison purposes. The growth temperature, the growth rate and arsenic overpressure were 450 °C, 1µm per hour, $1.2x10^{-5}$ Torr, respectively. The As:Ga beam equivalent pressure ratio as measured by an ionization gauge was approximately 12:1. The samples were rotated during growth in order to improve the uniformity of the layers. The layer structure is shown in Figure 5.1.

The samples consisted of a 0.2µm-thick GaAs buffer layer of which the first 0.1 µm was grown at 580 °C and the remaining 0.1 µm at 600 °C. The temperature was kept at 600 ^{0}C during deposition of the $Al_{0.45}Ga_{0.55}As$ matrix layer. This was followed by the deposition of 11Å $Al_{0.35}In_{0.65}As$ strained layer at 450 ^{0}C for the formation of 3.75 monolayers (MLs) QDs, a 50 nm $Al_{0.45}Ga_{0.55}As$ cap layer, and 10nm GaAs. The lattice constant mismatch between the InAlAs QDs and the AlGaAS matrix is ~ 4.6%.

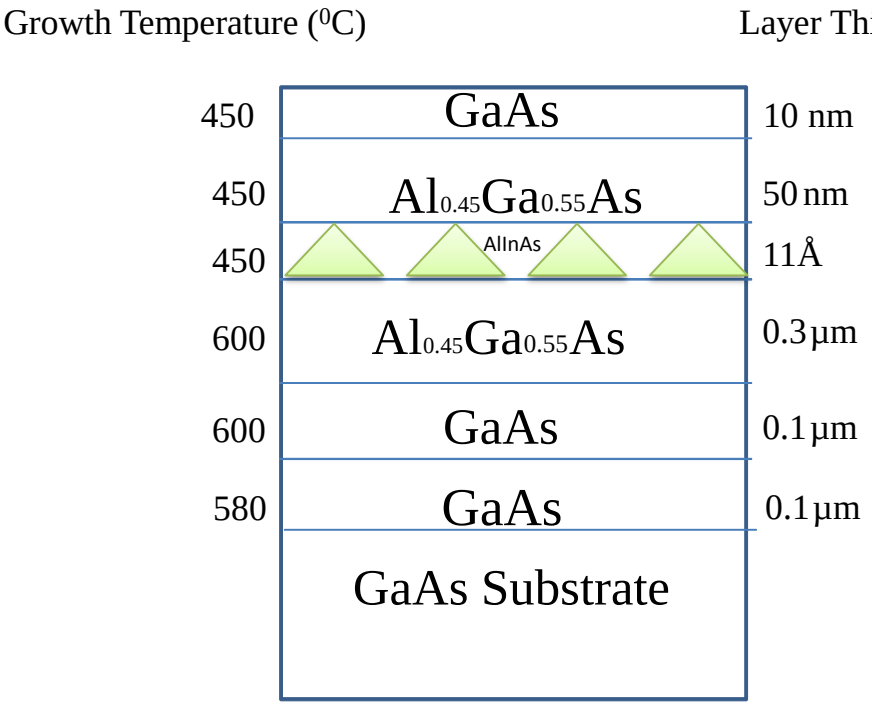

Figure 5.1: Schematics of the $Al_{0.35}In_{0.65}As/Al_{0.45}Ga_{0.55}As$ QD structures.

Figure 5.2 shows PL spectra at 8 K for all orientations. All the samples show PL emissions in the (1.7-1.9) eV region, which is lower than InGaAs QDs structures grown by MBE on GaAs substrates due to incorporation of Al atoms. The peak position, FWHM and the integral intensity have a strong dependence on the substrate orientation. The PL properties of these QDs are summarized in Table 5.1.

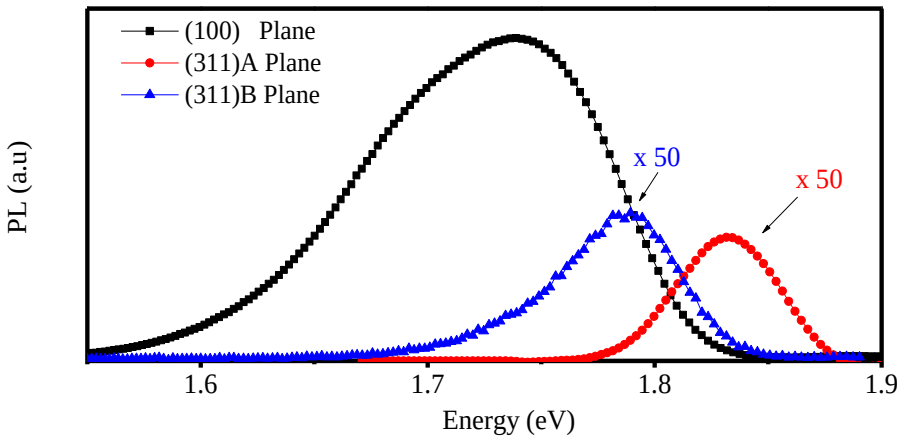

Figure 5.2: PL spectra of $Al_{0.35}In_{0.65}As/Al_{0.55}Ga_{0.45}As$ QDs grown on different GaAs substrate orientations.

Table 5.1: PL peak energy (eV), FWHM (meV) and PL intensity ratios between (100) QDs and high index QDs.

Plane	PL Energy (eV)	FWHM (meV)	PL intensity / PL intensity$_{(100)}$
(100)	1.74	125	1.00E+00
(311)A	1.835	44	0.7E-02
(311)B	1.77	59	0.9E-02

A blue-shift in PL peak position is observed (see Figure 5.3) for QDs grown on (311)A (1.835 eV) and (311)B (1.77 eV) with reference to (100) QDs (1.74 eV). (311)A QDs have a higher emission energy than (311)B QDs. For the (311) orientation the peak position depends upon whether the substrate is Ga terminated (A face) or As terminated (B face).

This energy shift can be accounted by the effects the substrate orientation has on the shape and average size of the overgrown QDs due to the different surface energy, strain and growth kinetic[24,29,30]. Generally speaking, QDs formed on high-index surfaces are smaller in size than those on the (100) substrate, because on (N11) surfaces, there is a high density of steps compared to the atomically flat (100) surface. These steps will limit the in-plane diffusion of atoms during the growth, and delay the formation of well-developed dots in terms of size with respect to the (100) substrate[31].

However, it is not clear why (311)A QDs have a larger blue shift than (311)B QDs. A possible explanation could be due to the slower diffusion of In and/or Al on the Ga face than on the As face.

It is important to note that emission from the wetting layer was not detected in the samples investigated in this work. The PL signature of the wetting layer is sometimes not detected as reported by P. Gonzilez-Borrero et al[32] for InGaAs QDs. They interrupted the growth for 1, and 3 minutes before and after depositing the dots, respectively. They explained the absence of the wetting layer emission due to driving much of the deposited indium to the island nucleation. This process leaves a very thin wetting layer, where carriers are generated and transferred very quickly (~ ps) to

the InGaAs QDs where they recombine radiatively. Similar explanation was given by Z.Y. Xu[33,34] for InAs/GaAs QDs.

S. Fafard et al[35] attributed the absence of emission from wetting layer to the high density of QDs. In their work they studied InAs/GaAs QDs grown on (100) GaAs substrates, and reported that as the coverage increases, the amplitude of the wetting layer PL peak decreases simultaneously with the increase of the QD PL peak intensity. This was attributed to the increase of QDs density.

For the InAlAs QDs system, it was reported[12] that the short surface diffusion of Al due to its high bonding energy with As was responsible for the achievement of high density of InAlAs QDs.

It is therefore concluded that the absence of the wetting letting PL signal in our samples is related to the Al diffusion, which causes a high density of QDs.

As shown in Figure 5.4, the FWHM of QDs grown on high index planes is smaller than those grown on (100) plane. The FWHM of (100), (311)B and (311)A QDs are 125 meV, 44 meV and 59 meV, respectively. J. He et al[36] showed that the PL FWHM drastically decreased as the uniformity of the QDs increased. It is well-known that the smaller the FWHM the higher structural quality of QDs. This means that (311)A QDs have a better size uniformity.

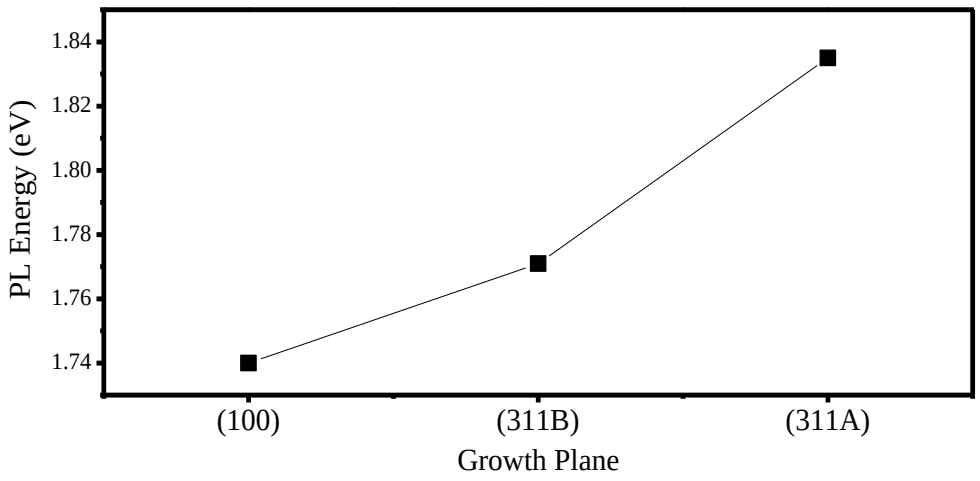

Figure 5.3: Effect of substrate orientation on the PL peak energy.

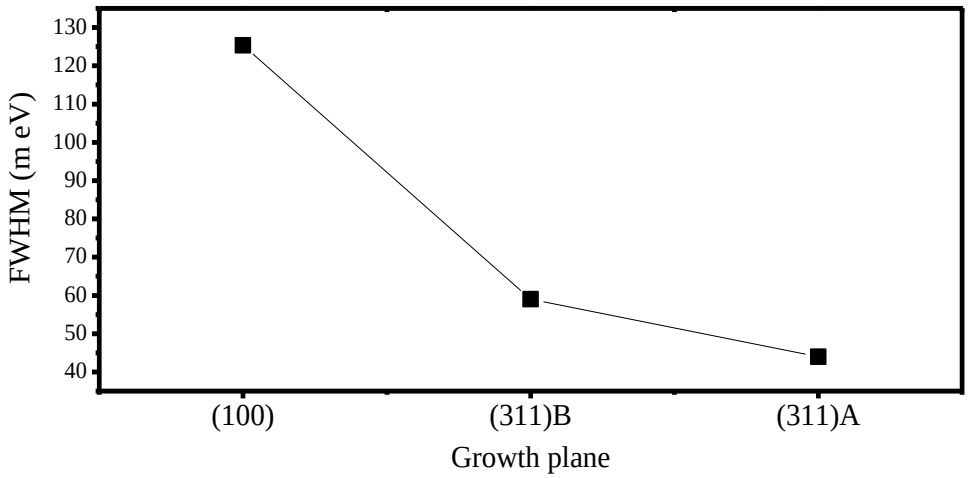

Figure 5.4: Effect of substrate orientation on the PL FWHM.

Figure 5.5 gives the relative PL intensity of $Al_{0.35}In_{0.65}As/Al_{0.45}Ga_{0.55}As$ QDs for each sample. The PL intensity is normalized relative to that of (100) QDs. Remarkably, the PL intensities for QDs on (311)B and (311)A surfaces are about two order of magnitude less than for (100). This is in contrast to other type of QDs, such as InAs and InGaAs[37-39] formed on high index surfaces, which are characterized by a stronger luminescence and a narrower linewidth than those grown on (100) surface. It has been reported that the critical thickness for the formation of QDs on high index plane is larger than for (100) plane[40]. The lower luminescence of (311)A/B QDs observed in this work may be due to the low amount of material deposited (11Å) to achieve well-formed QDs. The critical thickness θ_c (the number of monolayers of strained material necessary to induce the transition to island growth) after the initial layer-by-layer growth at which the 2D (layer) to 3D (island growth) transition occurs has been established to be strain dependent for $In_xGa_{1-x}As$ on GaAs[41,42].

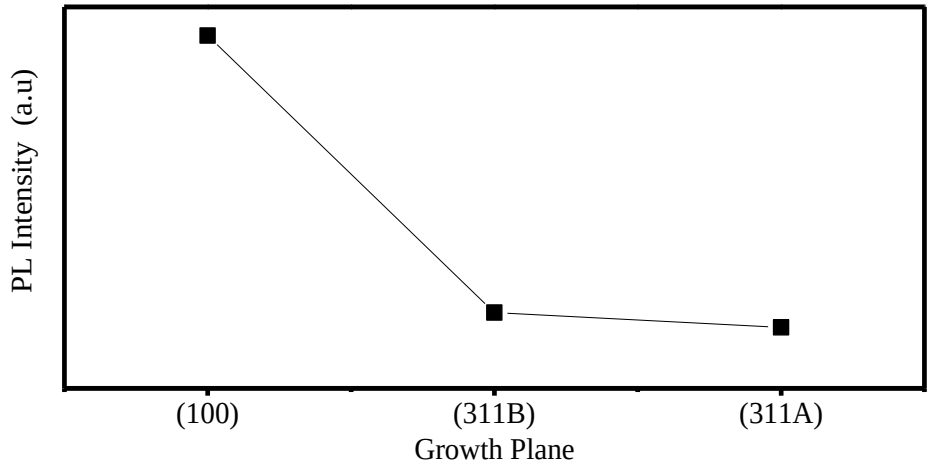

Figure 5.5: Relative integrated PL intensity of $Al_{0.35}In_{0.65}As/Al_{0.45}Ga_{0.55}As$ QDs for each sample. The integrated PL intensity is normalized relative to that of (100) QDs.

RHEED is generally used to determine the 2D/3D growth transition. Several authors[43,44] showed that the onset of the island nucleation for InAs QDs formation starts well before the RHEED pattern changes from streaks to spots (~ 1.6 MLs).

S. Sanguinetti et al[45] and Guryanov et al[46] showed an increase of SK growth mode onset as the growth substrate orientation departs from (100) towards (311) (see Figure 5.6). Such behaviour can be understood in terms of strain relaxation inhibition which takes place in low dimensional strained heterostructures grown on (N11) substrates.

By means of equilibrium theoretical model which includes the substrate orientation effects, S. Sanguinetti et al[40] demonstrated that the delay of formation of dots as the surface orientation departs from (100) towards (311) is a direct consequence of the degree of strain relaxation in the island. The in-island elastic strain relaxation becomes less efficient as the growth substrates departs from the (100) orientation. Such inhibition of strain relaxation inside the islands, by increasing the island internal energy term, should be the reason for the delay in the 3D growth mode onset on (N11) substrates.

Contrary to what was expected, the (100) InAlAs QDs optical properties are better than those of (311) QDs. The observed lower efficiency in our (311) InAlAs QDs

could be explained by the theoretical work for the formation of QDs on high index planes reported in Reference 40 .

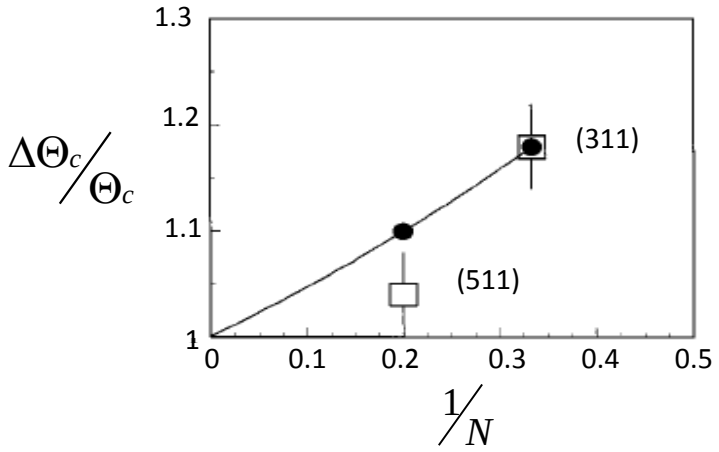

Figure 5.6: 2D/3D growth transition critical coverage shift $\frac{\Delta\Theta_c}{\Theta_c}$ as a function of the Miller index N for (N11) substrates (Θ_c is the critical coverage). Empty squares indicate the experimental points. Model predictions are indicated by black circles. The line is a guide for the eyes[40.]

In order to obtain further information about the properties of QDs grown on different planes, the temperature dependence of the PL spectra was also investigated. The excitation energy was 2.62 eV (473 nm) and the excitation power was kept at 40 mW. The data is presented in Figure 5.7.

The results show that the PL intensity from dots grown on different substrates quenches at different temperatures.

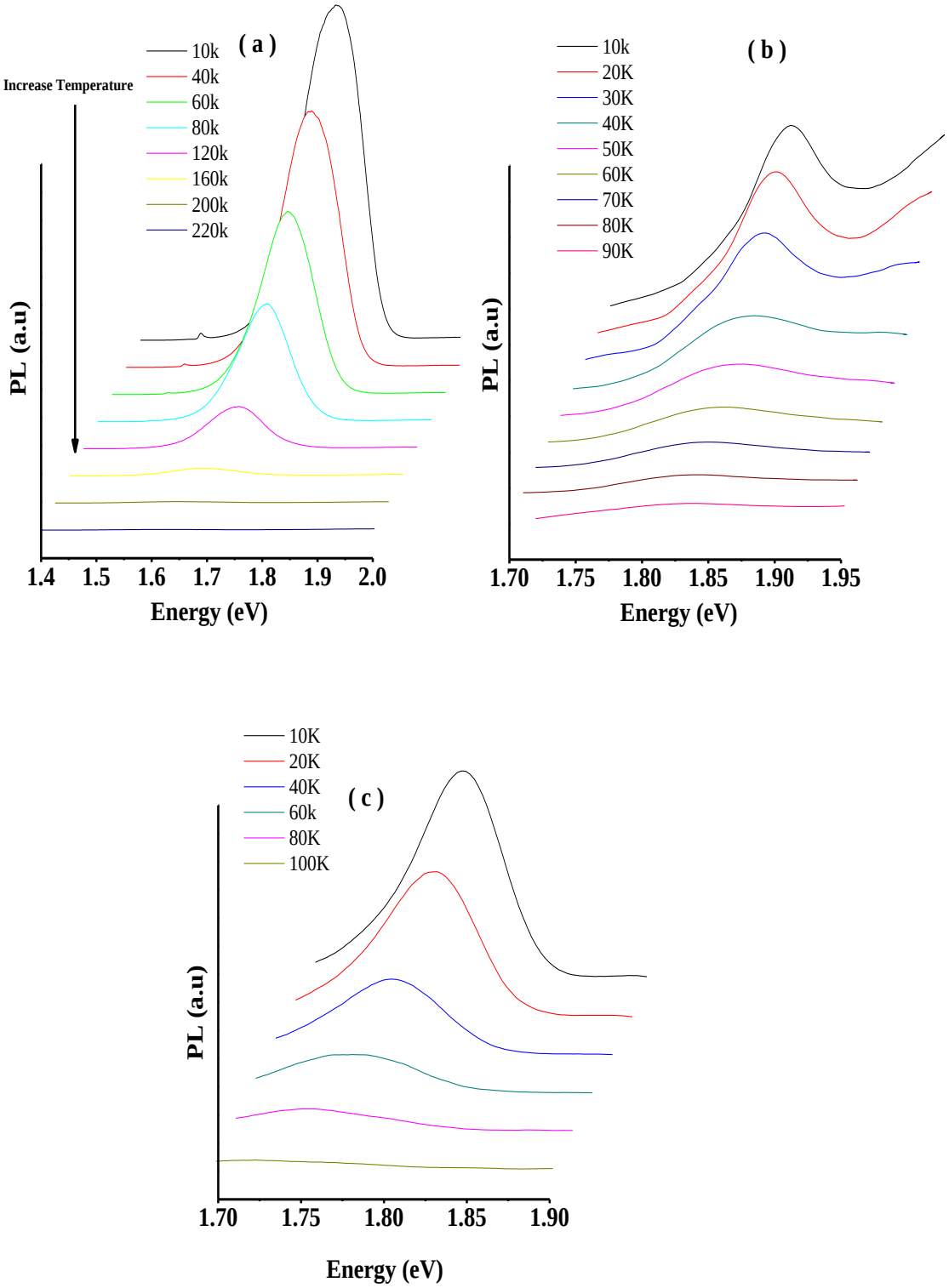

Figure 5.7: Temperature dependence of PL spectra of the QDs s grown on (a) (100); (b) (311)A; (c) (311)B Planes. (The spectra shifted for clarity).

Figure 5.8 illustrate the evolution of FWHM of the PL as a function of temperature for the QD samples grown on (100), (311) A and (311) B substrates. A significant difference can be seen for QDs grown on different substrates.

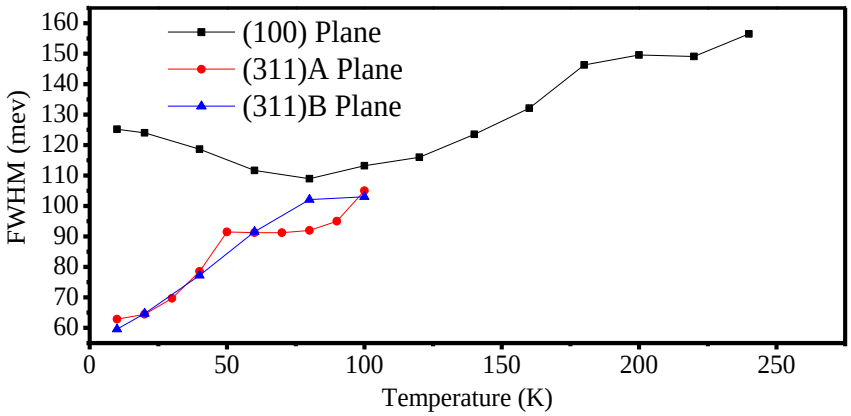

Figure 5.8: FWHM of PL spectra as a function of temperature for the QD samples grown on different substrate orientations.

The FWHM increases monotonously with temperature for QDs grown on high index planes. The FWHM increases from 44 and 59 meV at 10K for QDs grown on (311)A and (311)B respectively to 105 and 103 meV at 100K.

The increase of the linewidth with temperature was reported before in the InAs QDs, and attributed to electron phonon scattering[47]. However, in the case of QDs grown on (100) plane, an anomalous decrease of the linewidth with increasing temperature was observed in the temperature range from 10 to 80 K, followed by normal increase with the temperature.

This anomalous behavior of FWHM with temperature may be due to high dot density formed on (100) plane, and which could favour thermally activated dot-dot coupling channels. This can be explained as follows: at low temperatures, the PL line shape of QDs is determined by the inhomogeneous distribution of QD sizes. That is, PL arises from the sum of emission of many different dot sizes. When the temperature increases, the thermalized carriers can relax to a nearby dot and find a lower local-energy minimum, resulting in shrinkage of the linewidth[34]. When the temperature further increases (above 80K), the effect of electron-phonon scattering becomes a dominant contribution. Consequently, the FWHM increases with

temperature. These strange effects are not expected in an ideal QD structure in which all the dots are largely separated and decoupled from each other.

Y. T. Dai et al[48] studied this anomalous temperature dependent photoluminescence (TDPL) for 3, 4, and 5MLs InAs/GaAs QDs. They reported that the turning temperature (T_f) (the temperature of the minimal FWHM) strongly depends on the dot sizes. T_f is higher for larger dot size. This behaviour can be explained by the fact that the carriers in smaller dots have a higher ground state energy corresponding to a lower binding energy. Thus, the carriers can be easily thermalized, which causes the T_f of the smaller dot to appear at lower temperature.

The results of the temperature dependence of the PL peak position are shown in Figure 5.9. The variation of the PL peak position with temperature of bulk semiconductors can be attributed to the effect lattice stretching and electron-lattice interaction. The fast red-shift of the PL peak with increasing temperature in QDs system had previously been observed, and mainly had been attributed to the redistribution of carriers among QDs with different sizes[34, 49, 50].

The red lines in Figure 5.9 are the experimental results, and the black curves are fitting obtained by shifting the bulk InAlAs band gap along the energy axis, using the empirical Varshni equation[51].

$$E_g(T) = E_g(0) - \frac{\alpha T^2}{T + \beta}$$

Where α (eV/K) is a constant, β is the Debye temperature, $E_g(0)$ is the band-gap energy at 0K, and T is the measured temperature. The constant values used for the fitting shown in Figure 5.9 are based on Ref 53.

From Figure 5.9 (b), it can be seen that the peak energies of QDs grown on (311)A show a redshift with increasing temperature with a rate basically identical to the bulk material.

QDs grown on (100), and (311)B (Figure 5.9 a and c) show a faster red shift than the Varshin's relation of bulk InAlAs band gap. This unusual temperature dependence is a characteristic of QDs which cannot be explained by the temperature-induced band-

gap change alone, because of the strong deviation from the Varshin's relation of bulk InAlAs band gap.

The (100) and (311) B QDs PL peak is red shifted by 64 meV and 46 meV, respectively in the temperature region 10-100 K compared to 13 meV for the (311)A QDs in the same region.

This fast red shift of (100) and (311)B QDs PL compared to (311)A QDs can be explained by the larger inhomogeneous distribution and higher density of QDs on (100) and (311)B substrates than on (311)A. This is also reflected in their PL intensity and FWHM.

In the case of a multimodal distribution, at low temperatures, carriers are frozen randomly into the different dot states of different size QDs, and the PL spectra reveal the emission of the QD ensemble. With increasing temperature, carriers gain enough energy to be activated outside the dot into the wetting layer and/or the AlGaAs barrier and then relax into another dot. Carrier hopping between dots occurs by a transfer of carriers from dots having lower binding energy towards the dots having a higher binding energy. This results in a lower-energy emission with a narrow PL spectra followed by a red shift of the luminescence peak that is larger than that expected for the thermal shrinkage of the AlInAs band gap with increasing temperature (i.e. due to the high density of QDs, coupling between QDs occur and carriers transfer from the higher-energy to the lower-energy dot families resulting in the fast red shift). Within a one size QDs family, the PL energy temperature dependence normally follows the Varshni's law for the temperature-dependent shift of bulk energy gap.

Similar effects were observed by many groups. For example, H.Wang et al[52] studied two self-organized InAs/GaAs quantum dots grown by MBE on (100) oriented GaAs substrates using PL and scanning tunnel microscopy (STM). The samples have different dot densities of 1.9×10^{10} cm^{-2} and 3.0×10^{11} cm^{-2}. It was reported that faster red shift is observed in high density sample than lower density sample.

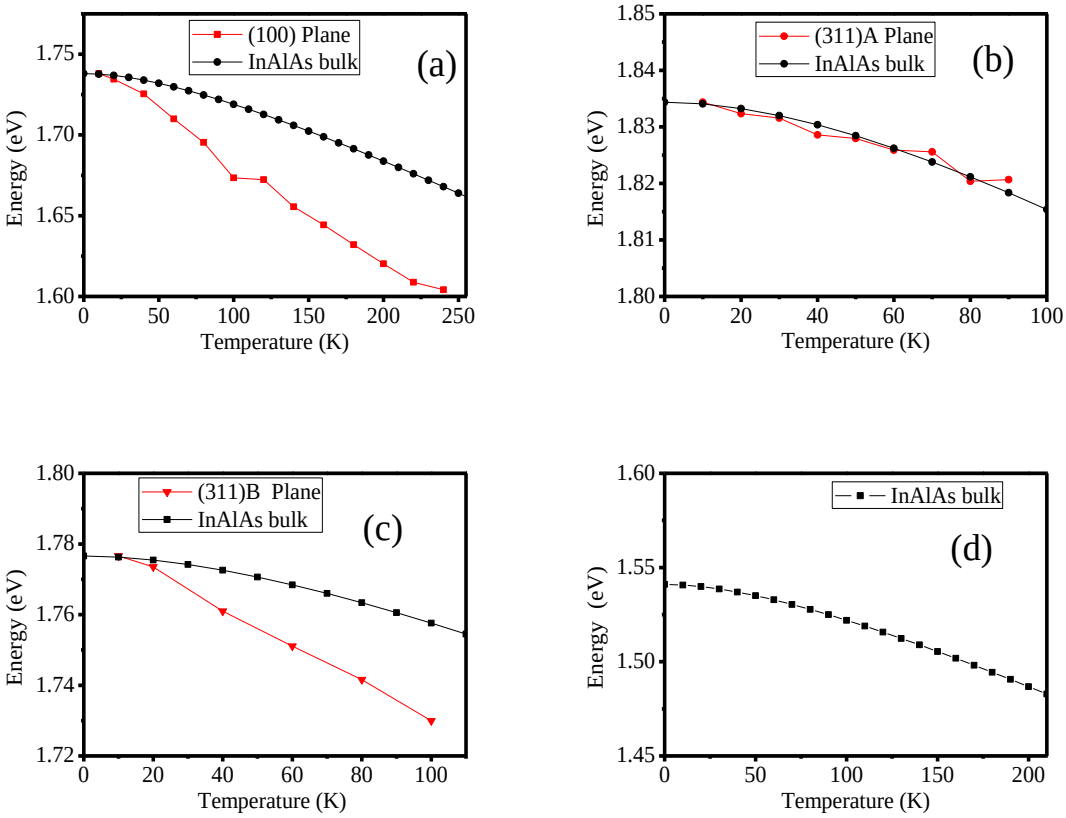

Figure 5.9: Temperature dependence of the PL peak energy for QDs samples grown on different substrate orientations (a) (100), (b) (311)A, (c) (311)B. The black lines are calculated according to the Varshni's law using the parameters of bulk InAlAs reported by D. Gaskill and co-workers[53] and are shifted along the energy axis, and (d) bulk InAlAs.

The optical quality of the InAlAs QDs on high index planes is found to be inferior to that of (100) QDs. This could be due to the non-optimized growth conditions and layer structure. It is worth pointing out that these samples were grown simultaneously, and therefore the growth conditions might not be optimal for each plane.

The following sections will report the effect of changing the growth conditions.

5.2.2 EFFECT OF INCREASING DEPOSITED InAlAs MATERIAL ON THE OPTICAL PROPERTIES OF QUANTUM DOTS GROWN ON DIFFERENT SUBSTRATE ORIENTATIONS.

The results reported in this section were obtained on $Al_{0.35}In_{0.65}As/Al_{0.45}Ga_{0.55}As$ QD samples which were grown under the same conditions and have the same layer structure as those samples previously discussed except that the deposited $Al_{0.35}In_{0.64}As$ material is 13 Å instead of 11 Å (i.e, increasing from 3.7 MLs to 4.4 MLs).

Figure 5.10 shows low temperature (8 K) PL spectra of 4.4 MLs $Al_{0.35}In_{0.65}As/Al_{0.45}Ga_{0.55}As$ As QDs for all substrate orientations. The excitation energy was 2.62 eV (473 nm) and the excitation power was kept at 40 mW. For these samples it is also found that the peak position, FWHM and the PL intensity have a strong dependence on the substrate orientation. The PL properties of these QDs are summarized in Table 5.2.

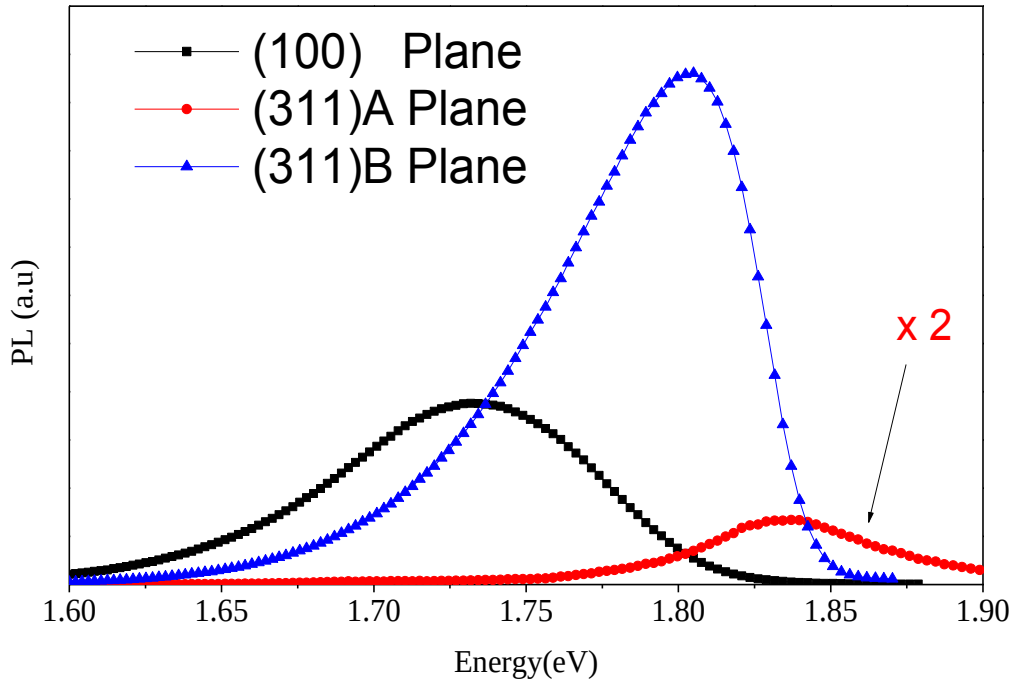

Figure 5.10: PL spectra of 13 Å (4.4 MLs) $Al_{0.35}In_{0.65}As/Al_{0.54}Ga_{0.45}As$ QDs grown on different GaAs substrate orientations.

Table 5.2: PL peak energy (eV), FWHM (meV), and PL intensity ratios between 13 Å (4.4 MLs) (100) QDs and high index QDs.

Plane	PL Energy (eV)	FWHM (meV)	PL intensity / PL intensity$_{(100)}$
(100)	1.729	99	1
(311)A	1.84	90	0.3
(311)B	1.799	86	2.87

By increasing the deposited material from 3.7 MLs to 4.4 MLs, QDs grown on (311)B plane exhibit a superior PL efficiency over the other QDs. The PL intensity of (311) B QDs is ~2.8 times larger than the PL intensity of (100) QDs. The weakest PL emission is observed for QDs grown on (311)A orientation. The PL efficiency reduction can be considered as evidence of a diminished number of optically active QDs[54]. However, compared to 3.7 MLs InAlAs QDs, the PL intensity of 4.4MLs QDs on both (311)A and (311)B have increased significantly with reference to (100) QDs, i.e. over 300 and 40 times for (311)B and (311)A, respectively. Superior optical quality of QDs grown on (311) B plane over QDs grown on (100) plane has been observed for many other QDs systems[37,55, 56].

The inferior optical quality of QDs grown on A face are observed for different QDs material systems. The lower density of QDs on this orientation and the rough surface could be responsible for this low emission efficiency. In fact, the TEM work of W. Zhou et al [57] showed that the areal densities of InAlAs/GaAlAs QDs from (311)B, (100), and (311)A surfaces are $2.8x10^{10}$, $2.4x10^{10}$, and $2.0x10^{10}$ cm^{-2}, respectively.

C. Loboa et al[58] carried out a systematic AFM study to compare InGaAs QDs grown on (100), (110), (111), (311)A, and (311)B GaAs substrates. The island shape, size, density, and calculated diffusion lengths of the different dots revealed a strong dependence on surface orientation and associated GaAs morphology. The dot densities are $7.1x10^{9}$ cm^{-2} on (100), $7.4x10^{8}$ cm^{-2} on (311)A, and $3.2x10^{10}$ cm^{-2} on (311)B. The calculated effective group III migration lengths on these surfaces are 0.12 mm on (100), 0.4 mm on (311)A, and 0.06 mm on (311) B. This higher surface diffusion for atoms on (311)A surface compared to (311)B, and (100) surfaces is responsible for the low dot density.

Theoretically[59], higher surface diffusion leads to roughening of the strained layer. Roughening is an alternative mechanism for relaxation of strained materials, which is different than the S-K growth mode.

The temperature dependence of the PL spectra was also investigated for this set of 13 Å (4.4 MLs) InAlAs of QDs in order to understand the effect of the substrate orientation on their optical properties. The excitation energy was 2.62 eV (473 nm) and the excitation power was kept at 40mW. The data is illustrated in Figure 5.11.

The quenching temperature of the PL emission increased from 100 K for the 3.7MLs InAlAs QDs to 180 K and 220 K for the 4.4MLs (311)A and (311)B InAlAs QDs, respectively. For the (100) QDs no appreciable change was observed.

By increasing the deposited InAlAs material from 11 Å (3.7MLs) to 13 Å (4.4MLs), no significant change of the energy peak position appears. However, the FWHM of QDs grown on (100) plane decreases from 125 meV to 99 meV. A similar behavior was reported by Z. Xu et al[34] in InAs/GaAs QDs, where the FWHM of 2 MLs InAs QDs (75 meV) was higher than that of 2.5 MLs InAs QDs (56 meV). The reason for this effect was not explained.

For QDs grown on high index planes, the FWHM increases with increasing the amount of deposited material from 11 Å (3.7 MLs) to 13 Å(4.4MLs). This can be understood in terms of fluctuation of their size distribution. The inhomogeneous broadening of both height and diameter of QDs causes a distribution of the density of states over a wide energy range, resulting in a spectrally broad luminescence.

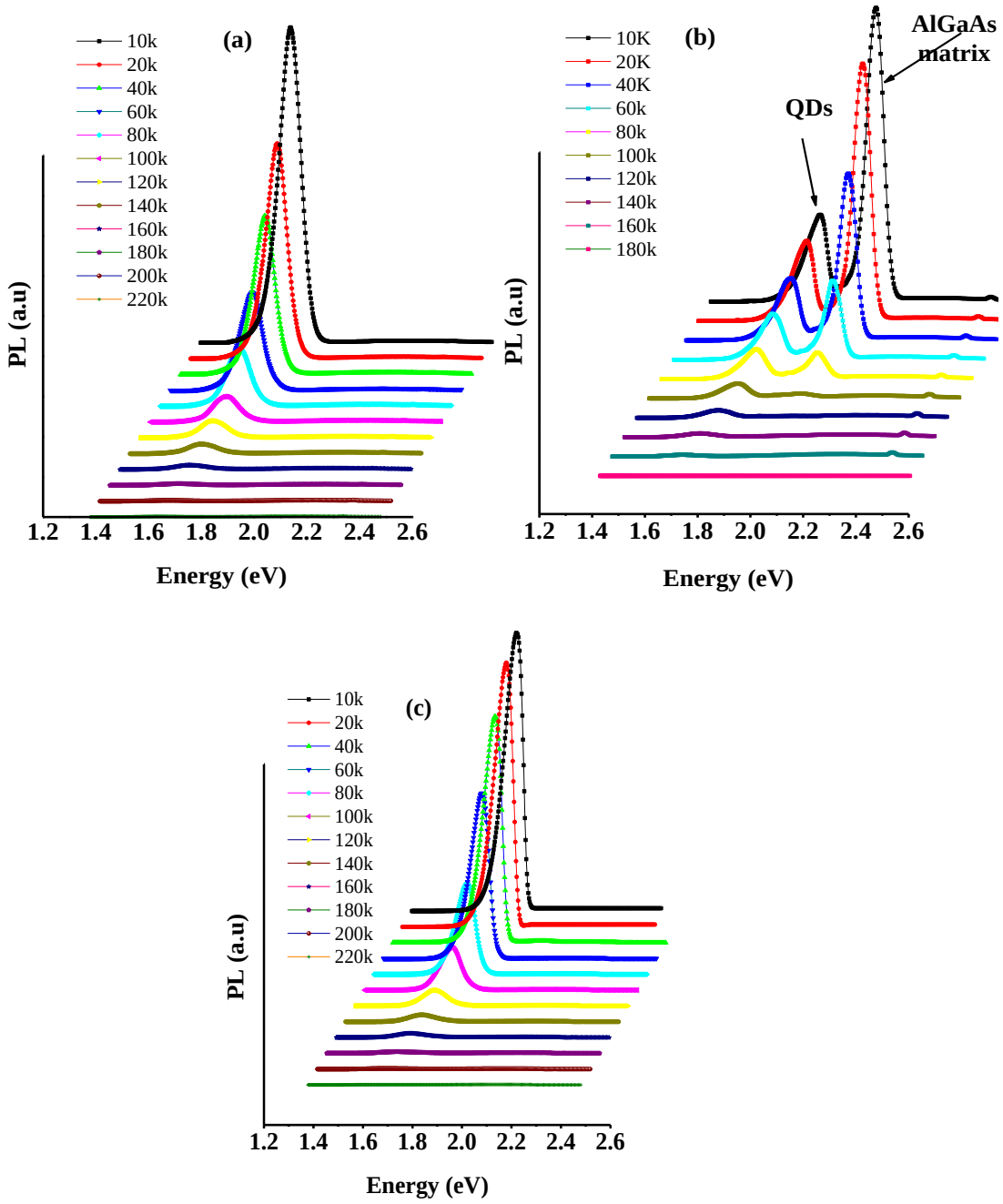

Figure 5.11: Temperature dependence of PL spectra of the QD samples grown on (a) (100), (b) (311)A, (c) (311)B planes. The data shifted for clarity.

Figure 5.12 illustrates the evolution of the FWHM of the PL spectra as a function of temperature for the QD samples grown on (311)B with different amount of deposited InAlAs material. A significant difference can be seen between 3.7MLs and 4.4 MLs InAlAs QDs. When the amount of InAlAs to form the QDs is smaller, i.e. 11Å, the FWHM increases monotonously with the temperature. However, in the case of the

4.4MLs QDs an anomalous decrease of the line width with increasing temperature was observed in the temperature range from 10 to 80 K. This is can be explained by the increase of the dot density caused by an increase of the amount of deposited material.

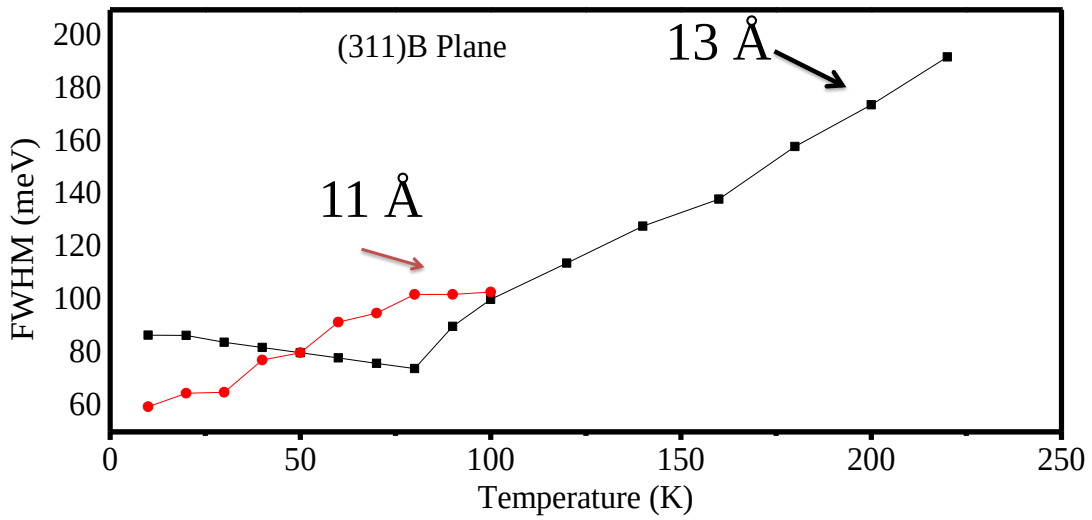

Figure 5.12: FWHM of PL spectra as a function of temperature for the InAlAs QD samples grown on (311)B with different amount of deposited material, namely 11Å(3.7MLs) and 13Å(4.4MLs).

Figure 5.13 shows that the PL energy of QDs grown on (311)B exhibit a faster red shift with increasing temperature than the PL energy of QDs grown on (311)A plane. In the temperature range 10 K- 180 K, the red shift of the PL peak for (311)B, (100) and (311)A QDs is 141 meV, 66 meV, and 45 meV respectively. This faster red shift for (311)B can be considered as a signature of the formation of high density of QDs on this plane.

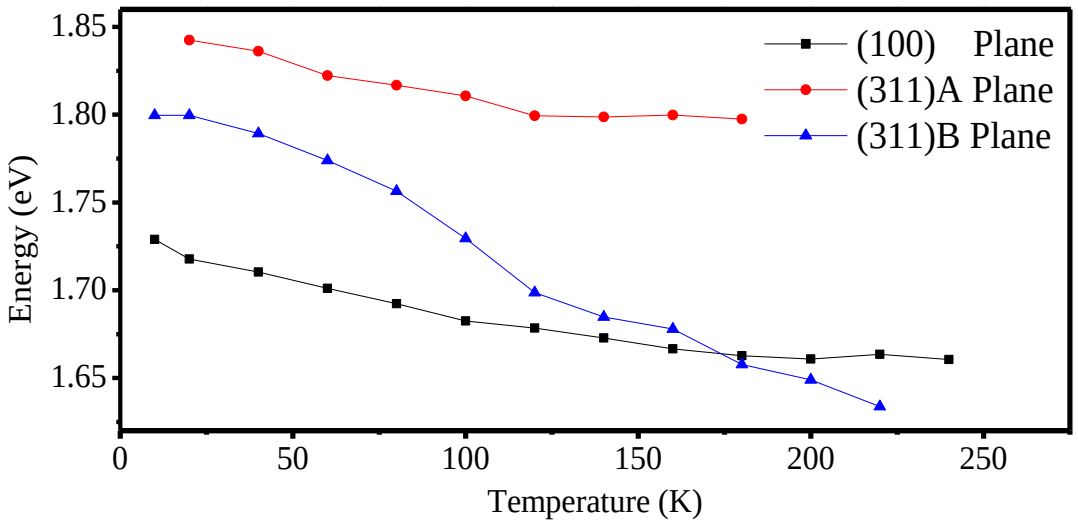

Figure 5.13: Temperature dependence of the PL peak energy for QDs samples grown on different substrate orientations, namely (100), (311)A, (311)B.

For (311)A sample there is a peak at around 2.3 eV which could be due to the AlGaAs matrix. The appearance of this peak is probably due to the low density of QDs formed on this plane. The PL intensity of AlGaAs matrix decreases drastically when the temperature changes from 10 to 80 K, contrary to that of QDs which persists up to 180 K (see Figure 5.14). This fast quenching with temperature can be explained by the decrease of the degree of confinement.

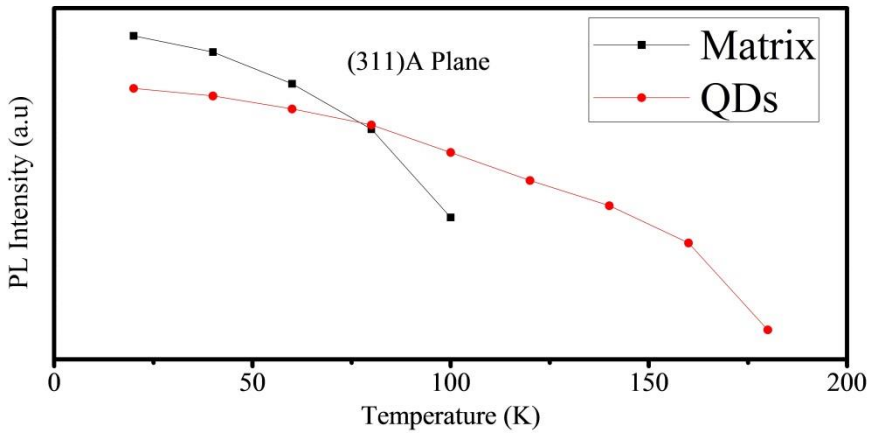

Figure 5.14: PL intensity as a function of temperature for InAlAs QDs and AlGaAs matrix for the (311)A sample.

In conclusion, the increase of the amount of $Al_{0.35}In_{0.65}As$ material to form QDs resulted in better optical efficiency for dots grown on high index planes. The best structure in terms of optical output consisted of 13 Å (4.4 MLs) $Al_{0.35}In_{0.65}As/Al_{0.45}G_{0.55}As$ grown on (311)B GaAs substrate. Therefore the above (311)B structure has been chosen to investigate the effect of the confining barrier on the QDs optical quality.

5.3 EFFECT OF THE AlGaAs CARRIER CONFINING POTENTIAL ON THE EMISSION ENERGY OF (311)B QDS

It is important to point out that the optical properties of (100) and (311)A 4.4 MLs Å $Al_{0.35}In_{0.64}As$ QDs grown on AlGaAs matrix with different Al percentages (25, 35, 45, and 55 %) are inferior to (311)B QDs counterpart with same Al percentage.

Therefore, the results presented in the following section are limited to the study of the effect of the confining potential barrier on the optical properties of 4.4MLs $Al_{0.35}In_{0.64}As$ QDs on $Al_yGa_{1-y}As$ QDs with y=0.25, 0.35, 0.45 and 0.55 grown on (311)B plane.

5.3.1 INTRODUCTION

For InAs QDs, it is well known that a high temperature stability of their optical properties can be achieved owing to deep localization of carriers in a matrix whose band gap is wider than that in GaAs[60].

A. Polimeni et al[61] carried out a systematic study of the PL properties of $InAs/Al_yGa_{1-y}As$ QDs over the Al compositional range y = 0 – 0.8 as a function of temperature from 10 to 290 K. For an Al content greater than 15%, the QD PL integrated intensity quenches very slowly with increasing temperature by less than an order of magnitude. This was explained by the fact that the AlGaAs energy levels are too distant from the dot ground state to have an appreciable thermal population.

The corresponding excitonic energy position has been calculated to be more than 400 meV away from the dot emission energy for y = 0.3. In contrast, for shallower confining potentials (y = 0 and 0.15) the barrier may play an important role in the thermal decrease of the QD PL. The PL signals of dots embedded in GaAs and $Al_{0.15}Ga_{0.85}As$ matrices decrease by factors of 200 and 80, respectively in the temperature range 10-290 K.

5.3.2 EXPERIMENTAL RESULTS AND ANALYSIS

The PL signal from QDs is known to quench at different temperatures due to the carrier loss which takes place through the mechanism of thermal excitation of electron-hole pairs into the $Al_{1-x}Ga_xAs$ barriers. For this mechanism, the carrier loss will be reduced or eliminated by increasing the activation energies, and this could be achieved by increasing the Al percentage of the barriers, or by increasing the indium concentration in the QDs. The latter is limited by the amount of strain which can be incorporated. In this section, an investigation of $In_{0.65}Al_{0.35}As$ QDs grown on AlGaAs matrix with different Al concentrations have been carried out.

The features of the four studied samples in this section are shown in Table 5.3. A 200 nm thick GaAs buffer layer and a 300 nm thick $Al_yGa_{1-y}As$ layer were grown by MBE at 600 °C on a (311)B GaAs substrate. Then the temperature was lowered to 450 °C and a 4.4MLs InAlAs layer was deposited to form QDs. Finally a 50nm thick $Al_yGa_{1-y}As$ cap layer was deposited. The Al mole fraction (y) is chosen to be 0.25, 0.35, 0.45, and 0.55.

Table 5.3: Investigated samples having different Al content in the confining barrier.

Sample Number	Substrate	Al mole fraction
NU1683 $QD^{0.25}_{(311)B}$	(311)B	25%
NU2735 $QD^{0.35}_{(311)B}$	(311)B	35%
NU2738 $QD^{0.45}_{(311)B}$	(311)B	45%
NU2745 $QD^{0.55}_{(311)B}$	(311)B	55%

By increasing the Al percentage in matrix, the energy difference between the InAlAs QDs and the $Al_yGa_{1-y}As$ barrier state is increased. This gives greater confinement of carriers in the QD. As a result, thermal activation effects could be less serious and therefore it may be possible to extend the PL emission of the InAlAs QD system to room temperature.

Figure 5.15 shows the PL spectra at 8 K for (311)B InAlAs QDs deposited on AlGaAs matrices containing different Al concentrations. The energy of QDs shows a small blue shift with increasing Al content in the matrix (Figure 5.16). This could be due to the diffusion of Al from the AlGaAs matrix with higher Al into the QDs resulting in enhanced Al incorporation in the InAlAs dots. The integral intensity has a strong dependence on the Al percentage in matrix. The PL properties of these QDs are summarized in Table 5.4.

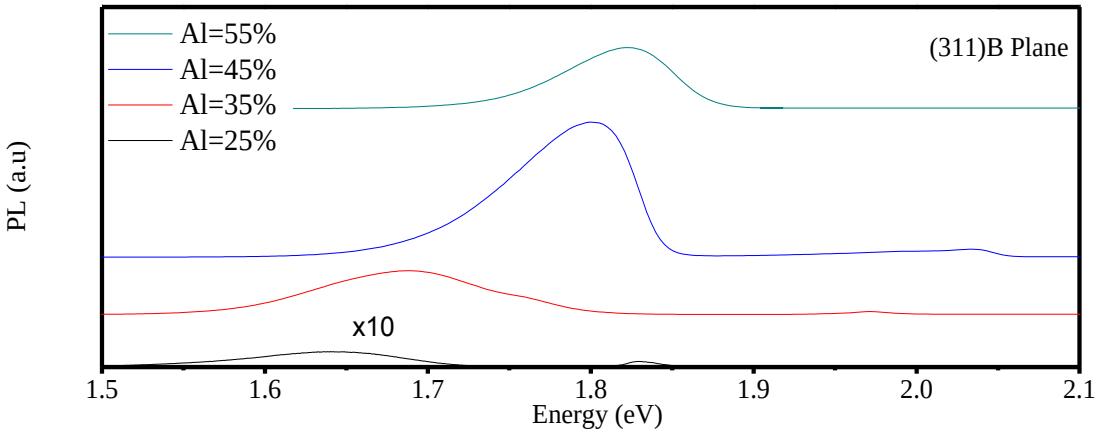

Figure 5.15: PL spectra of (311)B InAlAs QDs grown on AlGaAs matrix with different Al concentrations.

Table 5.4: The PL properties of $Al_{0.35}In_{0.65}As$ / $Al_yGa_{1-y}As$ QDs.

Al (%)	QD PL Energy (eV)	PL Energy of $Al_yGa_{1-y}As$ matrix (eV)	Difference between QD energy and AlGaAs matrix energy (meV)	PL intensity/ PL intensity of $QD^{0.25}_{(311)B}$
25	1.68	1.83	150	1
35	1.71	1.97	260	10
45	1.8	2.04	240	13
55	1.82	2.15	330	11

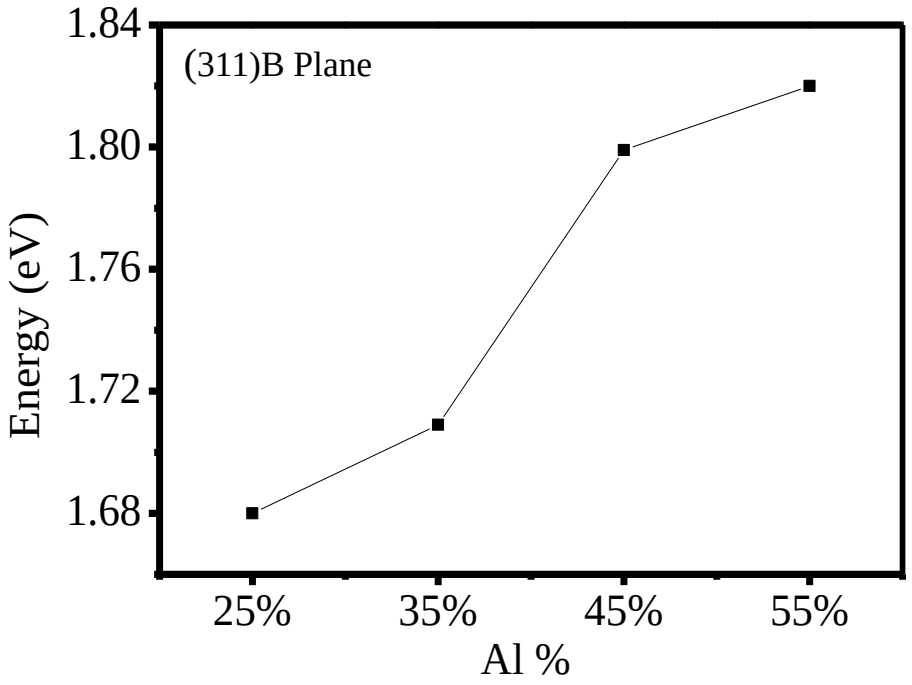

Figure 5.16: QD PL energy as function of Al percentage in matrix.

To further investigate the effect of the different Al concentration in matrix on the PL efficiency of the InAlAs QDs, the PL intensity (PLI) over the temperature range 10-220 K was determined for all four samples. The temperature dependence of the PLI for all four samples with different Al concentrations in matrix is shown in Figure 5.17.

The PLI of sample $QD^{0.25}_{(311)B}$ remains approximately constant up to 30 K, and then decreases by a factor of 1654 at 200K. This behaviour is typical for InAs/GaAs QDs and has been attributed to the thermal escape of the carriers from the QDs[34, 62]. When the Al content in GaAlAs matrix increases to 35% in sample $QD^{0.35}_{(311)B}$, the PL quenching improved from 200K to 220 K. The PL signal decreased by a factor of 644 in the temperature range 10-220 K. Further incorporation of Al to 45 % in sample $QD^{0.45}_{(311)B}$, the PLI decreases by a factor of less than 172 in similar temperature range. The data presented in Figure 5.17 clearly show that the temperature above which quenching of the PL occurs increases with the Al content in the GaAlAs matrix. For the sample with of 55% Al led to an improvement of the PL at low temperature as comparing to sample with 25% Al content. However, with

increasing temperature a faster quenching appears which may be explained by an increase of non-radiative defects that have been created due to the higher Al content used.

In comparison with sample $QD^{0.25}_{(311)B}$, at 100 K the PL intensity of sample $QD^{0.45}_{(311)B}$ is approximately 50 times higher as shown in Figure 5.18. These ratio values are enhanced with increasing temperature; an enhancement of the luminescence efficiency, particularly at high temperatures is highly desirable for optoelectronic applications.

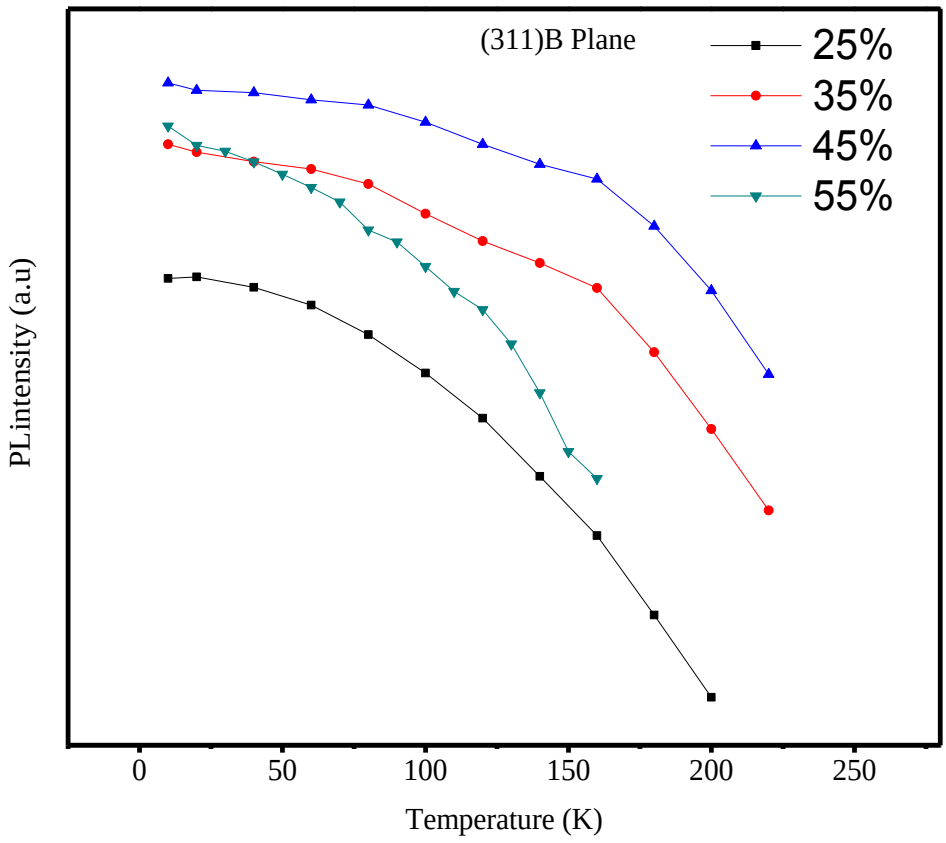

Figure 5.17: The temperature dependence of PL intensity of (311)B QDs grown on AlGaAs matrix with different Al concentrations. The lines are guide for the eyes.

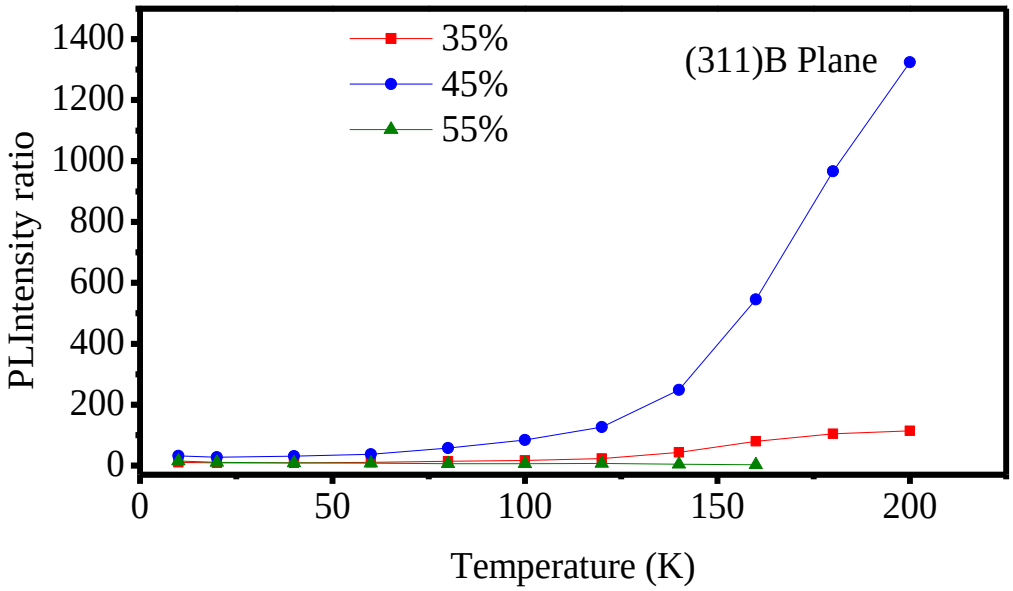

Figure 5.18: The ratio of PL intensity of samples $QD^{0.35}_{(311)B}$, $QD^{0.45}_{(311)B}$, and $QD^{0.55}_{(311)B}$ to sample $QD^{0.25}_{(311)B}$ as a function of temperature.

In conclusion, an AlGaAs confining barrier with 45% Al is found to provide higher optical efficiency of QDs grown on all planes (only results on (311)B are reported in this section). The optimum structure that gives the best optical properties consists of 4.4MLs $Al_{0.35}In_{0.65}As$ QDs/$Al_yGa_{1-y}As$ with y = 0.45 grown on (311)B wafer. Therefore this structure grown on the (311)B plane has been chosen to investigate the effect of the growth temperature (450 ^{0}C, 500 ^{0}C, 550^{0}C) on the QDs optical efficiency.

5.4 EFFECT OF GROWTH TEMPERATURE ON OPTICAL EFFICIENCY OF (311)B InAlAs QDs GROWN ON $Al_{0.45}Ga_{0.55}As$ MATRIX

$Al_{0.35}In_{0.65}As/Al_{0.45}Ga_{0.55}As$ (311)B QDs samples were grown under the same condition and have the same layer structure as the previous samples except that the deposited $Al_{0.35}In_{0.65}As$ QDs were grown at three different temperatures, namely 450 ^{0}C, 500 ^{0}C, and 550 ^{0}C.

The details of the three investigated samples in this section are shown in Table 5.5.

It is worth pointing out that the 4.4 MLs $Al_{0.35}In_{0.65}As$ QDs grown on (100) and (311)A planes at a growth temperature of 500 ^{0}C do not display any luminescence signal. The reason(s) of their poor optical quality is not clear at this stage. However, their optical properties were recovered and improved when grown at 550 ^{0}C (i.e. better than QDs grown at 450 ^{0}C) but still inferior than the (311)B QDs.. The results presented in the following section are therefore limited to the study of the effect of the growth temperature on the optical properties of (311)B QDs .

Table 5.5: $Al_{0.35}In_{0.65}As/Al_{0.45}Ga_{0.55}As$ (311)B QDs samples grown at various temperatures.

Sample Number	Substrate	Growth temperature
NU2738 $QD^{450}_{(311B)}$	(311)B	450 ^{0}C
NU2754 $QD^{500}_{(311B)}$	(311)B	500 ^{0}C
NU2757 $QD^{550}_{(311B)}$	(311)B	550 ^{0}C

Figure 5.19 shows PL spectra at 8 K for (311)B samples grown at various temperatures. The peak position, FWHM and the integral intensity have a strong

dependence on the growth temperature. The PL properties of these QDs are summarized in Table 5.6.

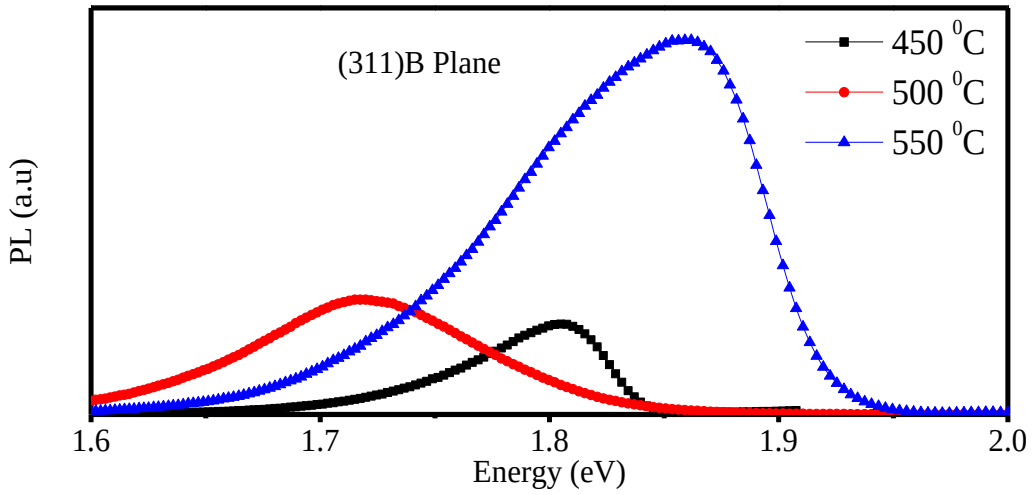

Figure 5.19: PL spectra of $Al_{0.35}In_{0.65}As/Al_{0.45}Ga_{0.55}As$ QDs grown at different growth temperatures on (311)B GaAs substrate orientation.

When the growth temperature increased from 450 ^{0}C to 500 ^{0}C, the peak position of QDs shifted to low energy, whereas the QD peak shifted to high energy when growth temperature was 550 ^{0}C. This red energy shift has been observed for InAs/GaAs QDs[63-65] and was explained by the increase of the surface migration of In atoms with increasing temperature. The distance between the In atoms which have assembled to form one dot is increased, and this results in the formation of larger dots.

The blue-shift of the peak energy of the QDs grown at 550 ^{0}C might be due to the emission related to the excited electron states in big QDs[66]. The other possible explanation of the blue-shift is the thermally enhanced intermixing of In and Ga atoms at the QD/matrix interface.

The PL intensity of QDs grown at the highest temperature is four times larger than the PL intensity of QDs grown at the lowest temperature. It is believed that the high intensity achieved at 550 ^{0}C is due to fewer defects formed at the higher growth temperature than the lower growth temperature. This argument is supported by the fact that the PL from samples grown at high growth temperature quenches at much higher temperature of 290 K (see Figure 5.20).

Table 5.6: Summary of PL properties of $Al_{0.35}In_{0.65}As/Al_{0.45}Ga_{0.55}As$ (311)B QDs samples grown at various temperatures.

Growth Temperature	FWHM (meV)	PL Energy (eV)	PL intensity / PL intensity ($_{QD}^{450}{}_{(311B)}$)
450 ^{0}C	86	1.799	1
500 ^{0}C	113	1.72	1.2
550 ^{0}C	128	1.86	4.15

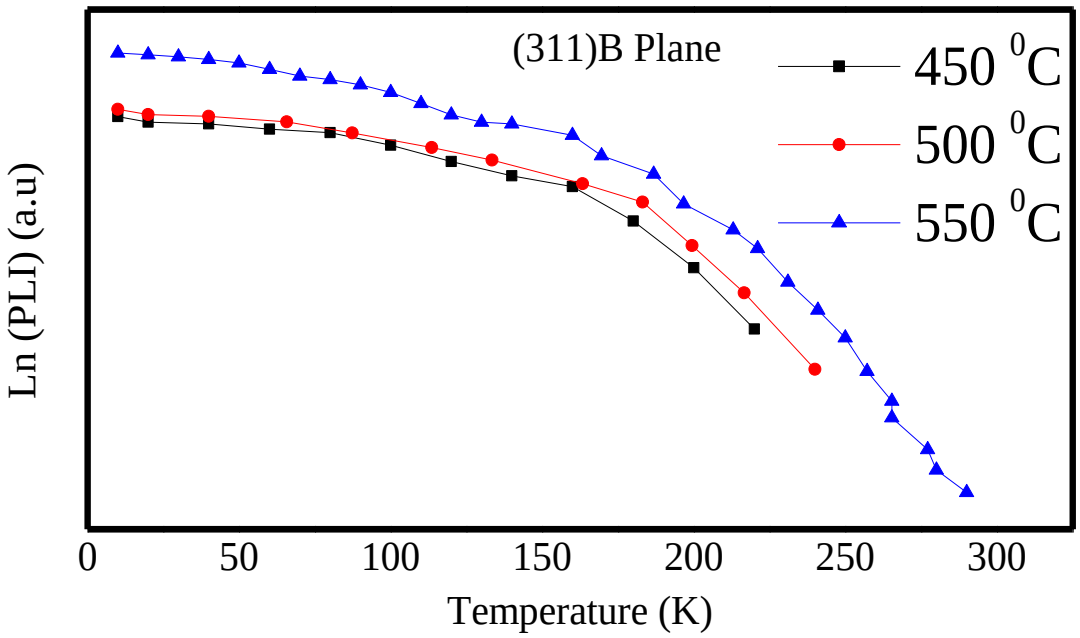

Figure 5.20: Temperature dependence of PL intensity of (311)B $Al_{0.35}In_{0.65}As/Al_{0.45}Ga_{0.55}As$ QDs grown at different growth temperatures. The lines are guide for the eyes.

In conclusion, an increase of the growth temperature results in a significant optical improvement. A temperature of 550 ^{0}C to grow AlInAs was the optimum condition to achieve high optical efficiency QDs emitting in the visible.

5.5 CONCLUSION

In summary, $Al_{0.35}In_{0.65}As$ QDs formed under different growth conditions on (100) and high-index GaAs substrates by MBE have been investigated. PL results confirmed that the formation of QDs occurs for all substrate orientations. The PL measurements revealed differences in the optical properties that are caused by substrate orientation effects. The PL emission energies of QDs grown on high Miller index surfaces are found to be strongly dependent on the atomic terminated surface [A (Ga face) or B (As face)] of the substrate.

The optical quality of the 3.7 MLs AlInAs QDs on high index planes is found to be inferior to that of (100) QDs. Due to the fact that all substrate orientations were grown simultaneously using growth conditions that are optimised for (100) substrates, the inferior optical quality of QDs grown on high index planes could therefore be due to the non-optimized growth conditions and layer structure. By increasing the deposited $Al_{0.35}In_{0.65}As$ material to 4.4MLs, the optical efficiency of QDs grown on (311)B improved, however the optical efficiency of (311)A QDs was still inferior to (100) QDs. The (100) QDs PL efficiency was not enhanced but the FWHM decreased. The lower density of QDs on the (311)A orientation could be responsible for the observed low emission efficiency. It is found that the improvement of PL efficiency from (311)B QDs is accompanied by an increase of the FWHM. This can be understood in terms of fluctuation of their size distribution.

By increasing the confinement barriers, i.e. increasing the Al content of the matrix to 45%, the temperature-dependent PL study shows that the PL thermal quenching of the QDs occurs at higher temperatures due to the higher confinement potential. An improvement of the optical quality accompanied by a blue shift from (311)B QDs has been observed by increasing the growth temperature from 450 ^{0}C to 550 ^{0}C.

REFERENCES

[1] D. J. Eaglemann, and M. Cerullo, Physical Review Letters, 64, 1943 (1990).

[2] D. Leonard, S. Fafard, K. Pond, Y. H. Zhang, J. M. Merz, and P. M. Petro, Journal of Vacuum Science and Technology B, 12, 2516 (1994).

[3] J. Y. Marzin, J. M. Gerald, A. Izrael, D. Barrier, and G. Bastard, Physical Review Letters,73, 716 (1994).

[4] F. Hatami, N. N. Ledentsov, M. Grundmann, J. Bohrer, F. Heinrichsdor, M. Beer, D. Bimberg, S. S. Ruvimov, P. Werner, U. Gosele, J. Heydenreich, U. Richter, S.V. Ivanov, B. Y. Meltser, P. S. Kopev, and Z. Alferov, Applied Physics Letters, 67, 656 (1995).

[5] A. Kurtenbach, K. Eberl, and T. Shitara, Applied Physics Letters, 66, 361 (1995).

[6] H. Marchand, P. Desjardins, D. Guillon, J. Paultre, Z. Bougrioua, R. Yip, and R.A. Masut, Applied Physics Letters, 71, 527 (1997).

[7] S. Fafard, Z. Wasilewski, J. Mccrey, S. Raymond, and S. Charbonneau, Applied Physics Letters, 68, 991 (1996).

[8] H. Li, J. Wu, B. Xu, J. Liang, and Z. Wang, Applied Physics Letters,72, 2123 (1998).

[9] R. Leon, S. Fafard, D. Leonard, J. L. Merz, and P. M. Petroff, Science, 274, 1350 (1996).

[10] R. Heitz, M. Veit, N. N. Ledentsov, A. Hoffmann, D. Bimberg, V. M. Ustinov, P. S. Kop'ev, and Zh. I. Alferov, Physical Review B, 56, 10435 (1997).

[11] W. Zhou, B. Xu, H. Z. Xu, F. Q. Liu, J. B. Liang, Z. G. Wang, Z. Z. Zhu, and G. H. LI, Journal of Electronic Materials, 28, 5, (1999).

[12] X. M. Lu, Y. Izumi, M. Koyama, Y. Nakata, S. Adachi, and S. Muto, Journal of Crystal Growth, 322, 6, (2011).

[13] R. Leon, S. Fafard, D. Leonard, J. L. Merz, and P. M. Petroffc, Applied Physics Letters, 67, 521 (1995).

[14] A. F. Tsatsul'nikov, A. Yu. Egorov, P. S. Kop'ev, A. R. Kovsh, N. N. Ledentsov, M. V. Maximov, A. A. Suvorova, V. M. Ustinov, B. V. Volovik, A. E. Zhukov, M. Grundmann, D. Bimberg, and Zh. I. Alferov, Applied Surface Science, 123, 381 (1998).

[15] H. Y. Liu, B. Xu, J. J. Qian, X. L. Ye, Q. Han, D. Ding, J. B. Liang, X. R. Zhong, and Z. G. Wang, Journal of Applied Physics, 90, 2048 (2001).

[16] B. L. Liu, Z. Y. Xu, H. Y. Liu, and Z. G. Wang, Journal of Crystal Growth, 220, 51 (2000).

[17] I. Alghoraibi, T. Rohel, N. Bertru, A. Le Corre, A. Létoublon, P. Caroff, O. Dehaese, and S. Loualiche, Journal of Crystal Growth, 293, 263 (2006).

[18] B. A. Joyce, and D. D. Vvedensky, Materials Science and Engineering: R: Reports, 46, 127 (2004).

[19] L. Sfaxi, L. Bouzaiene, H. Sghaier, and H. Maaref, Journal of Crystal Growth, 293, 330 (2006).

[20] M. Henini, Nanoscale Research Letters, 1, 32 (2006).

[21] Y. Temko, T. Suzuki, P. Kratzer, and K. Jacobi, Physical Review B, 68, 165310 (2003).

[22] T. Suzuki, Y. Temko, and K. Jacobi, Applied Physics Letters, 80, 4744 (2002).

[23] K. Jacobi, Progress in Surface Science, 71, 185 (2003).

[24] D. I. Lubyshev, P. P. Gonzalez-Borrero, E. Marega, J. E. Petitprez, and P. Basmaji, Journal of Vacuum Science and Technology B, 14, 2212 (1996).

[25] M. C. Xu, Y. Temko, T. Suzuki, and K. Jacobi, Physical Review B, 71, 075314 (2005).

[26] M. C. Xu, Y. Temko, T. Suzuki, and K. Jacobi, Surface Science, 576, 89 (2005).

[27] R. Notzel, N. N. Ledentsov, L. Daweritz, K. Ploog and M. Hohenstein, Physical Review B, 3507 (1993).

[28] S. Zhong-Zhe, L. Feng-Qi, W. Ju, Y. Xiao-Ling, D. Ding, X. Bo, L. Ji-Ben, and W. Zhan-Guo, Physica E, 8, 164 (2000).

[29] S. C. Fortina, S. Sanguintti, E. Grilli, M. Guzzi, M. Henini, A. Polimeni, and L. Eaves, Journal of Crystal Growth, 187, 126 (1998).

[30] M. Henini, III-Vs Rev., 11, 48 (1998).

[31] C. Lobo, and R. Leon, Journal of Applied Physics, 83, 4168 (1998).

[32] P. P. Gonzilez-Borrero, D. I. Lubyshev, E. Marega Jr, E. Petitprez, and P. Basmaji, Journal of Crystal Growth, 169, 428 (1996).

[33] Z. Y. Xu, Z. D. Lu, X. P. Yang, B. Z. Zheng, J. Z. Xu, W. K. Ge, Y. Wang, J. Wang, and L. L. Chang, Superlattices and Microstructures, 23, 381 (1998).

[34] Z. Xu, Z. Lu, X. Yang, Z. Yuan, B. Zheng, J. Xu, W. Ge, Y. Wang, J. Wang, and L. Chang, Physical Review B, 54, 11528 (1996).

[35] S. Fafard, Z. R. Wasilewski, C. Ni. Allen, D. Picard, M. Spanner, J. P. Mccaffrey, and P. G. Piva, Physical Review B, 59, 15368 (1999).

[36] J. He, Y. Zhang, B. Xu, and Z. Wang, Journal of Crystal Growth, 247, 49 (2003).

[37] B. Liang, Z. Wang, Y. Mazur, V. Strelchuck, K. Holmes, J. Lee, and G. Salamo, Nanotechnology, 17, 2736 (2006).

[38] W. Jiang, H. Xu, B. Xu, X. Ye, W. Zhou, D. Ding, J. Liang, and Z. Wang, Physica E, 8, 134 (2000).

[39] A. Polimeni, M. Henini, A. Patane, L. Eaves, and P. Main, and G. Hill, Applied Physics Letters, 73, 1415 (1998).

[40] S. Sanguinetti, G. Chiantoni, E. Grilli, M. Guzzi, M. Henini, A. Polimeni, A. Patane, L. Eaves, and P. Main, Europhysics Letters, 47 (6), 701 (1999).

[41] D. Leonard, M. Krishnamurthy, S. Fafard, J. Merz, and P. Petroff, Journal of Vacuum Science and Technology B, 12, 1063 (1994).

[42] D. Leonard, M. Krishnamurthy, C. M. Reaves, S. P. Denbaars, and P. M. Petroff, Applied Physics Letters, 63, 3203 (1993).

[43] M. Colocci, F. Bogani, L. Carraresi, R. Mattolini, A. Bosacchi, S. Franchi, P. Frigeri, M. Rosa-Clot, and S. Taddei, Applied Physics Letters, 70, 3140 (1997).

[44] A. Polimeni, A. Patane, M. Capizzi, F. Martelli, L. Nasi, and G. Salviati, Physical Review B, 53, 4213 (1996).

[45] S. Sanguinetti, G. Chiantoni, E. Grilli, M. Guzzi, M. Henini, A. Polimeni, A. Patane, L. Eaves, and P.C. Main, Materials Science and Engineering B, 74, 239 (2000).

[46] G. M. Guryanov, G. E. Cirlin, V. N. Petrov, N. K. Polyakov, A. O. Golubok, S. Tipissev, V. B. Gubanov, Yu. B. Samsonenko, N. N. Ledentsov, V. A. Shchukin, M. Grundmann, D. Bimberg, and Zh. I. Alferov, Surface Science, 352, 651 (1996).

[47] D. Gammon, S. Rudin, T. L. Reincke, D. S. Katzer, and C. S. Kyono, Physical Review B, 51, 16785 (1995).

[48] Y. T. Dai, J. C. Fan, Y. F. Chen, and R. M. Lin, S. C. Lee, and H. H. Lin, Journal of Applied Physics, 82, 4489 (1997).

[49] M. Hjiri, F. Hassen, H. Maaref, B. Salem, G. Bremond, O. Marty, J. Brault, and M. Gendry, Physica E, 17, 180 (2003).

[50] R. Songmuang, S. Kiravittaya, M. Sawadsaringkarn, S. Panyakeow, and O. G. Schmidt, Journal of Crystal Growth, 251, 166 (2003).

[51] Y. P. Varshni, Physica (Amsterdam), 34, 149 (1967).

[52] H. Wang, D. Ning, and L. Feng, Journal of Crystal Growth, 209, 630 (2000).

[53] D. K. Gaskill, N. Bottka, L. Aina, and M. Mattingly, Applied Physics Letters, 56, 1269 (1990).

[54] S. Sanguinettia, A. Miottoa, S. Castiglionia, E. Grillia, M. Guzzia, M. Henini, A. Polimeni, A. Patane, L. Eaves, and P. Main, Microelectronics Journal, 30, 419 (1999).

[55] D. I. Lubyshev, P. P. Gonzalez-Borrero, E. Marega, and P. Basmaji, Journal of Vacuum Science and Technology B, 14(3), (1996).

[56] S. Sanguinetti, S. Fortina, A. Miotto, E. Grilli, M. Guzzi, M. Henini, A. Polimeni, and L. Eaves, Thin Solid Films, 336, 9 (1998).

[57] W. Zhou, Z. M. Zhu, F. Q. Liu, B. Xu, H. Z. Xu, and Z. G. Wang, Journal of Crystal Growth, 200, 608 (1999).

[58] C. Loboa, and R. Leon, Journal of Applied Physics, 83, 4168 (1998).

[59] B. G. Orr, D. Kessler, C. W. Snyder, and L. Sander, Europhysics Letters, 19, 337 (1992).

[60] Y. S. Kim, U. H. Lee, D. Lee, S. J. Rhee, Y. A. Leem, H. S. Ko, D. H. Kim, and J. C. Woo, Journal of Applied Physics, 87, 241 (2000).

[61] A. Polimeni, A. Patane, M. Henini, L. Eaves, and P. Main, Physical Review B, 59, 5064 (1999).

[62] S. Sanguinetti, M. Henini, M. Grassi Alessi, M. Capizzi, P. Frigeri, and S. Franchi, Physical Review B, 60, 8276 (1999).

[63] T. Kaizu, and K. Yamaguchi, Japanese Journal of Applied Physics, 40, 1885 (2001).

[64] Y. Nakata, Y. Sugiyama, and M. Sugawara, Semiconductor and Semi-metals, Academic Press, San Diego (1999).

[65] V. G. Dubrovskiia, G. E. Cirlinb, Yu. G. Musikhina, Yu. B. Samsonenkob, A. A. Tonkikha, N. K. Polyakovb, V. A. Egorovb, A. F. Tsataul'nikova, N. A. Krizhanovskayaa, V. M. Ustinova, and P. Wernerc, Journal of Crystal Growth, 267, 47 (2004).

[66] S. P. Guo, A. Shen, Y. Ohno, and H. Ohno, Physica E, 2, 672 (1998).

CHAPTER 6: ANNEALING EFFECT ON InAlAs QUANTUM DOTS GROWN ON (100), (311)A, (311)B GaAs SUBSTRATES

This chapter reports the effect of the post growth annealing process on the optical properties of InAlAs self-organized quantum dots (QDs) grown on different GaAs substrate orientations, namely (100), (311)A, and (311)B.

6.1 INTRODUCTION

As reported in the previous chapter the self-organized InAlAs QDs are grown by MBE using the Stranski-Krastanow growth mode, which does not involve any substrate patterning process. Although these QDs have a well-defined shape, their random nucleation in single layer results in a broad distribution of QDs size, and limit their practical applications. Further developments in the use of QD structures for devices such as zero dimensional (0D) lasers are dependent on the achievement of tunability of dot dimensions and size dispersion in order to both control the wavelength and reduce the linewidth of the luminescence emission. Therefore, there is a need to control the size uniformity in QDs. In addition, most device processes also include high temperature annealing, and therefore it is very important to investigate the behavior of QDs during thermal treatment.

The post-growth thermal treatment is frequently used to modify the structural and optical properties of self-assembled InAs and InGaAs QDs[1,2]. These effects should be either strongly avoided or, on the opposite, can be used intentionally to modify the properties of the QD structures.

The effects of post-growth thermal annealing on QDs include a blue shift of interband transition energy and narrowing of the PL line width. Although these phenomena can be described by inter-diffusion between the QD and the barrier, the detailed mechanisms are still not very clear. There are considerable reports available in literature that have studied these phenomena but the PL data are different due to the different kinds of QD structures.

The inter-diffusion process depends on several factors like the quality of interface between dots and barrier, the density of defects such as vacancies, interstitials, and dislocations. The inter-diffusion mechanism is therefore closely correlated with the growth process of QDs (temperature, growth rate, growth plane, capping layer etc)[3,4].

To my knowledge there is no reported work about the influence of annealing on InAlAs QDs grown on the conventional (100) and high index plane except the data reported by C. Lobo et al [5] on dots grown on (100) plane.

C. Lobo et al5 have examined the effect of post-growth annealing on the inter-diffusion and the luminescence emission from red and infrared emitting self-assembled III–V quantum dots. Three different combinations of dot/barrier materials have been investigated: InAlAs/AlGaAs, InGaAs/AlGaAs and InGaAs/GaAs. In all cases, thermal intermixing was found to result in significant blue shifts of the PL emission. In addition, narrowing of the linewidth of the inhomogeneously broadened PL peak was observed. Both effects were found to be strongly dependent on the material system and average dot size. The extent of blue shifting increases with dot size across all material systems. The maximum blue shift was observed at an annealing temperature of 900 °C and ranges from 77 meV for the smaller InAlAs/AlGaAs QDs (28.6 nm) to 160 meV for the InGaAs/AlGaAs (46 nm) QDs. The PL emission from the single layer and multilayer stack of InGaAs/ GaAs (29.5 nm) QDs showed a blueshift of 97 meV after annealing at 900 °C for 30 s. In addition, it was found that the magnitude of the narrowing of the linewidth to be very sensitive to the nature of the QDs and the confining barrier, ranging from 50 meV for InAlAs/AlGaAs QDs to 30 meV for InGaAs/GaAs QDs, and just 10 meV for InGaAs/AlGaAs QDs annealed at 900 °C. This difference in linewidth narrowing suggests that both the magnitude and direction of the composition gradient across the dot/barrier interface are important in determining the effect of inter-diffusion on the PL emission.

Z. Zhang et al[6] have investigated the rapid thermal annealing (RTA) of InAs QDs under different strain layers ($In_xAl_{1-x}As/In_{0.2}Ga_{0.8}As$ combination overgrowth). The photoluminescence measurements demonstrated that the InAs QDs experience an abnormal variation during the course of RTA. The InAs QDs PL peak is blue shifted up to 260 meV after annealing at 800 ^{0}C. The magnitude of energy blue shift and change of shape of PL spectra was found to depend on the thickness of $In_xAl_{1-x}As$ layer. In order to explain the variation of the PL spectra (in terms of FWHM, intensity and energy), they claimed that the InAs QDs transformed into InAlAs and InGaAlAs QDs depending on the annealing temperature and $In_xAl_{1-x}As$ capping layer.

Z. Zaaboub et al[7] studied the effect of post-growth rapid thermal annealing on the PL properties of low density InAs/GaAs QDs emitting around 1170 nm. For an annealing temperature of 650 °C for 30 s, the emission wavelength and the inter-sublevel spacing energies remained unchanged while the integrated PL intensity increases. For higher annealing temperatures, blue shift of the emission energy up to 172 meV together with a decrease in the inter-sublevel spacing energies from 67 to 33 meV were shown to occur due to the thermal activated In–Ga inter-diffusion. The appearance of an additional excited state for annealing temperatures higher than 650 °C suggests a variation of the intermixed QDs' volume/diameter ratio toward QDs' enlargement.

W. Jiang et al[8] investigated the surface morphology and optical properties of InGaAs/GaAs QDs subjected to different annealing temperatures by TEM and PL techniques. The PL peak position is almost constant when the annealing temperature is 650 ^{0}C, indicating a weak inter-diffusion. A clear blue shift of the PL spectrum due to In/Ga inter-diffussion occurs at 700 ^{0}C, along with a narrowing of linewidth and an increase of PL intensity. TEM results show that higher annealing temperatures (higher than 850 ^{0}C) lead to the degradation of QD material and some clusters are formed which destroy the QDs significantly. The degradation is caused by surface roughing and formation of large clusters, due to the strong inter-diffusion of In, Ga atoms and strain relaxation.

I. J. Guerrero Moreno et al[9] have employed PL to study the effect of the annealing at 640 ^{0}C for 2 hours on MBE grown InAs QDs capped with different capping materials, such as GaAs and $Al_{0.3}Ga_{0.7}As$. They have shown that thermal annealing initiates the shift of PL peak positions into the high energy spectral range and the values of this blue shift are found to be dependent on the composition of capping layers. Furthermore, I. J. Guerrero Moreno and co-workers have investigated the temperature dependence of the PL peak positions of QDs in the range of 10–300 K and compared it with the temperature shrinkage of the band gap of bulk InAs crystal. This study allowed them to investigate the efficiency of the Ga(Al)/In inter-diffusion processes in relation to the nature/composition of the capping layer. Experimental and fitting parameters obtained for InAs QDs have been compared with known ones

for the bulk InAs crystal. It is revealed that the efficiency of the Ga(Al)/In inter-diffusion depends essentially on the composition of the capping layer.

It has been reported that strain free QDs can be obtained by using the modified droplet epitaxy (MDE) technique[10-12]. The formation of QDs by MDE is different than the well-known Stranski-Krastanov method. T. Mano et al[13] have employed PL and cross-sectional high-angle annular dark field scanning transmission electron microscopy (HAADF-STEM) to investigate the effects of post-growth annealing on structural and optical properties of self-assembled ring-shaped GaAs QDs grown by MDE. Negligible structural changes of the QDs were observed after the annealing process up to 800 ^{0}C while the intensity of PL emission increased drastically. The annealed laser structure with three layers of the ring-shaped QDs showed photo-pumped laser action with clear threshold at 77 K.

S. Sanguinetti et al[14] carried out a systematic study of the post growth annealing effects on the optical properties of self-assembled GaAs/AlGaAs QDs grown by MDE. The process of post-annealing strongly affects the optical properties of the MDE QDs. The post-annealing creates structural modifications of the MDE QD heterostructures by promoting the intermixing of the group III elements. The assessment of the modifications of the QD eigenstates and of the QD environment has been performed via optical measurements. They determined an inter-diffusion length (l) of Ga and Al (l = 1 nm) at relatively low annealing temperatures (520 ^{0}C), with a relatively slow increase with the annealing temperature. Low temperature growth used during QDs formation lead to the presence of a high concentration of out-of-equilibrium group III vacancies which in turn lead to the strong inter-diffusion process during the annealing. By applying the rate equation model they demonstrated that the quenching of PL with temperature in the case of as-grown samples is due to the escape of carriers from the GaAs QDs to the WL. However, for the annealed samples the PL quenching is accounted for by the excitation of carriers from QDs directly into the AlGaAs barrier.

S. Malik et al[15] have observed blue shift in the PL emission energies from an ensemble of self-assembled InAs QDs as a result of post-growth thermal annealing. Enhancement of the integrated PL emission and narrowing of the full width half-

maxima (from 55 to 12 meV) occur together with blue shifts up to 300 meV at annealing temperatures up to 950 °C. Evidence that the structures remain as dots at this high annealing temperature comes from the observation of level filling and photoluminescence excitation studies which reveal longitudinal phonon (LO) peaks occurring at multiples of 30 meV from the detection energies.

H. Park et al[16] have employed PL and TEM to study the effects of multi-steps RTA on the self-assembled InAs QDs, which were grown by MBE. Post-growth multi-steps RTAs are as follows: one step (20 s at 750 ^{0}C), two steps (20 s at 650 ^{0}C, 20 s at 750 ^{0}C), three steps (30 s at 450 ^{0}C, 20 s at 650 ^{0}C, 20 s at 750 ^{0}C). They found that significant narrowing of the luminescence linewidth (from 132 to 31 meV) from InAs QDs occurs together with about 150 meV blue shift by two-steps annealing as compared to as-grown InAs QDs. Analysis of TEM data confirm the existence of the dots under one- and two-steps annealing but the disappearance of the dots by three-steps annealing. Comparing with the samples under only one-step annealing, they demonstrate a significant enhancement of the inter-diffusion in the dot layer under multi-steps annealing.

S. J. Xu et al[17] studied the effect of RTA post-growth thermal process on the structural and optical properties of the self-assembled InAs QDs grown on GaAs substrates by MBE. It was found that significant narrowing of the luminescence linewidth (from 78.9 to 20.5 meV) from the InAs dot layer occurs together with about 260 meV blueshift at annealing temperatures up to 850 °C. This large blue shift was explained to be due to the thick SiO_2 capping layer used during the annealing process. Images of High Resolution TEM (HRTEM) show the existence of dots under lower annealing temperatures but disappearance of the dots annealed at 850 °C. The excited-state-filling experiments on the samples show that the luminescence of the samples annealed at 850 °C exhibits quantum well-like behavior, while no excited-state emissions were observed even at high excitation power. This also provides evidence of the disappearance of the QDs at high annealing temperatures. Comparing with a reference quantum well, they demonstrated significant enhancement of the inter-diffusion in the dot layer.

S. Martini et al[18] investigated In segregation from $In_{0.10}Ga_{0.90}As$/GaAs quantum wells grown on different GaAs (001) substrates with a miscut angle of 0° (nominal), 2°, 4° and 6° towards [110] using low temperature PL. Extra emission at low energy was only observed for the nominal sample and was related to In segregation. Its absence from the PL spectrum of quantum wells grown on vicinal surfaces is a strong indication that In segregation is modified on this type of surface. This feature was related to the trapping of free excitons by slightly In-rich islands that were present at the second interface as a result of In segregation. The presence of a high density of steps limits the surface migration of the adatoms.

F. Guimaraes et al[19] studied the influence of surface structure and morphology on indium segregation in InGaAs/GaAs quantum well structures grown by MBE on (100), (311)A and (311)B GaAs surfaces. They reported that indium surface segregation in (311)A GaAs surface is smaller than in the (100) and (311)B orientations. They state that surfaces with high step structures or density, such as in the case of (311)A surface, would favour the incorporation of indium at the step edges and therefore reducing In segregation. In addition, they found that by using the growth interruption technique at only the inverted GaAs-to-InGaAs interface In segregation is reduced for all orientations. They explained this effect by a change in the surface structure.

6.2 EXPERIMENTAL RESULTS AND ANALYSIS

The study of the annealing effect on the samples investigated in this section is the samples that gave the best optical efficiency as discussed in the previous chapter.
The samples consisted of a 0.2 µm-thick GaAs buffer layer of which the first 0.1 µm was grown at 580 °C and the remaining 0.1 µm at 600 °C. The temperature was kept at 600 ^{0}C during deposition of the $Al_{0.45}Ga_{0.55}As$ matrix layer. This was followed by the deposition of 13Å $Al_{0.35}In_{0.65}As$ strained layer at 550 ^{0}C for the formation of QDs, a 50 nm $Al_{0.45}Ga_{0.55}As$, and 10 nm GaAs cap layer .
Post-growth annealing is performed using proximity capping, meaning an annealing process involving a piece of GaAs substrate in close proximity to the sample

surface[5,20]. The samples cut from the as-grown wafer were proximity capped and RTA treated in argon ambient for 30 s at 600 ^{o}C, 700 ^{o}C, and 800 ^{o}C.

It is known that RTA of samples without any capping leads to surface degradation due to As out diffusion. It is well established that the sample capping during post-growth of strained InGaAs/GaAs multi quantum wells can critically influence the results of the annealing procedure[21].

To remove the effects of any variations in annealing temperatures between samples, all the samples were annealed simultaneously as a batch. PL measurements at 10 K were performed on each of the samples prior to annealing, and then again following the annealing process. Further anneals were then performed on the same samples with the low temperature PL recorded after each anneal.

6.2.1 LOW TEMPERATURE PHOTOLUMINESCENCE OF ANNEALED SAMPLES AT DIFFERENT TEMPERATURES

Figure 6.1 shows the 10 K PL spectra of as-grown, and 600 ^{0}C and 700 ^{0}C annealed (100), (311)A, (311)B QD samples.

The peak PL energy of (100), (311)A, and (311)B as-grown samples are 1.784, 1.96, and 1.859 eV with FWHM of 141, 65, 128 meV, respectively. The higher energy observed for QDs formed on high-index surfaces is due to their smaller size than those formed on the (100) substrate.

It is evident from figure 6.1 that almost no change of the peak position is observed when the annealing temperature is 600 ^{0}C for QDs grown on (100) and (311)A planes, while there is a small blue shift of 34 meV for (311)B dots. The FWHM of PL spectra for 600 ^{o}C annealed samples have different behavior for different planes. It decreases for QDs grown on (100) plane while it is constant for the QDs grown on high index planes. However, all annealed QDs show an enhancement of PL efficiency at this annealing temperature as demonstrated in Figure 6.1. By increasing the annealing temperature to 700^{0}C, (100) and (311)B QDs samples show a large blue shift of 103 and 130 meV, respectively in their PL peak energy and a significant narrowing of the PL linewidth as compared to the as-grown samples. The PL of (311)A QDs shows a very small blue shift of 3meV as compared to the as-grown

sample. It is worth noting that there is a substantial increase in the integrated PL intensity of all the samples annealed at 700 ^{0}C, as shown in Figure 6.1.

Table 6.1 gives a summary of luminescence emission parameters from as-grown and 700 ^{0}C annealed (100), (311)A, (311)B QDs.

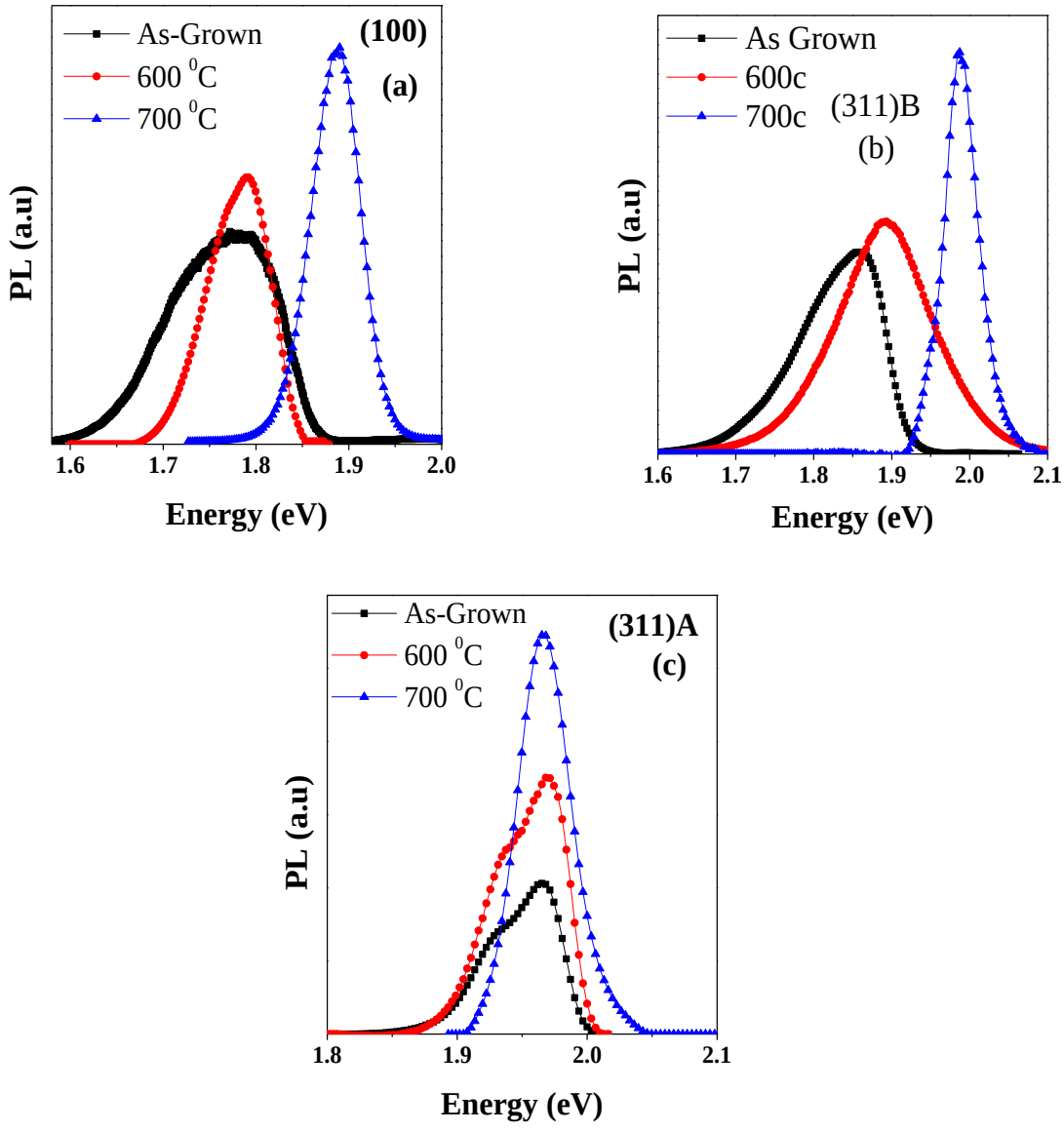

Figure 6.1: 10 K PL spectra of as-grown and annealed QD samples grown on different GaAs substrate orientations: (a) (100), (b) (311)B, (c) (311)A.

Table 6.1: Summary of photoluminescence emission parameters from (100), (311)A, (311)B QDs. Blue shifts and reductions in FWHM refer to samples annealed at 700 °C for 30 s.

Growth Plane	PL energy (eV)	FWHM (meV)	Blueshift (meV)	Percentage of Reduction in FWHM
(100)	1.784	141	103	56%
(311)A	1.965	65	3	29%
(311)B	1.859	128	130	60%

RTA thermal treatment at 800 ^{0}C has also been performed. It was observed that the PL of QDs disappears and the only peak present was due to the AlGaAs matrix. This suggests that the QDs dissolve into the surrounding materials. Dissolution of QDs after the RTA process at high temperature (850 ^{0}C for 50 s[17] or 950 ^{0}C for 30 s[15]) has previously been observed in InAs/GaAs QDs.

The blue shift with increasing annealing temperatures can be explained by the interfacial diffusion between the InAlAs QDs and the AlGaAs barrier, which should result in a change in the InAlAs QDs composition and an effective change in the QDs size[22].

An obvious narrowing of the FWHM is observed ranging from 141, 65, 128 meV for the as-grown samples to 61, 46, 50 meV for the (100), (311)A and (311)B samples annealed at 700 ^{0}C, respectively. This can be attributed to a substantial improvement of the size uniformity of the InAlAs QDs (see Figure 6.2).

Narrower linewidth resulting from higher annealing temperatures can be explained by a homogenization of sizes of the individual InAlAs QDs. A shallower confining potential results in the inter-diffusion which could also partly be accounted for by the narrower linewidth. The increase of PL intensity indicates that the annealing process eliminates nonradiative centers from the InAlAs QDs and the interfaces. This increase in intensity has been reported previously and attributed to the reduction of the concentration of point defects and other nonradiative recombination centers[23].

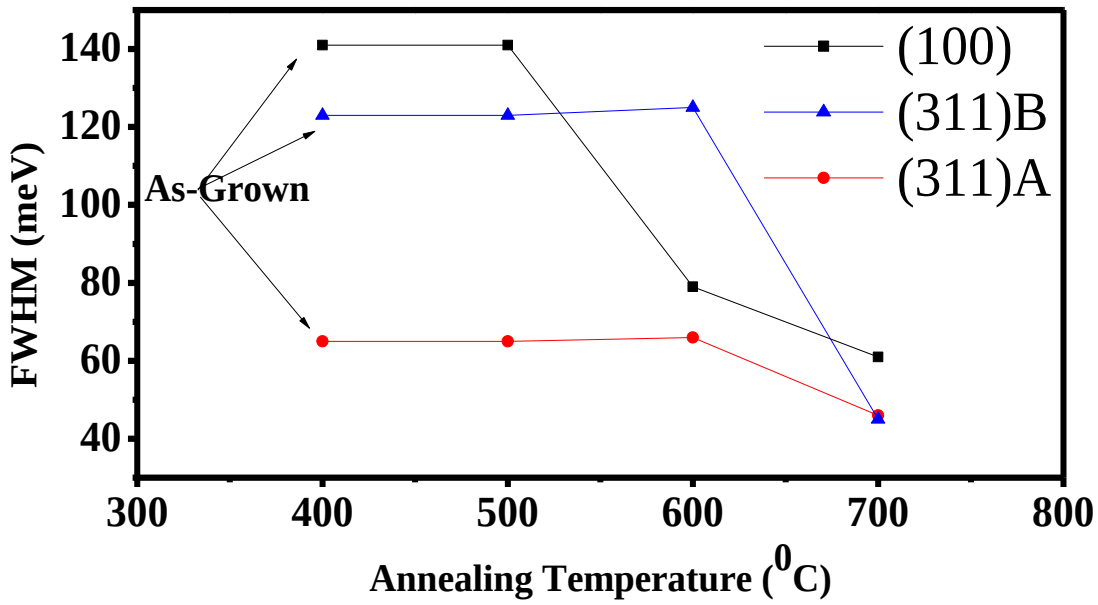

Figure 6.2: Evolution of PL linewidth (FWHM) with annealing temperature for dots grown on different planes. The data point at 400 ^{0}C corresponds to the sample without annealing.

The blue shift behavior is found to be dependent on the growth substrate direction indicating a different atomic inter-diffusion mechanism for the investigated samples (see Figure 6.3).

In case of PL from QDs grown on (100) and (311)B planes, the extent of blue shifting was found to increase monotonically with annealing temperatures. While in the case of QDs grown on (311)A plane there is a trivial blue shift with increasing the annealing temperature. The blue shift of the PL peak after annealing treatment is generally attributed to strong intermixing at the interface between QDs and the barrier layer. The inter-diffusion process strongly depends on the quality of the interface and the density of defects such as vacancies, interstitials, and dislocations. The inter-diffusion mechanism is closely correlated with the growth process of QDs and capping layer. Mixing Ga into InAlAs increases the energy bandgap inside the individual QDs, while diffusion of In into the AlGaAs barrier smoothens the confining potential for charge carriers. Both of these effects result in the observed blue shift[24].

The weak blue shift in case of (311)A QDs can be explained by one of the following two arguments:

(i) the inter-diffusion process strongly depends on the quality of the interface and the density of defects such as vacancies, interstitials, and dislocations3. It has been reported that the critical thickness for the formation of QDs on high index plane is larger than for (100) plane[25]. Since the amount of material used to grow the dots is the same in all samples as they were grown simultaneously, QDs grown on (100) plane has more strain. It has recently been shown that strain fields due to lattice mismatch extend from the QDs into surrounding GaAs matrix over distances ≥10 nm[26]. Such a strain field increases the concentration of vacancies and is likely to enhance the In/Ga inter-diffusion. In such a process, In atoms would replace Ga atoms in highly strained region around the QDs base. Therefore, the number of vacancies available for In/Ga inter-diffusion in (311)A samples are limited as compared to those existing in the (100) samples. This could explain the weaker blue shift of the (311)A QDs PL as a result of (nominally) defect-free inter-diffusion. However, this argument does not provide an answer regarding the large blue shift of QDs grown on (311)B plane.

(ii) the second argument that can be used is the smaller indium surface segregation and alloy disorder in the (311)A orientation than in the (311)B and (100) orientations. F. Guimaraes et al[19] performed a comprehensive study of the effects of surface structure and orientation on indium segregation process and alloy properties in InGaAs/GaAs quantum wells. They investigated the effects that segregation can have on the quantum well profiles and alloy quality for two non-equivalent (311)- and (100)-orientations. They obtained a larger activation energy (E_A = 3.14 eV) for the indium desorption from the (311)A surface as compared to E_A = 2.83 eV for (311)B surface. These experimental values of E_A are in agreement with the data obtained by Y. Kanter et al[27] and J. Reithmaier et al[28]. Actually, different activation energies for In desorption should be expected for the two chemically non-equivalent (311) surfaces. A double-dangling bond site exists for the elements of the group III on the A surface and a single-dangling bond site for the same group III elements on the (311)B surface[29]. Therefore, one would expect higher energy for In/Ga intermixing of In on the (311)A surfaces than for the (100) and (311)B.

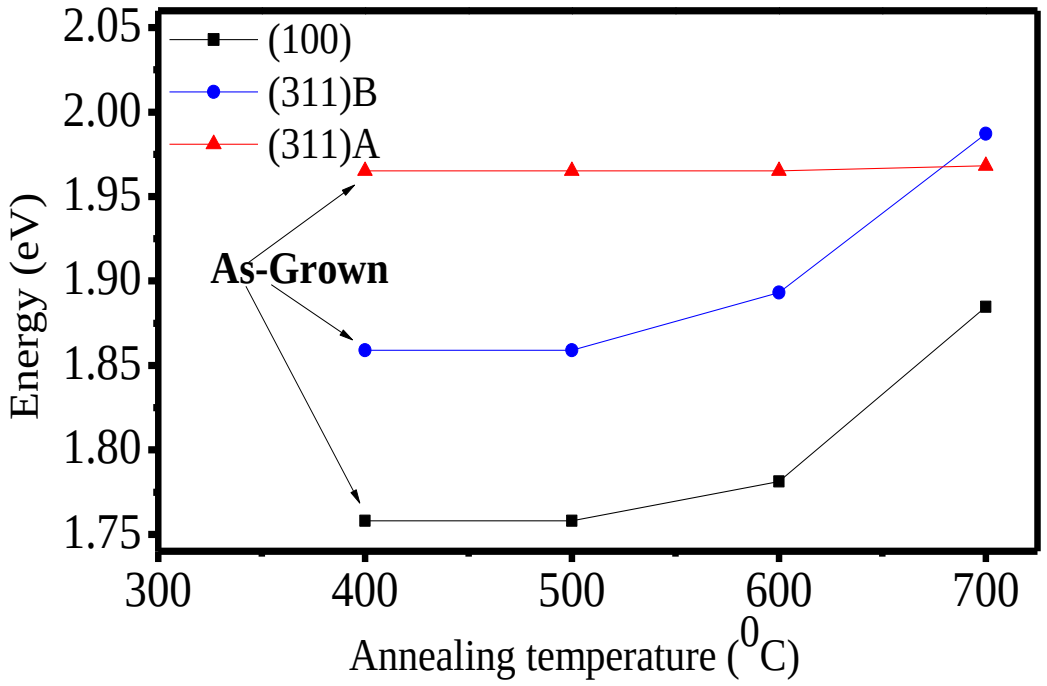

Figure 6.3: Photoluminescence peak energy position as a function of annealing temperature in the QDs samples grown on different substrate orientations. The data point at 400 ^{0}C corresponds to the sample without annealing.

6.2.2 TEMPERATURE DEPENDENCE OF PHOTOLUMINESCENCE: A COMPARISON BETWEEN AS-GROWN AND ANNEALED InAlAs QDs

The temperature dependence of the PL spectra of as-grown and annealed samples at different annealing temperatures was also investigated for this set of InAlAs of QDs in order to understand the effect of the annealing effect on their optical properties. The excitation energy was 2.62 eV (473 nm) and the excitation power was kept at 40mW.

In this section, the PL spectra of as-grown and 700 ^{o}C annealed QDs samples grown on (100), (311)A, and (311)B GaAs planes are recorded at different temperatures in order to gain insight on the change of the QD confinement during the annealing process that can be influenced by the substrate orientation. The reason why the 700 ^{o}C annealed samples were selected for these measurements is because at this

annealing temperature the inter-diffusion process has already taken place and a blue shift has occurred. The data is illustrated Figure 6.4.

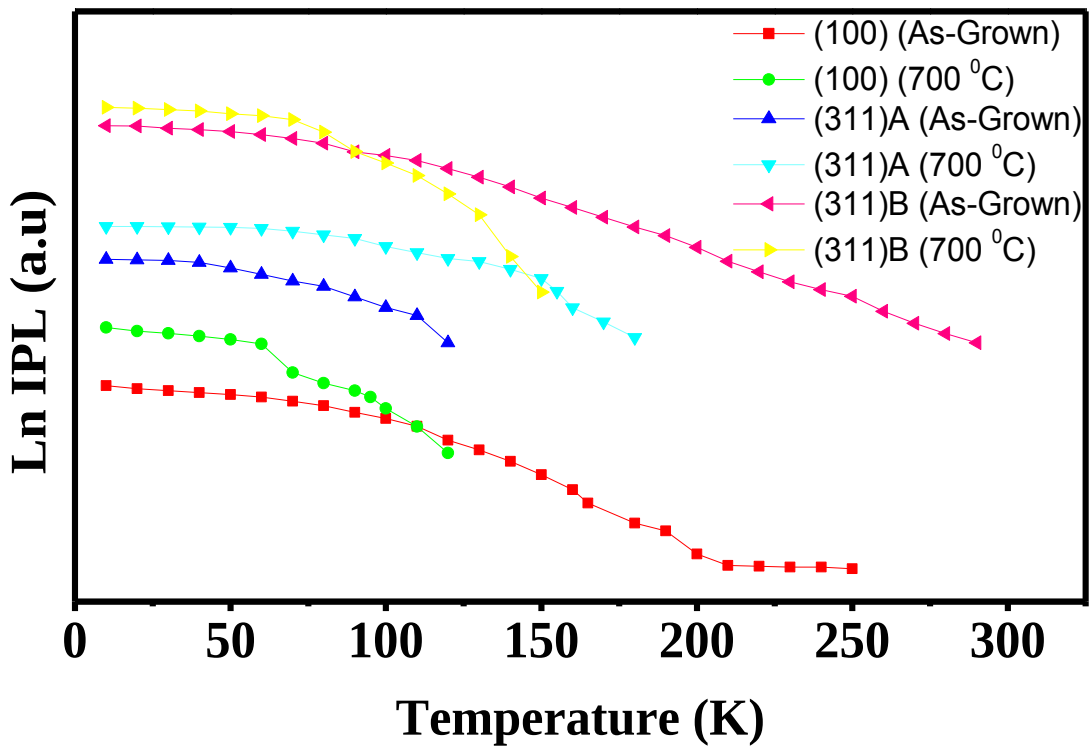

Figure 6.4: Integrated PL (IPL) intensities of as-grown (100), (311)B, and (311)A InAlAs QDs and thermally annealed QDs at 700 ^{0}C as a function of temperature.

The PL intensities in all samples decrease with increasing temperatures. The quenching of PL intensity of QDs with increasing the temperature can be attributed to the thermal escape of carriers from the QD ground state to higher state, to the wetting layer, or to the barrier.

As can be seen in Figure 6.4, the effect of annealing on the PL quenching is different for the various substrate orientations. For dots grown on (100) and (311)B planes, the PL signal extends to near room temperature, however, after annealing it quenches very rapidly at 120K and 150K, respectively. This faster quenching of PL in case of annealed samples could be due to the intermixing effect between the dots and the barrier which results in shallower confining potential and hence faster quenching with increasing temperature. It is worth pointing out that there is an enhancement of the PL intensity up to a temperature of ~100K as compared to as-grown samples in the same temperature range.

Although the PL intensity of (311)A as-grown QDs quenches faster and show worse thermal stability than as-grown (100) and (311)B QDs, annealed (311)A QDs display a better thermal stability than annealed (100) and (311)B QDs, especially in the temperature range from 80 to 190K. However, the rate of quenching of the PL from annealed (311)A QDs is slower than that of the PL of annealed (100) and (311)B QDs. It is believed that this phenomenon may due to the absence (or very small) intermixing for dots grown on (311)A plane.

At higher annealing temperatures, the QD composition and the effective size are altered due to significant material interdiffusion. The confining energy for holes and electrons are defined by the QD size and composition. When annealing cause intermixing between the QDs and surrounding matrix, these energies are modified. This results in a shift of the QD PL emission to higher energies and alters the confining energy. The (311)A QDs samples show no change at higher annealing temperatures. Thus, the carriers are better confined, and it is not surprising to observe that the carriers are less thermalized with temperature, and the integrated PL intensity is sustained up to higher temperatures, as shown in Figure 6.4.

The variation of integrated PL intensities versus temperature has been presented as well in the Arrhenius coordinates that permit to estimate the activation energies for PL thermal decay in different temperature regions (see figure 6.5).

These curves are fitted by using the formalism described in references[30-32]

$$I(T) = \frac{I(0)}{\left[1 + c_1 \exp(-E_1 / KT) + c_2 \exp(-E_2 / KT)\right]} \qquad (6.1)$$

Where I(T) and I(0) are the PL intensity at T, and PL intensity at the low-temperature limit, respectively. c_1 and c_2 are constants, E_1 and E_2 are thermal activation energies, and K is the Boltzman constant.

For proper fitting, one needs to assume two thermally activated processes characterized by E_1 and E_2. The E_1 and E_2 are reported in Table 6.2. The activation energy E_1 is derived from the slopes of the straight-line portion of the curves in the high temperature region.

The values of E_1 for as-grown (100) and (311)B are much higher than annealed samples. The decrease of E_1 with increasing annealing temperature can be interpreted as mostly from a reduction in the depth of the confining potential caused by interdiffusion of In and Ga atoms during annealing. On other hand, E_1 of (311)A does not change after annealing, which is expected due to the lower In segregation in this plane as explained above.

Activation energy E_2 of all samples, determined by curve fitting, is in the range ~4–18 meV. The activation energy E_2 could be attributed to trapped excitons or carriers thermalizing from localized regions resulting from potential fluctuation in the QDs[24] or thermal excitation of excitons from localized QDs states followed by capture of exciton by defects present in the samples[32].

Table 6.2: Arrhenius's parameters for the temperature dependence of the total integrated PL peak intensity for as-grown and annealed QDs grown on different GaAs substrate orientations.

Growth Plane	E_1 (meV)	E_2 (meV)
(100) As-Grown	156	4.4
(100) Annealed	42	3.9
(311B) As-Grown	120	8.4
(311)B Annealed	82	6.7
(311)A As-Grown	29	18
(311)A Annealed	24	16

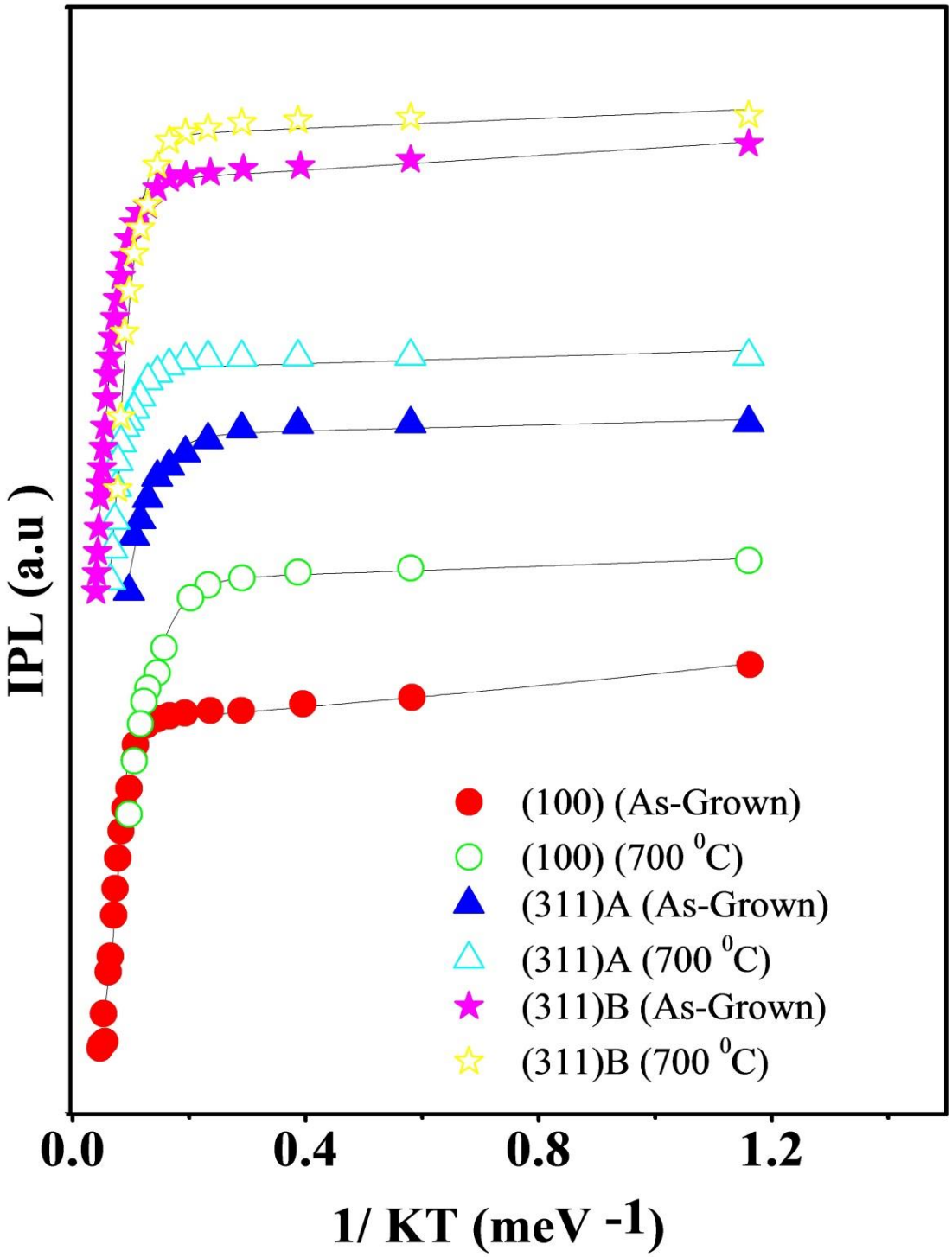

Figure 6.5: Integrated PL (IPL) intensities of as-grown (100), (311)B, and (311)A InAlAs QDs and thermally annealed QDs at 700 ^{0}C as a function of inverse temperature.

The PL peak energy as a function of sample temperature is shown in Figure 6.6, and fitting curves are plotted (solid lines) using the Varshni equation.

The variation of the PL peak position with temperature of bulk semiconductors can be attributed to the effects of lattice stretching and electron-lattice interaction. The fast red-shift of the PL peak with increasing temperature in QDs system had previously been observed, and mainly had been attributed to the redistribution of carriers amongst QDs with different sizes[33-35].

The scattered data in Figure 6.6 are the experimental results, and the solid curves are fittings obtained by shifting the bulk InAlAs band gap along the energy axis using the empirical Varshni equation[36].

$$E_g(T) = E_g(0) - \frac{\alpha T^2}{T + \beta}$$

Where α (eV/K) is a constant, β is the Debye temperature, $E_g(0)$ is the band-gap energy at 0 K, and T is the measured temperature. The constant values used for the fitting procedure shown in Figure 6.6 are based on Reference 37.

As-grown InAlAs QDs grown on (100), and (311)B (Figure 6.6 a and b) show a faster red shift than the Varshni's relation of bulk InAlAs band gap. This unusual temperature dependence is a characteristic of QDs. This fast red shift of (100) and (311)B QDs PL compared to (311)A QDs and bulk semiconductor can be explained by the larger inhomogeneous distribution and higher density of QDs on (100) and (311)B substrates than on (311)A. This has been discussed in the previous chapter.

From Figure 6.6 a and b it can be seen that the peak energies of annealed (100) and (311)B QDs show a redshift with increasing temperature with a rate basically identical to the InAlAs bulk material.

The slower rate of red shift of peak energies of annealed samples compared to as-grown ones could be explained by the homogenization of dot sizes caused by the annealing effect since the FWHM of PL at 10K decreased by 80 and 78 mev for (100) and (311)B QDs, respectively after annealing. It is well known that the FWHM of the PL peak is due to inhomogeneous broadening from QD size distribution.

This can be explained as follows. The Varshni equation describes the bandgap change in a single dot. When the temperature increases, the electrons with lower

binding energy escape from smaller QDs easily to larger-size QDs, lower-energy QDs. This results in the larger QDs having the dominant PL intensity. This explanation is further confirmed by the trend of FWHM with temperature of as-grown and annealed samples (see Figure 6.7).

The behavior of FWHM with temperature of as-grown (100) and (311)B QDs samples is anomalous, and could be due to fluctuation of sizes and high dot density, where dot-dot coupling would occur. However, for annealed QDs the FWHM increases monotonously with temperature as expected from uncoupled QDs.The uncoupling of QDs is due to the effect of annealing which results in more homogeneous dots.

S. Suraprapapich et al[24] have also reported a deviation from the Varshni's equation for as-grown InAs QDs system grown on (100) GaAs substrate. The quenching temperature of PL in annealed samples occur at a lower temperature (at around 100 K) compared with as-grown InAs QDs due to the smaller confinement potential barrier. It is worth pointing out that the PL energy follows Varshni's equation before the quenching of the PL signal occurs.

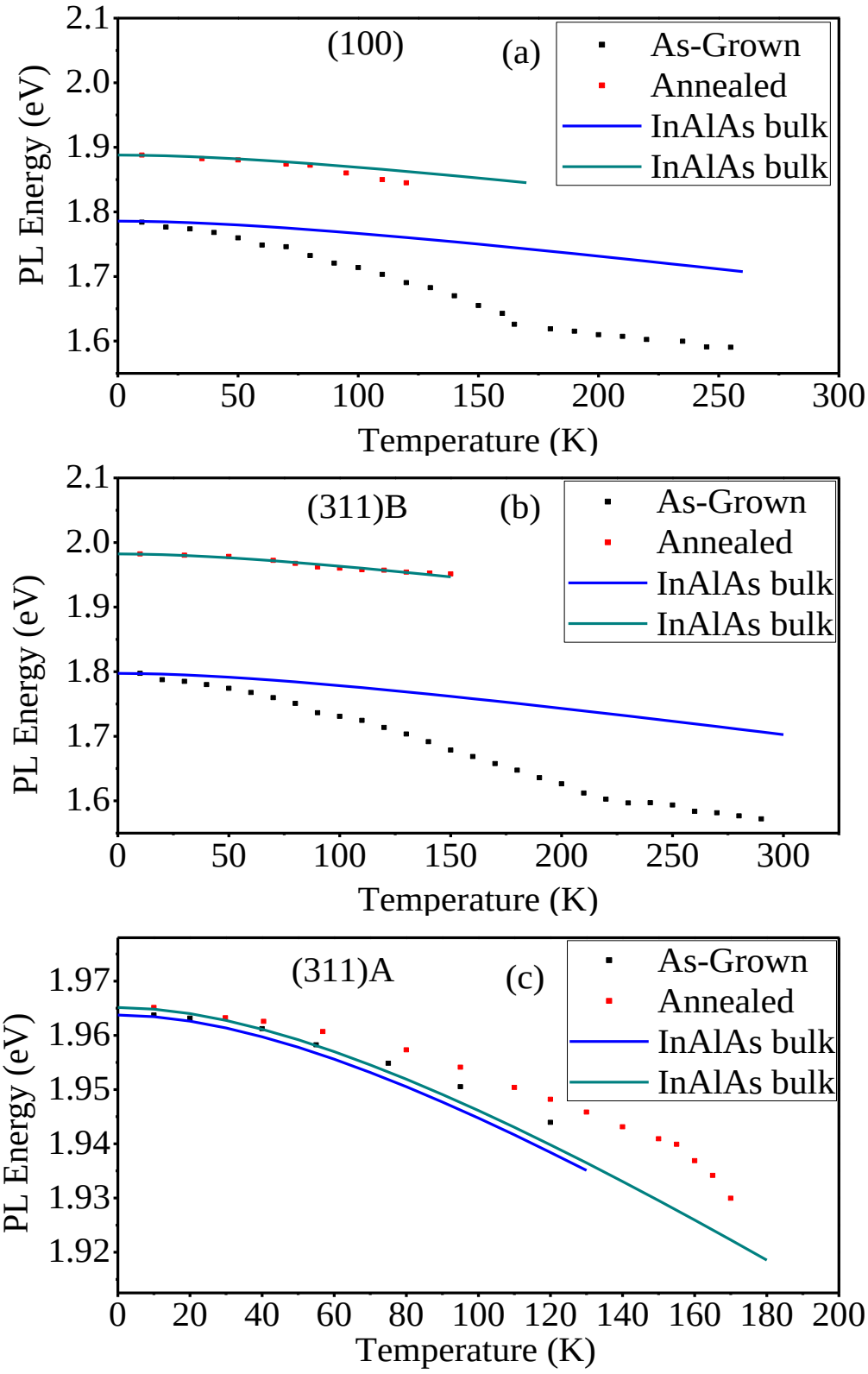

Figure 6.6: The temperature-dependence curves of the PL peak energies of as-grown and 700 ^{0}C annealed InAlAs QDs samples grown on different GaAs substrate orientations (a) (100), (b) (311)B and (c) (311)A. The solid lines are fitted using the Varshni equation.

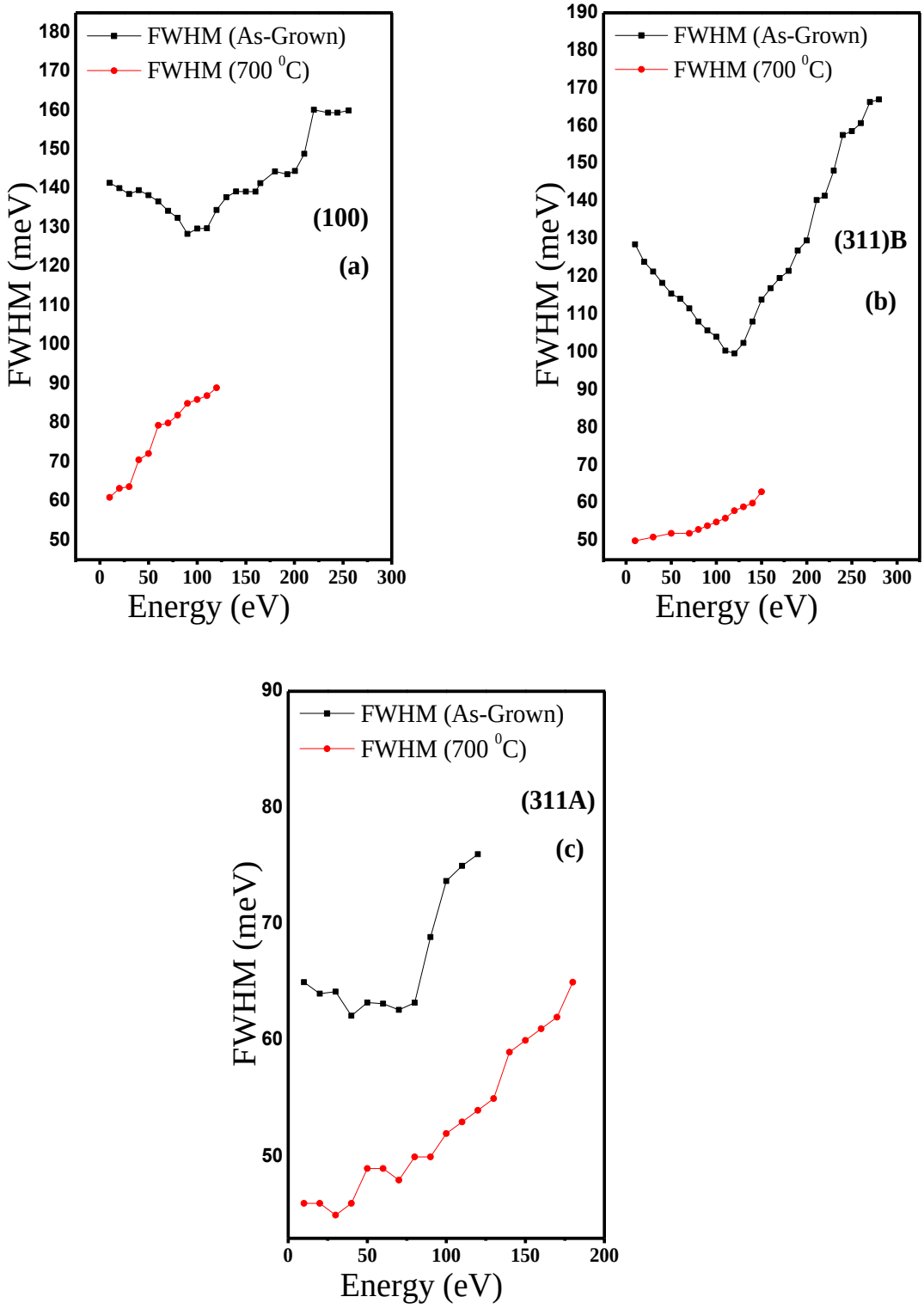

Figure 6.7: FWHM of PL spectra as a function of temperature for the as-grown and annealed InAlAs QD samples grown on various GaAs substrate orientations: (a) (100), (b) (311)B, (c) (311)A.

6.3 CONCLUSION

Large blue shift has been observed after thermal annealing of (311)B and (100) InAlAs/GaAlAs QDs. In contrast a very small blue shift was observed from (311)A QDs. This is explained by the smaller size of QDs, smaller strain, and lower In segregation from (311)A orientation. The temperature - PL intensity characteristics from the samples annealed at 700 ^{0}C show that the rates of PL quenching observed in QDs grown on (311)B and (100) planes are faster than those of as-grown samples. Annealed QDs grown on (311)A plane show better and improved thermal stability than as-grown one, and this observation could be explained by the intermixing effect that affects the carrier confining potential.

REFRENCES

[1] J. M. Garcia, G. Medeiros-Ribeiro, K. Schmidt, T. Ngo, J. F. Feng, A. Lorke, J. Kotthaus, and P. Petro, Applied Physics Letters, 71, 2014 (1997).

[2] H. Lee, R. R. Lowe-Webb, W. Yang, and P. Sercel, Applied Physics Letters, 71, 2325 (1997).

[3] G. Shi, P. Jin, B. Xu, C. M. Li, C. X. Cui, Y. L. Wang, X. L. Ye, J. Wu, and Z. G.Wang, Journal of Crystal Growth, 269, 181 (2004).

[4] N. Perret, D. Morris, L. Franchomme-Fosse, R. Cote, S. Fadard, and V. Aimez, J. Beauvais, Physical Review B, 62, 5092 (2000).

[5] C. Lobo, R. Leon, S. Fafard, and P. G. Piva, Applied Physics Letters, 72, 2850 (1998).

[6] Z. Y. Zhang, P. Jin, C. M. Li, X. L. Ye, X. Q. Meng, B. Xu, F. Q. Liu, and Z. G. Wang, Journal of Crystal Growth, 253, 59 (2003).

[7] Z. Zaâboub, B. Ilahi, L. Sfaxi, and H. Maaref, Materials Science and Engineering C, 28, 1002 (2008).

[8] W. Jiang, H. Xu, B. Xu, X. L. Ye, J. Wu, D. Ding, J. Liang, and Z. Wang, Journal of Crystal Growth, 212, 356 (2000).

[9] I. J. Guerrero Moreno, T. V. Torchynska, and J. L. Casas Espinola, Physica E, 51, 37 (2013) .

[10] K. Watanabe, N. Koguchi, and Y. Gotoh, Japanese Journal of Applied Physics, 39, L79 (2000).

[11] N. Koguchi, and K. Ishige, Japanese Journal of Applied Physics, 32, 2052 (1993).

[12] N. Koguchi, K. Ishige, and S. Takahashi, Journal of Vacuum Science & Technology B, 11, 787 (1993).

[13] T. Manoa, T. Kurodaa, K. Mitsuishia, M. Yamagiwaa, X. Guob, K. Furuyab, K. Sakodaa, and N. Koguchia, Journal of Crystal Growth, 301, 740 (2007).

[14] S. Sanguinetti, K. Watanabe, T. Kuroda, F. Minami, Y. Gotoh, and N. Koguchi, Journal of Crystal Growth, 242, 321 (2002).

[15] S. Malik, C. Roberts, M. Pate, and R.Murraya, Applied Physics Letters, 71 (14), 1987 (1997).

[16] H. Parka, J. Kima, J. Yoona, J. Sonb, D. Leec, H. Ryua, M. Jeona, and J. Leema, Journal of Crystal Growth, 300, 319 (2007).

[17] S. J. Xu, X. C. Wang, C. H. Wang, W. J. Fan, J. Jiang, X. G. Xie, and S. J. Chua, Applied Physics Letters, 72, 3335 (1998).

[18] S. Martini, A. A. Quivy, A. Tabata, and J. R. Leite, Journal of Vacuum Science & Technology B, 18, 1991 (2000).

[19] F. E. G. Guimara˜es, D. Lubyshev, V. A. Chitta, and P. Basmaji, Materials Science and Engineering: B, 35, 318 (1995).

[20] R. Leon, S. Fafard, P. Piva, S. Ruvimov, and Z. Liliental-Weber, Physical Review B, 58, R4262 (1998).

[21] S. Burkner , M. Baeumler , J. Wagner, E. Larkins, W. Rothermund, and J. Ralston, J. Applied Physics Letters,79, 6818 (1996).

[22] A. Kosogov, P. Werner, U. Gosele, N. Ledentsov, D. Bimberg, V. Ustinov, A. Egorov, A. Zhukov, P. Kop'ev, N. Bert, and Z. Alferov, Applied Physics Letters, 69, 3072 (1996).

[23] G. Zhang, and M. Pessa, Applied Surface Science, 75, 274 (1994).

[24] S. Suraprapapich, Y. Shen, Y. Fainman, Y. Horikoshi, S. Panyakeow, and C. Tu, Journal of Crystal Growth, 311, 1791 (2009).

[25] S. Sanguinetti, G. Chiantoni, E. Grilli, M. Guzzi, M. Henini, A. Polimeni, A. Patane, L. Eaves, and P. Main, Europhysics Letters, 47 (6), 701, (1999).

[26] L. Selen, L. Ijzendoorn, M. de Voigt, and P. Koenraad, Physical Review B, 61, 8270 (2000).

[27] Y. Kanter, A. Gutakovsky, A. Fedrow, M. Revenko, S. Rubanov, and S. Stenin, Thin Solid Films, 63, 497 (1988).

[28] J. Reithmaier, H. Richert, H. Schlotterer, and G. Weimann, Journal of Crystal Growth, 111, 407 (1991).

[29] W. Wang, E. Mendez, Y. lye, B. Lee, M. Kim and G. Stillman, Journal of Applied Physics, 60, 1834 (1986).

[30] S. M. Olsthoorn, F. A. J. M. Driessen, A. P. A. M. Eijkelenboom, and L. J. Giling Journal of Applied Physics 73 (1 l), 7798 (1993)

[31] A. Nishikawa, Y. G. Hong, and C. W. Tu, Journal of Vacuum Science & Technology B, 22, 1515 (2004).

[32] H. D. Sun, S. Calvez, M. D. Dawson, J. A. Gupta, G. C. Aers, and G. I. Sproule, Applied Physics Letters, 89, 101909 (2006).

[33] M. Hjiri, F. Hassen, H. Maaref, B. Salem, G. Bremond, O. Marty, J. Brault, M. Gendry, Physica E, 17, 180 (2003).

[34] Z. Xu, Z. Lu, X. Yang, Z. Yuan, B. Zheng, J. Xu, W. Ge, Y. Wang, J. Wang, L. Chang, Physical Review B, 54, 11528 (1996).

[35] R. Songmuang, S. Kiravittaya, M. Sawadsaringkarn, S. Panyakeow, O. G. Schmidt, Journal of Crystal Growth, 251, 166 (2003).

[36] Y. P. Varshni, Physica (Amsterdam) 34, 149 (1967).

[37] C. Loboa, and R. Leon, Journal of Applied Physics, 83, 4168 (1998).

CHAPTER 7: OPTICAL PROPERTIES OF Ga1-xInxNyAs1-y/GaAs DOUBLE QUANTUM WELL STRUCTURES GROWN ON (100), (311)A, and (311)B GaAs SUBSTRATES

This chapter reports on the effect of nitrogen incorporation on the optical properties of GaInAs/GaAs double quantum well (DQWs) grown on different GaAs substrate orientations, namely (100), (311)A, and (311)B.

7.1 INTRODUCTION

In most III–V materials, substituting an element for a smaller atomic radius one would reduce the lattice constant and increase the bandgap. However, Weyers et al.[1] found that replacing a fraction of arsenic atoms in GaAs with a certain amount of nitrogen reduces its bandgap. These so-called dilute nitrides, formed by alloying a small amount of nitrogen into arsenide- or phosphide-V semiconductor materials, are a new class of semiconductor compounds with new properties. III–V–N dilute nitrides are promising candidates for the fabrication of many optical components such as 1.3 μm lasers, solar cells, and heterojunction bipolar transistors[2]. For example, the band gap of GaAs can be reduced to the ideal value of ∼1 eV needed for the fourth junction of next generation solar cells while keeping lattice-matching to GaAs/Ge substrates[3].

Telecommunication edge-emitting lasers operating in the long-wavelength range are based on the conventional GaInAsP alloys grown on InP substrates. However, an alternative could be the important GaInAsN alloys grown on GaAs, which have many advantages over GaInAsP including cost. In addition, GaInNAs/GaAs materials system has potential in opening a new era of semiconductor lasers because high-performance and low-cost long-wavelength (1.3–1.6 μm) Vertical Cavity Surface Emitting Lasers (VCSEL) can potentially be realized[4-6]. For example, T. Kitatani et al[7] have fabricated a 1.3 μm GaInNAs/GaAs single-quantum-well VCSEL with high characteristic temperature (T_0) of 215 K under pulsed operation from 20°C to 80°C.

The GaInNAs combined with GaAs or other wide-gap materials is very promising to overcome the poor temperature characteristics of conventional long wavelength laser diodes. A GaInNAs/GaAs quantum well (QW) has high band discontinuity, i.e. over 350 meV, in the conduction band, which is three times larger than that of InGaAsP/InP[8].

M. Kondow et al[9] reported the successful CW operation of a GaInNAs edge emitting laser laser diode at room temperature and demonstrated high temperature performance with a characteristic temperature of 127 K.

7.2 LITERATURE REVIEW OF EPITAXIAL GROWTH OF GaInNAs ON (100) AND HIGH INDEX GaAs SUBSTRATES

Several groups were successful in growing good quality GaInAsN quantum wells (QWs) on the conventional (100) GaAs plane by different growth techniques.

H. Xin et al[10] have grown GaInNAs/GaAs multiple quantum wells (MQWs) with different N composition on semi-insulating (100) GaAs substrate by gas-source molecular beam epitaxy. A nitrogen radical beam source was used to incorporate N into GaInAs layers. High resolution X-ray rocking curves measurements indicated that the N composition in GaInNAs layer was increased from 0.009 to 0.03 with increasing N flow rate. Photoluminescence (PL) measurements showed that the PL wavelength red shifts with increasing N composition in GaInNAs layer. For a 7-period $Ga_{0.7}In_{0.3}N_{0.02}As_{0.98}$/ GaAs MQWs, a room temperature PL peak at 1.3 μm wavelength has been successfully observed. It is worth adding that the band offset ΔEc for $Ga_{0.7}In_{0.3}N_yAs_{1-y}$/GaAs increases from 0.26 eV to 0.56 eV with increasing N concentration from 0% to 3%.

The incorporation probability of N into GaAs is quite low, due to the large mismatch in both atom size and electronegativity between N and As. The ionic radii and electronegativity of As and N are 1.2 Å, and 0.75Å, and 2.18 and 3.0[11], respectively. From the material growth point of view GaAsInN alloy is a challenging material to grow because the end alloy constituents have different crystal structures: InGaN is wurtzite (hexagonal) and InGaAs is zinc blende (cubic). This results in a large miscibility gap in the alloys[12].

The growth of semiconductor layers and structures strongly depends on the substrate surface atomic arrangement. Thus, different substrate orientations exhibit various surface statuses, leading to different amount of nitrogen incorporation[13]. Using

unconventional high-index substrates could lead to improvement of nitrogen incorporation to reach higher wavelength easily without optical degradation. Irrespective of the polarity, both (311)A and (311)B GaAs substrates are effective for the improvement of the PL lifetime as demonstrated by X. Han et al[14]. They reported that the carrier lifetime in (311)B GaAsN is the longest as compared to GaAsN grown on other planes. High density of steps present on the high-index substrate surfaces are believed to contribute in reducing defects in the GaAsN epilayers[14], as was reported previously for layers grown on vicinal GaAs substrates[15,16]. Moto et al.[16,17] reported that a change of surface orientation of a substrate lead to an increase in PL efficiency of GaNAs grown on misoriented GaAs substrates due to some reduction of deep level transitions, impurity incorporation and alloy fluctuations.

There are a few reported but contradictory studies of Ga(In)AsN on high-index substrates. In the following the most important results in literature will be presented. Saito et al[18] studied the nitrogen doping on (311) A/B and (811) A/B GaAs substrates grown by metalorganic vapour phase epitaxy (MOVPE). As compared with the (100) surface, it was found that the N incorporation was enhanced in (n11)A surfaces and reduced in (n11)B surfaces.

J. Ibanez et al[19] have used photoreflectance (PR) and high-resolution x-ray diffraction (HRXRD) measurements to assess the composition of $In_xGa_{1-x}As_{1-y}N_y$ thin films ($x \sim 20\%$, $y \sim 3\%$) grown by molecular beam epitaxy (MBE) on GaAs substrates with different surface orientations (100), (511), (411), (311), and (111) planes. The aim of their work was to investigate the effect of substrate orientation on the incorporation of N and In into thin films. A combined analysis of the PR and HRXRD data showed that incorporation of In in (In, Ga) (As, N) depends very little on substrate orientation and does not differ much from that of (In, Ga)As. In particular, they found that the N content in (n11) samples (N=3, 4, 5) is lower than for the (100) and (111) samples.

X. Han et al[14] used PL and HRXRD to study N incorporation in undoped GaAsN/GaAs double heterostructures (DHs) which were grown on (311)A, (311)B, and (100) semi-insulating GaAs substrates over the temperature range of 420^0C –

460 ^{0}C by using a chemical beam epitaxy (CBE) system. The optimum growth temperature and annealing conditions for enhanced crystal quality were found to depend on the substrate orientation and surface polarity. Pronounced enhancement in N incorporation was achieved for the (311)B orientation. X. Han et al[20] have also reported that the nitrogen incorporation in different planes increased following this sequence: [N] (211)B > [N] (311)B > [N] (511)B > [N] (100) > [N] (511)A > [N] (311)A > [N] (211)A.

A. Arnoult et al[21] investigated the effects of substrate orientation and growth temperature on nitrogen incorporation in GaAsN grown by MBE on (100) and on As(B)- and Ga(A)-rich (111) substrates. The amount of nitrogen incorporated in GaAsN as a function of substrate temperature was measured by SIMS. The amount of nitrogen incorporated, N, was found to depend strongly on surface orientation. It is higher for (111)A than for (100), and lower for (111)B. Their results also show that, for each orientation [N] depends on the growth temperature. For the (111)A case, N is found to be relatively constant which would indicate an efficient and stable N incorporation for the temperature range 520 ^{0}C to 580^{0}C. On the contrary, for (111)B, N is reduced by about a factor of three when the growth temperature changed from 520^{0}C to 580^{0}C.

S. Blanc et al[22,23] studied the effect of the growth conditions on optical properties of GaAsN and GaInAsN/GaAs QWs grown on (111)A and (111)B substrates by MBE. N incorporation has been found to be highly dependent on the substrate orientation, substituting more efficiently As atoms in (111)A surface than in (111)B one. The influence of growth conditions and In concentration on the optical properties of (111)A and (111)B oriented GaAsN QWs has been determined. The orientation that provide good optical efficiency for both GaAsN layers and GaInAsN/GaAs QWs is the Ga-rich (A) face, i.e. (111)A. The very poor emission of Ga(In)AsN QWs grown on (111)B indicates the presence of defects within the material. The (111)B QWs emission is not affected by the concentration of indium. However, it was reported that the (111)A QWs PL efficiency is dependent on the indium content; it increases for In contents up to 15%, and deteriorate for In>15%.

T. Ishizuka et al[24] performed systematic measurements of PL spectra, PL-decay profiles and PR spectra in GaInNAs/GaAs single QWs grown on GaAs substrates with three offset angles of 2^0, 10^0 and 15^0 toward (111)A by MOVPE. It was found that an increase in the offset angle leads to an increase in the incorporation efficiency of N into the GaInNAs layer.

A. Moto et al[16] reported on the effect of substrate orientation on PL properties for GaNAs grown by MOVPE using dimethylhydrazine as a nitrogen precursor. The PL spectra showed improvements in the emission intensity and linewidth, and a decrease in a deep level emission when the surface tilted from (100) to (411)A towards (111)A. These improvements could be due to a reduction of deep level defects, residual impurity incorporations, and spatial fluctuations in nitrogen concentration in high index planes. The investigation of the peak position as a function of excitation intensity revealed a blue shift for the (100) but not for the higher-index substrates. In addition to the improved optical quality, (411)A showed a relatively large redshift in band gap for increased nitrogen concentrations.

7.3 EXPERIMENTAL RESULTS AND ANALYSIS

7.3.1 STUDY OF THE INFLUENCE OF THE SUBSTRATE ORIENTATION ON THE OPTICAL PROPERTIES OF $In_{0.36}Ga_{0.64}As_{1-1-y}N_y$/GaAs QUANTUM WELLS GROWN BY MBE ON (100), (311)A AND (311)B GaAs PLANES.

This section will report on the optical properties of $In_{0.36}Ga_{0.64}As_{1-y}N_y$ DQWs grown on the conventional (100) and high index planes, namely (311)A and (311)B GaAs substrates. The aim is to determine the optimal substrate orientation for the growth of these InGaAsN QWs.

The samples investigated in this work consist of three sets of $In_{0.36}Ga_{0.64}As_{1-y}N_y$/GaAs QWs.

Set 1: $In_{0.36}Ga_{0.64}As$ grown on (100), (311)A, and (311)B GaAs planes with 0% N (control samples).

Set 2: $In_{0.36}Ga_{0.64}As_{0.99}N_{0.01}$ QWs grown on (100), (311)A, and (311)B GaAs planes with a nominal 1% N.

Set 3: $In_{0.36}Ga_{0.64}As_{0.98}N_{0.02}$ QWs grown on (100), (311)A, and (311)B GaAs planes with a nominal 2% N.

All samples are grown by MBE on semi-insulating GaAs substrates. All the growths were carried out under the same conditions for comparison purposes. The growth rate of GaAs and AlAs were 0.5 μm and 0.538μm per hour, respectively. The As:Ga beam equivalent pressure ratio as measured by an ionization gauge was approximately 12:1. The nitrogen was generated using a commercial radio-frequency plasma source. The samples were rotated during the growth in order to improve the uniformity of the layers. The basic double QW structure consists of the following layers starting from the substrate: 100 nm GaAs buffer layer, 100 nm $Al_{0.35}Ga_{0.65}As$ barrier, 100 nm GaAs barrier, 7 nm $In_{0.36}Ga_{0.64}As_{1-y}N_y$ QW, 100 nm GaAs barrier, 4 nm $In_{0.36}Ga_{0.64}As_{1-y}N_y$ QW, 100 nm GaAs barrier, 100 nm $Al_{0.35}Ga_{0.65}As$ barrier, 10 nm GaAs cap layer. The growth temperatures of the $In_{0.36}Ga_{0.64}As_{0.99}N_{0.01}$ QWs and for the rest of the structure were 450 ^{0}C and 600 ^{0}C, respectively. Low growth

temperature of nitride alloys is required in order to ensure a smooth two-dimensional (2D) growth mode. Growth temperatures above 480 ^{0}C[25] result in a bad morphology. The layer structure is shown in Figure 7.1.

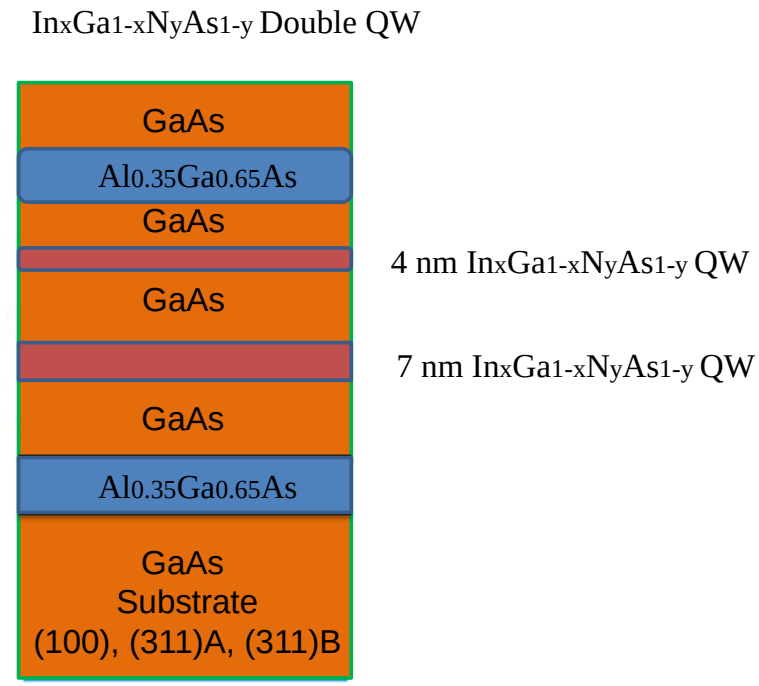

Figure 7.1: Schematics of the $In_xGa_{1-x}As_{1-y}N_y$ double QWs structures.

PL measurements were performed in a variable temperature (10-300 K) closed-cycle cryostat under the excitation of the 474 nm line of a diode laser. Signals from samples were detected by an InGaAs detector.

Figure 7.2 (a,b,c) show the PL spectra at 10 K for all orientations with nitrogen and without nitrogen. All samples show two PL features. Taking into consideration quantum confinement effect in the QW structures, the PL peak at the higher-energy side corresponds to the emission from the thin well (4nm), and the peak at the lower-energy side originates from the thick well (7nm).

The PL energy from the 4 nm (1.222 eV) and 7 nm GaInAs QW (~1.16 eV) control samples is shifted by more than 293 and 279 meV, respectively, with respect to the GaAs band gap (1.515 eV). This value of shift of PL energy by introducing 36% In

agrees with data reported in the literature[26,27]. The peak position, FWHM and the integral intensity have a strong dependence on the substrate orientation. The PL properties of these QWs are summarized in Table 7.1.

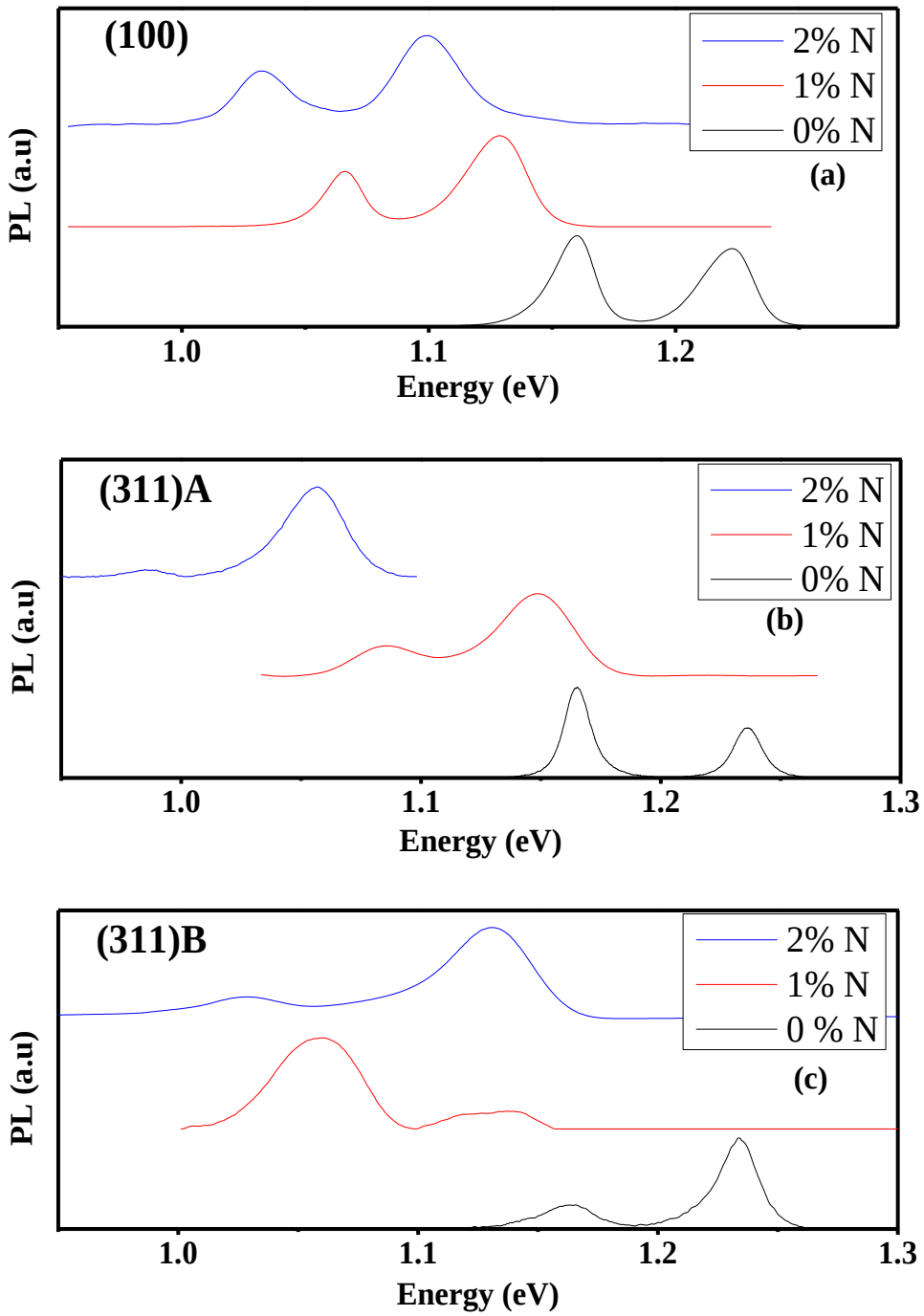

Figure 7.2: Low temperature photoluminescence spectra of $In_{0.36}Ga_{0.64}As_{1-y}N_y$ /GaAs with (y=0, 0.01, 0.02) double QWs grown on a) (100), b) (311)A, c) (311)B GaAs substrates. The data is normalized.

Table 7.1: Comparison of optical parameters of $In_{0.36}Ga_{0.64}As$ and $In_{0.36}Ga_{0.64}As_{1-y}N_y$ (x=1 and 2%) QWs grown on (100), (311)A and (311)B GaAs substrates.

Growth Plane	(100)	(100)	(311)A	(311)A	(311)B	(311)B
QW Thickness	4 nm	7 nm	4 nm	7 nm	4 nm	7 nm
PL peak energy (eV) of control sample with 0 % N	1.222	1.16	1.236	1.165	1.233	1.165
PL peak energy (eV) of sample with 1 % N	1.128	1.066	1.149	1.083	1.137	1.076
PL peak energy (eV) of sample with 2 % N	1.099	1.043	1.057	0.989	1.132	1.028
Shift of PL energy due to N incorporation (1%) (meV)	94	94	87	82	96	89
Shift of PL energy due to N incorporation (2%) (meV)	123	117	179	176	101	137
FWHM of control sample with 0% N (meV)	23	19	13	13	18	24
FWHM of sample with 1% N (meV)	27	19	32	25	38	29
FWHM of sample with 2% N (meV)	28	22	29	25	39	41

From the PL data, as expected the incorporation of nitrogen reduces the band-gap energy, i.e. shifts the PL energy to lower values for both QWs by an amount which depends on the substrate orientation (see Figure 7.3).

For the $In_{0.36}Ga_{0.64}As_{0.99}N_{0.01}$ samples, the red shift of PL energy due to 1% nitrogen incorporation is comparable for all the QWs grown on the three different planes. For

$In_{0.36}Ga_{0.64}As_{0.99}N_{0.02}$ samples, it is clear from Table 7.1 that QWs grown on (311)A plane show the highest red shift, while 7 nm QW grown on (100) plane and 4nm QW grown on (311)B show the lowest red shift. As shown in Table 7.1 the largest shift occurs for the 1% N 4nm QW grown on (311)B (96 meV) and 2% N 4nm QW grown on (311)A (179 meV). These results suggest that the (311)A plane provide enhanced incorporation of nitrogen as compared with the (100) and (311)B planes.

`

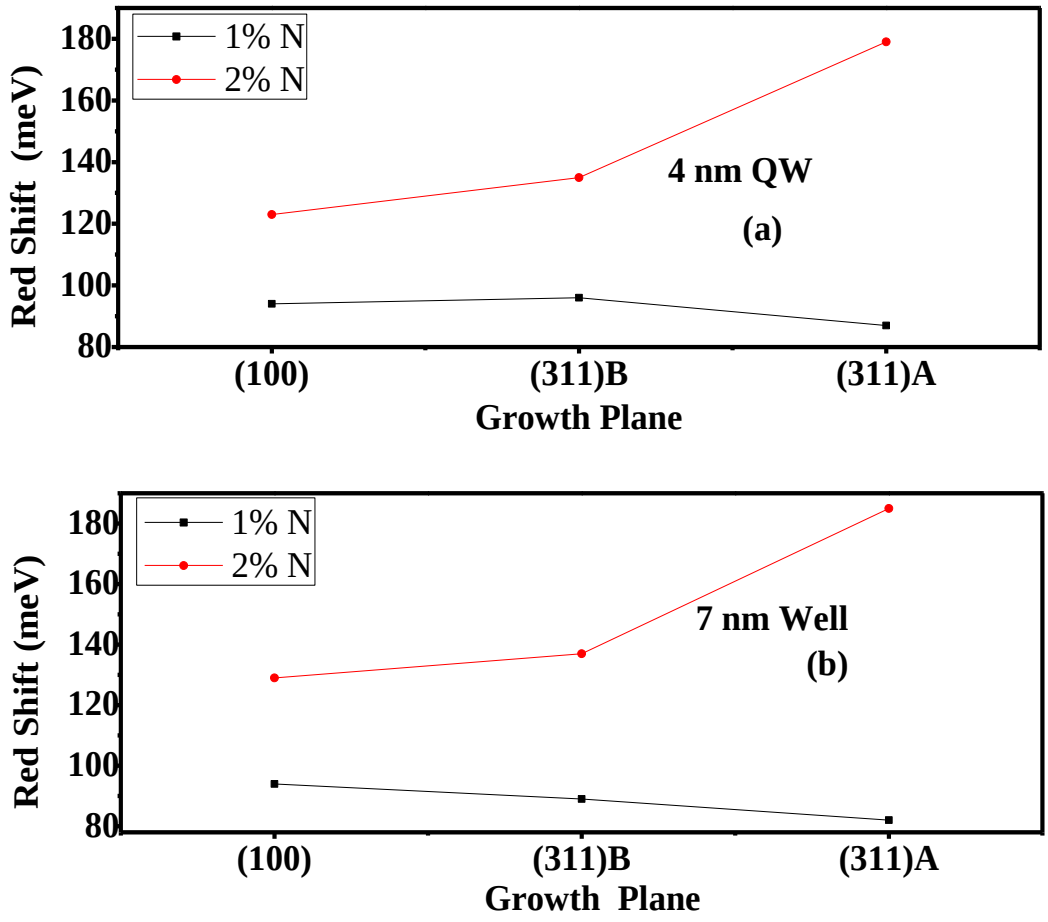

Figure 7.3: Shift of PL energy between InGaAs control samples and InGaAsN samples for (a) 4nm QW, (b) 7nm QW.

The values of PL energies from nitrogenated samples are comparable to values reported by A. Polimeni et al[28]. Polimeni et al have investigated $In_xGa_{1-x}As_{1-y}N_y$ /GaAs single QWs with different nitrogen percentages. The samples with (y=0.015, x=0.32) and (y=0.022, x=0.38) have PL energies at 10K of ~1 eV and ~0.9 eV, respectively.

This difference in N incorporation in QWs grown on different substrate orientations could be explained in light of atomic bonding geometries since the nitrogen atom replace the As atoms. The (n11)B surfaces consists of (100) terraces and (111) steps. The As atoms on the B steps are bonded with triple dangling bonds from Ga atoms, indicating that As atoms are difficult to be replaced by N atoms. On the other hand the (n11)A surface consists of (100) terraces and A-type steps. The As atoms on the A-type steps are bonded with single dangling bonds from the Ga atoms while those on the (100) terraces are bonded with double dangling bonds[18]. Figure 7.4 shows the atomic arrangement of the (n11)A and (n11)B surfaces.

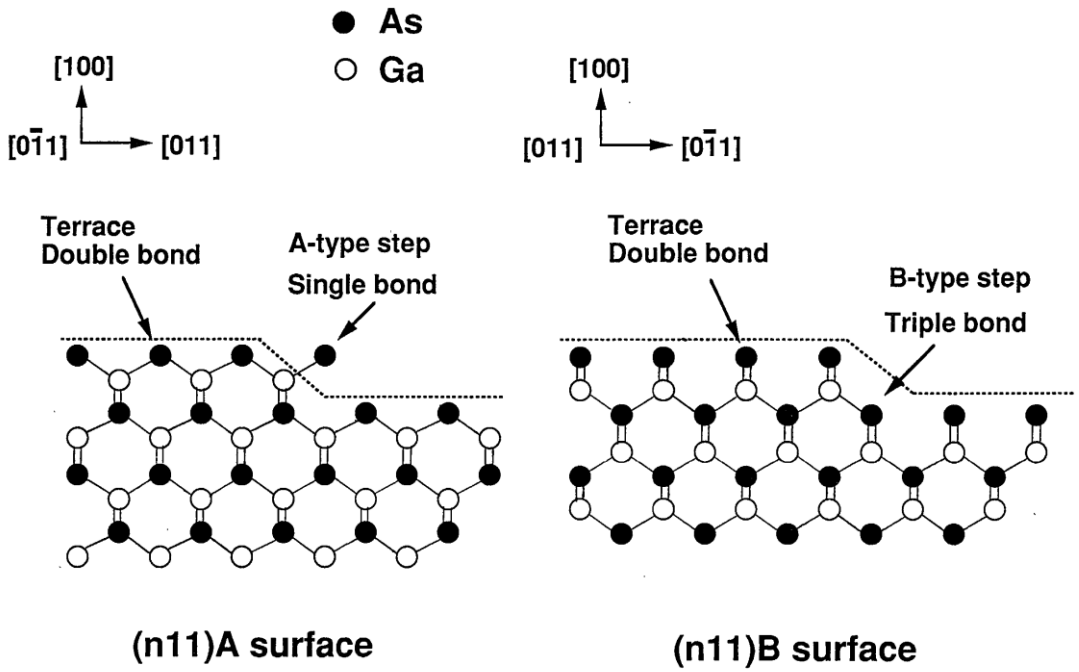

Figure 7.4: Atomic arrangements of the (n11)A and (n11)B surfaces[18]

.

Although the incorporation of nitrogen narrows the bandgap of InGaAs, it affects the PL intensity drastically. In this work the PL intensity decreases for all substrates with increasing nitrogen concentration. In fact the PL intensity quenches after incorporation of 2% N by nearly two order of magnitude, 50 times, and 30 times for QWs grown on (100), (311)B, and (311)A, respectively.

Polimeni et al[28] showed that the PL intensity is quenched by a factor of 7 and 130 upon increasing the nitrogen incorporation to 1.5% and 2.2%, respectively.

Earlier studies have pointed out that the incorporation of nitrogen into InGaAs increases the density of defects originating from compositional and structural inhomogeneities, and deteriorates the crystalline quality[29].

A correlation between the PL line width and nitrogen concentration is shown in Figure 7.5. The PL line width broadens with the increase of N incorporation. PL from nitrogenated QWs grown on (311)B show the highest FWHM among all planes.

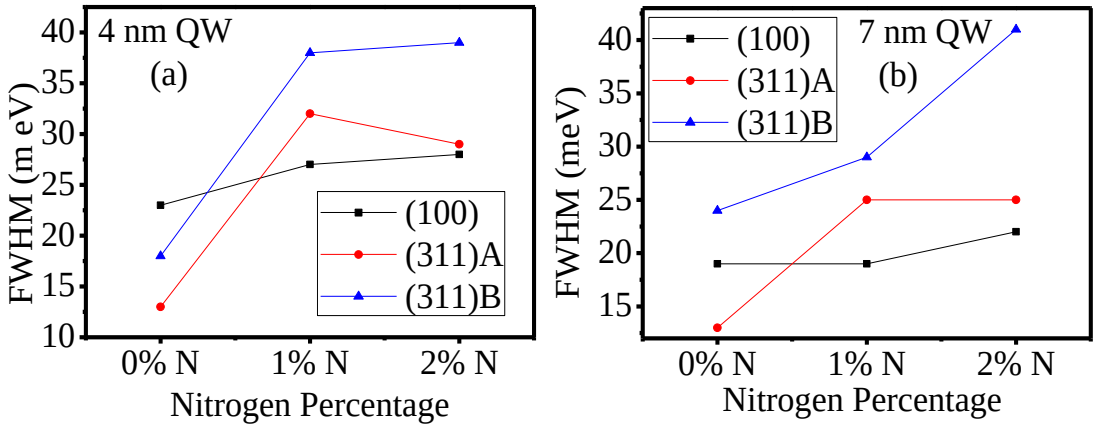

Figure 7.5: Effect of nitrogen incorporation on the FWHM for the three different growth planes (a) 4nm QW, (b) 7 nm QW.

The FWHM broadening phenomenon, which indicates an increase of the degree of compositional and structural disorder, is common in quaternary GaInAsN alloys and has been reported by several groups. M. Pinault and E. Tournie[25] showed that the FWHM increases from 12 meV for a GaInAs QW to 33 meV for a $GaInAs_{0.975}N_{0.025}$ QW, while S. Shirakata et al[30] observed that the FWHM increased from 9 meV for GaInAs QW to 16.5 meV for $GaInAs_{0.99}N_{0.01}$ QW. The lowest FWHM recorded for GaInAsN is 11 meV at 10K for samples grown by S. Shirakata et al[31] with 1% nitrogen.

7.3.2 CORRELATION BETWEEN TRANSMISSION ELECTRON MICROSCOPY IMAGES AND FULL WIDTH AT HALF MAXIMUM OF PL SPECTA OF $In_{0.36}Ga_{0.64}As_{0.99}N_{0.01}$/GaAs DOUBLE QUANTUM WELLS.

It is well known that there is a direct correlation between structural and optical properties of QWs, and therefore cross-section transmission electron microscopy (TEM) was used in order to compare the structural properties of the (100), (311)A and (311)B QWs.

The FWHM of the PL spectra is a very important parameter that gives an indication of the quality of the samples and uniformity of epitaxial growth.

Figure 7.6 illustrates the dependence of the FWHM on the growth plane for different samples. It is found that the FWHM of the PL spectra of the QWs grown on (311)B GaAs plane is the highest among all different QWs.

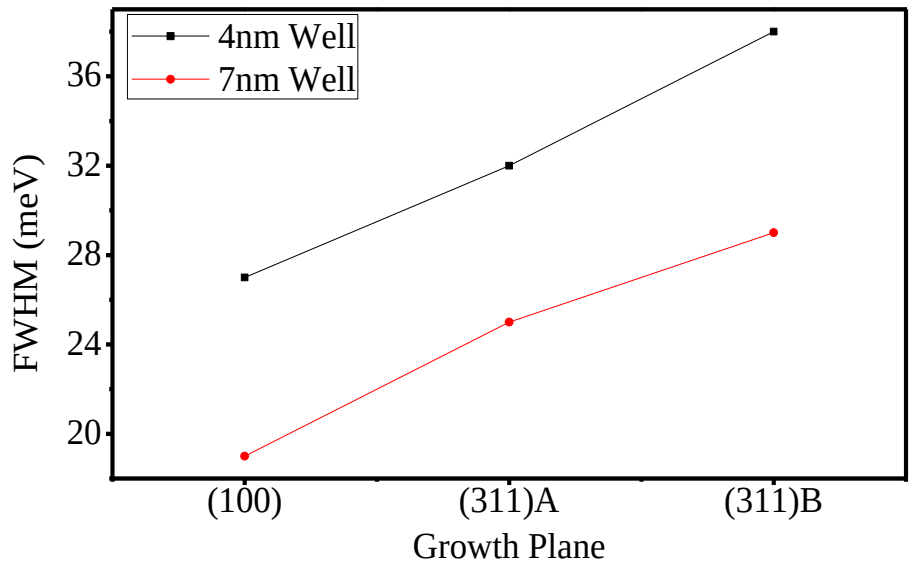

Figure 7.6: Dependence of FWHM of 4 nm and 7nm QWs with the substrate orientation.

The largest FWHM of the PL signal obtained from (311)B could be explained by the low interfacial and crystalline quality as can be seen from TEM images in Figure 7.7 for QWs grown on (100), (311)B and (311)A.

From the TEM images, the thicknesses of the two QWs (4nm and 7nm) grown on (311)A and (100) substrate are very uniform, and the interfaces are very flat as compared to those of the (311)B samples. (311)B QWs samples show some thickness variations and a lateral period of undulation. Undulations ("ripples") of the (311) B interfaces could be associated with the beginning of the growth. However, it doesn't seem that there is some thickness variation associated with this long-range undulation.

To further investigate the origin of different PL spectrum of QWs grown on different planes High Angle Annular Dark Field (HAADF) and energy dispersive X-ray (EDX) characterization were performed on different DQW samples. The EDX results of the indium composition measurement in different planes shows similar ratio of 20%, and 15% for 4nm and 7nm QW, respectively. The distribution of In inside both thin and thick wells over all planes (Figure 7.8) shows similar profile. However the HAADF images of the (311)B DQWs shows variation of contrast observed inside the wells compared to other planes and this is linked to the inhomogeneity of the indium distribution in this plane (see figure 7.9) The inhomogeneity of In distribution inside (311)B QW could accounts for the lower PL efficiency and higher FWHM of quantum wells grown on this plane.

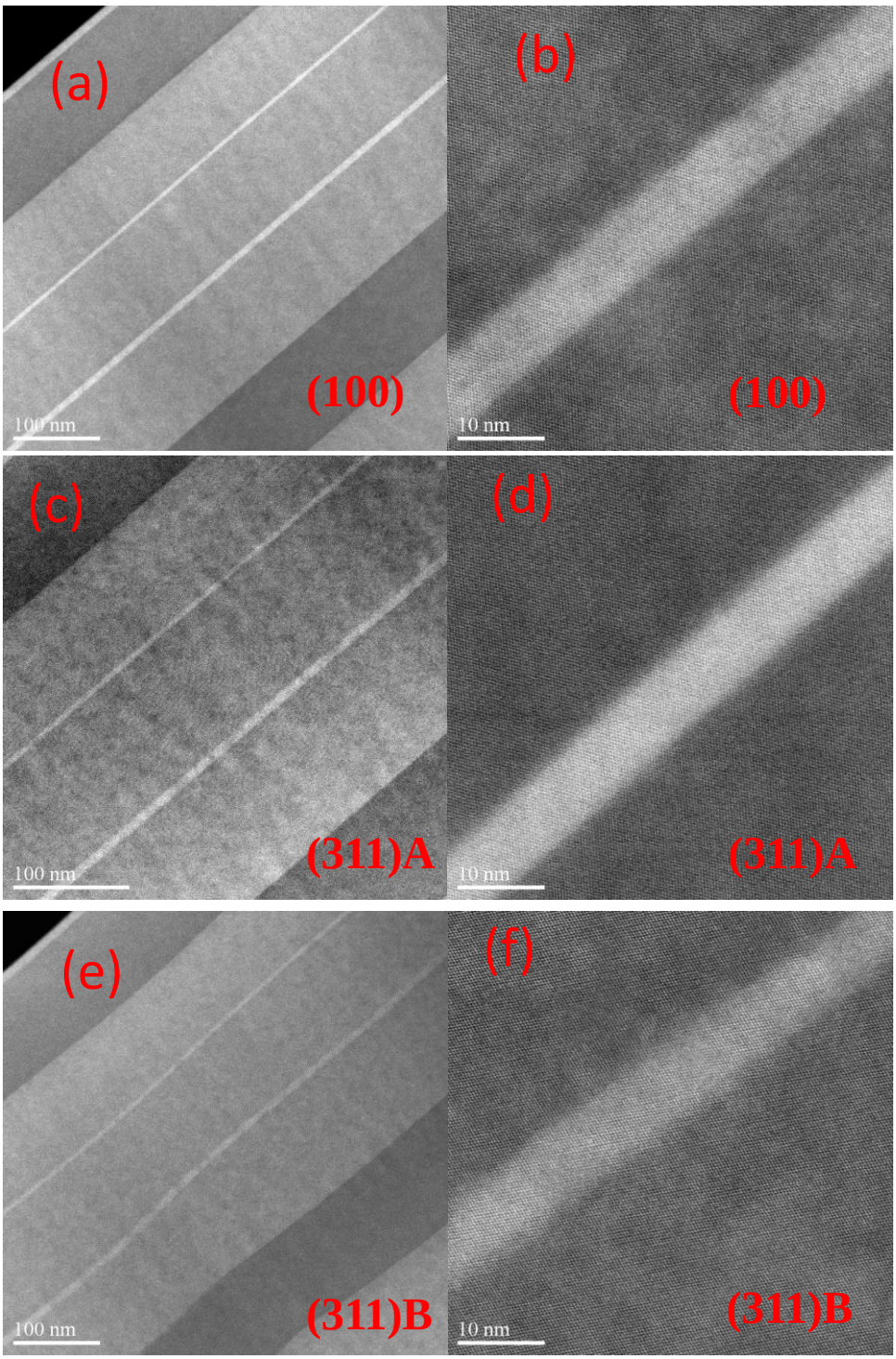

Figure 7.7: TEM cross sectional images of $In_{0.36}Ga_{0.64}As_{0.99}N_{0.01}$/GaAs (a) double QWs grown on (100) plane, (b) 7nm thick QW grown on (100) plane; (c) double QWs grown on (311)A plane, (d) 7nm thick QW grown on (311)A plane, (e) double QWs grown on (311) B plane, (f) 7nm thick QW grown on (311)B plane.

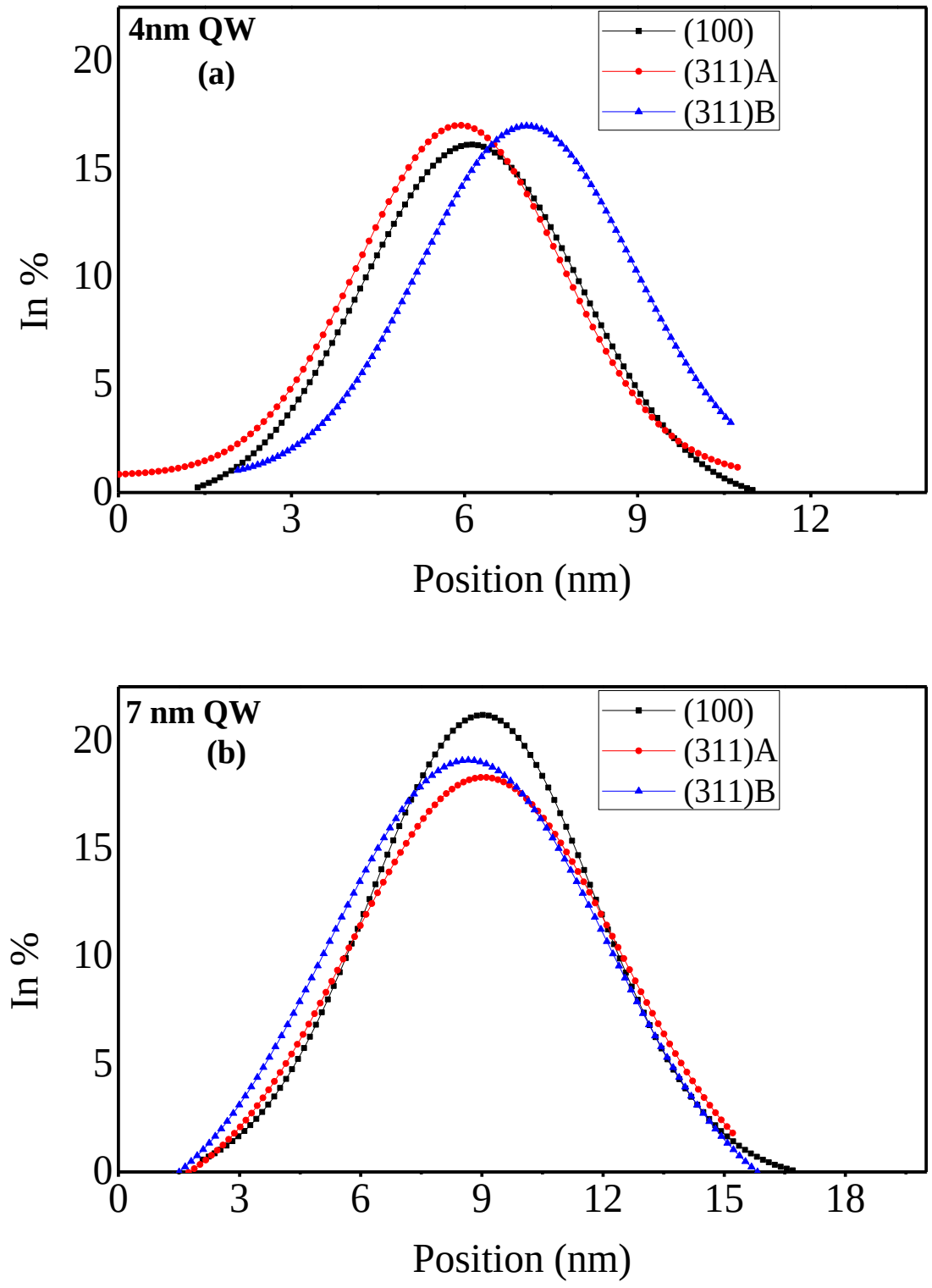

Figure 7.8: EDX profiles of In composition (a) 4nm QWs grown on (100), (311)A, (311)B planes, (b) 7nm QW grown on (100), (311)A, (311)B planes.

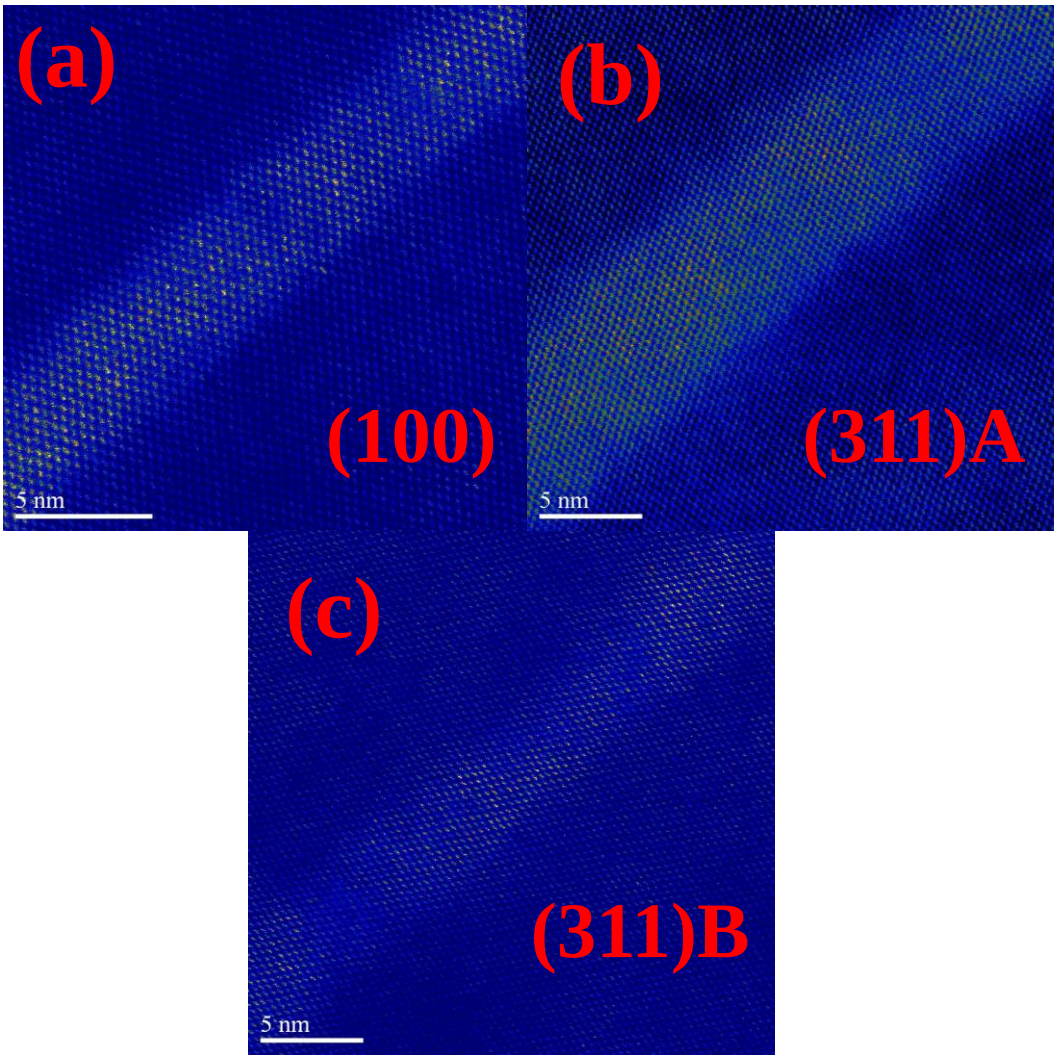

Figure 7.9: HAADF of 7nm $In_{0.36}Ga_{0.64}As_{0.99}N_{0.01}$/GaAs QW grown on (a) (100) plane, (b) (311)A plane, (c) (311)B plane.

7.3.3 TEMPERATURE DEPENDENCE OF PHOTOLUMINESCENCE: A COMPARISON AMONG $In_{0.36}Ga_{0.64}As_{1-y}N_y$/GaAs DOUBLE QWs GROWN ON DIFFERENT SUBSTRATES WITH DIFFERENT NITROGEN PERCENTAGE.

7.3.3.1 INTRODUCTION AND LITERATURE REVIEW OF TEMPERATURE DEPENDENCE OF PL FOR $InGaAs_{1-y}N_y$/GaAs QWs.

The PL energy of most crystalline semiconductors decreases monotonically as a function of temperature, following the conventional Varshni's formula. However, the PL energy of GaAsN or GaInAsN usually shows an anomalous temperature dependence behavior. The PL energy versus temperature plot shows red- blue - red shift as the temperature increases. This behavior, referred to as S-shape, is attributed to exciton localization effect due to local fluctuation of nitrogen concentration[32].

L. Grenouillet et al[33] reported an anomalous temperature dependence of the PL spectrum of a 7 nm $Ga_{0.72}In_{0.28}N_{0.028}As_{0.972}$ /GaAs single QW. The PL peak energy exhibited an inverted S-shape dependence with temperature. Below 100K, the PL integrated intensity showed temperature dependence similar to that of amorphous semiconductors. The observed anomalous behavior is explained by a strong localization of carriers at low temperatures that could be induced by the presence of nitrogen.

F. Laia et al[29] studied the temperature dependence of optical properties of InGaAsN/GaAs single QWs grown by MBE with N contents varying from 0% to 5.3% by PL. The evolution of the peak positions of InGaAs/GaAs samples were in agreement with the empirical Varshni model. However, pronounced temperature-dependent S-shaped peak positions were observed in PL spectra while increasing nitrogen concentration.

M. Pinault et al[34] have compared the PL-Temperature dependent properties of relatively high N-content (~0.04– 0.05) GaInAsN QWs with those of GaAsN and GaInAs QWs. Strong carrier localization is observed only in GaInAsN QWs with localization and delocalization temperatures at around 50K and 150 K, respectively.

The localization is stronger in the less PL efficient GaInAsN QWs. Their results demonstrate that the simultaneous presence of both In and N, and not solely of N, is responsible for carrier localization.

7.3.3.2 EXPERIMENTAL RESULTS

The temperature dependence of the PL spectra of $In_{0.36}Ga_{0.64}As_{1-y}N_y$/GaAs double QWs samples grown on different substrate orientations was also investigated in order to understand the effect of the nitrogen incorporation on their optical properties. The excitation energy was 2.62 eV (473 nm) and the excitation power was kept at 40mW.

In this section, the PL spectra of $In_{0.36}Ga_{0.64}As_{1-y}N_y$/GaAs double QWs samples grown on different substrate orientations are recorded at different temperatures in order to gain some insight on the influence of the substrate orientation on the change of the mechanism of recombination due to nitrogen incorporation. The data is illustrated in Figures 7.10, 7.11, and 7.12 for (100), (311)A, (311)B, respectively.

The PL emission from the control GaInAs/GaAs QWs samples is characterized by a symmetric and Gaussian-like shape. However, the emission from dilute nitride samples is characterized by asymmetric peaks with a low energy tail, which is more prominent in (311)B QWs. These tail states might originate from recombination of localized excitons trapped in potential fluctuations due to local fluctuations in nitrogen concentration.

A typical broad and non-symmetric PL spectrum is usually observed in GaAsInAs alloys due to recombination of photo-generated carriers trapped by fluctuating potential (localized states) induced by non-uniform insertion of the nitrogen atoms into GaAs crystal.

The mechanism responsible for the carrier localization observed in InGaAsN QWs is still under debate. However, this could be due to the possible occurrence of composition modulations and/or strong QW width fluctuations in InGaAsN QWs samples[35,36].

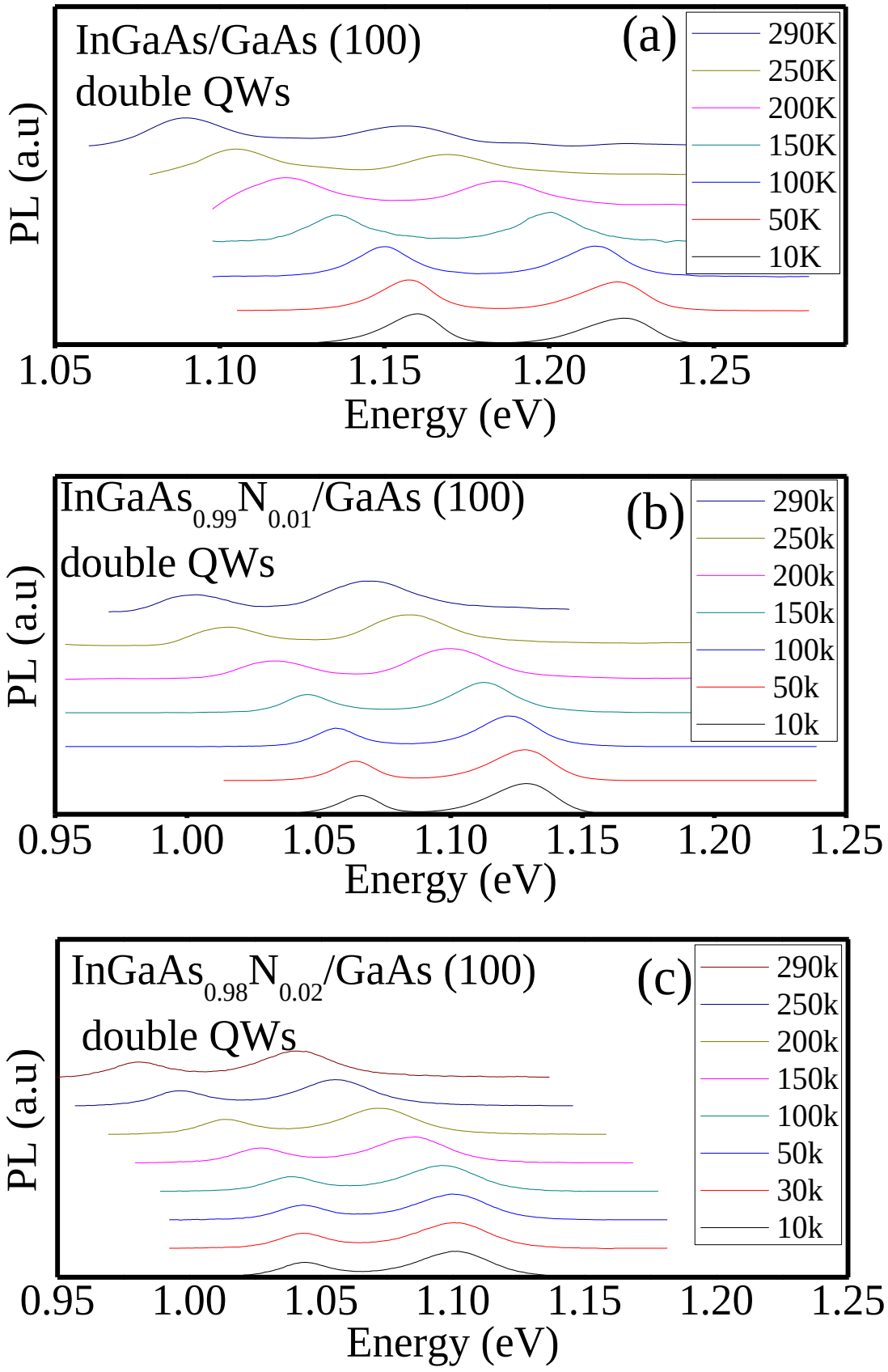

Figure 7.10: Temperature dependent PL of $GaInAs_{1-y}N_y/GaAs$ DQWs grown on (100) GaAs plane: (a) y=0, (b) y=0.01, (c) y=0.02.

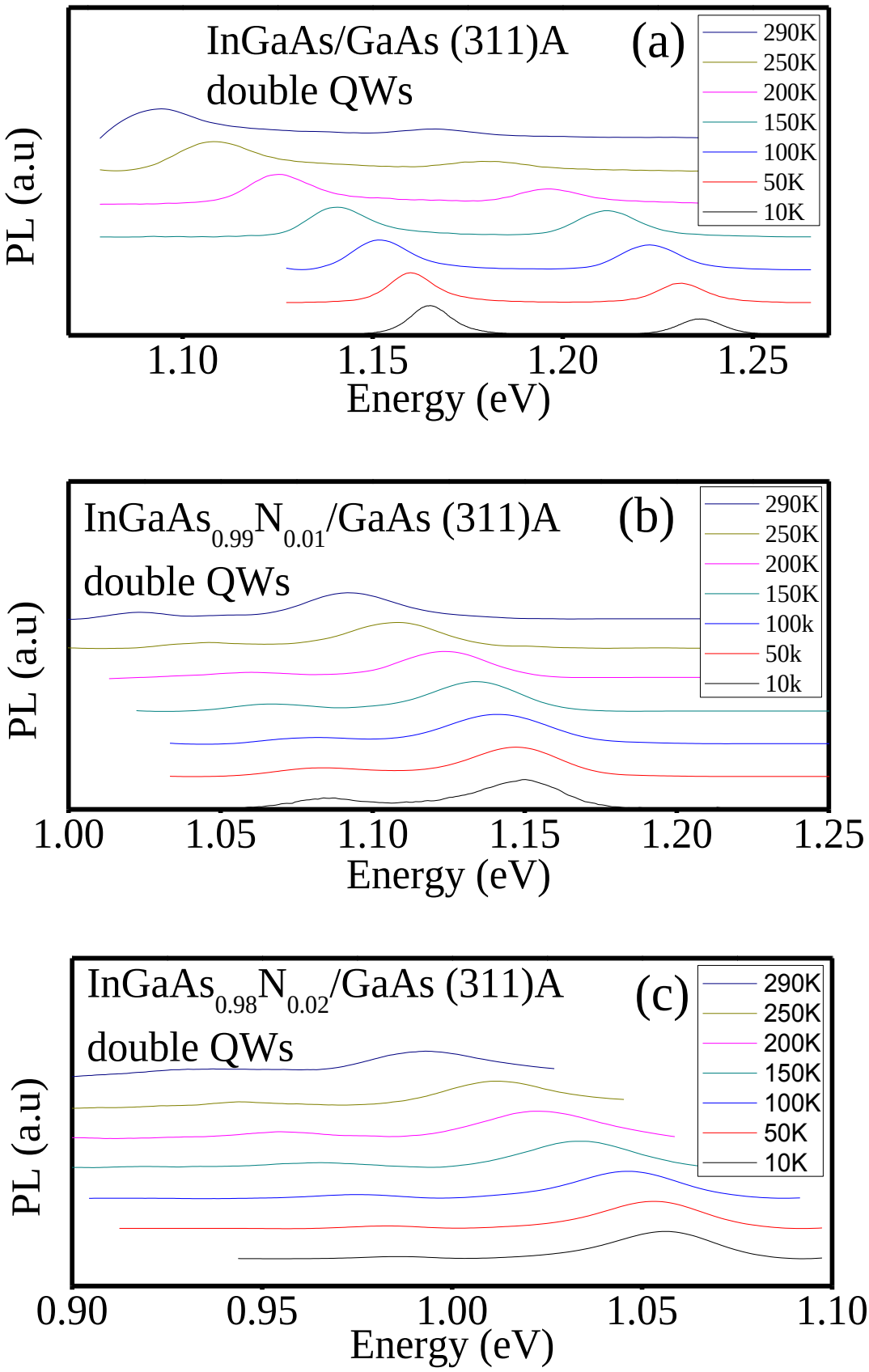

Figure 7.11: Temperature dependent PL of $GaInAs_{1-y}N_y/GaAs$ DQWs grown on (311)A GaAs plane: (a) y=0, (b) y=0.01, (c) y=0.02.

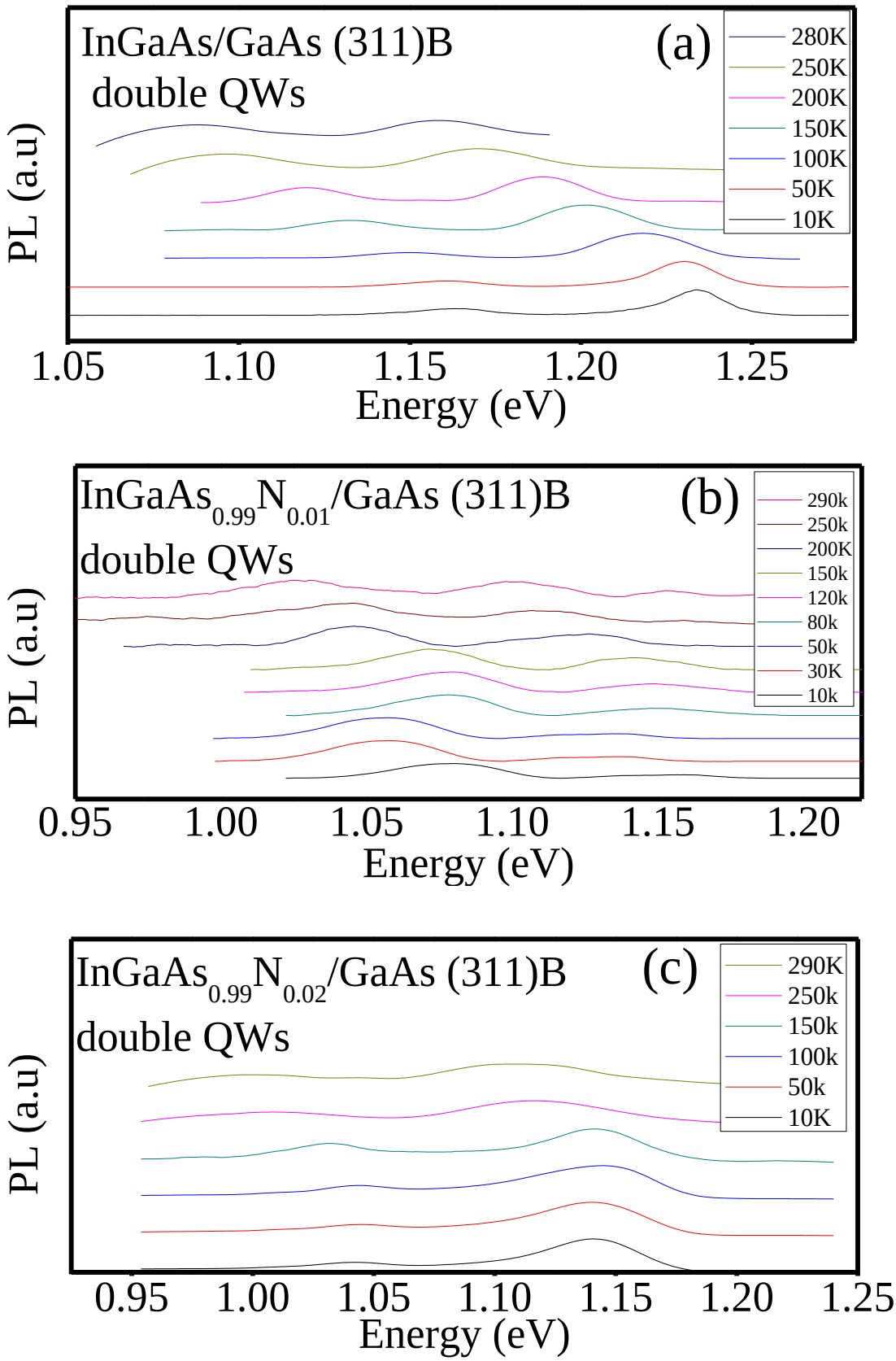

Figure 7.12: Temperature dependent PL of $GaInAs_{1-y}N_y/GaAs$ DQWs grown on (311)B GaAs plane: (a) y=0, (b) y=0.01, (c) y=0.02.

The PL energy of the 4 and 7 nm QWs at 10 K and 290 K for all planes are presented in Table 7. 2. A striking point in PL data is the fact that the redshift (ΔE) between 10 K and 290 K of the PL peak energy is noticeably lower for (311)B nitrogenated double QWs than (311)B control GaInAs/GaAs double QWs.

Table 7.2: PL energy of 4 and 7 nm $In_{0.36}Ga_{0.64}As_{1-y}N_y$/GaAs QWs at 10K and 290K.

Growth Plane	(100)		(311) A		(311) B	
QW Thickness	4nm	7nm	4nm	7nm	4nm	7nm
10K PL energy of GaInAs (eV)	1.222	1.16	1.236	1.165	1.233	1.165
290K PL energy of GaInAs (eV)	1.153	1.089	1.165	1.093	1.157	1.085
ΔE for GaInAs QW (meV)	70	74	73	75	76	80
10K PL energy of $In_{0.36}Ga_{0.64}As_{0.99}N_{0.01}$ (eV)	1.128	1.066	1.149	1.083	1.137	1.076
290K PL energy of $In_{0.36}Ga_{0.64}As_{0.99}N_{0.01}$ (eV)	1.067	1.004	1.092	1.022	1.098	1.024
ΔE for $In_{0.36}Ga_{0.64}As_{0.99}N_{0.01}$ QW (meV)	62	68	57	61	39	55
10K PL energy of $In_{0.36}Ga_{0.64}As_{0.98}N_{0.02}$ (eV)	1.099	1.043	1.057	0.989	1.132	1.028
290K PL energy of $In_{0.36}Ga_{0.64}As_{0.98}N_{0.02}$ (eV)	1.041	0.979	0.993	0.928	1.095	0.978
ΔE for $In_{0.36}Ga_{0.64}As_{0.98}N_{0.02}$ QW (meV)	60	63	63	60	36	49.9

The PL peak energy of the 4 and 7 nm GaInAs/GaAs QWs on all planes shows a monotonic decrease with increasing temperatures following the Varshni relation.

The temperature dependence of the peak energy is depicted in Figure 7.13 (a,b,c) for GaInAs grown on (100), (311)A, and (311)B, respectively. The red solid line represents the fitting results using the empirical Varshni model[37].

$$E(T) = E(0) - \frac{\alpha T^2}{\beta + T}$$

Where E(0) is the band gap energy at zero Kelvin, α and β are empirical parameters related to the material. The optimum fitting parameters, α and β, are given in Table 7.3 for all orientations. Reported values for the (100) are also added at the end of the table for comparison purposes.

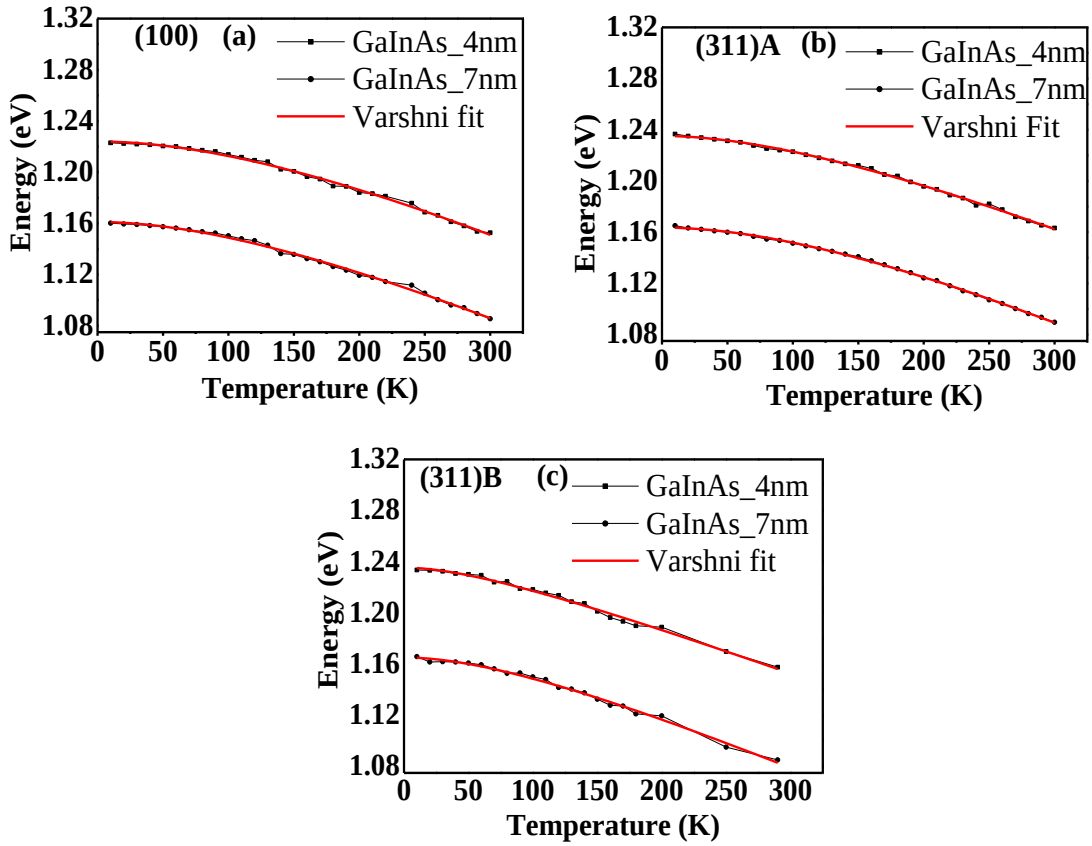

Figure 7.13: Evolution of PL peak energies as a function of temperature for 4 and 7nm GaInAs QWs grown on (a) (100) plane, (b) (311)A plane, and (c) (311)B plane. The solid red lines are fitting curves using the empirical Varshni model.

Table 7.3: Fitting parameters of Varshni empirical formula for 4 and 7nm GaInAs double QWs grown on different substrate orientations.

QW Thickness (Plane)	E_0 (eV)	α (10^{-4} meV/K)	β (K)
4 nm (100) QW	1.223	5.67	401
4 nm (311)A QW	1.235	4.8	293
4 nm (311)B QW	1.235	3.71	105
7 nm (100) QW	1.161	5.24	327
7 nm (311)A QW	1.163	5.61	379
7 nm (311)B QW	1.165	4.53	174
(100) GaInAs (Reference 29)	1.187	5.8	310
(100) GaInAs (Reference 34)	1.271	6	350
9 nm (100) GaInAs (Reference 38)	1.232	6.8	480

The dependence of PL peak energy on temperature for $InGaAs_{1-y}N_y/GaAs$ samples is plotted in Figure 7.14, and Figure 7.15 for samples with N=0.01, and 0.02 respectively. Obviously, the band gap evolution as a function of temperature of (311)B QWs does not follow the behavior of a semiconductor band gap predicted by Varshni's formula. The solid lines represent the fitting results using empirical Varshni's model. The fitting for (311)B samples is done only in the high temperature range (100-300)K.

The PL peak energy of (311)B $InGaAs_{1-y}N_y/GaAs$ QWs in (10-100)K temperature region exhibits a successive red-blue-red shift as shown in the plot of PL peak energy versus temperature.

The departure of the temperature dependence of the PL peak energy from its usual monotonic behaviour as described by Varshni's formula due to the regular carriers thermalization provides strong evidence that the carriers at low temperatures (<~100 K) are localized. With increasing the temperature, the PL peak energy decreases monotonically with temperature. This unusual behaviour of PL energy with temperature is commonly attributed to the localized behavior of the excitons due to the N-induced potential fluctuations.

Band tail states in the density of states[39] originating from the defects introduced by nitrogen is responsible for this unusual temperature dependence shape of emission energy, which only appears for (311)B QWs. At low temperatures, the excitons are localized in the band-tails in the density of states. The exciton localization in the III-V-N alloys is caused by potential fluctuations at the band edges due to the perturbations of the conduction band induced by local fluctuation in nitrogen concentration (i.e non uniform nitrogen insertion). This behavior has been discussed previously in section 2.8.3 which dealt with the properties of dilute nitride alloys.

As the temperature is increased, the excitons gain sufficient thermal energy to overcome small potential barriers and become trapped in the adjacent lower-energy states where they recombine with reduced emission energies (red-shift). As the temperature increases further to a T_{trans} value (~30 K), excitons start to gain sufficient thermal energy and the occurrence of a blueshift is observed due to the transfer of thermally activated excitons from lower- to higher-energy band-tail states. At T_{deloc} the excitons have become almost delocalized and from then on the emission energy as a function of temperature follows a Varshni-like shape.

T_{trans} and T_{deloc} are defined as the temperature at which localized excitons begin to transfer to higher energy localized states and the temperature at which delocalization of the carriers is complete, respectively.

The carrier localization energy at any temperature is given by the difference $E_{loc}(T) = E(T) - E_{PL}(T)$. The localisation energies at 10 K are given in Figures 7.14, and 7.15 for samples with N=0.01, and 0.02 respectively. A superposition of the Varshni fit and experimental data for (100) and (311)A DQWs indicates that the carriers are fully delocalized. The localization energies at 10 K and the values of T_{trans} and T_{deloc} are reported in Table 7.4.

The PL peak energies of (311)B $InGaAs_{1-y}N_y$/GaAs QWs show a successive red/blue/redshift in the temperature range 10-290 K. The PL peak energies in the temperature ranges 10-30K, 30-100K, and >100K redshift, blueshift, and redshift, respectively. This anomalous behaviour is known as the ‘‘S shape’’. This behaviour has been observed in InGaN[40] and AlGaN[41] bulk materials, and in QW heterostructures such as GaAs/InGaP[42], CdS/ZnSe[43] and InGaNAs/GaAs[33,44]. This S-behaviour is absent in the (100) and (311)A InGaAsN QW samples investigated in

this thesis. The PL peak energies of nitrogenated QWs grown on (100) and (311)A planes show a usual behaviour of monotonic decrease with temperature.

H. Dumont et al[32] compared the optical properties of $GaAs_{1-y}N_y$/GaAs epilayers and QW structures grown by MOVPE. A difference in the temperature behavior of the PL peak energy between the GaAsN epilayer and QWs was observed. H. Dumont et al showed that the PL emission at low temperature from GaInAs QWs results from direct gap transition with band to band origin. Electron–holes confinement energy in the QWs that leads to radiative recombination becomes stronger than the exciton localization energy (i.e confinement of carriers can screen the local potential fluctuation due to nitrogen atoms). An S-shape dependence of the peak energy versus temperature for the GaAsN epilayer was reported. A localization effect due to the non-uniform insertion of nitrogen is stronger in epilayer samples. The "S-shape" behavior which is attributed to exciton localization effect is due to local fluctuation of nitrogen concentration[32] or QW width fluctuations. These could be absent in QWs grown on (100) and (311)A due to good uniformity of QW/barrier interface as demonstrated by TEM images in contrast to (311)B QW/barrier interface that shows undulations. The absence of this well-known S-behavior in (100) and (311)A QWs could be as well due to the low nitrogen concentration of 1% and 2%.

Table 7.4: Varshni's parameters for the temperature dependence of the PL peak energy for DQWs grown on different substrate orientations with different N concentrations.

QW Thickness (Plane)	E_0 (eV)	α (meV / K)	β (K)	E_{loc} (10 K) (meV)	T_{trans} (K)	T_{deloc} (K)
4nm (311)B QW (1%N)	1.166	0.37	163	43	50	100
7nm (311)B QW (1%N)	1.098	0.458	200	35	60	100
7nm (311)B QW (2%N)	1.15	0.98	1142	37	60	100
7nm (311)B QW (2%N)	1.046	0.37	180	30	40	80
4nm (100) QW (1%N)	1.13	1.41	1619	-------	--------	-------
7nm (100) QW(1%N)	1.066	0.711	635	-------	--------	-------
4nm (100) QW(2%N)	1.102	2.5	3105	-------	--------	-------
7nm (100) QW (2%N)	1.099	1.78	2029	-------	--------	-------
4nm (311)A QW (1%N)	1.15	0.275	120	-------	--------	-------
7nm (311)A QW(1%N)	1.082	0.416	291	-------	--------	-------
4nm (311)A QW (2%N)	1.056	0.32	178	-------	--------	-------
7nm (311)A QW(2%N)	0.99	0.28	117	-------	--------	-------

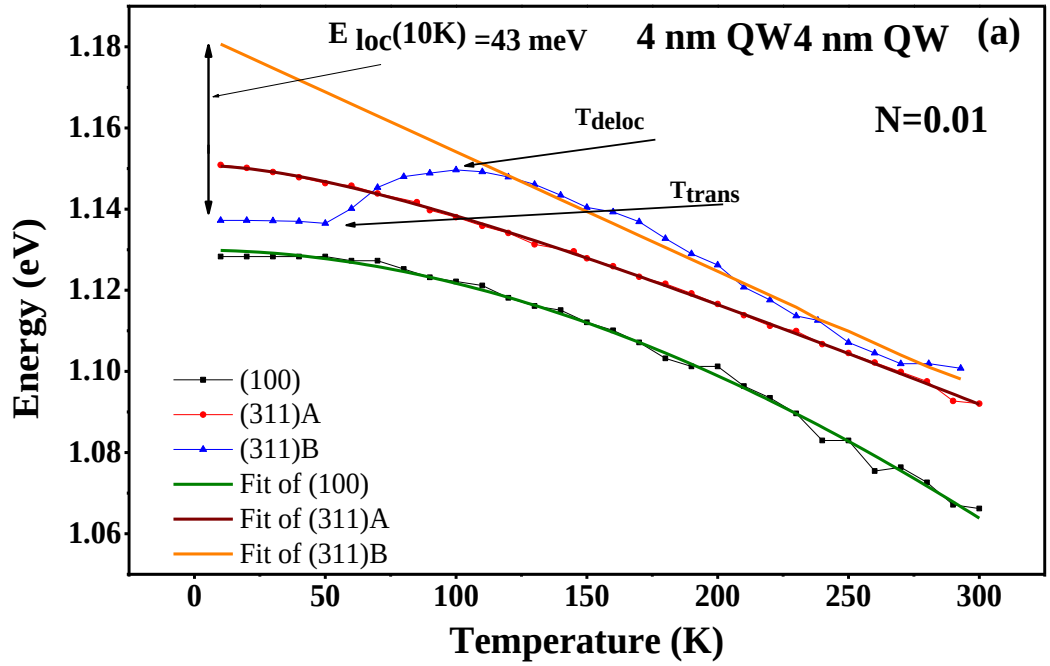

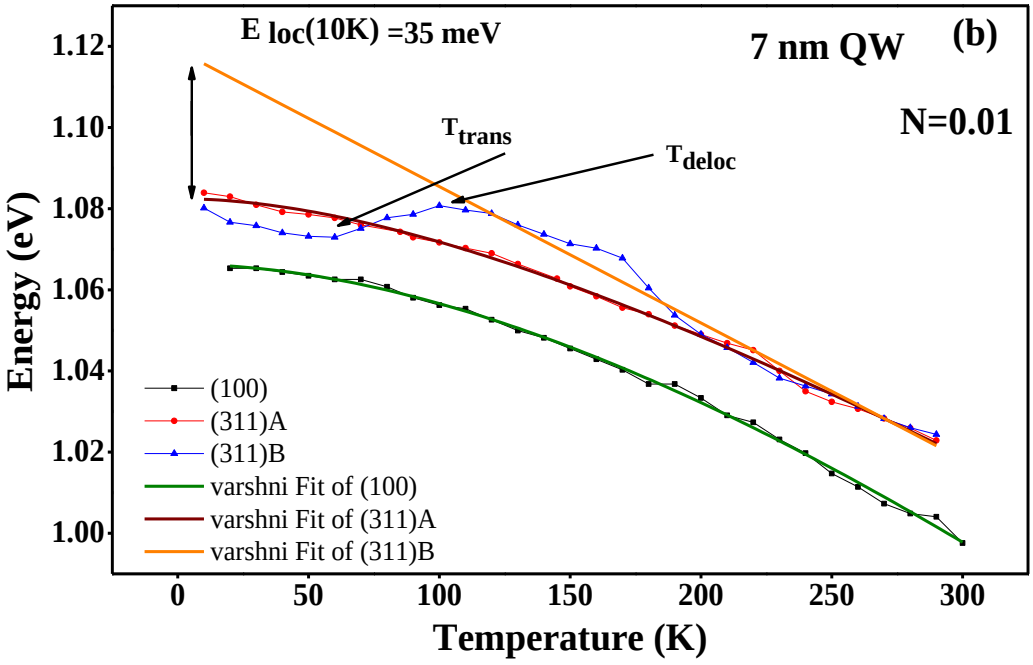

Figure 7.14: Evolution of the temperature of the PL peak energies of the $GaInAs_{0.99}N_{0.01}$/GaAs QWs grown on (100), (311)A, (311)B GaAs planes; (a) QW=4nm (N=0.01); (b) QW=7nm (N =0.01).

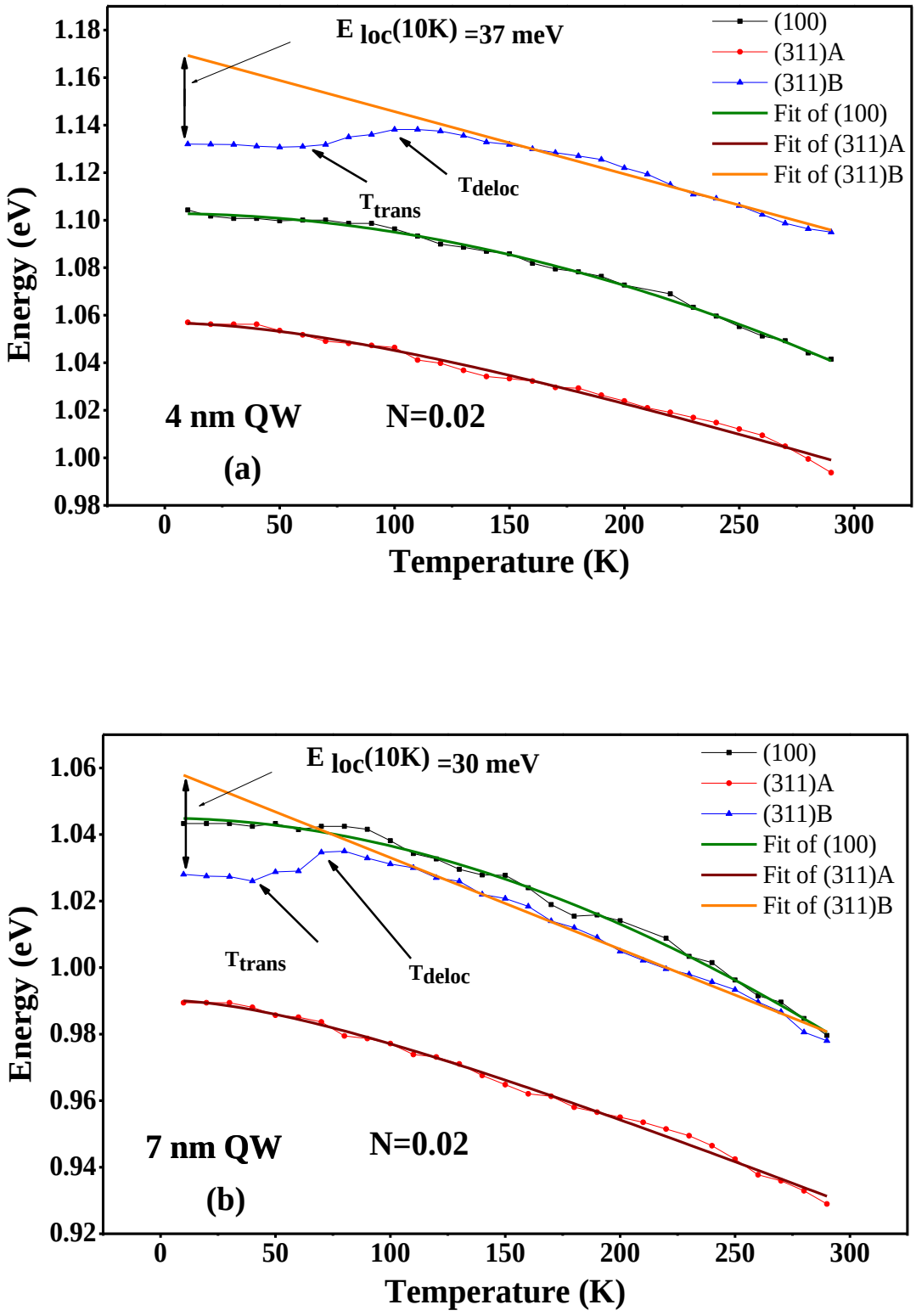

Figure 7.15: Evolution of the temperature of the PL peak energies of the $GaInAs_{0.98}N_{0.02}$/GaAs QWs grown on (100), (311)A, (311)B GaAs planes (a) QW=4nm (N=0.02); (b) QW=7nm (N=0.02).

7.4 CONCLUSION

The influence of nitrogen content on the optical properties of InGaAsN/ DQWs grown on different GaAs crystal orientations has been studied by photoluminescence (PL), Transmission Electron Microscopy (TEM), High Angle Annular Dark Field (HAADF) and Energy Dispersive X-ray (EDX).

The PL efficiency was found to decrease with increasing nitrogen content for all planes but with different order of magnitudes. This phenomenon suggests that the nitrogen incorporation creates defect-related nonradiative centers, whose concentrations are plane dependent.

An enhanced N incorporation is observed in (311)A GaInAsN QWs as compared with (311)B and (100) samples.

The peak PL energies of InGaAs/GaAs and InGaAsN/GaAs DQWs grown on the different planes follow the empirical Varshni model, except for the (311)B InGaAsN/GaAs DQWs where a pronounced S-shaped behavior was observed. These latter results demonstrate that the nitrogen incorporation into the (311)B plane has strong influence on carrier localization. Cross-sectional TEM images show that the (311)B QWs are undulated, which may account for this potential fluctuation and carrier localization.

REFRENCES

[1] M. Weyers, M. Sato, and H. Ando, Japanese Journal of Applied Physics, 31, L853 (1992).

[2] Semicond. Sci. Technol. 17(8) (2002), special issue on dilute nitrides, Journal of Physics: Condensed Matter, 16(31) (2004).

[3] D. Friedman, and S. Kurtz, Progress in Photovoltaics Research and Application, 10, 331 (2002).

[4] T. Jouhti, O. Okhotnikov, J. Konttinen, L. Gomes, C. Peng, S. Karirinne, E. Pavelescu, and M. Pessa, New Journal of Physics, 5, 84.1 (2003).

[5] K. Choquette, J. Klem, A. Fischer, O. Blum, A. Allerman, I. Fritz, S. Kurtz, W. Breiland, R. Sieg, K. Geib, J. Scott, and R. Naone, Electronics Letters, 36, 1388 (2000).

[6] G. Steinle, A. Egorov, and H. Riechert, Electronics Letters, 37, 93 (2001).

[7] T. Kitatani, K. Nakahara, M. Kondow, K. Uomi, and T. Tanaka, Japanese Journal of Applied Physics, 39, L86 (2000).

[8] M. Kondow, K. Uomi, A. Niwa, T. Kitatani, S. Watahiki, and Y. Yazawa, Japanese Journal of Applied Physics, 35, 1273 (1996).

[9] M. Kondow, T. Kitatani, K. Nakahara, and K. Uomi, Lasers and Electro-Optics Society Annual Meeting, LEOS '98 IEEE (1998).

[10] H. Xina, and C. Tu, Applied Physics Letters, 72, 2442 (1998).

[11] J. Phillipsin, A. Alper, J. Margrave, and A. Nowick, Eds. Bonds and Bands in Semiconductors, Academic Press, New York, 54 (1973).

[12] H. Ho, and G. Stringfellow, Materials Research Society Symposia Proceedings, 449, 871 (1997).

[13] B. Lee, S. Bose, M. Kim, A. Reed, G. Stillman, W. Wang, L. Vina, and P. Colter Journal of Crystal Growth, 96, 27 (1989).

[14] X. Han, T. Tanak, N. Kojima, Y. Ohshita, M.Yamaguchi, and S.Sato, Applied Physics Letters, 100, 032108 (2012).

[15] H. Suzuki, M. Inagaki, T. Honda, Y. Ohshita, N. Kojima, and M. Yamaguchi, Japanese Journal of Applied Physics, 49, 04DP08 (2010).

[16] A. Moto, M. Takahashi, and S. Takagishi, Japanese Journal of Applied Physics, 39, L1267 (2000).

[17] M. Takahashi, P. Vaccaro, T. Watanabe, T. Mukaihara, F. Koyama, and K. Iga, Japanese Journal of Applied Physics, 35, 6102 (1996).

[18] H. Saito, T. Makimoto, and N. Kobayashi, Japanese Journal of Applied Physics, Part 2, 35, L1644 (1996).

[19] J. Ibanez, M. Henini, R. Kudrawiec, J. Misiewicz, M. Schmidbauer, and M. Hopkinson, Journal of Crystal Growth, 552, 301 (2007).

[20] X. Han, H. Suzuki, J. Lee, M. Inagaki, N. Kojima, Y. Ohshita, and M. Yamaguchi, Proc. 35th IEEE Photovoltaic Specialist Conference Honolulu, HI, 20, (2010).

[21] A. Arnoult, F. Gonzalez-Posada, S. Blanc, V. Bardinal, and C. Fontaine, Physica E, 23, 352 (2004).

[22] S. Blanc, A. Arnoult, H. Carrere, and C. Fontaine, Physica E, 17, 252 (2003).

[23] S. Blanc, A. Arnoult, H. Carrère, E. Bedel, G. Lacoste, C. Fontaine, M. Cabié, A. Ponchet, and A. Rocher, IEE Proc-Optoelectron., 150, 64 (2003).

[24] T. Ishizuka, H. Doi, T. Katsuyama, J. Hashimoto, and M. Nakayama, Journal of Crystal Growth, 298, 116 (2007).

[25] M. A Pinault, and E. Tournie, Applied Physics Letters, 79 (21), 3404 (2001).

[26] C. Chana, J. Wub, Y. Huangb, H. Hsuc, K. Tiongd, and Y. Sue, Materials Chemistry and Physics, 124, 1126 (2010).

[27] N. Nishiyama, M. Arai, S. Shinada, T. Miyamoto, F. Koyama, and K. Iga, Journal of Crystal Growth, 221, 530 (2000).

[28] A. Polimeni, M. Capizzi, M. Geddo, M. Fischer, M. Reinhardt, and A. Forchel, Applied Physics Letters, 77, 2870 (2000).

[29] F. Laia, S. Kuo, J.S. Wangc, R. Hsiao, H. Kuo, J. Chi, S. Wang, H. Wang, C. Liang, and Y. Chen, Journal of Crystal Growth, 291, 27 (2006).

[30] S. Shirakata, M. Kondow, and T. Kitatani, Applied Physics Letters, 79, 54 (2001).

[31] S. Shirakata, M. Kondow, and T. Kitatani, Journal of Physics and Chemistry of Solids, 64, 1533 (2003).

[32] H. Dumont, L. Auvray, Y. Monteil, F. Saidi , F. Hassen, and H. Maaref, Optical Materials, 24, 303 (2003).

[33] L. Grenouillet, C. Bru-Chevallier, G. Guillot, P. Gilet, P. Duvaut, C. Vannuffel, A. Million, and A. Chenevas-Paule, Applied Physics Letters, 76, 2241 (2000).

[34] M. Pinault, and E. Tournié, Applied Physics Letters, 78, 1562 (2001).

[35] H. Xin, K. Kavanagh, Z. Zhu, and C. Tu, Applied Physics Letters, 74, 2337 (1999).

[36] Y. Soo, S. Huang, Y. Kao, J. Chen, S. Hulbert, J. Geisz, S. Kurtz, J. Olson, S. Kurtz, E. Jones, and A. Allerman, Physical Review B, 60, 13605 (1999).

[37] Y. Varshni, Physica (Utrecht), 34, 149 (1967).

[38] P. Sitarek, K. Ryczko, G. Sezk, J. Misiewicz, M. Fischer, M. Reinhardt, and A. Forchel, Solid-State Electronics, 47, 489 (2003).

[39] A. Kaschner, T. Luttgert, H. Born, A. Hoffman, A.Yu. Egorov, and H. Riechert, Applied Physics Letters, 78 (10), 1391 (2001).

[40] H. Schenk, M. Leroux, and P. Mierry, Journal of Applied Physics, 88, 1525 (2000).

[41] Y. Cho, G. H. Gainer, J. Lam, J. Song, W. Yang, and W. Jhe, Physical Review B, 61, 7203 (2000).

[42] E. Laureto, E. Meneses, W. Carvalho, A. Bernussi, E. Ribeiro, E. da Silva, and J. de Oliveira, Brazilian Journal of Physics., 32, 314 (2002).

[43] A. Dinger, M. Baldauf, S. Petillon, A. Hepting, D. Luerssen, M. Grun, H. Kalt, and C. Klingshirn, Journal of Crystal Growth, 214, 660 (2000).

[44] A. Kaschner, T. Luttgert, H. Born, A. Hoffmann, A. Egorov, and H. Riechert, Applied Physics Letters, 78, 1391 (2001).

CHAPTER 8: POST GROWTH ANNEALING OF $Ga_{1-x}In_xN_yAs_{1-y}$/GaAs DOUBLE QUANTUM WELL STRUCTURES GROWN ON (100), (311)A, and (311)B GaAs SUBSTRATES

This chapter reports the effect of the post-growth annealing process on the optical properties of $Ga_{1-x}In_xN_yAs_{1-y}$/GaAs double quantum well structures grown on (100), (311)A, and (311)B GaAs substrates.

8.1 INTRODUCTION

The introduction of nitrogen into the GaAs lattice by replacing As atoms creates localized energy states near the conduction band edge. This leads to a huge band gap bowing[1] that affects the electrical and optical properties of the materials[2]. However, nitrogen also occupies the non-substitutional sites in the lattice of GaAs (i.e. the nitrogen atoms may incorporate in locations other than the group V lattice sites[3]) leading to the formation of N-related defects that can degrade the optical quality of the crystal by decreasing the optical efficiency and carrier lifetime[4,5]. The usage of radio frequency (RF) plasma source to generate nitrogen atoms and the relative low growth temperature are also responsible for the creation of these defects and low optical quality.

In order to recover these qualities it is common practice to subject the material to appropriate thermal treatment to improve the optical properties of nitrogen-based III-V compounds[6]. However, the annealing process can have also a negative effect on the material quality and the defects present in the host material.

Shafi et al[7] used deep level transient spectroscopy (DLTS) and Laplace DLTS techniques to study the annealing effect on Si-doped GaAsN layers containing nitrogen concentrations in the range 0.2 – 1.2%. Seven defect states were observed in the as-grown GaAsN (N=0.2%) samples. Post-growth thermal annealing eliminated four of these defects. However, in the samples of high nitrogen content $\geq 0.8\%$, both creation and annihilation of some of the traps have been observed upon annealing.

Gao et al[8] studied the effect of rapid thermal annealing on the evolution of electrically active defects in metalorganic vapour phase epitaxy (MOCVD) grown p-type GaAsN epitaxial layers using DLTS. Annealing between 600 ^{0}C and 900 ^{0}C generated six new deep hole traps. Most of these were stable in this temperature

range. However, there were variations in their concentrations with the annealing temperature.

S. Spruytte et al3 investigated GaNAs QW by high resolution x-ray diffraction. They observed that the lattice parameter does decrease linearly with increasing nitrogen concentration up to 2.9 % as expected by Vegard's law. By increasing the nitrogen percentage above this value deviation from Vegard's low occurred. The fact that Vegard's law is not observed for all nitrogen contents indicates that nitrogen incorporates in locations other than the group V lattice sites. X-ray photoelectron spectroscopy (XPS) revealed that nitrogen exists in two bonding configurations: a Ga–N bond and another nitrogen complex in which N is less strongly bonded to gallium atoms. The authors reported that post growth annealing removes the second nitrogen complex and improves the PL intensity. A combined nuclear reaction analysis and Rutherford backscattering technique showed that as-grown GaNAs contains a significant concentration of interstitial nitrogen that disappears upon anneal.

Annealing studies of nitride materials reported in the literature have contradictory results regarding its effect on PL energy. While some reports show a blue shift[9] of the PL emission upon thermal annealing others show a red shift of PL energy[10].

The thermal anneal-induced blue shift is mainly attributed to two distinct mechanisms; the rearrangement of local nitrogen bonding configurations[11] and the interdiffusion between Ga and In atoms across the QW interfaces[12].

A brief survey about the different effect in PL energy after annealing is given below.

V. Liverini et al[13] analyzed several QWs with different nitrogen contents after different RTA annealing conditions. The main conclusion of their systematic studies of RTA on GaInNAs single QWs is that the blue shift of the energy band gap after annealing is dependent on the N content of the QW while the PL integrated intensity improvement is not. By comparing the effect of the annealing process carried out at the same conditions on samples with different nitrogen concentration, they found that the highest blue shift occurs in samples that have the highest N content.

There are two blue shift regimes, namely strong and weak regimes, depending on the RTA temperature. In the strong regime (up to 700 ^{0}C) the blue shift experiences a rapid increase with increasing RTA temperature, while in the weak regime above

this temperature it saturates. By using high resolution x-ray diffraction (HRXRD), the authors concluded that the larger PL blue shift observed in GaInNAs cannot be explained just by In out-diffusion.

These findings contradict with the results reported by H. Liua et al[12] who showed suppression of blue shift after annealing in samples with higher nitrogen content. H. Liua et al used X-ray to study the effect of post-growth annealing on GaInAs/GaAs and GaInNAs/GaNAs multiple quantum wells (MQWs) grown by MBE. The evolution of X-ray diffraction patterns indicates that In/Ga inter-diffusion occurs in both types of MQWs due to post-growth thermal annealing. The diffusion length deduced from the dynamic simulations shows a decrease with the increase of N concentration. Alloying nitrogen with GaInAs is interpreted to cause suppression in Ga/In inter-diffusion. These observations may be attributed to the formation of strong N-related bonds inside the QW and to a reduced strain in nitrogen-contained QWs.

8.2 EXPERIMENTAL RESULTS AND ANALYSIS

This section will report on the results of the annealing effect on six samples of $Ga_{1-x}In_xN_yAs_{1-y}$/GaAs double quantum well structures grown on (100), (311)A, and (311)B GaAs planes with two nitrogen concentration (0% and 1%).

The features of the six studied samples in this section are shown in Table 8.1. All samples are grown by MBE and are described in details in Chapter 7, section 7.3. The samples cut from the as-grown wafer were proximity GaAs capped and RTA treated in argon ambient for 30 s at 500 ^{0}C, 600 ^{0}C, and 700 ^{0}C. The detailed post-growth annealing procedure is similar to the one adopted to heat treat self-assembled quantum dots (see Chapter 6, section 2).

It is worth pointing out that GaAs proximity capping technique, which inhibits surface degradation due to As out diffusion, induces thermal intermixing upon RTA[14], while SiO_2[15] and Si_3N_4[16] capping layers have been reported to enhance impurity-free interdiffusion. For example the effect of the capping layer (GaAs and SiO_2) on the optical properties of RTA strained InGaAs/GaAs MQWs has been

investigated by S. Burkner et al[14]. They found that the PL energy shift upon annealing of SiO_2 capped samples resulted up to four times larger than in GaAs capped samples. This behavior was explained by the quick diffusion of the top most Ga atoms at the surface into SiO_2, creating Ga vacancies which diffuse into the MQWs region. For the GaAs capped layers, the only available Ga vacancies contributing to the interdiffusion are the intrinsic Ga vacancies that originate from the substrate and the buffer layers. This translates to a lower concentration of Ga vacancies leading to a smaller degree of intermixing in the MQWs region.

To remove the effects of any variations in the annealing process between samples, all the samples were annealed simultaneously as a batch. PL measurements at 10 K were performed on each of the samples prior to annealing, and then again following the annealing process. Further anneals were then performed on the same samples with the low temperature PL recorded after each anneal.

Table 8.1: Investigated samples grown on different substrate orientations and having different nitrogen contents.

Sample Number	Substrate	Nitrogen mole fraction
MBE2226 $DQW^{0.0N}_{(100)}$	(100)	0%
MBE2227 $DQW^{0.0N}_{(311)A}$	(311)A	0%
MBE2228 $DQW^{0.0N}_{(311)B}$	(311)B	0%
MBE2223 $DQW^{0.1N}_{(100)}$	(100)	1%
MBE2225 $DQW^{0.01N}_{(311)A}$	(311)A	1%
MBE2224 $DQW^{0.01N}_{(311)B}$	(311)B	1%

8.2.1 PHOTOLUMINESCENCE OF ANNEALED $Ga_{1-x}In_xAs/GaAs$ DQWs SAMPLES AT DIFFERENT TEMPERATURES

Figure 8.1 shows the 10 K PL spectra of as-grown, 500 ^{0}C, 600 ^{0}C and 700 ^{0}C annealed (100), (311)A, and (311)B $Ga_{1-x}In_xN_yAs_{1-y}/GaAs$ DQWs samples with y=0% .

The PL energy of as-grown 4nm QW grown on (100), (311)A, and (311)B samples are 1.222, 1.236 , and 1.233 eV with FWHM of ~25 , ~13 , ~17 meV, respectively. While The PL energy of as-grown 7nm QW grown on (100), (311)A, and (311)B samples are 1.160, 1.165 , and 1.167 eV with FWHM of ~20, ~13, and ~19 meV, respectively.

It is evident from Figure 8.2 that almost no change of the peak position is observed when the annealing temperature is 500 ^{0}C for QWs grown on (311)A and (311)B planes, while there is a small red shift of 8 meV, and 12 meV for 4 nm, and 7 nm (100) QWs, respectively. By increasing the annealing temperature to 600 ^{0}C, this red shift of PL from (100) quantum wells recovered again, while the PL energy of 600 ^{0}C annealed (311)A sample red shifted and reaches its lowest value of 1.231 eV, and 1.162 eV for 4 nm and 7 nm wells, respectively. Further increase of the annealing temperature to 700 ^{0}C, the PL energy from QWs grown on all planes exhibit a blue shift of equal amount of 20 meV for the 4nm QW and of a comparable amount of 10, 15, and 13 for the 7 nm (100), (311)A, and (311)B QW, respectively.

The PL blue-shift at higher annealing temperature is most likely due to Ga and In inter-diffusion, which seems to be nearly the same for all planes. The inter-diffusion which results in shallower QW is believed to cause the quantum-confined states to shift upwards in energy[17,18].

The blueshift of the PL has been explained theoretically[19] by a change in the electron and hole confinement profile due to the annealing-induced interdiffusion of atoms across the QW interfaces.

The increasing of the PL blue shift with increasing annealing temperature could be accounted for by the increasing of the diffusion length of atoms at higher annealing temperature[20].

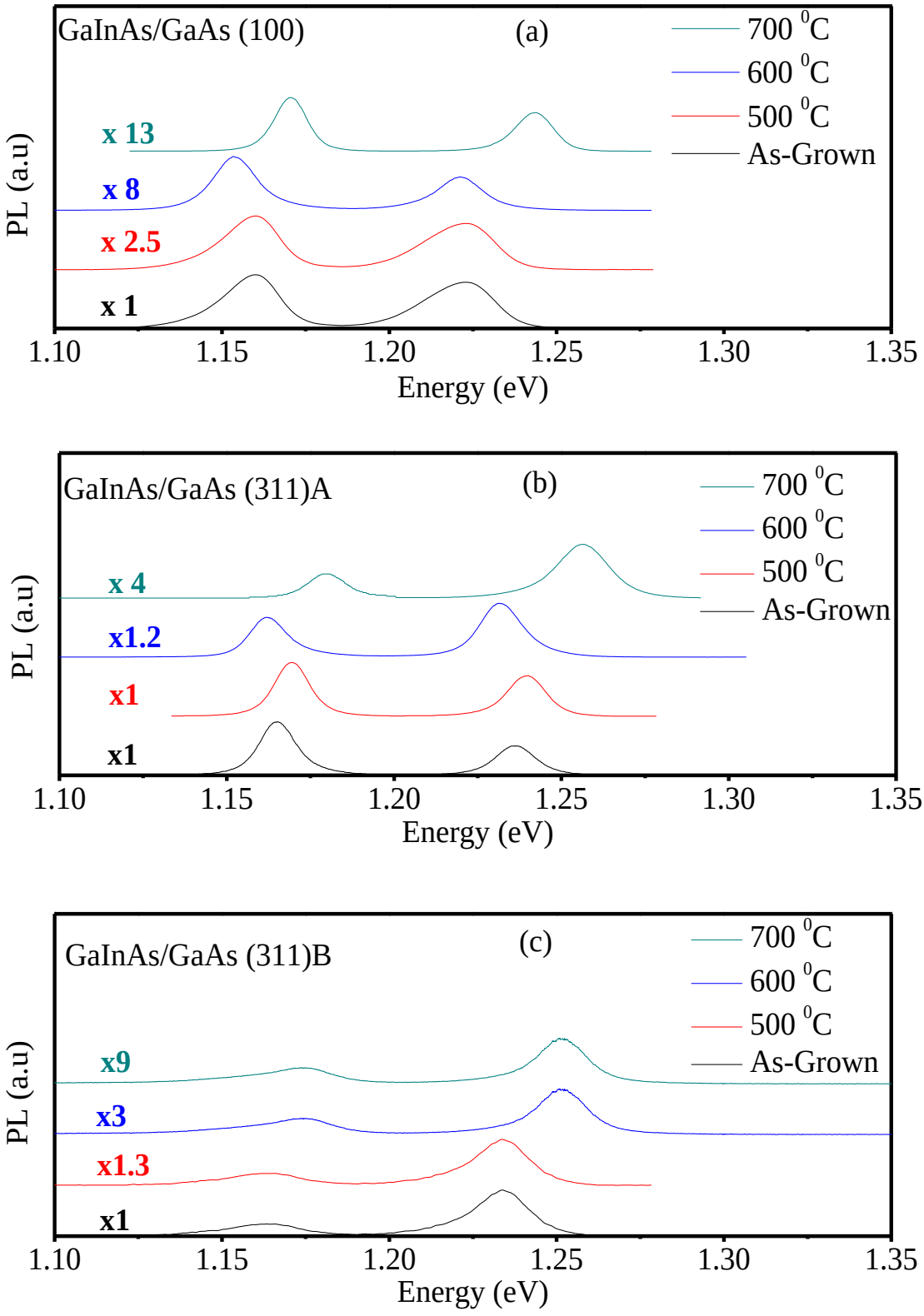

Figure 8.1: 10 K PL spectra of as-grown, and 500 ^{0}C, 600 ^{0}C and 700 ^{0}C annealed $In_{0.36}Ga_{0.64}As$/GaAs DQWs samples: (a) (100), (b) (311)A, (c) (311)B. The times number in front of each spectrum corresponds to the PL relative intensity, referred to as enhancement factor $F=I_{peak}$ (annealed)/I_{peak} (as-grown).

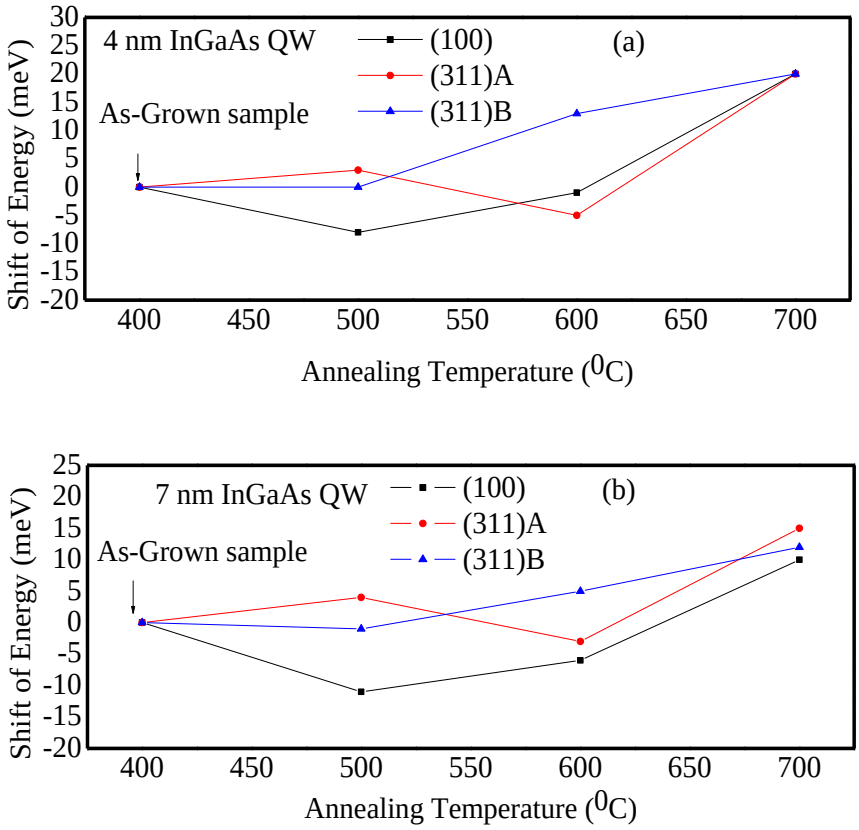

Figure 8.2: Dependence of PL energy-shift on RTA temperature for $In_{0.36}Ga_{0.64}As/GaAs$ QWs grown on (100), (311)A, and (311)B GaAs planes: a) 4nm QW samples; b) 7nm QW samples. The data point at 400 ^{0}C corresponds to the sample without annealing, i.e. as-grown.

By increasing the annealing temperature, the PL intensity from the QWs grown on all planes increases but with different orders of magnitude. The times number in front of each spectrum in Figure 8.1 corresponds to the PL relative intensity, referred to as enhancement factor $F=I_{peak}$ (annealed)/I_{peak} (as-grown).

The maximum intensity appear for samples annealed at 700 ^{0}C. The PL intensity from the samples annealed at 700 ^{0}C is nearly 13, 4, and 9 times the PL intensity of as-grown (100), (311)A, and (311)B samples, respectively. This kind of enhancement of PL intensity, which is also observed in other QW material systems, may be due to the reduction of the non-radiative centers following post-growth thermal treatment[20]. The different level of enhancement of the PL intensity for different planes may be accounted for by different contents and types of defects that

are present in each plane. The lower PL intensity of the as-grown samples as compared to the annealed samples could be accounted for by a larger concentration of nonradiative centers. It could therefore be argued that the PL intensity difference between as-grown and annealed sample is evidence of lower concentration of nonradiative centers. As demonstrated by L. H. Li et al[20] the increase of the PL intensity was attributed to the removal of defects and impurities in the well and heterointerface regions.

M. Albrecht et al[21] analyzed the influence of annealing on compositional fluctuations in InGaAsN quantum wells by means of composition-sensitive high-resolution transmission electron microscopy (HR-TEM) and PL. They observed an improvement of the PL intensity after annealing and explained this enhancement by the homogenization of the In distribution in the QW. In addition, they attributed the PL shift to homogenization of the In concentration and to diffusion of N out of the quantum well.

In this work, it is suggested that more detailed analysis, for example by using deep level transient spectroscopy (DLTS) measurements[22], would be required to show the nature and evolution of the defects with respect to the growth plane and annealing temperatures.

The FWHM of PL spectra for annealed samples have different behavior for different planes. It decreases monotonically for QWs grown on (100) plane while it is constant for the QWs grown on high index planes. However, FWHM slightly increases for the 4nm QW grown on (311)A after annealing at 700 ^{0}C (see Figure 8.3).

The reduction of FWHM of PL of (100) QWs by annealing might be caused by the improvement of the uniformity of In-content in GaInAs well layer as a result of the rearrangement and reconstruction at the atomic level brought about by thermal annealing[23] and the reduction of thickness fluctuation of the well[20].

It seems that the annealing temperature has no effect on FWHM of PL from QWs grown on high index planes. It is important to point out that the as-grown (311)A QWs have the smallest FWHM among all as-grown samples.

The smallest FWHM of 13 and 11 meV were observed for both 4 nm and 7 nm (100) QWs annealed at 700 ^{0}C, respectively.

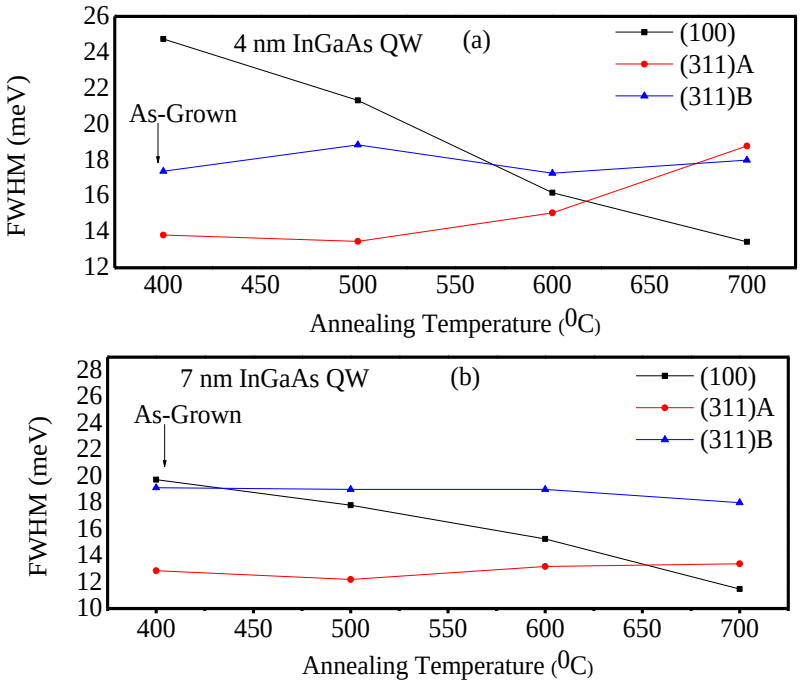

Figure 8.3: Dependence of PL FWHM on RTA temperature for (100), (311)A, and (311)B $In_{0.36}Ga_{0.64}As/GaAs$ QWs: a) 4nm QW samples; b) 7nm QW. The data point at 400 ^{0}C corresponds to the sample without annealing, i.e. as-grown.

8.2.2 PHOTOLUMINESCENCE OF ANNEALED $Ga_{1-x}In_xN_yAs_{1-y}/GaAs$ DQWs SAMPLES AT DIFFERENT TEMPERATURES

Figure 8.4 shows the 10 K PL spectra of as-grown, 500 ^{0}C, 600 ^{0}C, and 700 ^{0}C annealed (100), (311)A, (311)B $Ga_{1-x}In_xN_yAs_{1-y}/GaAs$ DQWs samples with y=1% .

As discussed in the pervious chapter the PL energy is red shifted by nitrogen incorporation so the PL energies of as-grown samples are lower than nitrogen free samples. The PL energies of as-grown 4nm QW grown on (100), (311)A and (311)B samples are 1.283, 1.150, and 1.137 eV with FWHM of 28, 28, and 40 meV, respectively. While the PL energy of as-grown 7nm QW grown on (100), (311)A and (311)B samples are 1.066, 1.083, and 1.080 with FWHM of 18, 20, and 40 meV, respectively.

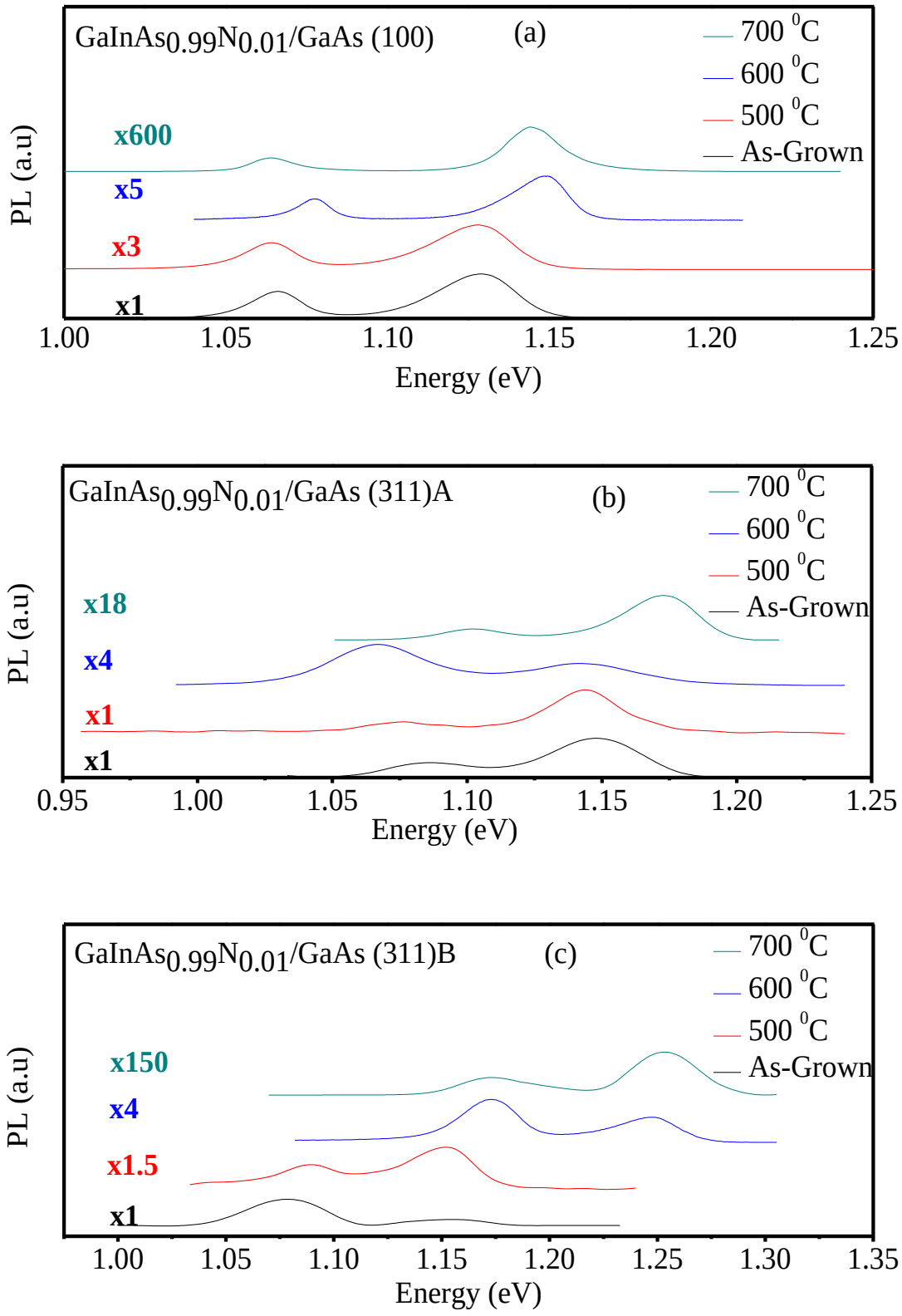

Figure 8.4: 10 K PL spectra of as-grown, and 500 ^{0}C, 600 ^{0}C and 700 ^{0}C annealed $In_{0.36}Ga_{0.64}N_{0.01}As_{0.99}$/GaAs DQWs samples: (a) (100), (b) (311)A, (c) (311)B. The times number in front of each spectrum corresponds to the PL relative intensity, referred to as enhancement factor $F=I_{peak}$ (annealed)/I_{peak} (as-grown).

It is evident from Figure 8.5 that almost no change of the peak position is observed when the annealing temperature is 500 ^{0}C for QWs grown on different planes. However, by increasing the annealing temperature, the QWs PL energy behaves in a way that depends on the growth plane. For the QWs grown on (100) plane, the PL energy shows a blue shift after annealing by an amount comparable (20 meV at 700 ^{0}C) to the blue shift observed in the free nitrogen sample (i.e. GaInAs/GaAs). For QWs grown on (311)B plane, the PL energy show a larger blue shift (120 meV at 700 ^{0}C) as compared to 20 meV for free nitrogen sample. On the other hand the QWs grown on (311)A plane show red shift instead of blue shift that increases with increasing annealing temperature up to 600 ^{0}C; further increase of the annealing temperature results in a blueshift. For the 700 ^{0}C anneal the PL energy shift from (311)A QWs becomes comparable to that of (100) QWs.

Since the PL energy shifts with annealing for free nitrogen QWs grown on different planes are comparable, the discrepancy in the shifts of PL energy with annealing temperature for nitrogenated QWs could be related to nitrogen behavior with annealing rather than In. This effect could be attributed to a rearrangement of the nearest neighbour configuration of the N atoms[10].

The red shift in the case of (311)A QWs could be explained by some interstitial nitrogen atoms that migrated and substituted As atoms.

Francoeur et al.[24] reported a redshift in the luminescence peak detected in MOCVD grown InGaAsN layers after annealing at 650 ^{0}C for 5 minutes. A shift of 15 meV in a sample containing 0.7% N was observed. From the XRD measurement they attributed this redshift to the increase of nitrogen incorporation.

As shown in Figure 8.4 and indicated by the PL enhancement factor for every annealing temperature, the annealing process has resulted in an increase of the PL intensity for all planes. The times numbers inside Figure 8.4 relate to the PL enhancement factor at each annealing temperature. The magnitude of PL enhancement factors of nitrogen-containing samples are larger than those of N-free samples for all planes. The larger increase in the PL intensity of the N-containing samples would suggest that there is a larger concentration of non-radiative centers associated with N incorporation. In other words, the traps responsible for the

decrease of the luminescence efficiency of the as-grown nitride-samples are related to a crystal defect or an impurity associated with nitrogen, but not related to indium3.

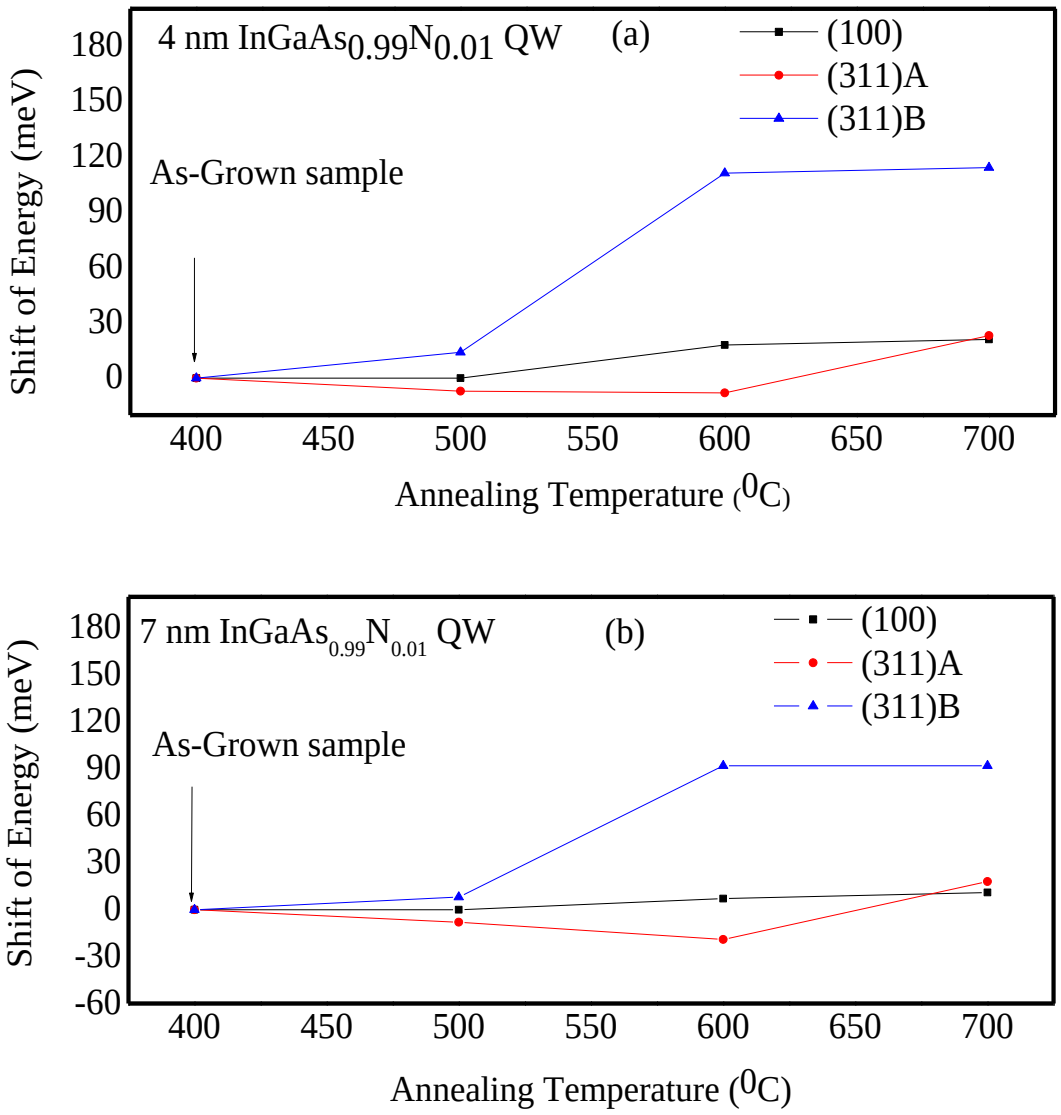

Figure 8.5: Dependence of PL energy-shift on RTA temperature for (100), (311)A, and (311)B $InGaAs_{0.99}N_{0.01}$/GaAs QWs: a) 4nm QW samples b) 7nm QW. The data point at 400 ^{0}C corresponds to the sample without annealing, i.e. as-grown.

8.3 SIMS OF AS-GROWN and ANNEALED $Ga_{0.64}In_{0.36}N_{0.1}As_{0.99}$/GaAs DQWs SAMPLES AT DIFFERENT TEMPERATURES

In order to elucidate the origin of the PL blue shift, composition profile analysis by the time of flight secondary ion mass spectrometry (ToF-SIMS) has been made. Figure 8.6 shows the composition profiles of In, and Ga of as-grown, 600 ^{0}C and 700 ^{0}C annealed samples grown on (100), (311)A, and (311)B planes. Figure 8.7 shows the composition profiles of nitrogen for the same samples.

The two QWs and barriers can be seen clearly by the sharp change of both In and Ga composition with the sputtering time. SIMS profiles of as-grown and annealed GaInNAs/GaAs DQWs showed that after annealing, In atoms diffused out of the quantum well region and the Ga concentration in the QW increased for all planes. This behavior is illustrated in Figure 8.6 where the In distribution inside the QW has reduced intensity, and becomes broader and less well resolved than prior to the annealing process. However, the total integrated areas under the In distribution profiles before and after annealing are constant. In addition, as can be seen in Figure 8.6 there is a noticeable interdiffusion between In and Ga atoms occurring at the annealing temperature of 600^{0}C.

In the 4nm and 7 nm QW samples annealed at 700 ^{0}C the In distribution broadens by a factor of 4, 4.5, and 6 in comparison with the as-grown samples grown on (100), (311)A, and (311)B, respectively. These factors represent the ratios of the FWHM of the SIMS profiles of the annealed and as-grown samples. This indicates that the In atoms strongly diffuse into the GaAs barrier regions from the QW layers by different order of magnitudes, and the diffusion process depends on the orientation of the substrate. It is worth pointing out that the ability to resolve the separate In layers in the samples annealed at 700 ^{0}C decreases gradually in the following order (100) > (311)A > and (311)B where the two layers are eventually observed as being intermixed for the (311)B. The In diffusion is more towards the substrate side.

Therefore, the SIMS results provide an unambiguous evidence that the PL blue shift originates from changes in the QW region where interdiffusion of In–Ga between the QWs and barriers occurs.

The In and Ga profiles across the structures do not show any dramatic difference for the 600 ^{0}C annealed samples in comparison with the as-grown samples. This leads to the conclusion that the improvement of the PL intensity at the annealing temperature of 600 ^{0}C is not correlated with changes of the QW structure, but is correlated with the annihilation of nonradiative centers in the QW region.

Fig. 8.7 displays typical SIMS profiles showing depth distribution of nitrogen element. The total N concentrations inside the two as-grown QWs regions containing nominal 1% nitrogen are nearly the same for all planes.

From these SIMS measurements, it can be seen that the concentration of nitrogen does not change significantly during annealing of (100), and (311)A QWs. On the other hand concentration of nitrogen for (311)B decreases after 600 ^{0}C anneal and becomes not detectable after 700 ^{0}C anneal. These SIMS results are consistent with the results of PL measurements, which provide evidence that the cause of the blue shift of the PL energy observed in annealed (100) and (311)A QWs originates from the interdiffusion of In–Ga rather than to the incorporation of nitrogen substitutionally (N on arsenic site). However, while the larger PL blue shift in annealed (311)B QWs could be due to a combination of both mechanisms.
H. Liu et al[25] showed that thermal annealing up to 850 ^{0}C has no effect on the nitrogen concentration and distribution as measured by SIMS or the in-plane strain of $GaN_{0.023}As_{0.977}$ thin films grown on (100) plane, but it does change the redistribution of the configurations of local nitrogen bonding in the GaNAs films, such as for example the N-N split interstitial to the N-As split interstitial and substitutional. These results agree with the (100) and (311)A SIMS data discussed above, and can be explained by the stable N configurations.

A tentative explanation of the N behavior with annealing for (311)B can be explained using the argument of X. Chen et al[26] who demonstrated out-diffusion of nitrogen using SIMS upon annealing up to 700 ^{0}C. XPS showed that further annealing causes an increase of interstatial N-N on the expenses of substitional nitrogen $N_{As.}$

Another explanation of the different nitrogen behavior upon annealing in different planes might be due to the different N-bond configuration these planes.

P. Klar and co-workers[27] who investigated annealed implanted (Ga,In) (As,N) alloy system attributed the blue-shifted bandgap to N bond reordering. They explained that rearrangement of the N nearest-neighbour environments from Ga-rich to In-rich (from N–Ga_4 to In–N–Ga_3, In_2 –N–Ga_2, In_3–N–Ga or In_4–N) changes the bandgap.

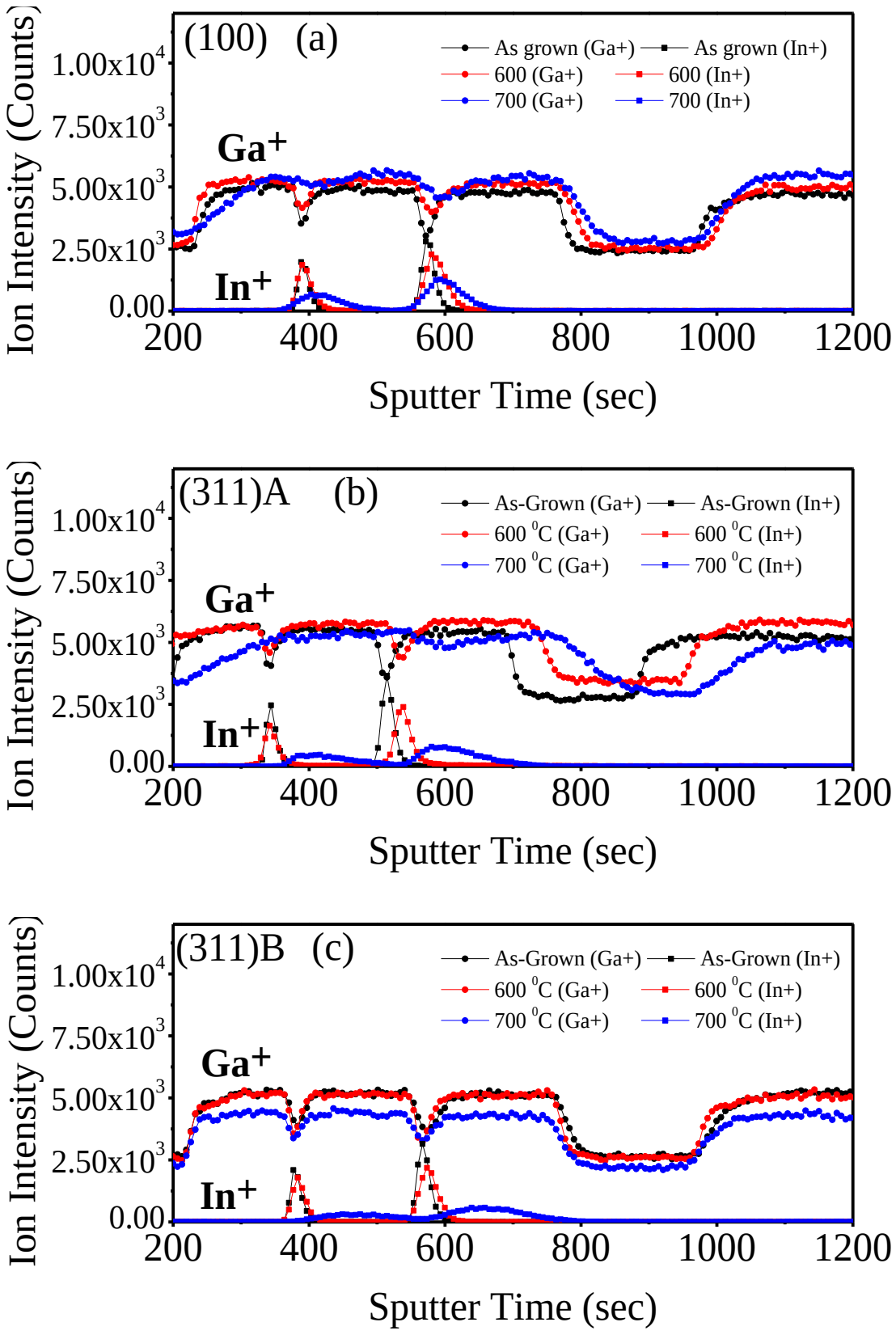

Figure 8.6: ToF-SIMS depth profile of In and Ga ions in as-grown and annealed $In_{0.36}Ga_{0.64}N_{0.01}As_{0.99}$/GaAs DQWs samples: (a) (100), (b) (311)A, (c) (311)B.

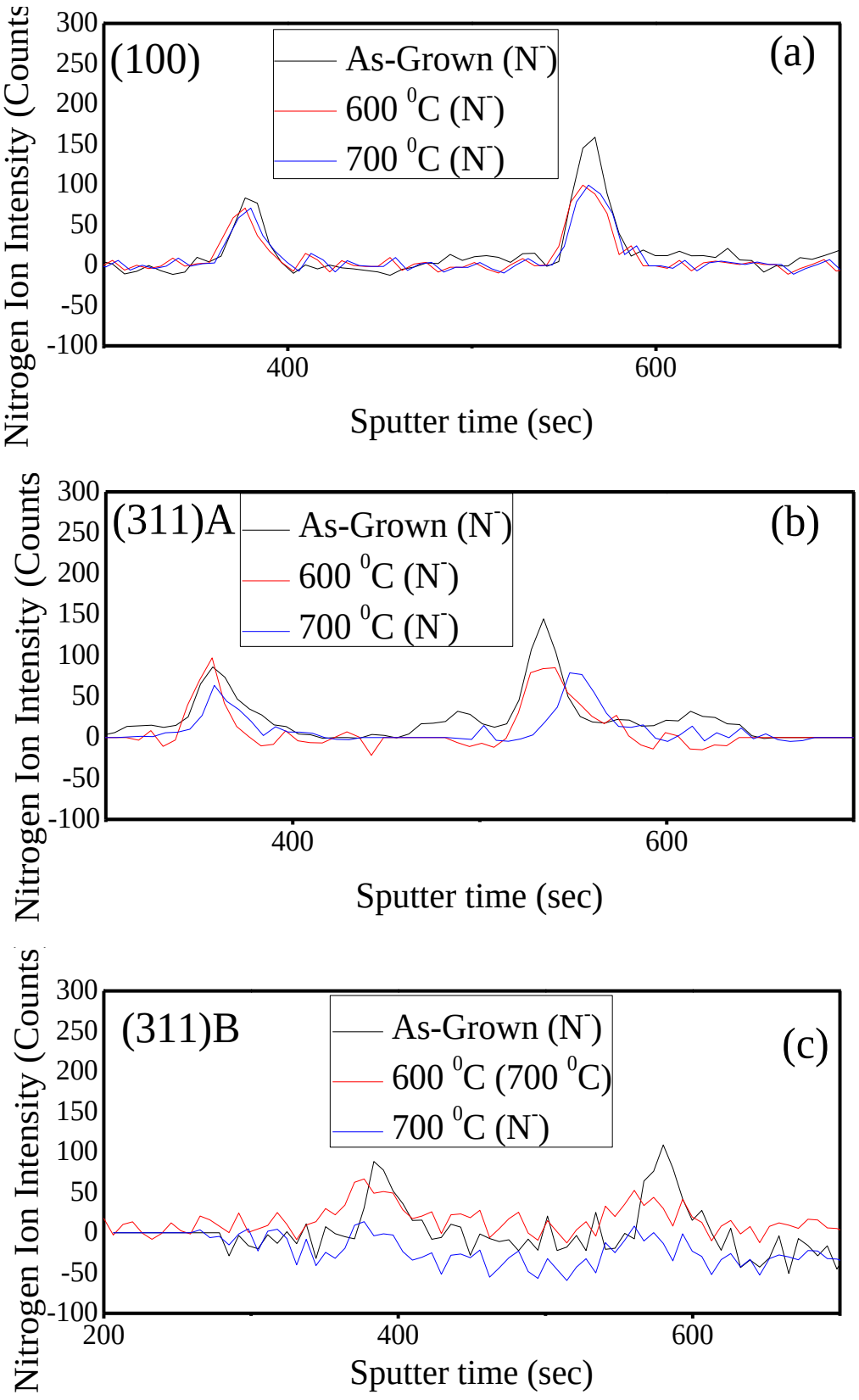

Figure 8.7: SIMS profile of nitrogen atoms in as-grown and annealed $In_{0.36}Ga_{0.64}N_{0.01}As_{0.99}$/GaAs DQWs samples: (a) (100), (b) (311)A, (c) (311)B.

8.4 CONCLUSION

The main finding of these systematic studies of RTA on GaInAs and $GaInN_{0.01}As_{0.99}$ DQWs grown on different planes is that the blueshift of the peak PL energy upon annealing is dependent on the growth plane and N content of the QW, and it is attributed to Ga/In intermixing at the interface between QW and matrix. The enhancement factors for all samples (without and with nitrogen) are greater than one, confirming that the anneal process has reduced the non-radiative defects. However, the enhancement factors of the nitrogenated samples is higher than those of the control samples without nitrogen for all planes. This suggests that the incorporation of nitrogen introduces more non-radiative centers in the host materials. The ToF-SIMS composition profile confirmed the PL results which are explained by the appearance of Ga/In intermixing at the interface between the QW and the barrier upon annealing. The amount of diffusion of In out of the QW depend on the growth plane. It is larger for (311)B plane for both 4 and 7 nm QWs as compared to the other planes. However, in contrast to the (311)B QWs the nitrogen content in the (100) and (311)A QWs doesn't change upon annealing.

REFERENCES

[1] L. Bellaiche, S. H. Wei, and A. Zunger, Physical Review B, 54, 17568 (1996).

[2] S. A. Ding, S. R. Barman, K. Horn, H. Yang, B. Yang, O. Brandt, and K. Ploog, Applied Physics Letters, 70, 2407 (1997).

[3] S. Spruytte, C. Coldren, J. Harris, W. Wampler, P. Krispin, K. Ploog, and M. Larson, Journal of Applied Physics, 89, 4401 (2001).

[4] S. R. Kurtz, A. A. Allerman, C. H. Seager, R. M. Seig, and E. D. Jones, Applied Physics Letters, 77, 400 (2000).

[5] A. Fleeck, B. J. Robinson, and D. A. Thompson, Applied Physics Letters, 78, 1694 (2001).

[6] E. V. K. Rao, A. Ougazzaden, Y. Le Bellego, and M. Juhel, Applied Physics Letters, 72, 1409 (1998).

[7] M. Shafi, Electrical and Optical Studies of Dilute Nitride and Bismide Compound Semiconductors, PhD thesis, Nottingham University, (2010).

[8] Q. Gao, H. H. Tan, C. Jagadish, and P. N. K. Deenapanray, Japanese Journal of Applied Physics, 42, 6827 (2003).

[9] M. J. Milla, A. Guzma, R. Gargallo-Caballero, J. M. Ulloa, A. Hierro, Journal of Crystal Growth, 323, 215 (2011).

[10] R. Gargallo-Caballero, A. Guzman, M. Hopkinson, J. M. Ulloa, A. Hierro, and E. Calleja, Physics Status Solidi C, 6, 1441, (2009).

[11] K. Uno, M. Yamada, I. Tanaka, O. Ohtsuki and O. Takizawa, Journal of Crystal Growth, 278, 214 (2005).

[12] H. F. Liua, N. Xianga, H. L. Zhoub, S. J. Chuac, P. Yangd, H. O. Moser, Journal of Crystal Growth, 301, 548 (2007).

[13] V. Liverini, A. Rutz, U. Keller, S. Schon, Journal of Crystal Growth, 301, 556 (2007).

[14] S. Burkner , M. Baeumler , J. Wagner, E. C. Larkins, W. Rothermund, J. D. Ralston, Applied Physics Letters, 79, 6818 (1996).

[15] H. D. Sun, R. Macaluso, S. Calvez, and M. D. Dawson, F. Robert, A. C. Bryce, J. H. Marsh, P. Gilet, L. Grenouillet, A. Million, K. B. Nam, J. Y. Lin, and H. X. Jiang, Journal of Applied Physics, 94 (12), 7581 (2003).

[16] J. Zhao, Z. C. Feng, Y. C. Wang, J. C. Deng, and G. Xu, Surface & Coatings Technology, 200, 3245 (2006).

[17] H. P. Xin, K. L. Kavanagh, M. Kondow, and C. W. Tu, Journal of Crystal Growth, 201/202, 419 (1999).

[18] F. Martelli, M. Grazia Proietti, M. Gabriella Simeone, M. Rita Bruni, and M. Zugarini, Journal of Applied Physics, 71, 539 (1992).

[19] M. C. Y. Chan, C. Surya, and P. K. Wai, Journal of Applied Physics, 90, 197 (2001).

[20] L. H. Li, Z. Pan, W. Zhang, Y. W. Lin, Z. Q. Zhou, and R. H. Wu, Journal of Applied Physics, 87, 245 (2000).

[21] M. Albrecht, V. Grillo, T. Remmele, P. Strunk, A. Y. Egorov, Gh. Dumitras, H. Riechert, A. Kaschner, R. Heitz, and A. Hoffmann, Applied Physics Letters, 81, 2719 (2002).

[22] M. Shafi, R. H. Mari, A. Khatab, M. Henini, A. Polimeni, M. Capizzi, and M. Hopkinson, Journal of Applied Physics, 110, 124508 (2011).

[23] T. Kitatani, K. Nakahara, M. Kondow, K. Uomi, and T. Tanaka, Journal of Crystal Growth, 209, 345 (2000).

[24] S. Francoeur, G. Sivaraman, and H. Temkin, Applied Physics Letters, 72, 1857 (1998).

[25] H. F. Liua, N. Xianga, and S. J. Chua, Journal of Crystal Growth, 290, 24 (2006).

[26] X. Z. Chen, D. H. Zhang, Y .J. Jin, J. H. Li, J. H. Teng, and N. Yakovlev, Journal of Crystal Growth, 362, 197 (2013).

[27] P. Klar, H. Gruning, J. Koch, S. Schafer, K. Volz, W. Stolz and W. Heimbrodt Physical Review B, 64, 121203 (2001).

CHAPTER 9: CONCLUSION AND FUTURE WORK

9.1 CONCLUSION

This chapter summarizes the research work carried out on the optical properties of III-V QDs semiconductors, namely InAlAs/AlGaAs QDs, and the optical and structural characterization of dilute nitrides InGaAsN quantum wells grown on different GaAs substrate orientations.

As these material systems are comparatively new, it is very important to investigate if their MBE growth on non-conventional GaAs planes helps to improve their optical and structural properties. Acquiring knowledge and deeper understanding about their electronic and optical properties is important in order to develop novel devices based on these materials for electronic and optoelectronic applications.

In addition, suggestions for future work will be highlighted. The MBE samples used in this thesis were investigated by PL, TEM, EDX and SIMS techniques.

9.1.1 InAlAs QUANTUM DOTS

In this work, a systematic study was carried out on the effect of the growth parameters of self-assembled InAlAs/AlGaAs QDs deposited on different GaAs substrate orientations by molecular beam ebitaxy (MBE).
Generally it was found that the optical quality of InAlAs QDs strongly depends on the growth conditions and GaAs substrate direction.
Photoluminescence (PL) has been used to investigate the optical properties of InAlAs QDs grown both on the conventional (100) and non-(100) GaAs substrates. These include:

(i) Effect of amount of deposited material of $Al_{0.35}In_{0.65}As/Al_{0.45}Ga_{0.55}As$ QDs (3.7MLs, and 4.4MLs) grown on (100), (311)A, and (311)B GaAs planes.

(ii) Effect of confinement on 4.4MLs $Al_{0.35}In_{0.65}As/Al_yGa_{1-y}As$ QDs with y = 25%, 35%, 45%, and 55% grown on (311)B GaAs planes.

(iii) Effect of growth temperature, namely 450 ^{0}C, 500 ^{0}C and550 ^{0}C.

The experimental results have shown the following:

(i) The optical quality of the 3.7MLs $Al_{0.35}In_{0.65}As/Al_{0.45}Ga_{0.55}As$ QDs grown on high index planes is found to be inferior to that of (100) QDs. This could be due to the non-optimized growth conditions and layer structure.

(ii) The optical efficiency of 4.4MLs $Al_{0.35}In_{0.65}As/Al_{0.45}Ga_{0.55}As$ QDs grown on different planes increased following this sequence (311)B > (100) > (311)A. The lower density of InAlAs QDs on the (311)A orientation could be responsible for this low emission efficiency.

(iii) By comparing the optical efficiency of QDs with four different Al concentrations in the confining barrier matrix (25%, 35%, 45%, and 55%) it is found that the PL emission from $Al_{0.35}In_{0.65}As/Al_{0.45}Ga_{0.55}As$ QDs have better thermal stability amongst all QDs.

(iv) By comparing the optical efficiency of QDs grown at three different growth temperatures (450 ^{0}C, 500 ^{0}C, and 550 ^{0}C) it is established that $Al_{0.35}In_{0.65}As/Al_{0.45}Ga_{0.55}As$ QDs grown at the growth temperature of 550 ^{0}C show better efficiency but with largest FWHM, which indicates large inhomogeneous distribution of the dots.

In order to improve the optical quality of $Al_{0.35}In_{0.65}As/Al_{0.45}Ga_{0.55}As$ QDs grown on (100), (311)A, and (311)B planes, a rapid thermal annealing study has been carried out.

QDs grown on different substrate orientations have been annealed for 30 seconds at four different temperatures (500 ^{0}C, 600 ^{0}C, 700 ^{0}C, and 800 ^{0}C). The 500 ^{0}C annealing temperature did not change appreciably the peak position or intensity. A stronger PL intensity and narrower line width with increasing annealing temperature up to 700 ^{0}C for all planes have been observed, indicating improvement of the material quality

Blueshift of the PL emission peak with increasing annealing temperature has also been observed which is due to the interdiffusion of group III atoms during the annealing process. The amount of blueshift and hence the extent of interdiffusion depends on the growth plane. A larger blue shift is observed for (311)B and (100) QDs. In contrast a very small blue shift was observed from (311)A QDs. Annealed

(311)A QDs show better and improved thermal stability than as-grown QDs, and this observation could be explained by the intermixing effect that affects the carrier confining potential. By increasing the annealing temperature to 800 ^{0}C, no PL signal was detected which may be due to dissolution of QDs at this high temperature.

9.1.2 InGaAsN QUANTUM WELLS

In this part of work, a detailed and systematic study of the optical and structural properties of $In_{0.36}Ga_{0.64}As_{1-y}N_y$/GaAs double QWs (4, and 7 nm) grown by MBE on GaAs has been carried out. These include:

i) Effect of GaAs substrate orientation ((100), (311)A, and (311)B) on optical and structural properties.
ii) Effect of nitrogen percentage, namely 0%,1%, and 2% on optical and structural properties.

The experimental results have shown the following:

The PL efficiency was found to decrease with increasing nitrogen content for all planes but with different order of magnitudes. This phenomenon suggests that the nitrogen incorporation creates defect-related non-radiative centers, whose concentrations are plane dependent.

It was also found that the PL energy decreases with incorporating 1% nitrogen by comparable amount for all substrate orientation (82-96 meV). However, by increasing the nitrogen to 2%, the PL energy reduction is strongly dependent on the substrate orientation suggesting that the nitrogen incorporation is plane dependent. QWs grown on (311)A GaAs plane show higher nitrogen incorporation over all the other planes.

The temperature dependence of the PL peak energy indicated significant exciton localization at low temperatures for QWs grown on (311)B and the band gap varies more weakly with temperature than in QWs without nitrogen.

TEM measurements show that (311)B QWs have inferior structural properties than QWs grown on (311)A and (100). TEM images demonstrated that the (311)B QWs interfaces are undulated and not uniform. In contrast QWs grown on (311)A and (100) display very uniform and very flat interfaces.

Indium composition profiles in different planes were determined by Energy dispersive X-ray (EDX) measurements. The results show similar In distributions for all planes. However, High Angle Annular Dark Field images display inhomogeneity of the indium distribution in the QWs grown on (311B) plane.

The effect of thermal annealing on the optical properties of $In_{0.36}Ga_{0.64}As_{1-y}N_y/GaAs$ double QWs grown on different planes was investigated for two sets of samples having 0% and 1% nitrogen. It was found that annealing at 700 ^{0}C for 30 seconds is the optimum annealing temperature which improves the PL efficiency for all QWs. The PL enhancement is larger in samples with 1% nitrogen than 0%. This PL improvement, which may be explained by the annihilation of defects introduced by the incorporation of nitrogen, is accompanied by a blue shift. Secondary ion mass spectroscopy (SIMS) shows that In/Ga intermixing, which occurs at the interface between QW and barrier, could account for the origin of this energy shift in QWs grown on (311)A and (100) planes. The amount of diffusion of In out of the QW depends on the growth plane. It is larger for QWs grown on (311)B plane as compared to the other planes. However, in contrast to the (311)B QWs the nitrogen content in the (100) and (311)A QWs doesn't change upon annealing.

9.2 SUGGESTIONS FOR FUTURE WORK

1- It will be of paramount importance to carry out a further study to investigate the effect of arsenic overpressure and growth rate on the optical properties of InAlAs QDs.

   Higher As pressures in MBE growth produce better quality epitaxial layers on high-index GaAs (n11) substrates as reported by K. Fujita [1].

2- The decrease of the optical efficiency of $InAlAs/Ga_{1-y}Al_yAs$ QDs with y=55% grown at higher temperatures is still an open question. This needs

further investigation by techniques like deep level transient spectroscopy (DLTS) to investigate the possible defect which may be incorporated at this higher Al percentage.

3- Although I believe that the low optical efficiency of QDs grown on (311)A plane compared to other planes is due to the low dot density formed on this plane as reported for another types of dots, structural characterization like atomic force microscopy is required to confirm this explanation.

   Low-density QDs are preferred for spintronics spectroscopy; InAlAs QDs have a disadvantage in this respect, since their density tends to be high compared to InAs QDs. The (311)A plane gives the opportunity to grow InAlAs QDs with lower density which facilitate the single dot study. Studying the spintronics of single InAlAs/AlGaAs QDs is important for quantum information processing such as quantum computing.

4- Three sets of dilute nitride samples (GaAsInN) with three nitrogen percentage, namely 0%, 1% and 2% have been studied.

   The lowest energy is obtained for 7nm QW grown on (311)A plane. This energy, which has a value of 0.928 eV (1.33μm) at 290 K, is technologically important for telecommunication applications since silica fiber has the lowest dispersion at this wavelength. More samples have to be grown with larger nitrogen concentration to reach 1.55 μm where silica fiber has minima in loss.

   Due to the limitation of PL, further work is proposed to probe the exact nature and concentrations of the defect states related to nitrogen incorporation in GaAs materials by using some other useful techniques, such as DLTS technique. This may provide answers about the PL degradation after nitrogen incorporation, and PL enhancement after post growth annealing.

REFERENCES

[1] K. Fujita, P.O. Vaccaro, Current Topics in Crystal Growth Research, 3, 1 (1997).